STELLAR POPULATIONS AND FORMATION HISTORIES OF MASSIVE GALAXIES DERIVED FROM DEEP HUBBLE SPACE TELESCOPE GRISM DATA

A Dissertation

by

VICENTE ESTRADA-CARPENTER

Submitted to the Graduate and Professional School of
Texas A&M University
in partial fulfillment of the requirements for the degree of

DOCTOR OF PHILOSOPHY

Chair of Committee,	Casey Papovich
Committee Members,	Robert Kennicutt
	Jonelle Walsh
	Jianhua Huang
Head of Department,	Grigory Rogachev

August 2021

Major Subject: Astronomy

ABSTRACT

A key question in the field of galaxy evolution is: How do massive quiescent galaxies form in the early universe? Many works have shown the existence of massive quiescent galaxies up to redshifts of z $>$ 3 (when the age of the universe was < 2.2 Gyr). These galaxies are puzzling because they have been able to form massive amounts of stellar mass (log(M/M$_\odot$) > 10) in a relatively rapid fashion, even simulations have struggled to recreate these galaxies. Therefore we are lacking some knowledge about the formation of massive galaxies. My research has focused on understanding the star-formation, chemical, morphological, and quenching histories of high redshift ($0.7 < z < 2.5$) massive galaxies using *HST* WFC3 grism spectra + photometry from the CLEAR (CANDELS Lyman-α Emission at Reionization) survey. Utilizing the data from the CLEAR survey has allowed me to study large samples ($\sim$ 100) of spectra from massive galaxies, something not currently possible from ground-based surveys. By studying these massive galaxies at high redshift we can better constrain their star-formation histories as the uncertainty on the timescales(and therefore the ages) of stars and stellar populations are quasi-logarithmic. My work has touched upon topics such as the mass - stellar metallicity relationship (showing that this relationship does not evolve with redshift up a z = 1.7), the link between a galaxies formation redshift, and its morphology (providing evidence that the most compact galaxies get their compact morphologies from having formed in the early universe), and the evolution of galaxies as they cross the green valley (showing that galaxies form more rapidly at high redshift and that fast quenching occurs more in high mass galaxies). These works have begun to outline how massive quiescent galaxies in the early universe formed.

DEDICATION

Dedicated to my son, Damien.

ACKNOWLEDGMENTS

I would like to thank my advisor Dr. Casey Papovich for all his support and mentorship during my Ph.D. His guidance has helped me develop into the scientist I am today. I am deeply grateful for all the support and encouragement from my wife, Jamie Estrada-Carpenter, who has always pushed me to accomplish my goals. I would like to express my sincere gratitude towards my family for all their support specifically my mother for always believing in me, my father for instilling in me a hard work ethic, and my grandfather for encouraging my love of astronomy. Last I would like to thank my collaborators in the CLEAR survey for helping to guide and develop my science.

CONTRIBUTORS AND FUNDING SOURCES

Contributors

This work was supported by a dissertation committee consisting of Professor Casey Papovich, Professor Robert Kennicutt and Professor Jonelle Walse of the Department of Physics and astronomy and Professor Jianhua Huang of the Department of Statistics.

Chapter 2 also includes contributions from Dr. Ivelina Momcheva, Dr. Gabriel Brammer, Dr. James Long, Dr. Ryan F. Quadri, Dr. Joanna Bridge, Dr. Mark Dickinson, Dr. Henry Ferguson, Dr. Steven Finklestein, Dr. Mauro Giavalisco, Dr. Catherine M. Gosmeyer, Dr. Jennifer Lotz, Dr. Brett Salmon, Dr. Rosalind E. Skelton, Dr. Jonathan R. Trump, and Dr. Benjamin Weiner.

Chapter 3 includes contributions from Dr. Ivelina Momcheva, Dr. Gabriel Brammer, Dr. Raymond Simons, Dr. Joanna Bridge, Nikko J. Cleri, Dr. Henry Ferguson, Dr. Steven Finklestein, Dr. Mauro Giavalisco, Dr. Intae Jung, Dr. Jasleen Matharu, Dr. Jonathan R. Trump, and Dr. Benjamin Weiner.

Chapter 4 includes contributions from Dr. Ivelina Momcheva, Dr. Gabriel Brammer, Dr. Raymond Simons, Dr. Mauro Giavalisco, Dr. Jasleen Matharu, Dr. Jonathan R. Trump, and Dr. Benjamin Weiner.

Funding Sources

This work was received support from the NASA Headquarters under the Future Investigators in NASA Earth and Space Science and Technology (FINESST) award 19-ASTRO19-0122, as well as support from the Hagler Institute for Advanced Study at Texas A&M University. This work is based on data obtained from the Hubble Space Telescope through program number GO-14227. Support for Program number GO-14227 was provided by NASA through a grant from the Space Telescope Science Institute, which is operated by the Association of Universities for Research in Astronomy, Incorporated, under NASA contract NAS5-26555. This work is supported in part by the National Science Foundation through grants AST 1614668. The authors acknowledge the Texas

A&M University Brazos HPC cluster and Texas A&M High Performance Research Computing Resources (HPRC, `http://hprc.tamu.edu`) that contributed to the research reported here.

TABLE OF CONTENTS

Page

LIST OF FIGURES

FIGURE Page

LIST OF TABLES

TABLE Page

1. INTRODUCTION

The field of galaxy evolution aims to describe how galaxies form, age, quench, and passively evolve. This is done by studying the stars that makeup galaxies. These stellar populations contain information about the formation histories, chemical enrichment, stellar mass, and ages of galaxies.

Massive galaxies are key to the field of galaxy evolution. Their high stellar masses make them easy to study and provide plenty of high signal-to-noise data. Therefore we have a good understanding of the properties of massive galaxies, relative to their lower mass peers. Yet the origins of high redshift massive quiescent galaxies are still not yet understood. Some of the questions these galaxies produce are how do they form their high stellar masses ($\log(M/M_{\odot})$ > 10) in such a rapid fashion, what are the details of their chemical enrichment histories including how they enrich up to Solar metallicities so quickly, and where do they get their compact morphologies from. Simulations struggle to recreate the fractions of massive quiescent galaxies that we observe at high redshift (18; 19), therefore something is missing in our understanding of the evolution of massive galaxies at high redshift. By uncovering these details we can better understand the physical processes of the early universe such as gas accretion, star-formation efficiency, feedback, and metal production/retention (20; 21; 22).

Many works have made strides in this area of galaxy evolution, and from these studies, we can begin to piece together what the story of the formation of high redshift quiescent galaxies is. These galaxies form their stellar mass rapidly (23; 24; 25), leaving behind a galaxy with compact morphology (14; 26). They are made up of old stellar populations (10; 5; 27; 13), with high ($\sim$ Solar) overall metallicity (13; 8; 28).

To study the stellar populations of galaxies we need spectral information, which we gather as either photometric data (low sampling with high signal-to-noise) or spectral data (higher sampling with lower signal-to-noise). Because of its higher sampling rate, spectral data is more desirable as it is more information-dense, though currently our samples of quiescent galaxies are limited at high redshift to small populations at the high mass end. This is because high redshift massive

quiescent galaxies are not ideal targets. They lack young stellar populations and short-lived stars and therefore have much lower luminosities than their star-forming counterparts. In addition, the fraction of quiescent galaxies decreases at higher redshifts going from $\approx 60\%$ at z = 0.5 to $\approx 30\ \%$ at z = 2 (29; 30; 31), making collecting large samples difficult. Also, many of the optical age and metallicity features within the spectra (such as e.g., Ca HK, the 4000 Å break, Balmer absorption lines, Mg_b) of these galaxies have been redshifted into the IR. This makes collecting spectral data for these galaxies from the ground difficult due to the presence of a high density of telluric emission lines (32). Collecting spectral data of the optical age and metallicity features is important because these information-dense features are well studied and well modeled.

One solution to the limiting factors is to use the *HST* WFC3 grism to study the rest-frame optical spectra from these high redshift massive quiescent galaxies. The *HST* WFC3 grism provides low-resolution slitless spectroscopy with *HST* levels of resolution. The *HST* WFC3 G102 and G141 grisms have an observed frame wavelength coverage of $0.8 < \lambda <$ 1.7 micron. This wavelength window allows for coverage of the optical age and metallicity features at $0.7 < z < 2.7$. The slitless nature of the grisms means that we can collect large samples of galaxies by only observing a single *HST* field. The CANDELS Lyman-α Emission at Reionization (CLEAR) survey is a *HST* WFC3 G102 survey of 12 fields in GOODS North AND GOODS South with $\sim$ 12 orbit depth per field. At this depth, we can recover $\sim$ 400 galaxies per field. These large sample sizes make the *HST* WFC3 grisms a great instrument to build large samples of spectra. The spectra are, however, low resolution (G102: R $\sim$ 200, G141: R $\sim$ 100). This is not strictly negative though. Because the light is not highly dispersed we can recover the spectra of lower mass targets. The grism spectra also benefit from the excellent stable / accurate flux calibration from *HST* something that is difficult to obtain from ground based telescopes.

The analysis of stellar populations using grism data is still a fairly new field. The goal of this research is to use a forward modeling process to fit the stellar populations of high redshift massive galaxies using data from the CLEAR survey. The forward modeling process, outlined in Chapter 2, is a way to model galaxy spectra while including all the systematics from the grism. The main

systematic we need to account for is morphological broadening (33). This effect occurs because the grism is slitless, therefore when the light is dispersed each wavelength is recorded using the morphology of the entire galaxy. This means that the more extended a galaxy is the more light from one wavelength will seep into others, effectively broadening the spectra. This effect is unique to each galaxy and roll angle, as several roll angles are used for each field as a way to identify and remove contamination.

The tools and techniques outlined in this dissertation have allowed for the study of several relationships at their highest redshifts yet.

In this dissertation we do the following: In Chapter 2 we test how well we can recover stellar population parameters using our forward modeling spectral energy distribution (SED) fitting technique. This was done in an effort to recover light-weighted ages and metallicities from high redshift massive quiescent galaxies using only *HST* WFC3 G102 grism data from the CLEAR survey. In Chapter 3 we use updated constraints (derived from fitting grism spectra + photometry) to study the link between a galaxies formation redshift and its morphology. In Chapter 4 we characterize galaxies as they cross the green valley on their way to quenching. We study the ages at which galaxies begin to quench and what happens to their morphologies as they quench.

2. AGES AND METALLICITIES OF QUIESCENT GALAXIES AT $1.0 < z < 1.8$ DERIVED FROM DEEP HUBBLE SPACE TELESCOPE GRISM DATA*

2.1 Introduction

Astronomers have recently developed a general picture of the formation, chemical enrichment, and evolution of massive galaxies ($\log M_*/M_\odot \sim 10-11$) from $z \sim$ 3–4 to the present day. These galaxies formed their stellar populations early, reaching a peak star-formation rate (SFR) at $z > 2$ (e.g., 34; 23; 35; 36), and quenching as early as $z \sim 3-4$ (37; 38; 39; 40; 41). Massive galaxies continue to quench and remain in phases of quiescent evolution to lower redshift, where the fraction of quiescent galaxies with $\log M_*/M_\odot > 10.5$ rises from $\sim$ 30% at $z \sim 2$ to ≈60% by $z = 0.5$ (29; 30; 31). Because these massive galaxies formed their stars and quenched so early, they are testing grounds for physical processes associated with gas accretion, star-formation efficiency, feedback, metal production and retention (20; 21; 42).

The next step is to understand in greater detail the galaxies' star-formation and chemical enrichment histories. These effects are all encoded in the colors and spectral features of the galaxies' stellar populations, which allows one to constrain the ages and metallicities using features that are sensitive to independent changes in these parameters. For example, line indexes (such as e.g., D_n4000, Hδ_A+Hγ_A, Hβ, Mgb, [MgFe]$'$, [Mg$_2$Fe]) have long been used to study these properties in galaxies, and to study their evolution with mass and redshift (e.g., 43; 44; 27; 10; 5; 45; 4; 46).

Regarding the evolution of metals in galaxies, most studies have focused on the relation between the gas-phase metallicity (usually measured from emission line ratios in active galaxies) and galaxy stellar-mass, and their evolution with redshift (e.g., 47; 48; 49; 50; 51). It has been more difficult to measure evolution of metallicity of the stellar populations in galaxies. The spectral absorption

**Reprinted with permission from "CLEAR I: Ages and Metallicities of Quiescent Galaxies at $1.0 < z < 1.8$ Derived from Deep Hubble Space Telescope Grism Data" by Estrada-Carpenter, Vicente; Papovich, Casey; Momcheva, Ivelina; Brammer, Gabriel; Long, James; Quadri, Ryan F.; Bridge, Joanna; Dickinson, Mark; Ferguson, Henry; Finkelstein, Steven; Giavalisco, Mauro; Gosmeyer, Catherine M.; Lotz, Jennifer; Salmon, Brett; Skelton, Rosalind E.; Trump, Jonathan R.; Weiner, Benjamin, 2019. The Astrophysical Journal, Volume 870, 133, Copyright 2019 by The American Astronomical Society.*

and continuum features are sensitive to both α-elements and Iron-peak elements (which dominate the opacity in stellar photospheres). Analyzing the spectra of quiescent galaxies at low-redshift ($z0.1$), many studies have found that massive galaxies have Solar (or super-Solar) metallicities and abundance ratios, with formation epochs at $z > 2$ (e.g. 27; 52; 10; 45; 53). (5, hereafter Gal14) conducted one of the first studies at higher redshift ($z \sim 0.7$), and showed that the spectra of quiescent galaxies with $\log M_*/M_\odot > 10.5$ are already consistent with high metallicity ($Z \sim Z_\odot$), while star-forming galaxies have sub-Solar metallicities (and require additional enrichment from $z \sim 0.7$ to the present-day, see also 8). The implication is that some fraction of the massive, quiescent galaxy population must have enriched to approximately Solar metallicities at even higher redshift, presumably at $z > 2$.

To understand the evolution of massive quiescent galaxies therefore requires that we push spectroscopic studies to higher redshift, closer to the quenching epoch of these galaxies. The reason for this is that evolutionary changes in stellar populations occur on timescales $d\log t \propto dt/t$ (see e.g., 54). Therefore, galaxy properties change more rapidly at higher redshift (55; 56; 57; 58), and more accurate (relative) measures of galaxy ages can be made by observing quiescent galaxies at $z > 1$. The difficulty is that all the rest-frame optical spectral features used to measure both stellar population metallicities and ages shift above $\sim$1 for galaxies at $z > 1$, where studies from ground-based telescopes are subject to higher backgrounds and a high density of telluric (night-sky) emission lines (see, 32). Several studies have now measured galaxy metallicities at high redshift with near-IR spectrographs on ground-based telescopes (e.g., 25; 59; 60; 61), but are often limited to one or a few objects or require stacking. An attractive alternative solution is to take advantage of space-based spectroscopy using, for example, the *HST* grisms, which have been used to study the properties of stellar populations in distant galaxies (e.g., 62; 63; 33; 64; 65; 7; 66; 8; 67).

Here, we use deep grism spectroscopy taken with *HST* spectroscopy with WFC3 using the G102 grism, covering wavelengths ≈8000 Å to 11,500 Å. We study the stellar populations of a sample of massive ($\log M/M_\odot \geq 10$) quiescent galaxies at $1 < z < 1.8$. At these redshifts, the G102 spectra cover crucial rest-frame optical absorption features at spectral resolution of $R \sim 210$,

including the strength of the redshifted 4000 Å break, Balmer lines (Hδ, Hγ,Hβ), Ca HK, and Mgb absorption features) sensitive to stellar population ages and metallicities of galaxies down to $J \simeq 23 - 24$ AB mag. The G102 data also provide much improved measurements of the galaxy redshifts. We use a Bayesian method with a forward-modeling approach, whereby we simulate stellar population models of the two–dimensional (2D) WFC3/G102 spectra using the galaxies' accurate morphologies at the appropriate roll-angle for *HST* combined with the G102 spectroscopic resolution.

One of the goals of this project is to determine the accuracy of stellar population properties measured with lower-resolution grism data. This has important implications for the next generation of space telescopes (*JWST* and *WFIRST*), and will allow the study of stellar populations of galaxies in much larger samples and at higher redshifts. As we push to higher redshifts, all important age- and metallicity-sensitive spectroscopic features shift into the IR. As we show here, even relatively low resolution ($R \sim 100 - 200$) spectroscopy can recover metallicity and age diagnostics of higher redshift galaxies (provided the spectra cover the age– and metallicity–sensitive features). This will have a wide range of application for future space missions.

The remainder of this paper is organized as follows: In Section 2 we describe the parent sample selection. In Section 3 we summarize the *HST* observations, data reduction, and spectral extraction methods. In Section 4 we describe the G102 spectral modeling procedure, including tests to demonstrate our ability to recover accurate stellar population parameters. We then discuss the model fits to the G102 data for the galaxies in our sample. In Section 5 we discuss the constraints on metallicities and (light-weighted) age for these galaxies, as well as implications for the formation, quenching and evolution of these galaxies. In Section 6 we present our conclusions and describe future work using this method. In the Appendices we show the model fits to the full galaxy sample, discuss our method to derive errors on model templates, discuss the Bayesian evidence in support of different stellar populations derived from the modeling, and we test our posterior stacking technique.

Throughout we use a cosmology with $\Omega_M = 0.3$, $\Omega_\Lambda = 0.7$, and h = 0.7, where $H_0 = 100\ h$ km s^{-1} Mpc^{-1} consistent with the recent constraints from Planck (68) and the local distance scale

of (69). All magnitudes are in "absolute bolometric" (AB) units (70).

2.2 Parent Sample and Sample Selection

The *HST* WFC3 G102 grism wavelength coverage ($8000 < \lambda < 11500$ Å) provides a wealth of information for distant galaxies as it probes the rest-frame UV and optical range for redshifts $z \sim 1$ (rest-frame coverage: $4000 < \lambda < 5750$ Å) to $z \sim 1.8$ (rest-frame coverage: $2850 < \lambda < 4100$ Å). These wavelengths cover many age– and metallicity–sensitive spectral features, including Ca HK, the 4000 Å/Balmer break, Balmer-series lines, several Lick indices, Mg*b*, and some Fe1 lines (though not all features are covered at all redshifts by the G102 grism, as we will discuss below). With this in mind, we focused on a sample of quiescent galaxies selected to have low levels of star formation compared to their past averages. By modeling the spectra of such galaxies, we are able to constrain the galaxies' star-formation histories (SFHs, when did they form their stars and when did they quench?), and enrichment histories (when did they form their metals?).

The CLEAR survey includes G102 observations within the CANDELS coverage of the GOODS-North deep (GND) and GOODS-S deep (GSD) fields (71; 72). We selected galaxies from an augmented version of the photometric catalog from 3D-HST (16; 65) that includes photometry from Y–band imaging (using the WFC3 F098M and/or F105W imaging), which exists over the majority of the GND and GSD CANDELS fields (72)[1]. More importantly, the WFC3 F098M and F105W filters provide imaging at comparable wavelengths covered by the WFC3 G102 grism, and is important for object extraction and identifying the locations of nearby objects that may cause spectral contamination.

The original 3D-HST data release did not include the F098M nor F105W data in the GOODS fields (because these have less uniform coverage, and are only available in two of the five CANDELS fields). Because we require them for our program, we have added them to the 3D-HST photometric catalog following the identical approach as (16). We first matched the PSFs of the F098M and F105W images to the detection image (using a weighted combination of the WFC3 F125W +

[1] All of the GND fields and most of the GSD fields are covered by F105W from CANDELS (71; 72) and from the direct imaging associated with our grism program, see Section 3. The northern portion of the GSD overlaps with the WFC3 ERS field (73) for which F098M is available.

F140W + F160W images). We then reran SExtractor (v2.8.6, 74) in dual-image mode, using the detection image to photometer sources in the F098M and F105W images. We then inserted these fluxes into the existing 3D-HST catalogs along with rederived photometric redshifts and rest-frame $U-V$ and $V-J$ colors using EAZY (75), and stellar masses from FAST (76) (using a (77) IMF). For details of the procedures, see (16).

It is our goal to select galaxies that are mostly devoid of star-formation, with a redshift that places the 4000 Å/Balmer break in the G102 grism wavelength coverage). We first selected a parent sample of galaxies to have photometric redshifts (z_{phot}) in the range $0.8 < z_{\rm phot} < 2.0$ and stellar mass $\log(M_*/M_\odot) > 10.0$. This z_{phot} redshift range ensures that we select *all* galaxies that possibly place the 4000Å/Balmer break in the G102 wavelength coverage, when accounting for errors on the photometric redshifts. Our stellar-mass constraint ensures that the spectra have sufficient signal-to-noise for accurate modeling (see below). We filter stars from our parent sample, using objects that have stellarity values from the 3D-HST catalog (defined by SExtractor) with `CLASS_STAR` < 0.8. We remove any source with an X-ray detection (within a search radius of 05) in the 2 Ms Chandra Deep Field-North Survey (78) and 7 Ms Chandra Deep Field-South Survey catalogs (79).

Based on the rest-frame $U-V$ and $V-J$ colors, we selected galaxies that are actively star-forming from those in quiescent phases of evolution (compared to star-forming/active galaxies, 80; 2; 81). We selected a parent sample of quiescent galaxies from our augmented 3D-HST catalog using the definition in (2),

$$\begin{aligned} (U-V) &\geq 1.382\,\mathrm{mag}, \\ (V-J) &\leq 1.65\,\mathrm{mag},\ \mathrm{and} \\ (U-V) &\geq 0.88\times(V-J)+0.59 \end{aligned} \tag{2.1}$$

Figure 2.1 shows the $U-V$ versus $V-J$ color distribution for the full galaxy catalog and for

Table 2.1: Properties of the $1 < z < 1.8$ Quiescent Galaxy Sample

ID (1)	z_{phot} (2)	J_{125} (Mag) (3)	Log $(M_*/M_\odot)$ (4)	SNR (5)
GND23758	$0.94^{+0.04}_{-0.04}$	20.5	11.0	12.3
GND37955	$0.97^{+0.03}_{-0.03}$	21.3	10.8	7.3
GND16758	$0.99^{+0.04}_{-0.03}$	21.2	10.8	10.1
GSD43615	$1.04^{+0.04}_{-0.04}$	21.7	10.7	6.9
GSD42221	$1.04^{+0.04}_{-0.04}$	21.7	10.5	7.7
GSD39241	$1.04^{+0.05}_{-0.04}$	20.9	10.9	12.4
GSD45972	$1.05^{+0.03}_{-0.02}$	21.1	10.9	12.3
GSD44620	$1.08^{+0.03}_{-0.03}$	22.1	10.5	4.8
GSD39631	$1.08^{+0.03}_{-0.03}$	21.3	10.7	9.2
GSD39170	$1.08^{+0.03}_{-0.02}$	20.3	11.1	20.8
GND34694	$1.09^{+0.04}_{-0.03}$	21.0	10.9	9.9
GND23435	$1.09^{+0.06}_{-0.06}$	22.5	10.3	4.4
GSD47677	$1.10^{+0.04}_{-0.04}$	22.5	10.1	4.2
GSD39805	$1.16^{+0.03}_{-0.03}$	22.5	10.6	3.9
GSD38785	$1.18^{+0.04}_{-0.03}$	21.5	10.9	7.5
GND32566	$1.18^{+0.05}_{-0.05}$	21.7	10.6	6.6
GSD40476	$1.19^{+0.03}_{-0.03}$	21.9	10.6	8.6
GND21156	$1.20^{+0.04}_{-0.04}$	20.9	11.2	15.8
GND17070	$1.22^{+0.04}_{-0.04}$	21.2	10.9	5.3
GSD35774	$1.23^{+0.03}_{-0.03}$	21.0	10.9	10.0
GSD40597	$1.24^{+0.03}_{-0.03}$	20.9	11.0	16.3
GND37686	$1.27^{+0.04}_{-0.04}$	21.3	10.9	8.4
GSD46066	$1.32^{+0.03}_{-0.03}$	21.7	10.8	3.4
GSD40862	$1.33^{+0.04}_{-0.04}$	21.7	10.9	4.9
GSD39804	$1.36^{+0.04}_{-0.03}$	21.6	10.9	4.5
GND21427	$1.48^{+0.05}_{-0.05}$	22.0	10.7	2.5
GSD40623	$1.49^{+0.11}_{-0.09}$	22.3	10.8	4.7
GSD41520	$1.64^{+0.04}_{-0.04}$	22.2	10.9	3.4
GSD40223	$1.65^{+0.05}_{-0.05}$	22.7	10.7	2.3
GSD39012	$1.66^{+0.06}_{-0.06}$	22.6	11.1	1.8
GSD44042	$1.67^{+0.05}_{-0.05}$	21.8	11.0	4.0

Table 2.2: (1) Galaxy ID number in the GND or GSD 3D-HST catalog. (2) photometric redshift from the 3D-HST catalog; (3) observed J_{125} magnitude from the 3D-HST catalog; (4) stellar mass derived using FAST; (5) SNR per pixel measured at 8500-10500 Å in the stacked G102 spectrum.

those galaxies in our parent sample. Galaxies in the quiescent UVJ region typically have specific SFRs (sSFRs) $< 10^{-2}$ Gyr^{-1} (82), indicative of galaxies with lower current SFRs compared to their

past averages (e.g., for a galaxy with a current stellar mass 10^{11} $M_\odot$ and sSFR=10^{-2} $M_\odot$ yr^{-1}, the current SFR is Ψ=1 $M_\odot$ yr^{-1}, whereas the SFR averaged over the past Hubble time is $\langle\Psi\rangle \sim 20$ $M_\odot$ yr^{-1}). Galaxies with such low sSFR qualify as having "suppressed" SFRs (83). Past studies of the evolution of these galaxies show they follow "passive" evolution of their mass-to-light ratios from redshifts as high as $z \sim 2$ (e.g., Fum16).

From the parent sample, we further require that all galaxies fall within the CLEAR *HST*/WFC3 G102 coverage (which includes 12 WFC3 pointings divided evenly between the GND and GSD fields, see Section 3). We then refit the galaxy redshifts using the G102 grism spectra themselves (as described in Section 2.5.1 below), and kept only those galaxies with $1.0 < z_{grism} < 1.8$ to ensure the G102 data cover the redshifted 4000 Å/Balmer break for all galaxies (this last step does exclude some galaxies with low SNR in the G102 data, typically $\langle SNR\rangle < 1.5$, see below). This yields our final sample of 31 galaxies. Table 2.1 shows the physical details of these galaxies.

For quiescent galaxies, the stellar mass limit of $\log M_*/M_\odot > 10.0$ corresponds roughly to a magnitude limit of $J_{125} \leq 22.7$ mag at $z < 1.8$. For such galaxies we measure a mean signal-to-noise ratio (SNR) in the G102 data of $\langle$SNR$\rangle$ $\sim$3 per pixel, averaged over λ=0.85–1.05 (see Figure 2.2 and below). Most of the quiescent galaxies in our sample lie at stellar masses well above this limit, where the median mass is $\log(M_*/M_\odot) = 10.87$ with an interquartile range (spanning the 25th to 75th percentile) of $\log(M_*/M_\odot) = 10.67$ to 10.96.

2.3 *HST* WFC3/G102 Observations and Data Reduction

2.3.1 *HST* Observing Strategy

We use *HST* slitless spectroscopic data taken from the CANDELS Lyman-α Emission at Reionization (CLEAR; *HST* GO 14227, PI: Papovich). CLEAR covers 12 fields in the GND and GSD portions of CANDELS, with deep WFC3/G102 grism observations (12 orbits, when combined with some existing data). For unresolved sources the G102 dispersion is 24.5 Å/pixel^{-1} (for the native WFC3 pixel scale, ≈013/pixel), yielding a resolution of $R \sim 210$ at 1.0 .

The observations for CLEAR were taken over dates ranging from 2015 Nov 14 to 2017 Feb 19.

Each pointing was observed for 10 or 12 orbits, with direct imaging in the WFC3 F105W (Y_{105}) paired with the G102 grism exposures. We followed the sub-pixel dither pattern used by 3D-HST (84). The observations for each pointing were divided into 3 pointings of 4-orbits each (except in GND and the ERS field) separated by $\pm$10 degrees in roll angle to mitigate collisions of spectra from nearby objects and to avoid detector defects. In addition, we combined the CLEAR data with existing 2–orbit–depth data from other programs. The observations in the GND were only 10 orbits, and were combined with existing 2-orbit-depth data from the G102 from program GO 13420 (PI: Barro). The observations in the ERS were combined with existing 2-orbit-depth G102 data from the WFC3 ERS program (PI: O'Connell; see 73; 85).

During the scheduling of the CLEAR observations, care was taken to protect the G102 grism data from a known time-variable background. This background is due to He1 emission from the Earth's atmosphere at 10830 Å, which contributes to the background in the Y–band (and G102 grism) when *HST* observes at low limb angles (see 86; 87; 88). Following the strategy of the *Hubble* Frontier Fields (88), we monitored the predicted observational ephemeris of each CLEAR observation. We then structured the observing sequence to place the direct imaging (F105W) observation at the end (or start) of the orbit when the He1 emission was expected to have the largest impact, and to place the grism (G102) observation at the start (or end) of the orbit to take advantage of the lower background levels.

2.3.2 *HST* Spectroscopic Data Reduction

The data reduction of the G102 spectra follow the procedures from the 3D-HST pipeline[2,3] (84; 65) and custom scripts[4]. This includes interlacing of the data to reduce pixel-to-pixel correlations (c.f., drizzling). Following the `calwf3` processing, we inspect the images for artifacts (satellite trails) and any regions of elevated background. Satellites typically affect a single WFC3 grism read, and in those instances, we remove the read (or reads) containing the satellite trail. If they persisted we masked them. We then rejected cosmic rays by using `AstroDrizzle`.

[2]https://github.com/gbrammer/threedhst
[3]https://github.com/gbrammer/unicorn
[4]https://github.com/ivastar/clear

To calibrate the G102 images we first divided them by the WFC3/F105W imaging flat field (see 84) and then subtracted the background following the methods in (86). We then subtracted the masked column average in each image to create the final background–subtracted images and to remove low-level residuals not accounted for in the backgrounds. Lastly, we combined the exposures taken at the same ORIENT using the interlacing discussed in (65). This provided stacked grism images containing between two and four orbits of data.

From these stacked grism images we extracted 2D and 1D spectra for individual objects in our sample defined in Section 2.2 using the procedures in (65). We required a reference direct image to provide the positions and morphologies of each object for spectroscopic extraction. As described by (65), the pipeline uses the direct image to identify and model the expected location of spectral traces associated with contaminating sources, using the positions and redshifts of sources in the input catalog (see Section 2.2).

We used the WFC3 F105W mosaics for all extractions, and for the modeling and subtraction of contamination from nearby sources (we found that using the F105W provided the best contamination modeling and subtraction compared to other WFC3 bands, likely because the F105W matches the wavelength coverage of the G102 data).

Prior to stacking spectra for each object, we visually inspected the data to ensure they were not affected by severe contamination or by other cosmetic issues. In most cases, the pipeline removed most of the contamination from nearby sources. In rare cases we identified residual contamination present in one of the stacks (in all but one case for our sample this affected only one ORIENT). In this case we either discarded the contaminated stack, or if the contamination was minor, we masked affected pixels before stacking the extracted spectra.

Figure 2.3 shows the CLEAR data for one of the galaxies in our sample (GSD 39170 with a redshift derived from the grism spectrum of $z_{grism} = 1.02$, see below), which shows the direct imaging and grism data extracted from the 4-orbit depth stacks at each of the three different roll angles (ORIENTs). This target highlights the contamination subtraction capabilities of the CLEAR pipeline, as a contaminating source lies near our target. In one orient its spectrum falls near the

target, and in another it lies directly over our spectrum. Using multiple orients we can characterize the contaminating source spectrum, and subtract it from the raw data.

2.3.3 Tests of the *HST* G102 Grism Flux Calibration

Our study requires that the relative flux calibration of the *HST* WFC3/G102 grism data be accurate as we use the continuum in our analysis of the galaxy stellar populations. In general, the absolute flux calibration of *HST* is very stable with average temporal variations constrained to be less than 1% (89), and allows us to use the continuum for this purpose. This is a significant advantage of space-based slitless spectroscopy compared to slit-fed spectroscopy from the ground, which suffers from systematics associated with terrestrial, astronomical, and instrumental backgrounds (32), and partly explains why slitless spectroscopy with *HST* is superior in some aspects compared to ground-based 10 m-class telescopes (65; 87), even though the current *HST* IR instruments operate at lower spectral resolution.

We tested the flux calibration of the extracted grism data for objects in our sample by comparing the spectra with the broad-band flux measurements from *HST* broad-band imaging. We synthesized photometry from the grism spectra by integrating them with the *HST* ACS F850LP and WFC3 F098M filters (z_{850} and Y_{098}), as these cover wavelengths also covered by the G102 grism. Figure 2.4 shows a comparison of the (flux-calibrated) extracted G102 spectra for two objects in our sample (GSD 39170 and GND 21156) to their broad-band photometry from our augmented 3D-HST catalog (see Section 2). The overall agreement between the broad–band and synthesized photometry is better than 3%.

Next, we investigated the accuracy of the relative flux as a function of wavelength (i.e., the accuracy of the "color" of the spectra as these would impact our ability to measure stellar population parameters, such as the ages and metallicity). The G102 grism covers wavelengths also covered entirely by the ACS F850LP and WFC3 F098M filters, and we therefore focus only on the subset of objects in the GSD (ERS) that have coverage in both band-passes. Figure 2.5 compares the $z_{850} - Y_{098}$ color synthesized from the G102 data to the color measured directly by these bands in our photometric catalog, plotted as a function of SNR in the G102 grism spectrum measured

at 8500-10500Å. Taking all objects, the median color difference is $\Delta(z_{850} - Y_{098}) = 0.05$ mag, this is consistent with a measurement of 0.0 mag as our measured errors are larger than the offset. Therefore we conclude that the grism flux calibration is accurate (compared to the broad-band colors), and we consider any systematic uncertainty in flux calibration to be negligible in our analysis.

2.4 Methods and Tests of Model Fitting

Our primary goal is to constrain the ages and metallicities of the quiescent galaxies in our sample. Here, we describe our method to model the spectra, to fit them to the data, and to extract posteriors of the stellar population parameters.

2.4.1 Forward Modeling of *HST* Grism Data Using Stellar Population Models

We use composite stellar population models in order to investigate the SFHs, ages, and metallicities of the quiescent galaxies at $1.0 < z_{grism} < 1.8$ in our sample. To generate model spectra, we tested two sets of models: the Flexible Stellar Population Synthesis (FSPS) models (90; 91); and the set of models from (92, BC03). The FSPS models use isochrones from the Padova stellar evolution tracks, with the MiLeS empirical stellar library for wavelengths $3500 < \lambda/\text{Å} < 7500$ (and BaSeL theoretical spectra elsewhere). The BC03 models use the Padova tracks and isochrones combined with the STELIB empirical stellar library for wavelengths $3200 < \lambda/\text{Å} < 9500$ and BaSeL spectra elsewhere. For both the BC03 and FSPS models we assume a (93) IMF (although this has minimal impact on the age or metallicity constraints we infer).

While we consider both BC03 and FSPS for our model fitting. In Appendix A.4, we find Bayesian evidence against the BC03 models in favor of the FSPS models. Fum16 obtain similar results, where they show that FSPS models provide better agreement (lower χ^2 values) for fits to stacked quiescent galaxy spectra of similar resolution and rest-frame wavelength. We therefore report results from the FSPS for the remainder of this work in light of the Bayesian evidence against the BC03 models.

We generated a large range of spectra from the FSPS models, spanning a range in age ($t =$

$0.5 - 6.0$ Gyr, in steps of 0.1 Gyr), metallicity ($Z = 0.1 - 1.6\ Z_{\odot}$ in steps of 0.05 $Z_{\odot}$), and SFH ($\tau = 0.0 - 3.0$ Gyr in steps of 0.1 Gyr). Regarding the metallicity, as we fit to the full spectra, our measurements of the metallicities are affected both by the individual elements in the spectral absorption features and those that affect the stellar opacities that make up the continua. Since the latter are dominated primarily by Iron peak elements (53), we expect that the "metallicity" (Z) here is a proxy for [Fe/H]. Nevertheless, there is evidence for higher abundances of [α/Fe] in massive galaxies at low redshift (see, e.g., 43; 27; 4; 53, and references therein) and some evidence for this in galaxies at high redshift (60; 94). Future modeling of the abundance of individual elements would provide more detailed insight into chemical enrichment histories of galaxies.

We assume "delayed τ" SFHs that increase linearly with time followed by an exponential decay characterized by an e-folding timescale τ, such that the star-formation rate (SFR, $\Psi(t)$) at a given age, t, is parameterized by $\Psi(t) \propto t \times \exp(-t/\tau)$. These best represent the average SFHs of quiescent galaxies at early and late times (e.g., 95; 96; 97; 98). In our analysis we marginalize over τ as a nuisance parameter.

For the remainder of this work, we interpret the age using the "light–weighted" ages, $\langle t \rangle_L$, which have been averaged over the past SFH weighted by the luminosity of the stellar population. This is because $\langle t \rangle_L$ best corresponds to the age of the stellar populations that dominate the galaxy light. This is more robustly quantifiable than the SFH itself (see e.g., 99; 100), and best represents the age of the stars that dominate the observed spectrum (see also Fum16). We derive the light-weighted ages using the SFHs and (instantaneous) ages as

$$\langle t(t^*, \tau) \rangle_L = \frac{\int_0^{t^*} \Psi(t, \tau)\ L(t^* - t, \tau)\ (t^* - t)\ dt}{\int_0^{t^*} \Psi(t, \tau)\ L(t^* - t, \tau)\ dt} \tag{2.2}$$

where t^* is the instantaneous age of the model. The quantity $L(t^* - t, \tau)$ is the luminosity at an age of $t^* - t$, for a given SFH, $\Psi(t, \tau)$, measured in a given filter band (we use the SDSS g band in the rest frame).

To include the effects of dust, we attenuate the model spectra by the value $A(V)$ using the (101)

dust law (to be consistent with the dust measurements from 3D-HST 16).

$$F(\lambda)_{\rm observed} = F(\lambda)_{\rm unattenuated} \times 10^{-0.4\ k(\lambda)\ A(V)/R(V)} \tag{2.3}$$

where $k(\lambda)$ is the starburst reddening curve, and $R(V)$ is the total–to–selected attenuation in the V-band, with $R(V) = 4.05$.

We then simulated the 2D and 1D grism spectra from using the stellar population models with the software package *Grizli* (the grism redshift and line analysis software), developed by CLEAR team member (G. Brammer)[5]. *Grizli* uses as input the stellar population model spectrum, the galaxy redshift, and the galaxy image to correctly model the 2D grism data. For this latter step, we use imaging from F105W (or F098M) from CANDELS. Using the correct morphology is highly important, as the galaxy morphology effectively "smooths" the resolution of the (slitless) grism spectrum (referred to as "morphological broadening", 33), which is caused by the image of the galaxy dispersed over the range of wavelengths covered by the grism. The broadening of features is therefore correlated to the morphology of the galaxy (and at the resolution of our data this is the dominant effect; we can neglect the contribution from dynamical motions within the galaxy). The correlation with morphology means the spectral resolution decreases with increasing galaxy size (where narrow lines can be lost or smoothed over). More compact galaxies, due to their smaller size, will produce the least morphologically broadened spectra (i.e., they will have higher spectral resolution). This modeling process of the data is illustrated in Figure 2.6.

We further adopt an additional "uncertainty" to account for systematic errors, which could either arise from incompleteness or inaccuracies in the stellar population models, or from systematic errors in the data (see e.g., discussion in 99; 75). To counter this "model error" we add an additional systematic error term (a template error function) following (75) (detailed in Appendix A.3) .

[5]https://github.com/gbrammer/grizli

2.4.2 Fitting Grism Models to Grism Data

In what follows we describe fitting the 1D spectral models derived from *Grizli* and the stellar populations to the 1D G102 data for each galaxy. Because we are considering only a small number of parameters at present, we generate models over a grid of parameter values. We derive a χ^2 goodness-of-fit measurement for each combination of model for the G102 data, and we then calculate a likelihood distribution using the following,

$$P(D|\Theta) \propto \exp(-\chi^2/2) \tag{2.4}$$

where D is the data and Θ is the set of parameters we consider. We derive the joint probability density function using Bayes' theorem

$$P(\Theta|D) \propto P(D|\Theta)P(\Theta) \tag{2.5}$$

where $P(\Theta)$ represents prior information. Here we assume "flat" priors over the parameter range (see discussion in 100); for metallicity, (light-weighted) age, SFH, and redshift. For the dust attenuation, we use a prior derived by fitting a skewed Gaussian to the distribution of $A(V)$ values derived from broad-band photometry from 3D-HST for galaxies in our redshift and mass range. We then marginalize to get posteriors on individual parameters. For example, given Θ = (X, Y, Z), we would derive the posterior on parameter X as,

$$P(X) = \int_Y \int_Z P(X, Y, Z|D)\, dZ\, dY \tag{2.6}$$

In the sections that follow, we test the ability of our method to recover model parameters using simulated data. We first test the results for model stellar populations in different redshift ranges (Section 2.4.2.1). Next, we test the accuracy of recovered stellar population parameters for models fit to simulated data with and without the spectral continua (Section 2.4.2.2). As a result of these tests we concluded a best practice to (1) sub-divide galaxies by redshift so that the G102 spectra

cover different spectral features which allows us to study systematics resulting from differences in rest-frame wavelength coverage, and (2) fit the full spectrum including the continua as this provides the most accurate constraints on the stellar population parameters. Following these tests we apply these methods to (re-)measure galaxy redshifts from the G102 grism data (Section 2.5.1). We then fit the grism data to derive stellar population parameters for the galaxies in our sample. (Section 2.5.2).

2.4.2.1 Tests using Simulated Data in Different Redshift Ranges

We tested our ability to measure meaningful constraints on model parameters of galaxies at different redshifts. We selected (direct) images and redshifts from four real galaxies in our sample, and input models with 6 different combinations of parameter values spaced throughout a plausible range of values; $t = 1.9$ to 4.5 Gyr, $Z = 0.42$ to 1.32 $Z_{\odot}$, and a delayed SFH with $\tau = 0.5$ Gyr. In all cases, we simulated model spectra, as illustrated in Figure 2.6. For the simulated "data" we added real noise measured from extracted the G102 spectral data.

We then fit the simulated model data using the method described in Equations 2.4–2.6, fixing redshift to the true value and setting A(V)$= 0$. We repeated these simulations 1000 times (for each set of "truth" parameters) to generate likelihoods for the accuracy of the recovered parameters. One limitation of this simulation is that model spectra exactly match the (simulated) "data", but this allows us to determine the limitations of the fitting procedure in the idealized case before applying it to real data. We then derived posteriors on the model parameters.

Inspecting our results, we identified four natural redshift ranges which probe different rest-frame spectroscopic features, and therefore have slightly different systematics in the results from the fitting. These redshift ranges have medians of approximately $z = 1.1$, 1.2, 1.3, and 1.6, and correspond to where the different age– and metallicity–sensitive spectral features shift in and out of the grism wavelength coverage, as illustrated in Figure 2.7. At all redshifts ($1.0 < z_{grism} < 1.8$) the G102 spectra contain the 4000 Å/Balmer break, which provides constraining power on the ages and metallicities of the stellar populations.

Figure 2.8 shows the measured distributions on (light-weighted) age (t) and metallicity (Z) for simulated models, for one combination of "true" (light-weighted) age t =2.5 Gyr and metallicity

Z =1 $Z_{\odot}$, in each of the four redshift bins (we obtain similar results for other combinations of age and metallicity, but show these as they are close to the values we derive for the real data for the galaxies in our sample).

In what follows we qualitatively describe the fits in each subgroup for one set of parameters. This set was chosen as it represents a region of the parameter space we expect to be well populated. We quote values for fits of spectra with SNR = 10 (as an example of how well "good" spectra can constrain parameters), though we find that we are able to recover the parameters accurately down to SNR $\sim$ 3.

For the first redshift subgroup, ($1.00 < z_{grism} < 1.16$), the G102 data cover wavelengths that probe features out through Mgb. Unlike the Balmer lines, which are mostly age dependent, including the Mgb feature provides improved constraints on metallicity. The age constraints are also reliable, but suffer from the lack of spectral coverage the rest-frame U-band data.

The second redshift subgroup, ($1.16 < z_{grism} < 1.30$), includes features out through Hβ. The lack of Mgb could make constraining metallicity more difficult, but with a better defined 4000 Å break and coverage of the rest-frame U band these data probe the shape of the rest-frame U–B continuum and yields relatively accurate constraints on the age and metallicity.

The third redshift subgroup, ($1.30 < z_{grism} < 1.45$), contains galaxy spectra that lack coverage of Mgb and Hβ, but still contain the G+Hγ features. The constraints on the age are aided due to stronger presence of the rest-frame U–B continuum.

The fourth subgroup is our highest redshift group, ($1.45 < z_{grism} < 1.70$). The most prominent features of the group are the 4000 Å break and the large amount of U–B continuum. This group differs from the group by having the H_{γ} feature in a noisy region of the spectra.

For the all groups, we are able to recover the metallicities and light-weighted ages with typical uncertainties of $\sigma(Z)\approx$0.30 $Z_{\odot}$ and $\sigma(t)\approx$0.3 Gyr ($\sigma(t)\approx$0.2 Gyr for) respectively. The tighter constraint seen in the age measurement is an artifact of the definition of SNR. We use the SNR per pixel, averaged over 8500–11,500 Å. For $z \sim 1.6$, this observed wavelength range mostly covers the U band, and the portion around (and above) the rest-frame 4000 Å/Balmer break has much

higher S/N.

When taking all redshift subgroups, and parameters into account, Figure 2.8 indicates there may be a slight bias in light-weighted age and metallicity on the order of $\approx +10\%$ and $\approx -10\%$, respectively (for SNR > 5). However, these biases are small relative to the constraints we derive on these parameters for each galaxy. We therefore make no attempt to correct these.

2.4.2.2 Tests Using Simulated Data with and without Continua

We performed an additional test to determine the importance of fitting to the galaxy spectra including the continuum and fitting with the continuum divided out. Although we show in Section 2.3.1 that the flux calibration is not a significant source of error, past studies frequently remove the continuum, allowing for fits directly to the stellar population features, and mitigating against uncertainties in flux calibration (91, Fum16). However, there is information in the continuum as it is the superposition of the photospheres of the composite stellar populations, whose characteristics depend strongly on age, metallicity and SFH. As we have determined that the *HST* flux calibration is both accurate and stable, including the continuum provides important information for the model fits.

For our test, we removed the continua (on the models and simulated "data") by dividing the spectra with a third order polynomial fit, masking out regions with possible emission or absorption features except for the 4000 Å break. We then fit the models to the data, derived likelihoods, and marginalized over parameters to derive posteriors.

Figure 2.9 compares the recovered parameters derived by fitting simulated spectra with and without the continuum. The abscissa in both the top and bottom panels show the difference between the true value and the derived median value. We smooth the distribution of points with a kernel density estimator to derive the likelihood. While we recover, on average, the true value for both cases, using the continuum provides a tighter and more symmetric distribution, with improved results. Formally, using the continuum, we derive median and 68% confidence intervals for the offset in metallicity and light-weighted age as $\Delta Z_c = -0.013^{+0.19}_{-0.22}\ Z_\odot$ and $\Delta t_c = -0.26^{+0.59}_{-0.46}$ Gyr. Using fits to data where the continuum has been divided out, we derive $\Delta Z_{nc} = -0.013^{+0.32}_{-0.27}\ Z_\odot$

and $\Delta t_{nc} = -0.08^{+0.71}_{-0.86}$ Gyr. For the case that includes fits to the full spectra (i.e., including the continua and all absorption features), the offsets and uncertainties are smaller (and the posterior is more symmetric). We therefore fit to the full spectra in our analysis of the galaxies in our sample=.

2.5 Results

2.5.1 Measuring Redshifts from the Grism G102 Data

It is important to have accurate redshifts when modeling the galaxy stellar populations. We therefore re-derived galaxy redshifts, z_{grism}, by fitting the model grism spectrum to the data, using an iterative method. We firstly fit z_{grism} over a coarse grid of model parameters to estimate its value. We secondly fit z_{grism} over the full set of parameters but limiting the range of redshifts. These two steps saved computation time by a factor of ≈25.

For the first z_{grism} iteration, we generated models with fixed τ = 100 Myr over a coarser grid of metallicities and ages, with a very fine grid of redshift ($\Delta z = 0.001$) over a range of $0.8 < z < 2.0$. For the galaxies in our sample, the choice of τ does not affect the measurement of z_{grism} for $\tau < 500$ My for the quiescent galaxies in our sample. We fit using the set of parameters $\Theta = (Z, t, z_{grism})$, and then marginalize to obtain a posterior on z_{grism},

$$P(z_{grism}) = \int_Z \int_t P(Z, t, z_{grism})\, dt\, dZ \tag{2.7}$$

From the $P(z)$ we derive median values and a 68%-tile range on z_{grism} for each galaxy. These median values are used in our full model fitting (below) to set the redshift range used (where we fit over a range $z_{median} \pm dz$ with $dz = 0.02$ (which spans the peak and majority of the probability mass in redshift space for galaxies in our sample). Table 2.3 reports the median and 68% confidence interval on z_{grism} from these fits. The grism-derived redshifts have typical uncertainties $\sigma_z 0.004$, and are significantly improved compared to the broad-band-derived photometric redshifts with $\sigma_z \approx 0.02 - 0.11$ (see Table 2.1 and Figure 2.10). Similar results are seen in (65)

2.5.2 Measuring Stellar Population Parameters from the CLEAR G102 Data

To constrain the stellar population parameters for the galaxies in our sample, we generated a large range of spectra from the FSPS models. Our parameter space consists of metallicity, age, and SFH (ranges defined in Section 2.4.1), the redshift range described in Section 2.5.1, and a range of dust attenuation of $0.0 < \mathrm{A}(V)/\mathrm{mag} < 1.0$.

As discussed above, the use of delayed-τ SFHs is justified by the fact that our sample consists of quiescent galaxies, where the light-weighted ages are typically many times the e–folding timescale. Such SFHs are motivated by studies that find galaxy SFRs rise at early times and decline at later times (e.g. 95; 100; 97; 102). We note that using other parameterizations of the SFH would change the stellar–population ages and metallicities by <0.1 dex (see e.g., Gal14). Our tests using purely exponentially declining SFHs (e.g., SFR(t) $\propto exp(-t/\tau)$) results in (light-weighted) ages younger by $\approx$15% compared to the results here using delayed-τ models. This would push the formation redshifts of the galaxies in our sample to later epochs, but the effect is systematic and would not effect our overall conclusions.

We fit the models to each galaxy individually. For each galaxy, we generate the suite of 2D model spectra using the galaxy's F105W (or F098M) image and extract a 1D spectrum as illustrated in Figure 2.6. We then fit the models to the data for each galaxy using Equations 2.4 to 2.6, where we marginalize to generate posteriors on each parameter. We then derive median and 68% confidence intervals on each parameter. Table 2.3 lists these values for each galaxy in our sample; including fits to the (lighted-weighted) age, metallicity, τ, z_{grism}, and dust attenuation.

Figure 2.11 shows an example fit for one galaxy in our sample. The model has the median values derived for the stellar population parameter posteriors (i.e., this is not the *best fit* model, but instead is the model with metallicity and light-weighted age matching the median of the posterior distributions). The right panel of Figure 2.11 shows the corresponding joint posterior on (light-weighted) age and metallicity, $P(t, Z)$ and individual parameter posteriors, $P(t)$ and $P(Z)$. This figure also shows the benefits of using the light-weighed age rather than the instantaneous age. Based on our tests, the light-weighed age is best at breaking the metallicity– age degeneracy and we

see an anti-correlation in the joint $P(t, Z)$ posteriors. As a result, the distributions on the individual parameters (Z and t) are more symmetric and well constrained. In Appendix A.2 we show similar plots for all the galaxies in our sample, along with their respective median fit models, and metallicity and age joint likelihoods.

We observe possible Hβ emission in 3 of the galaxies ($<$10%) in our sample. When this residual Hβ emission is present we mask out this region when fitting. We have also refit all the galaxies in our sample, removing the central region of Hβ, and find no measurable impact on the parameter fits (in 11 out of 18 galaxies), with random (i.e., not systematic) changes of $<$10% in the median fits on parameters in the other cases. We therefore make no correction for Hβ (or other nebular) emission.

Although it is our goal to derive model fits solely from the G102 grism data for each galaxy in this study, we have compared the best-fit model fits from our analysis to available broad-band photometry (from 16). A quantitative comparison yields limited information as the best-fit models do not capture the full range of allowable parameter values, but they do offer guidance to the fidelity of the model parameters. We find that the broad-band photometry and best-fit model fits span the same range of color across out to longward of (rest-frame) 1 in 70% of cases, and this is improved to nearly 100% when we fix the dust content in the models to be $A(V) = 0$ mag. Because we marginalize over dust attenuation here, our uncertainties include this information. We plan to explore this more fully in a future work, using all available grism and broad-band data to constrain the stellar populations of galaxies.

2.5.3 Stacked Results for Galaxies in Redshift Subgroups

To derive parameter constraints for all galaxies in each redshift subgroup, we adapt the "stack-smooth-iterate" technique discussed in (103). This allows us to combine the posterior likelihoods, $P(Z)$ and $P(t)$, derived from each individual galaxy, placing constraints on the subgroups *as a population*.

The steps in our "stack–smooth–iterate" method are as follows. We explain the steps in greater detail below.

1. Sum the posteriors using weights to remove large peaks from the summed distribution.

2. Apply a prior derived from the previous iteration (the prior is flat on the first iteration).

3. Smooth the distribution to remove smaller residual peaks.

4. Set this smoothed distribution as the new prior.

5. Iterate until asymptotically reaching the parent distribution.

The process begins by deriving the weights, w_i. To do this we take the inverse variance derived by a jackknife process. The jackknife begins by summing the posteriors to create a distribution $Y(\Theta)$

$$Y(\Theta) = \frac{1}{n}\sum_i P(\Theta|D)_i \tag{2.8}$$

where n is the total number of posteriors. We then quantify the effect a single posterior has on $Y(\Theta)$ by leaving it out of a newly summed distribution $\bar{Y}(\Theta)_i$

$$\bar{Y}(\Theta)_i = \frac{1}{n-1}\sum_j^{j\neq i} P(\Theta|D)_j \tag{2.9}$$

We then calculate the weights w_i to be

$$w_i = \frac{1}{\int_\Theta (\bar{Y}(\Theta)_i - Y(\Theta))^2 d\Theta} \tag{2.10}$$

Here we find the variance between $Y(\Theta)$ and $\bar{Y}(\Theta)_i$, where we excluded the ith posterior and integrated over Θ. The advantage of weighting in this way is that the weights naturally handle individual $P(\Theta|D)_i$ that are sharply peaked (e.g., a distribution approximately that of a δ-function), as this would otherwise dominate an average of the subgroup distributions.

We then stack our posteriors using a weighted sum

$$P^*(\Theta) = \frac{\sum_i w_i P(\Theta|D)_i P(\Theta)}{\int_\Theta \sum_i w_i P(\Theta|D)_i P(\Theta) d\Theta}\ . \tag{2.11}$$

$P(\Theta)$ is a prior on Θ, which is derived from the data itself (i.e., $P(\Theta)$ is flat in the 1st iteration, then

taken as $P(\Theta) = P^*(\Theta)$ on successive iterations, see below).

We then iterate to calculate $P^*(\Theta)$ from Equation 2.11. On each iteration (including the first) we smooth the $P^*(\Theta)$ distribution using local linear regression (104) to remove any residual peaks. While the choice of smoothing algorithm is not as important, the smoothing step is important because it will remove any peaks on the distribution that the weights did not. During the iteration process these residual peaks (because it is a multiplicative process) will begin grow and shift the distribution.

Once smoothed we set $P(\Theta) = P^*(\Theta)$, and iterate. In this way we derive the prior $P(\Theta)$ from the data itself. (Note that we apply this "prior" only to derive the stacked likelihood here, and not to alter the likelihoods for individual galaxies derived above.) After several iterations $P^*(\Theta)$ will converge to reach a distribution, which is an estimate of the parent distribution of the sample. We emphasize that these are approximations of the parent distributions, and larger sample sizes would more reliably recover these distributions. Appendix A.5 describes our tests to check the accuracy of this method to recover a true known parent distribution.

Figures 2.12 and 2.13 show the stacked spectra and models with the median parameters from the stacked posteriors for the galaxies in each of our redshift subgroups. The stacked spectra are the weighted average of the spectra for each galaxy in each subgroup: we first shift these all to the rest-frame, then average, weighting by the inverse variance as a function of wavelength for each spectrum. Each figure shows the "median" model, which is the stellar population with parameters equal to the median light-weighted age and metallicity from the stacked parameter posteriors (i.e., these are not best fits). Nevertheless, the agreement between the model spectra and the data is high. This gives us confidence that the models reliably represent the data and therefore inform us about the stellar population parameters for these galaxies.

From the stacked posteriors we derive median and 68%-tile ranges on the light weighted ages and metallicities for the galaxies in the different redshift subgroups. Based on our tests (in Appendix A.5) we interpret the 68%-tile distributions as an estimate of the intrinsic scatter in parent distribution of the population. Table 2.5 lists these values as well as the mass range and number of

galaxies for each redshift subgroup.

Table 2.3: Measured parameters for individual galaxies from this work

ID	z_{grism}	Metallicity ($Z_{\odot}$)	Age (Gyr)	τ (Gyr)	A(V) (Mag)
(1)	(2)	(3)	(4)	(5)	(6)
GND16758	$1.015^{+0.002}_{-0.002}$	$1.23^{+0.25}_{-0.32}$	$3.56^{+0.76}_{-0.50}$	$0.31^{+0.24}_{-0.21}$	$0.06^{+0.08}_{-0.05}$
GSD39241	$1.017^{+0.002}_{-0.002}$	$1.24^{+0.23}_{-0.27}$	$3.74^{+0.75}_{-0.55}$	$0.27^{+0.22}_{-0.18}$	$0.17^{+0.11}_{-0.09}$
GSD42221	$1.018^{+0.005}_{-0.005}$	$1.20^{+0.27}_{-0.50}$	$1.24^{+0.85}_{-0.31}$	$0.26^{+0.67}_{-0.20}$	$0.20^{+0.18}_{-0.12}$
GSD43615	$1.020^{+0.002}_{-0.005}$	$1.12^{+0.31}_{-0.38}$	$3.86^{+0.90}_{-0.78}$	$0.27^{+0.24}_{-0.19}$	$0.48^{+0.20}_{-0.16}$
GSD39170	$1.023^{+0.002}_{-0.002}$	$1.40^{+0.13}_{-0.24}$	$3.42^{+0.31}_{-0.34}$	$0.48^{+0.14}_{-0.28}$	$0.04^{+0.04}_{-0.03}$
GND37955	$1.027^{+0.005}_{-0.002}$	$1.24^{+0.25}_{-0.54}$	$2.67^{+0.45}_{-0.36}$	$0.68^{+0.22}_{-0.33}$	$0.63^{+0.23}_{-0.25}$
GSD45972	$1.041^{+0.002}_{-0.002}$	$0.73^{+0.42}_{-0.23}$	$3.48^{+1.05}_{-0.77}$	$0.27^{+0.25}_{-0.18}$	$0.08^{+0.09}_{-0.06}$
GSD39631	$1.057^{+0.002}_{-0.010}$	$0.64^{+0.50}_{-0.29}$	$3.56^{+1.00}_{-0.90}$	$0.25^{+0.24}_{-0.18}$	$0.19^{+0.13}_{-0.11}$
GSD47677	$1.117^{+0.002}_{-0.005}$	$1.05^{+0.38}_{-0.47}$	$3.11^{+0.90}_{-0.67}$	$0.30^{+0.26}_{-0.21}$	$0.30^{+0.22}_{-0.16}$
GND23435	$1.139^{+0.005}_{-0.007}$	$0.73^{+0.57}_{-0.43}$	$2.23^{+0.65}_{-0.73}$	$0.34^{+0.34}_{-0.24}$	$0.38^{+0.27}_{-0.20}$
GND34694	$1.145^{+0.002}_{-0.002}$	$1.12^{+0.29}_{-0.39}$	$2.21^{+0.71}_{-0.47}$	$0.18^{+0.21}_{-0.12}$	$0.25^{+0.14}_{-0.13}$
GND32566	$1.148^{+0.005}_{-0.002}$	$1.15^{+0.31}_{-0.48}$	$2.11^{+0.39}_{-0.63}$	$0.54^{+0.31}_{-0.35}$	$0.36^{+0.24}_{-0.19}$
GND23758	$1.161^{+0.005}_{-0.002}$	$0.60^{+0.61}_{-0.45}$	$2.10^{+0.28}_{-0.25}$	$1.02^{+0.21}_{-0.24}$	$0.90^{+0.07}_{-0.14}$
GSD38785	$1.169^{+0.005}_{-0.002}$	$0.80^{+0.50}_{-0.53}$	$2.47^{+0.63}_{-0.56}$	$0.43^{+0.28}_{-0.29}$	$0.29^{+0.22}_{-0.16}$
GND17070	$1.175^{+0.005}_{-0.014}$	$1.09^{+0.34}_{-0.43}$	$2.10^{+0.50}_{-0.67}$	$0.34^{+0.33}_{-0.25}$	$0.15^{+0.14}_{-0.10}$
GSD40476	$1.209^{+0.002}_{-0.002}$	$0.51^{+0.45}_{-0.27}$	$1.83^{+0.68}_{-0.57}$	$0.22^{+0.28}_{-0.15}$	$0.44^{+0.24}_{-0.19}$
GSD40597	$1.221^{+0.002}_{-0.002}$	$1.22^{+0.25}_{-0.40}$	$2.49^{+0.21}_{-0.34}$	$0.63^{+0.16}_{-0.25}$	$0.20^{+0.14}_{-0.12}$
GSD35774	$1.227^{+0.002}_{-0.005}$	$1.28^{+0.21}_{-0.27}$	$1.65^{+0.52}_{-0.34}$	$0.12^{+0.11}_{-0.08}$	$0.57^{+0.26}_{-0.24}$
GSD39805	$1.243^{+0.051}_{-0.019}$	$1.06^{+0.38}_{-0.59}$	$2.10^{+0.36}_{-0.47}$	$0.59^{+0.27}_{-0.31}$	$0.40^{+0.29}_{-0.22}$
GND21156	$1.249^{+0.002}_{-0.002}$	$0.83^{+0.36}_{-0.34}$	$2.20^{+0.58}_{-0.52}$	$0.26^{+0.22}_{-0.17}$	$0.31^{+0.16}_{-0.14}$
GND37686	$1.256^{+0.001}_{-0.002}$	$0.58^{+0.43}_{-0.24}$	$3.10^{+0.78}_{-0.63}$	$0.23^{+0.24}_{-0.16}$	$0.49^{+0.20}_{-0.18}$
GSD46066	$1.326^{+0.012}_{-0.002}$	$1.04^{+0.31}_{-0.28}$	$3.48^{+0.57}_{-0.58}$	$0.18^{+0.17}_{-0.12}$	$0.44^{+0.28}_{-0.22}$
GSD40862	$1.328^{+0.002}_{-0.005}$	$1.15^{+0.30}_{-0.45}$	$2.52^{+0.72}_{-0.69}$	$0.19^{+0.19}_{-0.13}$	$0.45^{+0.27}_{-0.23}$
GSD39804	$1.333^{+0.005}_{-0.001}$	$0.94^{+0.37}_{-0.28}$	$3.17^{+0.67}_{-0.54}$	$0.21^{+0.20}_{-0.15}$	$0.28^{+0.21}_{-0.16}$
GSD44620	$1.334^{+0.005}_{-0.007}$	$0.80^{+0.54}_{-0.48}$	$0.96^{+0.53}_{-0.26}$	$0.22^{+0.33}_{-0.14}$	$0.62^{+0.25}_{-0.28}$
GSD40623	$1.413^{+0.019}_{-0.005}$	$1.02^{+0.29}_{-0.23}$	$3.08^{+0.56}_{-0.50}$	$0.16^{+0.16}_{-0.11}$	$0.27^{+0.19}_{-0.15}$
GND21427	$1.506^{+0.072}_{-0.022}$	$0.91^{+0.44}_{-0.46}$	$2.43^{+0.64}_{-0.60}$	$0.25^{+0.24}_{-0.18}$	$0.40^{+0.27}_{-0.21}$
GSD40223	$1.595^{+0.005}_{-0.005}$	$0.81^{+0.49}_{-0.42}$	$1.82^{+0.44}_{-0.48}$	$0.47^{+0.22}_{-0.22}$	$0.48^{+0.29}_{-0.24}$
GSD41520	$1.605^{+0.002}_{-0.002}$	$0.97^{+0.46}_{-0.49}$	$1.98^{+0.66}_{-0.55}$	$0.18^{+0.18}_{-0.12}$	$0.73^{+0.17}_{-0.20}$
GSD39012	$1.612^{+0.010}_{-0.024}$	$0.75^{+0.55}_{-0.43}$	$1.87^{+0.58}_{-0.53}$	$0.45^{+0.27}_{-0.27}$	$0.42^{+0.30}_{-0.23}$
GSD44042	$1.612^{+0.002}_{-0.002}$	$1.28^{+0.22}_{-0.85}$	$2.33^{+0.33}_{-0.28}$	$0.47^{+0.11}_{-0.20}$	$0.22^{+0.18}_{-0.13}$

Table 2.4: (1) Galaxy ID number in the GND or GSD 3D-HST catalog; (2) measured grism redshift; (3) median metallicity; (4) median light-weighted age; (5) median e-folding time for delayed τ SFH; (6) median A(V) for Calzetti dust law; all measurements provided with 68% confidence intervals; horizontal lines show the galaxies in each of the separate redshift subgroups

Table 2.5: Measured parameters for each redshift subgroup

Redshift group (1)	Metallicity ($Z_\odot$) (2)	Age (Gyr) (3)	Mass Range ($\log(M_*/M_\odot)$) (4)	Sample Size (N) (5)
	$1.16^{+0.26}_{-0.33}$	3.2 ± 0.7	10.1–11.1	12
	$1.05^{+0.32}_{-0.36}$	2.2 ± 0.6	10.6–11.2	9
	$1.00^{+0.31}_{-0.31}$	3.1 ± 0.6	10.5–11.0	5
	$0.95^{+0.37}_{-0.40}$	2.0 ± 0.6	10.7–11.1	5

Table 2.6: Values on (light-weighted) age and metallicity correspond to the median and 68% confidence range for each parameter, which we interpret as an estimate of the intrinsic scatter in the subgroup (see text); The columns show (1) Redshift of the sub-group of the stacked posteriors; (2) metallicity; (3) light-weighted age, (4) Mass range of the galaxies in each of the samples; (5) number of galaxies in each redshift sub-group.

2.6 Discussion

Our dataset and analysis allow us to explore the correlations between stellar mass, (light-weighted) age, and metallicity in galaxies at $z > 1$, much closer in time to the galaxies' quenching time. We can use these to constrain both the SFHs and enrichment histories of these galaxies. In the sections that follow, we interpret the results of our modeling.

It is important to note that throughout (unless otherwise specified) all ages correspond to "light weighted" ages (see above) as these are better constrained because they correspond to the stellar populations that dominate the light in the galaxies' spectra (when weighted by their luminosity). These are related to the parametric form of the SFHs through Equation 2.2, and different choices in this can impact the (light-weighted or mass-weighted) ages by $\sim$0.4 Gyr (e.g., 102). We will explore the effects of different SFHs in a future work.

2.6.1 The Ages and Metallicities of Quiescent Galaxy Populations from $z \sim 1.1$ to 1.6

Generally, our modeling of the quiescent galaxies from to favor (light-weighted) ages of $\simeq$2–4 Gyr (with age increasing with decreasing redshift) and near Solar metallicities. Here, we comment on the values and quality of the model fits.

For each redshift subgroup, Figures 2.12 and 2.13 show the stacked posterior on the age and

metallicity. The model fits in the Figures have metallicity and age equal to the median value from these stacked posteriors (that is, these are *not* best fit models to the stack). Rather, the posteriors are derived by stacking the posteriors of the individual galaxies in each redshift subgroup using the method in Section 2.5.2, and the data are the stacks of the individual galaxies (weighted by their inverse variance). The agreement between the models and data match is qualitatively quite good.

The subgroup has median parameter values of $Z = 1.16 \pm 0.29\ Z_{\odot}$, $t_L = 3.2 \pm 0.7$ Gyr (Figure 2.12 top panel). The regions around Hβ and Mgb are particularly well reproduced by the model. This may be expected as the S/N of the data are highest in those regions and these features are age and metallicity sensitive. The model agrees well with the data at bluer wavelengths, but it does not capture all the apparent features. For example, the data show possible absorption at Hδ that is not reproduced in the model. However, the G102 grism has less sensitivity at these wavelengths, reflected by the larger uncertainties on the data in this part of the spectrum, and the spectral regions at bluer wavelengths constrain the models less. Furthermore, we would have expected stronger Hδ absorption to be accompanied by stronger Hγ absorption, which is not seen in the data (providing additional constraints on the models).

The sample has median parameter values of $Z = 1.05 \pm 0.34\ Z_{\odot}$, $t_L = 2.2 \pm 0.6$ Gyr (Figure 2.12 bottom panel). Qualitatively, we see excellent agreement between the model and data, especially in the regions from the 4000 Å/Balmer break out past Hβ, and these features drive the constraints on the model parameters.

The sample has median parameter values of $Z = 1.00 \pm 0.31\ Z_{\odot}$ and $t_L = 3.1 \pm 0.6$ Gyr (Figure 2.13 top panel). The 68%-tile confidence intervals on light-weighted age and metallicity are as tight as those at and samples (see Table 2.5), implying the shape of the continuum has important constraining power even as important features (like Hβ and Mgb) shift out of the wavelength coverage. Most of the information constraining the models comes from the wavelength region of the 4000 Å break to the rest-frame B-band, where the S/N is highest.

The sample has median parameter values of $Z = 0.95 \pm 0.39\ Z_{\odot}$, and $t_L = 2.0 \pm 0.6$ Gyr (Figure 2.13 bottom panel). The 68%-tile range on the light-weighted age is nearly as tight as for

the lower redshift subgroups. The metallicity measurements place this group as slightly sub-solar, with a fairly broad 68%-tile range.

2.6.2 On the Star-Formation and Quenching Histories of Quiescent Galaxies at $z > 1$,

Figure 2.14 shows the measured (light-weighted) ages as a function of redshift for the galaxies in our sample. The Figure shows the median values and 68% confidence intervals on the ages for each quiescent galaxy in our sample, as well as the ages derived from the stacks for each redshift subgroup. Generally, galaxies in our sample have ages $2 - 4$ Gyr, where there is a trend that higher redshift galaxies have younger ages. In Figure 2.14 we also compare the (light-weighted) ages for the galaxies in our study to some other studies in the literature that also report ages. Comparing our derived age measurements to many other studies is complicated by the fact that there are different definitions and conventions of "age". There are three widely used definitions of age: the instantaneous age of the stellar population model; mass-weighted ages, and light (luminosity-)weighted ages (we use the latter here). For a given (declining) SFH , the instantaneous age is the oldest as it measures the time since the onset of star-formation. Mass–weighted and light-weighted ages will be younger than instantaneous ages as they average over the mass (or light) of stars that continue to form after the initial burst of star-formation. As discussed above, the light-weighted ages are more robust against uncertainties in the SFH. For this reason we only show other results for light-weighted ages in Figure 2.15 as they are most directly comparable to the ones here.

The ages we derive for the galaxies in our sample tend to be larger than some other values for galaxies at similar redshift taken from the literature (cf. 6; 3; 7). This may result from systematic effects owing to different definitions of age in previous studies, and the fact that we treat the metallicity as a free parameter. As seen in the right panel of Figure 2.11, the metallicity–age degeneracy shows that lower metallicity solutions push the median age higher (consistent with the offsets between our work and most literature studies). For example, (102) allow the metallicity to be free and find similar (mass-weighted) ages for quiescent galaxies in the same redshift range as our sample here.

Interestingly, the light-weighted ages we derive are consistent with predictions of (r–band

light-weighted) from the semi-analytic model (SAM) based on the Millennium simulation from (9). Figure 2.14 shows the 68% scatter in ages from galaxies from this SAM selected to be quiescent (defined by sSFR$< 10^{-10}$ yr^{-1}). This implies that the quenching epochs predicted in the models are consistent with the results we derive here for our sample. (We plan a more detailed comparison in a future study.)

Figure 2.14 also shows that the light-weighted ages of the quiescent galaxies in our sample have a nearly constant offset from the age of the Universe at the observed redshifts of the galaxies in our sample. This implies the galaxies all quenched at approximately the same time in the past. Figure 2.15 illustrates this by showing the formation redshift $z_{\rm form}$ for each galaxy in our sample (and showing galaxies from the literature for comparison). Indeed, the galaxies in our samples show a near constant formation redshift, $z_{\rm form} > 2.5$.

We can relate $z_{\rm form}$ to the amount of stellar mass the galaxies had formed at this formation time. This requires integrating the SFHs, accounting for the light-weighted ages and mass losses from stellar evolution. This is not straight-forward: for example there is no analytical solution (to our knowledge) to the integral in Equation 2.2, owing to the dependence of $L(t^* - t)$ on light-weighted age, metallicity, and SFH. However, we can make an approximation as the ages of the quiescent galaxies in our samples are all in the regime where $t^* \gg \tau$ (where t^* is the instantaneous age of the model and τ is the e-folding time constant of the SFR). In this case we compare $\langle t(t^*, \tau)\rangle_L$ (the light-weighted age) to $\langle t(t^*, \tau)\rangle$ (i.e., the mass-weighted age), which we define as

$$\langle t(t^*, \tau)\rangle = \frac{\int_0^{t^*} \Psi(t, \tau)\ (t^* - t)\ dt}{\int_0^{t^*} \Psi(t, \tau)\ dt} \tag{2.12}$$

For the case where $t^* > \tau$ it will always be the case that

$$\langle t(t^*, \tau)\rangle_L < \langle t(t^*, \tau)\rangle. \tag{2.13}$$

For the case $t^* \gg \tau$, it can be shown that for delayed-τ SFHs, equation 2.12 reduces to

$$\langle t(t^* \gg \tau, \tau) \rangle \approx t^* - 2\tau. \tag{2.14}$$

That is, the light-weighted age is always less than the (mass-weighted) age because for our galaxy sample the stellar populations fade monotonically. This leads to an upper bound on the light-weighted age, $\langle t(t^*, \tau) \rangle_L$,

$$\langle t(t^*, \tau) \rangle_L < t^* - 2\tau. \tag{2.15}$$

Empirically, we find that Equation 2.15 holds for $\langle t(t^*, \tau) \rangle_L > 1.5$ Gyr, and $t^* \geq 4\tau$. For younger light-weighted ages, there is a bias of $<$15% (so long as $t^* \geq 4\tau$ is satisfied).

The stellar–mass formed for a SFH parameterized as a "delayed-τ" model is then

$$M(t, \tau) = m(t, \tau)\, C \int_0^t t'\, e^{-t'/\tau}\, dt' \tag{2.16}$$

where $m(t, \tau)$ is the fractional mass loss function (and depends on age, SFH and stellar population model). C is a constant we can solve for by setting $t = t^*$ and $M(t^*, \tau) = M_{obs}$ (the measured stellar mass).

Substituting in the value for C leads to

$$M(t \mid M_{obs}, t^*, \tau) = \frac{m(t, \tau)\, M_{obs} \int_0^t t'\, e^{-t'/\tau}\, dt'}{m(t^*, \tau)\, \tau^2\, (1 - e^{-t^*/\tau}[1 + t^*/\tau])} \tag{2.17}$$

Using the approximation for $\langle t(t^*, \tau) \rangle_L < t^* - 2\tau$, we find a lower limit on the stellar mass formed at $\langle t(t^*, \tau) \rangle_L$ (called the "quenching mass", M_Q),

$$M_Q > M(t = 2\tau) = \frac{0.6\, m(2\tau, \tau)\, M_{obs}}{m(t^*, \tau)\, (1 - e^{-t^*/\tau}[1 + t^*/\tau])} \tag{2.18}$$

Finally, again applying the limit of $t^* \gg \tau$, we can approximate M_Q to be

$$M_Q > 0.6 \times \frac{m(2\tau, \tau)}{m(t^*, \tau)} \times M_{obs} \tag{2.19}$$

The values of m are determined by the stellar population model, including the effects of the IMF. For a Salpeter IMF $M_Q > 0.68\ M_{obs}$, and for a Chabrier IMF $M_Q > 0.75\ M_{obs}$. Therefore, for the assumed SFHs, the galaxies in our sample would have formed $\sim$70% of their stellar mass by the redshift that corresponds to their light-weighted ages, which we define as $z_{\rm form}$.

Both z_{70} and M_Q are related to the assumed star-formation history. To test how different parameterizations for this affect our light-weighted ages, we refit our galaxies with both τ and delayed τ models. The only effect seen on the light-weighted ages was a systematic shift (delayed τ models produce lower light-weighted ages). Using τ-models rather than delayed-τ models increases the light-weighted ages and shifts the formation redshifts to $z_{\rm form} > 4$.

Compared to the galaxies in our sample, quiescent galaxies at lower redshifts have lower formation redshifts (see Figure 2.15, and 3; 4; 5; 6; 7; 8, although a direct comparison is complicated by the different definitions of "age" in some studies). This is likely a consequence of progenitor bias, where the progenitors of quiescent galaxies at $z < 1$ are a mix of quiescent galaxies and some star-forming galaxies at $z > 1$ (that quench at later time). Because some fraction of the population is star-forming at higher redshift, they will be younger at lower redshift and shift the mean formation redshift lower. Similarly, quiescent galaxies could become "younger" if they accrete enough mass through minor (dry) mergers of (quenched) lower mass galaxies with younger ages (see discussion in 4).

Our results imply there should exist a population of massive quiescent galaxies at redshifts as high as $z > 3$. Indeed, candidates of such galaxies have been identified (e.g., 45; 105; 37; 38; 106), where recent spectroscopic confirmation shows the rest-frame optical light strong Balmer absorption features (i.e., dominated by A-type stars), indicative of recent quenching (39; 40).

We can gain insight into the evolution of these objects by comparing the (comoving) number

densities of these massive galaxy candidates at $z > 2$ to those in our sample. Figure 2.15 shows that roughly one-third of our sample experienced early quenching, with $z_{70} > 3$. (37) measure a number density when considering *all* massive galaxies ($\log M_*/M_\odot > 10.6$) at $3 < z < 4$ of 5.1×10^{-5} Mpc^{-3}. We can compare this to number density of quiescent galaxies in our sample ($1 < z_{grism} < 1.8$) with $\log M/M_\odot > 10.85$ (the higher mass here is needed to account for the $\sim 30\%$ growth expected as our estimates of the "formation redshift", z_{70}, correspond to the point where our galaxies had formed 70% of their mass). Using this mass limit we find a number density of $1.3(\pm 0.2) \times 10^{-4}$ Mpc^{-3}, where the uncertainty is purely Poissonian. Taking one-third of this number density (to account for the one-third of objects that quenched at $z_{70} > 3$), this is consistent with the measured number density from (37), but it requires that ≈all of the massive galaxies at $z > 3$ quench to account for the galaxies with high z_{70} in our sample.

The rest of the galaxies quench at lower redshift ($2 < z < 3$, see Figure 2.15). Integrating the galaxy stellar mass functions from (30), we find that quiescent galaxies with $\log M_*/M_\odot > 10.6$ have a number density of 1.3×10^{-4} Mpc^{-3}. These are equal to the density number we derive for quiescent galaxies in our sample, showing we can account for all the population of quiescent galaxies we observe at $1 < z < 1.8$ (not even accounting for uncertainties or from changes in stellar mass through mergers, but see below). This evidence supports the z_{70} values we derive.

2.6.3 The Mass–Metallicity Relation for Quiescent Galaxies at $z > 1$

The CLEAR WFC3 G102 data allows us to measure stellar metallicities for quiescent galaxies at $z > 1$. Because our sample is closer (in redshift) to the epoch when the galaxies quenched, we can better constrain their enrichment history.

Figure 2.16 shows the mass-metallicity relation for the quiescent galaxies in our sample at $1 < z_{grism} < 1.7$. The figure shows evidence that (1) quiescent galaxies at this redshift have near Solar Metallicities, and (2) that a mass–metallicity relationship for these quiescent galaxies is nearly unchanged from the $z \sim 0.1$ to $z > 1$.

The mass-metallicity relation for $z \sim 1 - 1.7$ quiescent galaxies is either flat (no dependence) with stellar mass or slightly increasing with stellar mass. We fit a linear relation to the data of the

form,

$$\log(Z_*/Z_\odot) = A\log(M_*/10^{11}\ M_\odot) + B \tag{2.20}$$

for all the $1 < z_{grism} < 1.7$ galaxies in our sample. This yielded a fit with $A = 0.15 \pm 0.13$, $B = 0.08 \pm 0.03$, with a covariance, $\sigma_{AB} = 0.002$, which is illustrated as the shaded area in the figure.

The zero-point and shallow slope of the mass-metallicity relation show that the galaxies in our sample are consistent with Solar metallicity. Furthermore, Figure 2.16 shows that the stacked posteriors of galaxies in each redshift subgroup are strongly clustered around Solar metallicities, and that the distribution (histogram) of median metallicities for all the galaxies in our sample are likewise peaked around Solar metallicities. Therefore, we interpret this as strong evidence for Solar-metallicity enrichment in quiescent galaxies at $z \sim 1 - 1.7$.

In contrast, there is no evidence for evolution in the slope and zeropoint of the mass-metallicity relation for quiescent galaxies from $1z1.7$ to $z \sim 0.2$. Figure 2.16 shows that the measurements for galaxies at $z < 0.22$ from SDSS (10) and at $z \sim 0.7$ (Gal14) are consistent with the same mass-metallicity relation we infer at $z > 1$. (Similar results are found by 25; 59; 8). This is consistent with the assertion that these galaxies enriched rapidly while they formed their stars up to Solar metallicities, they have evolved passively since.

At higher redshift, $z > 2$, there is some evidence that massive ($\log(M_*/M_\odot) > 11.0$) quiescent galaxies include objects with ≈Solar (and super-Solar) metallicities, as well as objects with less (sub-Solar metallicity) enrichment (60; 61; 67), with (in at least one case) evidence for super-Solar [α/Fe] enrichment (e.g., 60). This could imply that at these epochs we are seeing the quenching of the cores of galaxies, which may evolve to higher metallicity at later times through mergers (see below, and discussion in Kriek et al. 2016). However, current constraints at $z > 2$ are based on only a few (four) galaxies (highlighting the difficulty of these measurements) and larger galaxy samples are required.

Similarly interesting would be to study the evolution of the metallicity ([Fe/H]) and the α-element enrichment ([α/Fe]) in our galaxies. This is clearly an important problem given that

massive quiescent galaxies at low redshifts show evidence for [α/Fe] > 0 (e.g., 52; 53), with some recent evidence at high redshift (e.g., 60; 94). This is likely related to their short SFHs combined with delay times in of Type Ia supernovae (e.g., 107; 108). Given that the $z \sim 1 - 1.7$ quiescent galaxies in our sample likely have similar histories to those at $z \sim 0$ (see discussion below), we may expect them to be similarly α-enriched. We plan to study this in a future work.

2.6.4 Implications for Enrichment and Quenching of $z > 1$ Quiescent Galaxies

Star-forming galaxies show a (gas-phase) mass-metallicity relation that evolves strongly with redshift. This contrasts strongly with the (lack of) evolution in the mass-metallicity relation for quiescent galaxies we find out to $1.0 < z < 1.7$. For example, the mass-metallicity relation for galaxies from SDSS at $z \sim 0.1$ derived from nebular emission lines shows that the gas-phase metallicity rises quickly with mass, and is Solar (or exceeds Solar) for the most massive galaxies (with stellar masses $\log M_*/M_\odot > 10.5$, 47; 109). This evolves with redshift: at $z \sim 2.3$ the metallicities of star-forming galaxies at $\log(M_*/M_\odot)$=10.5 are lower by about a factor of $\sim$2 compared to $z \sim 0.1$ (110; 49; 51, although this depends slightly on systematics owing to different metallicity indicators), and by about a factor of $\sim$3 at $z \sim 3.3$ (50). This evolution persists even for absorption-line studies, where Gal14 report a similar offset in the stellar metallicity for star-forming galaxies at $z \sim 0.7$ at fixed stellar mass (in contrast to their mass-metallicity relation for quiescent galaxies which shows no evolution to $z \sim 0.7$).

What does it mean that the metallicities of quiescent galaxies at $1 < z < 1.7$ all favor near Solar metallicities? The lack of evolution in their mass-metallicity relation means that the progenitors of the galaxies in our sample presumably also had Solar metallicities at the time of quenching, $z_{70} > 2.$. However, this makes their star-forming progenitors strong outliers in metallicity, offset from the gas–phase mass-metallicity relation observed at $z \sim 2.3$ and $z \sim 3.3$ for galaxies with stellar mass $\log M_*/M_\odot > 10.5$ (50; 51, see above). Observationally, there are few (if any) star-forming galaxies at these masses and redshifts with Solar metallicity that are candidates for the progenitors of the quiescent galaxies in our sample (this is assuming metallicity indicators used for quiescent and star forming galaxies are consistent, which is unclear).

Insight may be garnered from theory. In simulations of galaxies at these redshifts, the slope and scatter of the gas–phase mass-metallicity relation is a result of the combination of gas accretion, gas fraction, feedback, and metal-retention efficiency (20; 42). The slope of the gas-phase mass-metallicity relation is a result of mass-dependent gas accretion and feedback, resulting in lower metal retention efficiency for lower mass galaxies. This reproduces the observed evolution of the gas-phase mass-metallicity relation (e.g., 42).

The simulations show that at $z \sim 2$ the mean metallicity of massive galaxies is sub-Solar. However, the distribution extends to higher values and some galaxies have roughly Solar metallicity (42). One explanation is that gas accretion has ceased in these galaxies (or slowed down, possibly as the galaxies are in the act of quenching, see below), and/or their metal retention efficiencies are higher (related to the fact that their escape velocities are larger), making it easier for them to enrich to higher metallicities faster. Interestingly, the lack of evolution in the observed mass-metallicity relation for quiescent galaxies out to $z > 1$ could mean that these processes of galaxy quenching are redshift independent, which would set a requirement on simulations.

Why is it then that quiescent galaxies observed at nearly all redshifts have Solar metallicity? It could be that obtaining Solar metallicity is a symptom of the processes that lead to quenching and be related to the observational differences between quiescent and star-forming galaxies. One way to correlate the build-up of metals to quenching is by connecting the metal retention efficiency to galaxy feedback and galaxy size (111; 112). Quiescent galaxies are known to have smaller effective radii compared to mass-matched star-forming galaxies (113), and this observation has led to theories such as the process of "compactification", which relates sizes sizes to quenching (e.g., 114; 115). Such scenarios could also lead to a natural connection between the high Solar metallicity and quenching in galaxies: as galaxies become more compact, the increase in their mass- and SFR-surface densities leads to stronger feedback, likely pushing the galaxy beyond the quenching point (116; 115); the increase in their escape velocities and SFR leads to higher metal production and retention (117; 42). This is a plausible explanation for our observations, but it remains to be seen if simulations can reproduce the detailed values and evolution. For example, one prediction if

the metal enrichment occurs prior to quenching is that more compact star-forming galaxies should likewise have higher metallicity (consistent with some results for galaxies in the SDSS, see 117). We plan to test this at higher redshift in a future study.

Regardless, if the Solar metallicities in our sample are correct, then their progenitors must exist *somewhere*. Some may be related to the compact star-forming galaxies discussed above (115). It is also possible that the time for galaxies to enrich from $\sim$1/3–1/2 $Z_{\odot}$ to $Z_{\odot}$ is very short-lived, in which case they may be very rare in surveys. For example, if quenching is tied to the process of "compaction", the timescales could be $\ll 1$ Gyr (118), such that finding metal-rich star-forming galaxies in this stage is rare. This "rapid" phase would also be consistent with high [α/Fe] abundances (e.g., 60, and we plan to test for this in future work). However, as surveys of $z > 2$ galaxies become larger (24), we expect them to include examples of this population.

Another possible explanation for the lack of metal-rich star-forming progenitors is that current samples of spectroscopically studied galaxies at $z \sim 2$ and 3 contain components of metal-enriched gas, but only in regions with heavy dust obscuration. In this case, the (rest-frame optical) spectra only probe the lower-metallicity gas (possibly diluted by recent inflows of pristine gas), yielding a mass-metallicity relation biased low. Alternatively, it may be that current spectroscopic studies of star-forming galaxies lack the progenitors of the quiescent galaxies in our samples entirely because the former are *completely* attenuated by dust. Massive, dusty star-forming galaxies are known to exist (e.g., 23; 119; 120), with the space densities that connect them to quiescent galaxies (37; 121). Some dusty star-forming galaxies are observed to have compact gas reservoirs (122; 123), which likewise make them candidate progenitors to quiescent galaxies at lower redshifts. Future observations at at (rest-frame) near-IR to far-IR wavelengths (such as with the *James Webb Space Telescope* [*JWST*] and the *Atacama Large Millimeter Array* [ALMA]) may identify this galaxy population (and/or the higher- metallicity gas components in galaxies at these redshifts, see previous paragraph). It may also be possible to resolve these regions of high metallicity through higher angular resolution studies (e.g., with the Giant Segmented Mirror Telescopes [GSMTs] combined with adaptive optics).

2.7 Summary

In this work we used deep *HST* spectroscopy to constrain the metallicities and light-weighted ages of massive ($\log M_*/M_\odot > 10$), quiescent galaxies at $1.0 < z < 1.8$. We selected 32 galaxies from existing *HST* and multi-wavelength imaging in the GOODS-N and -S fields also covered by our deep, 12–orbit WFC3/G102 grism pointings from CLEAR. For redshifts $1.0 < z < 1.8$ the data cover important stellar population features in the rest-frame optical, including the Ca HK feature, 4000 Å break, Balmer lines, Mgb, several other Lick indices and Fe1 Iron lines, which are sensitive to stellar population age and metallicity. All galaxies are selected to have rest-frame optical colors ($U - V$ and $V - J$) indicative of quiescent stellar populations, so that we can use the *HST* grism data to study the relation between galaxy star-formation and enrichment histories and galaxy quenching.

We developed a method to forward model stellar population models, combining the grism dispersion model with the galaxy morphology to model accurately the galaxy spectra and contamination from spectra of nearby sources. We extracted 1D spectra from these models so they match the 1D spectra measured from the data. We validated this method by fitting these models to simulated data from which we are able to recover stellar population ages and metallicities. We showed that there are four redshift subgroups with median redshifts, , , , , which contain different spectral features in the G102 wavelength coverage, and we discussed the systematic differences and statistical uncertainties in the results for stellar population parameters for galaxies that fall in these redshift subgroups.

We then fit the suite of stellar population models to the 1D G102 grism data for each galaxy in our sample, taking into account the galaxies' morphologies to correctly model the grism resolution. We first re-fit for galaxy redshifts using the grism data, and find small corrections from the photometric redshifts derived from broad-band photometry. The grism redshifts yield an accuracy of $\sigma_z \approx 0.005$ compared to the typical photometric redshift from broad-band photometry, $\sigma_z \approx 0.02 - 0.10$. Using the grism redshifts, we then fit the models to derive posterior likelihood distributions for metallicity and light-weighted age for each galaxy. We considered two sets of stellar population models: FSPS and BC03, but we argue the FSPS models are a better representation for these galaxies based on

evidence from Bayes Factors derived from the fitting these models to all the galaxies. We then stack the posteriors for light-weighted ages and metallicities from the fits of stellar population models to each galaxy in each of the four redshift subgroups to derive constraints on the stellar population parameters for the galaxy populations.

Because we are observing the quiescent galaxies closer to their quenching epoch, our results place tighter constraints on their formation history than has generally been possible. Considering the full range of SFHs in our models, we derive light-weighted ages for the galaxies at $1.0 < z < 1.8$ that correspond to a "formation" redshift of $z_{70} > 2$, with approximately one-third of the sample showing $z_{70} > 3$. We show that for the SFHs, these formation redshifts correspond to the epoch when the galaxies had formed formed $> 70\%$ of their stellar mass. The implication is that quiescent galaxies formed the bulk of their stellar mass early. This connects them to recently identified quiescent galaxies at redshifts as high as $z \sim 3 - 4$ (e.g., 39; 40).

We derive constraints on the metallicities of the quiescent galaxies at $1.0 < z < 1.8$, which show that these massive galaxies had enriched rapidly to approximately Solar metallicities as early as $z_{70} \sim 3$. We also show that a mass-metallicity relation exists for $1 < z_{grism} < 1.7$ quiescent galaxies, and that this is consistent with *no* evolution from $z \sim 1.7$ to $z < 0.1$.

Logically, the star-forming progenitors of these galaxies must have been similarly enriched to approximately Solar metallicities prior to quenching. Because there are few galaxies (at any mass) at $z \sim 2 - 3$ with Solar gas-phase metallicities, the progenitors of the quiescent galaxies would be outliers in existing samples. This means there is something special about galaxies on the verge of quenching in the high redshift Universe: either they are more compact with higher metal retention efficiencies (possibly these are the blue-compact galaxies seen at $z > 2$), very short lived phases ($\ll 1$ Gyr), or their progenitors are deeply attenuated by dust which current surveys (that select in the rest-frame optical, i.e., H-band or K-band) are biased against. It also may be that some combination of these effects are in play. The key to understanding the quenching of quiescent galaxies observed at $1z1.7$ will be to identify their Solar-metallicity star-forming progenitors at $z > 2 - 3$. Such studies will be possible in the future with *JWST*, ALMA, and the GSMTs.

We wish to thank our colleagues in the CANDELS, 3DHST, and CLEAR collaborations for their intense work to make these datasets usable. The authors thank the anonymous referee for their constructive report, which improved the quality and clarity of this paper. We also thank them (and others) for productive conversations, comments, suggestions and information, including Charlie Conroy, Romeel Davé, Sandy Faber, Kristian Finlator, Rob Kennicutt, Marcin Sawicki, Corentin Schreiber, and Sarah Wellons. VEC acknowledges generous support from the Hagler Institute for Advanced Study at Texas A&M University. This work benefited from generous support from George P. and Cynthia Woods Mitchell Institute for Fundamental Physics and Astronomy at Texas A&M University. This work is based on data obtained from the Hubble Space Telescope through program number GO-14227. Support for Program number GO-14227 was provided by NASA through a grant from the Space Telescope Science Institute, which is operated by the Association of Universities for Research in Astronomy, Incorporated, under NASA contract NAS5-26555.

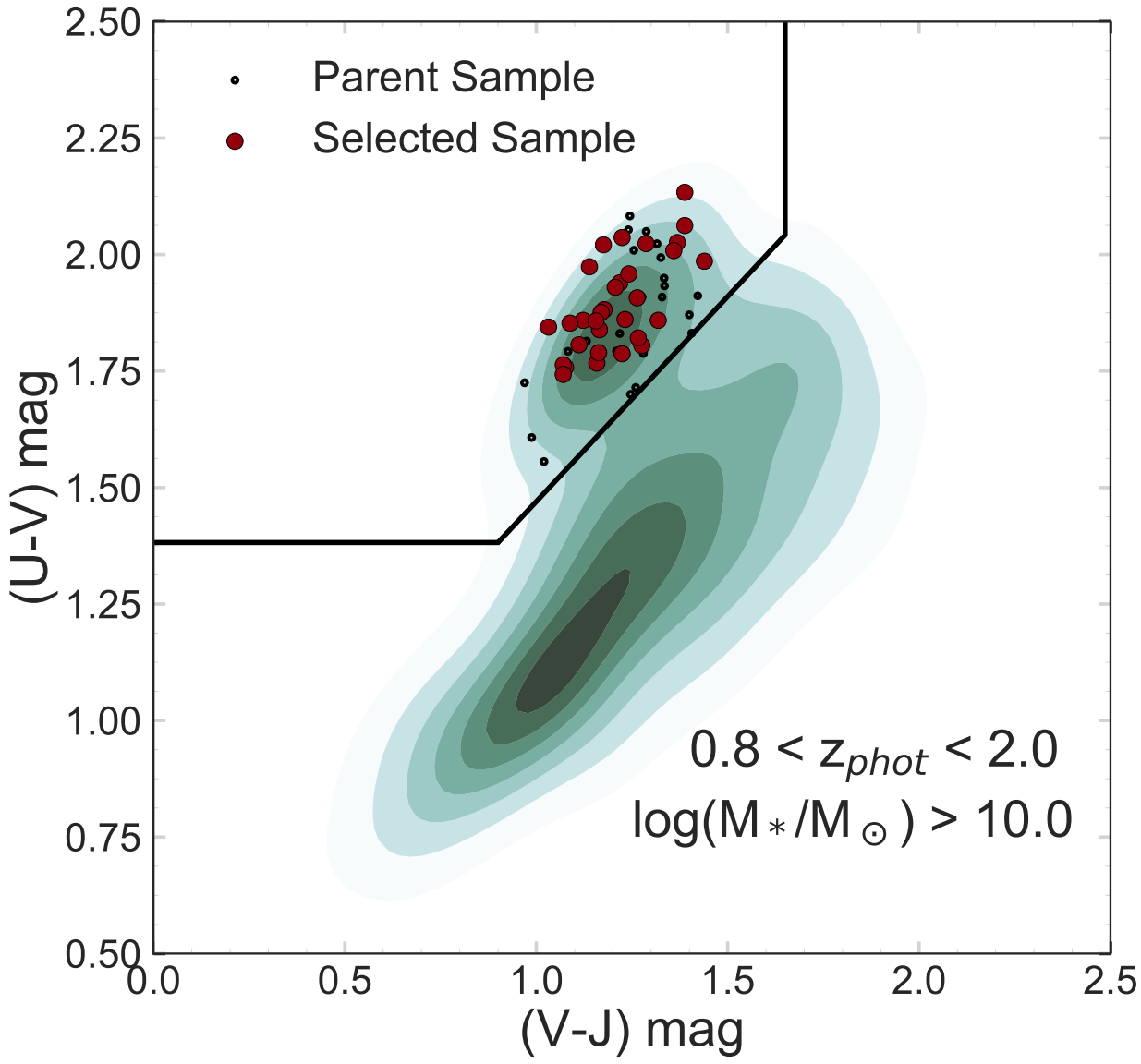

Figure 2.1: Distribution of rest-frame $V - J$ and $U - V$ colors of the galaxies in the GND and GSD galaxy samples. The green–shaded regions show the distribution of all galaxies in the parent catalog with $0.8 \leq z_{\rm phot} \leq 2.0$, CLASS_STAR < 0.8 from SExtractor, and $\log(M_*/M_\odot) \geq 10.0$ (the two-dimensional shows all galaxies in this redshift and mass range, smoothed using an (1) kernel density estimation). The polygon delineates "quiescent" galaxies (upper left region) from "star-forming" (everywhere else) using the definition of (2). Red points mark the sample of quiescent galaxies used here (these galaxies satisfy our selection requirements and fall in fields covered by the deep *HST*/WFC3 G102 spectroscopy). Unfilled points mark the sample of galaxies which were covered in the data and met most of the selection requirements, but were rejected from the final sample.

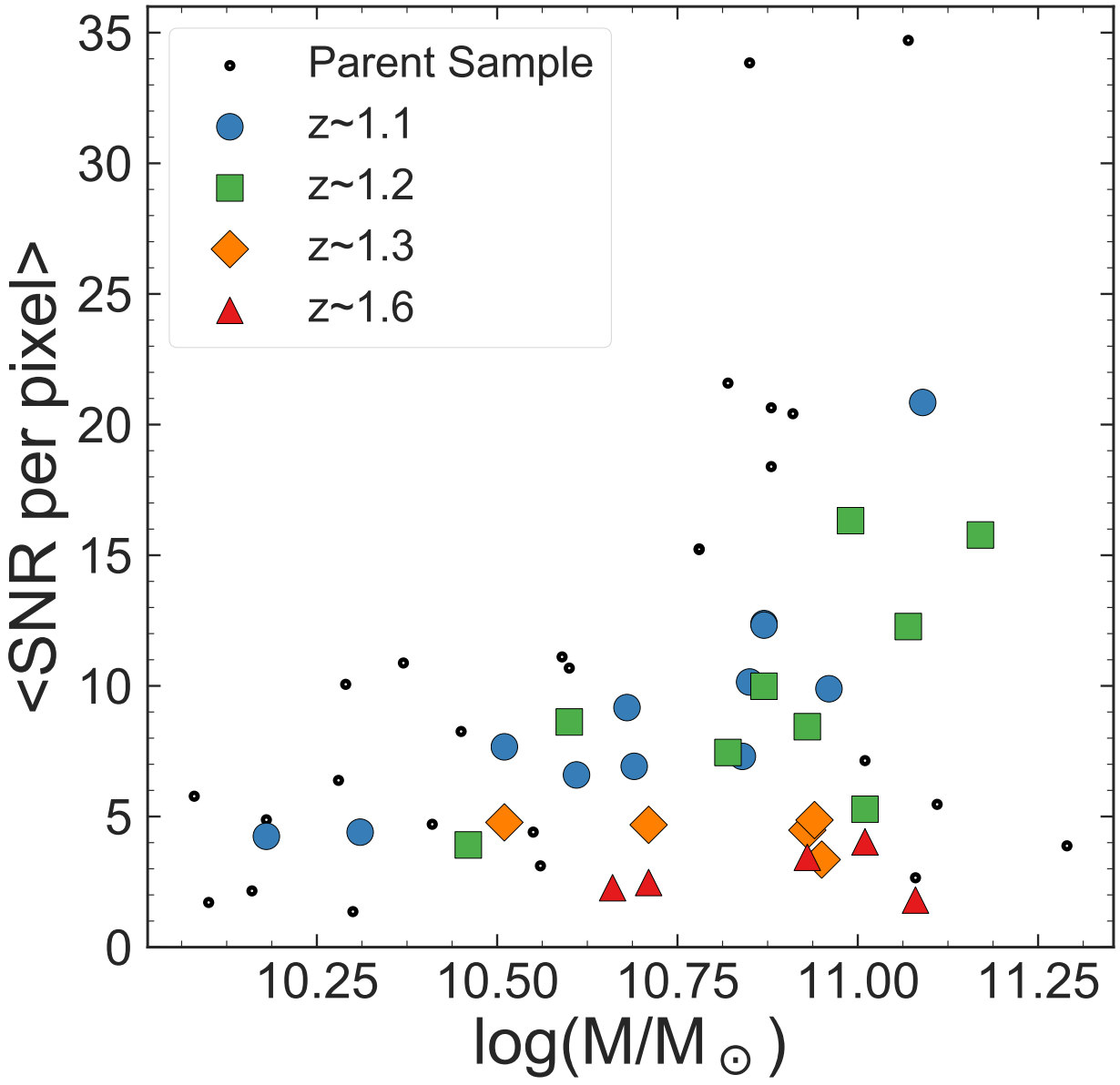

Figure 2.2: The average Signal-to-Noise ratio (SNR) measured in the *HST*/WFC3 G102 grism data for the galaxies in our samples as a function of galaxy stellar mass. For each galaxy, we measured the average SNR per pixel in the 1D spectrum over wavelengths $8500 < \lambda < 10500$ Å. For the majority of galaxies the average SNR is >3 per spectral pixel, where our tests show we are able to derive "good" physical constraints on the galaxy stellar population parameters.

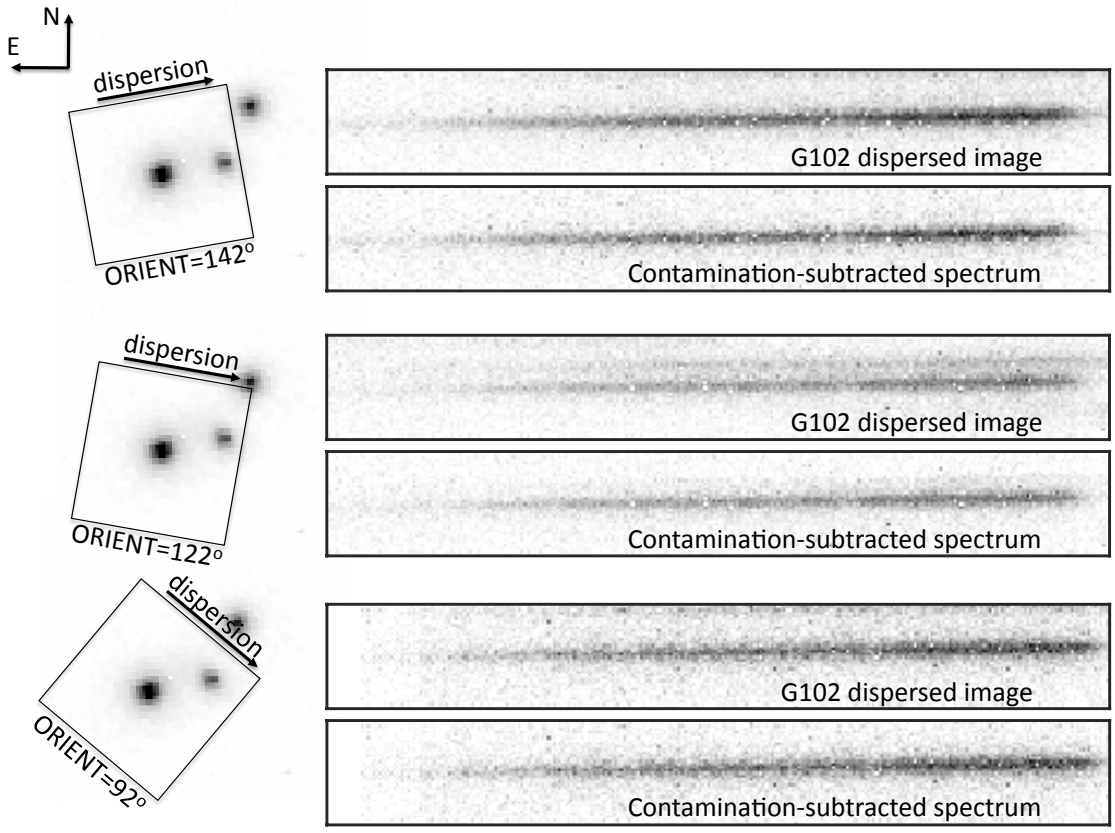

Figure 2.3: Example of *HST* imaging and spectroscopy for one object in our sample. The panels show the extracted F105W direct image and 2D G102 grism spectra for object GSD39170. The data are taken at three different PAs (ORIENT=142, 122, and 92 deg, as labeled). In each direct-imaging panel, the arrow shows the direction of the spectroscopic dispersion in the associated G102 image. Each panel contains a stack from four orbits at each PA, and shows the spectrum both before and after the subtraction from nearby sources (modeled during the the extraction process).

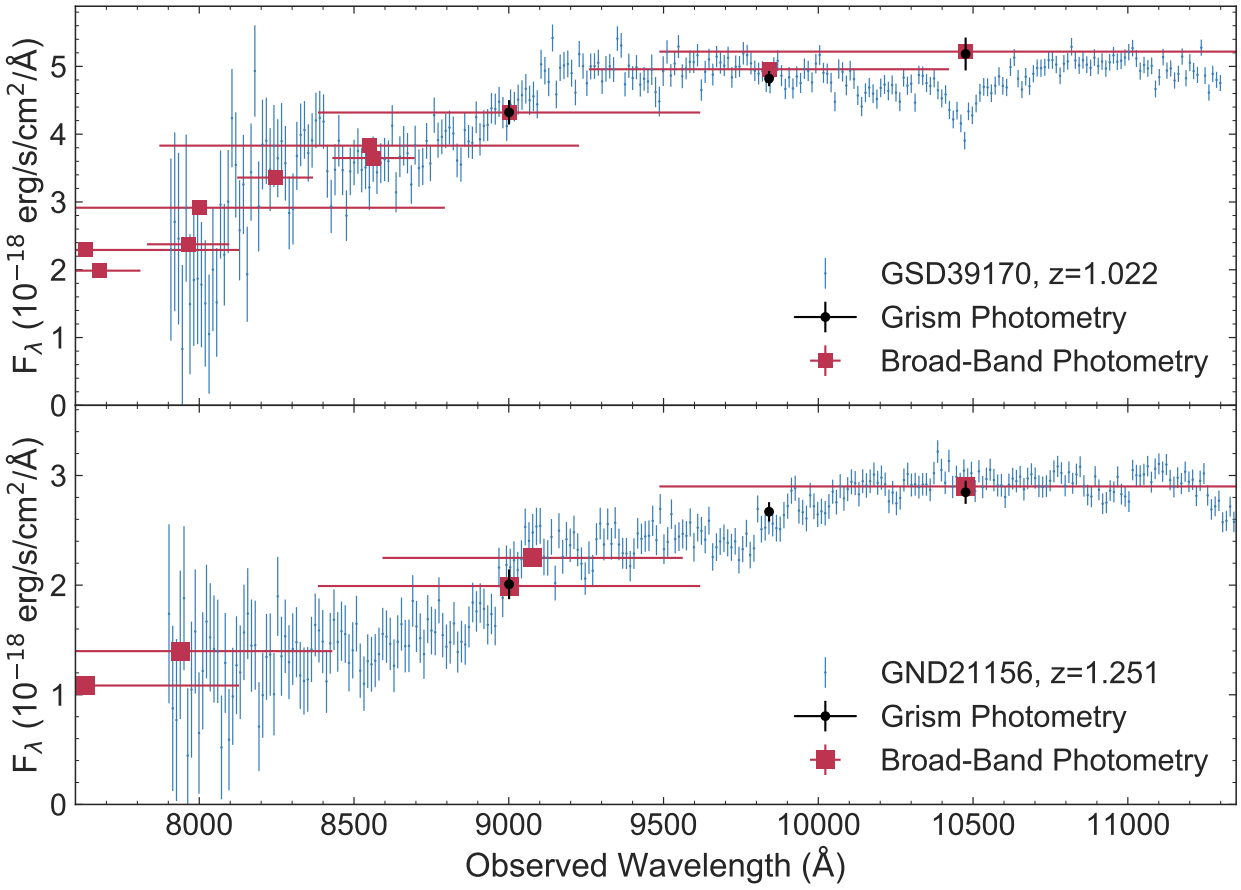

Figure 2.4: Example comparison of the flux-calibration of our 12-orbit depth 1D G102 grism spectra (blue) to the broad-band photometry (red) from our 3D-HST catalog (that includes available z_{850}, Y_{105}, or Y_{098} data) for two objects in our sample. Black points show the synthesized z_{850}, Y_{105}, and Y_{098} measurements from the grism data. The horizontal bars on the photometric points show the FWHM of the broad-band filter transmission curves. Vertical error bars show the 1 sigma errors. Filters included in the top panel are the F775W, IA767, IA797, F814W, IA827, I, IA856, z_{850}, Y_{098}, and Y_{105} bandpasses. The filters included in the bottom panel are the F775W, I, z_{850}, Z, and Y_{105} bandpasses.

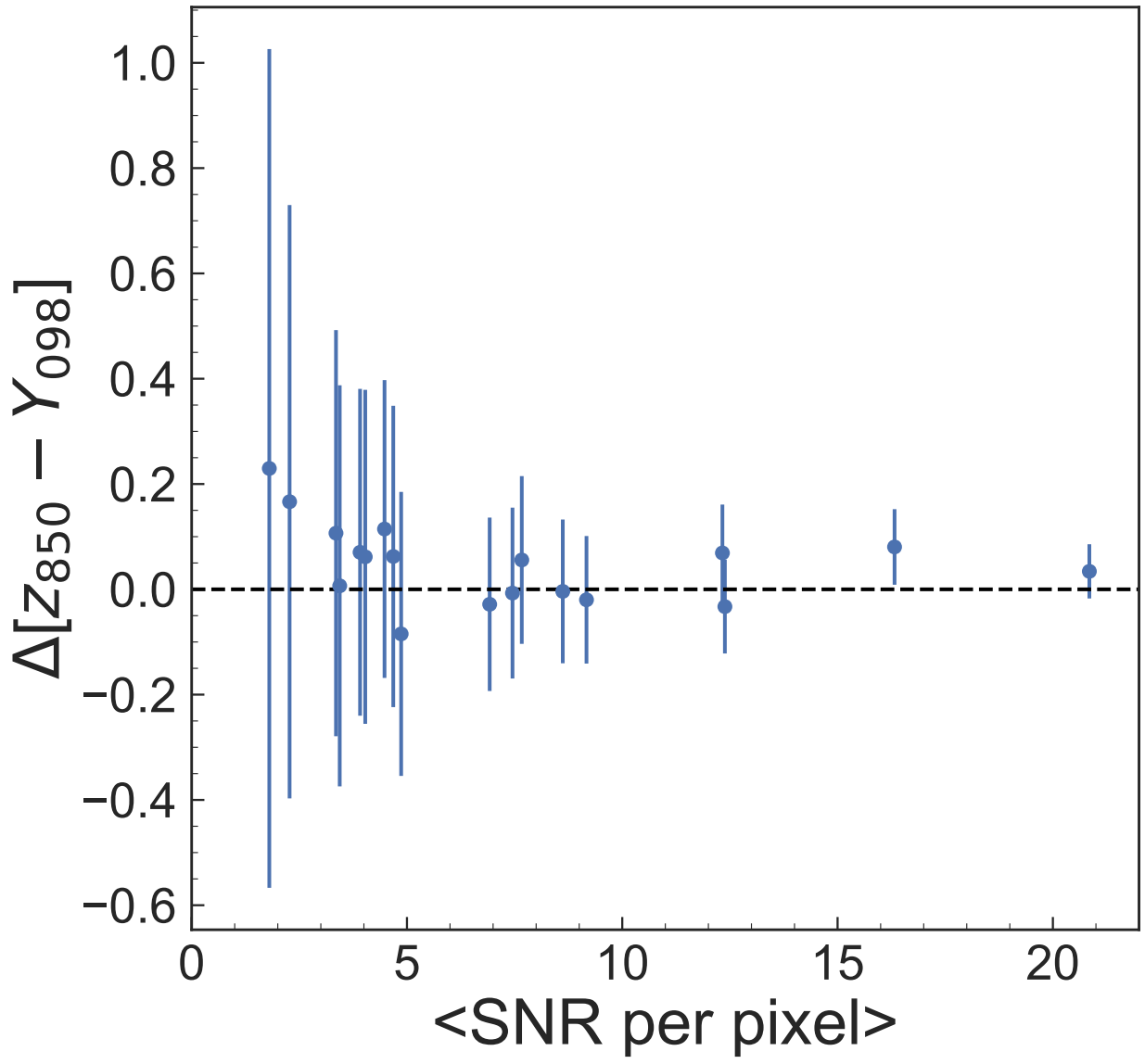

Figure 2.5: Difference between the $z_{850} - Y_{098}$ color derived from broad-band photometry and the color in those bands synthesized from the G102 spectra, plotted as a function of the G102 SNR measured at 8500-10500 Å. Here we can see the residuals are consistent with zero.

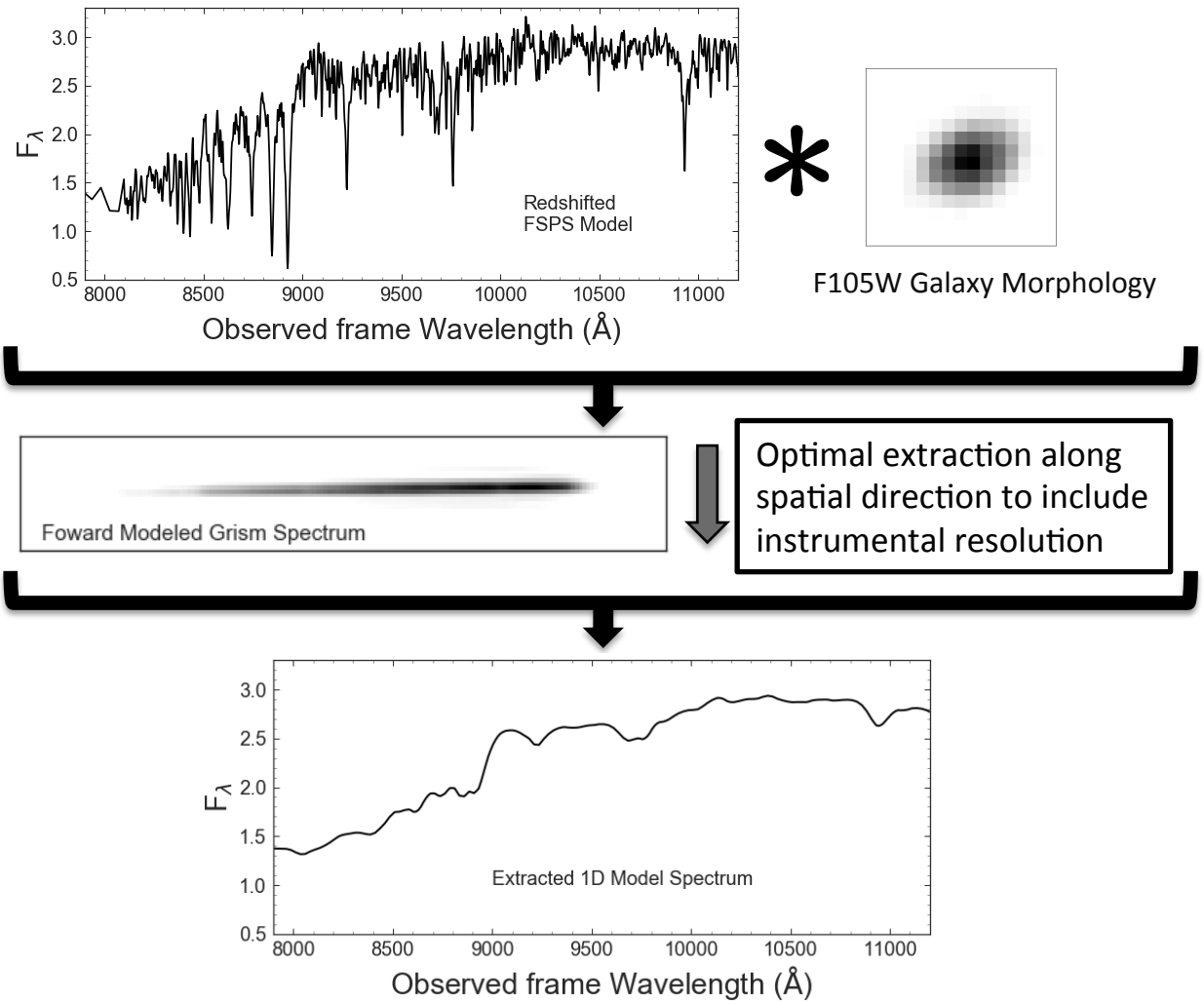

Figure 2.6: Flow chart of the forward modeling process for the G102 spectra. Top row shows the input, observed frame spectrum with the native resolution of the stellar population synthesis model (in this case FSPS; top left panel). This is then convolved with the Y–band (F105W or F098M) imaging (second right panel) and G102 grism resolution to produce an accurate model of the 2D G102 spectrum for this galaxy for this stellar population model (illustrated in the middle row). We then optimally extract a 1D spectrum for this model, which now includes an accurate G102 spectroscopic resolution (that includes the morphological broadening appropriate for each galaxy). For each galaxy we build a suite of these models over a range of stellar population parameters, which we then fit to the observed spectra for each galaxy.

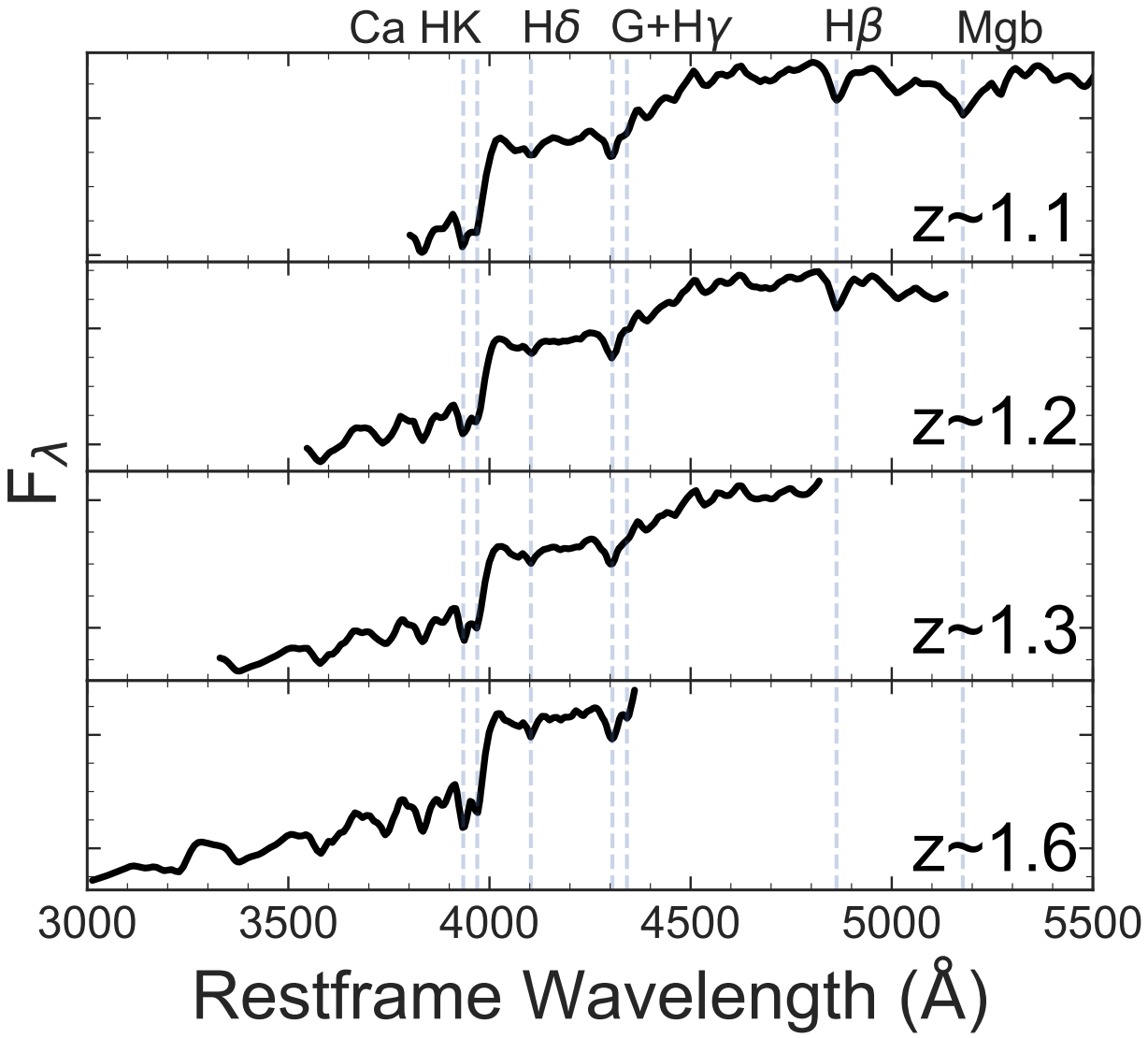

Figure 2.7: Comparison of redshift subgroups. Each panel shows the portion of the rest-frame spectrum covered by the G102 in each redshift subgroup. Important age– and metallicity–sensitive spectral features are labeled.

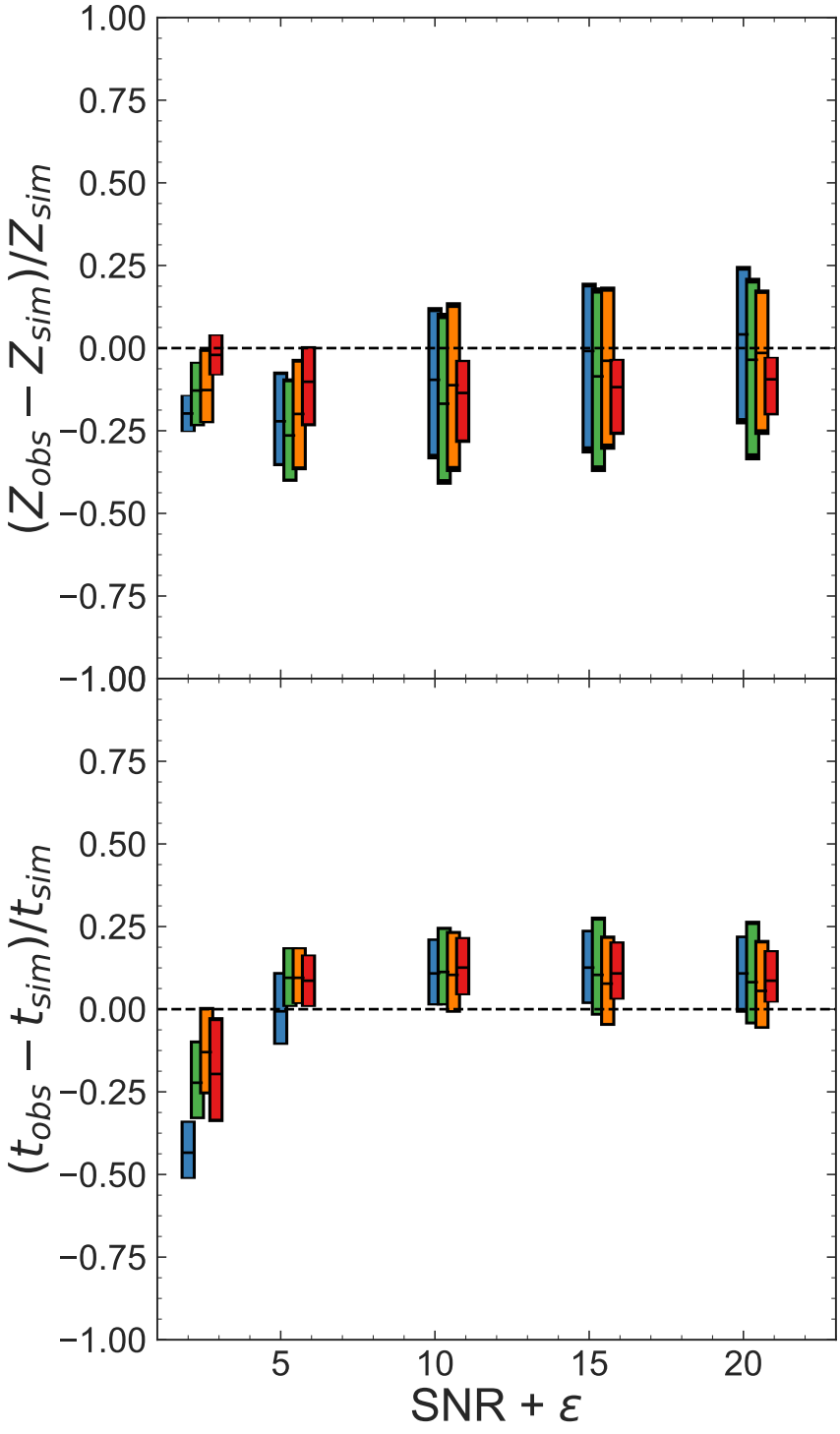

Figure 2.8: Illustration of the distribution of fits on stellar population parameters derived from fits to simulated data. This was done for each redshift subgroup as a function of SNR (shown with a slight offset (ϵ) for readability). Fits shown here are in relation to simulated spectra with "true" values t =2.5 Gyr and Z =1 $Z_{\odot}$. Because the G102 spectrum probes different portions of the rest-frame spectrum, the accuracy of the derived parameters changes as the important features shift across the grism coverage.

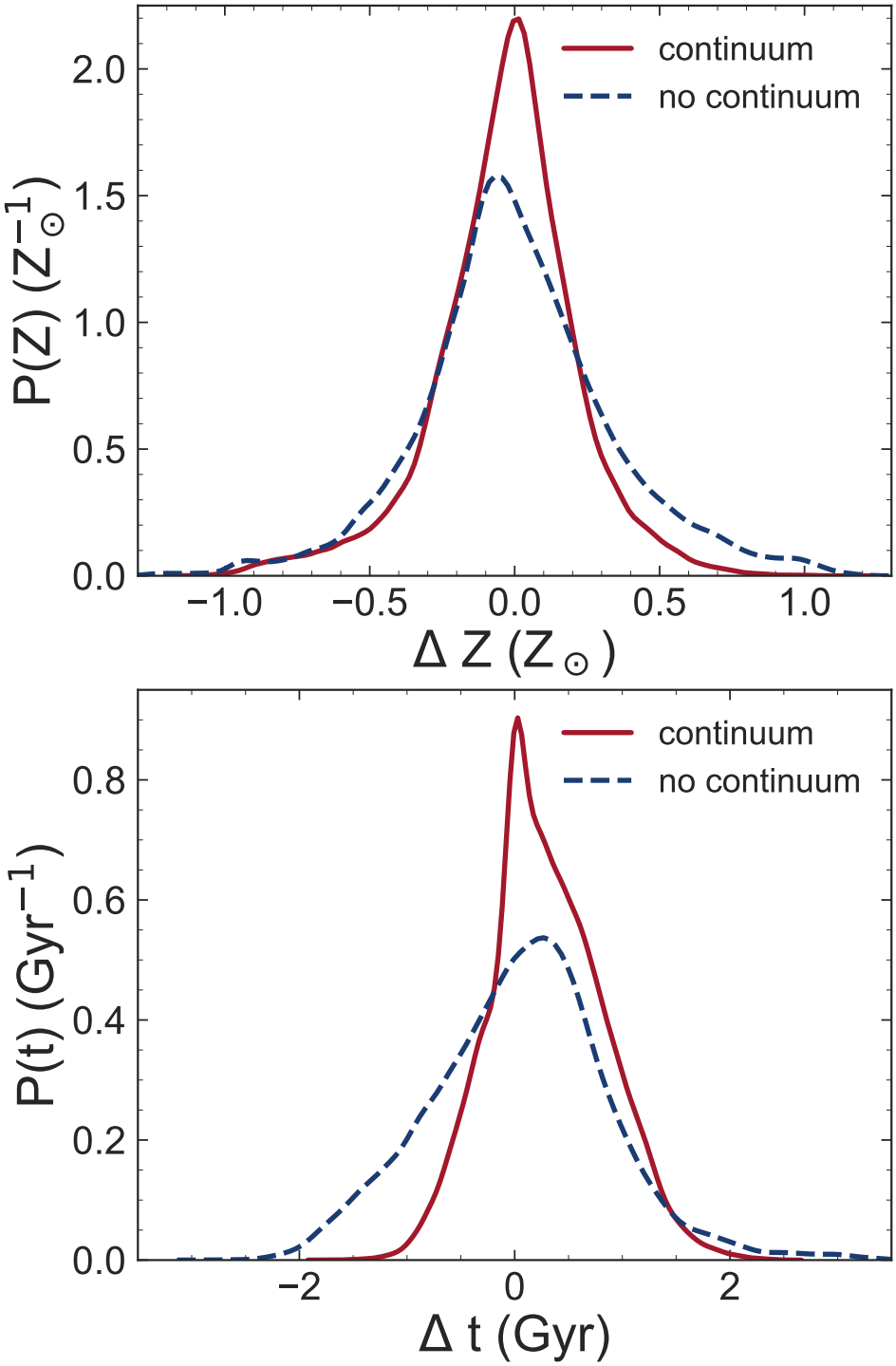

Figure 2.9: Comparison of parameter distributions from fitting with and without the continuum. The top panel shows the posteriors on the metallicity distributions. The bottom panel shows the light-weighted age distributions.

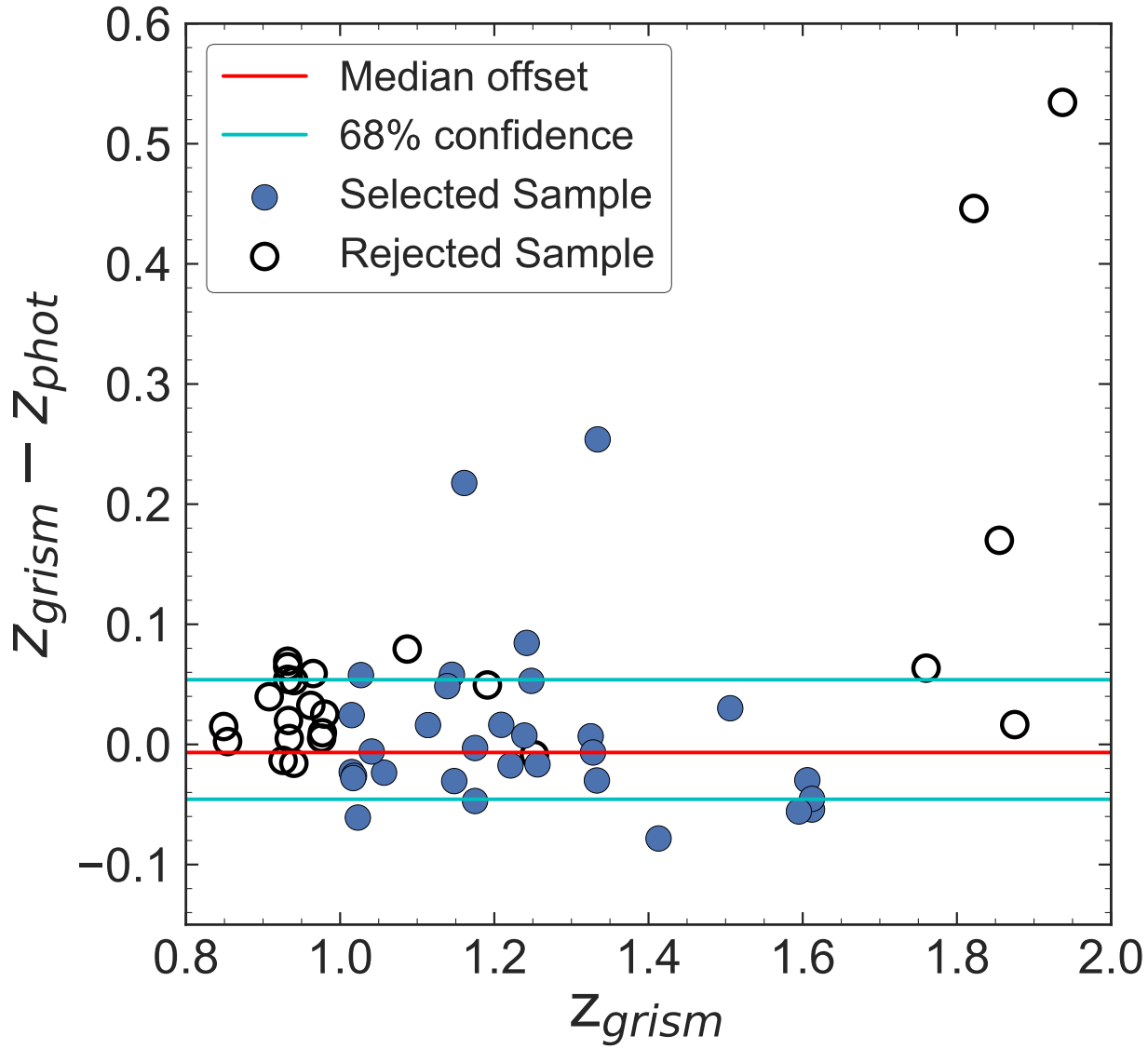

Figure 2.10: Comparison of our photometric redshifts derived from the deep CLEAR G102 spectra (z_{grism}) to those derived from broad–band photometry from 3D-HST (z_{phot}). The median offset between the two redshifts ($\Delta z \sim 0.01$) is marked by a red line and the 68% scatter intervals ($-0.07 < \Delta z < 0.04$) are bounded by cyan lines. Empty circles mark the rejected sample; this includes the sample of galaxies rejected after fitting z_{grism}.

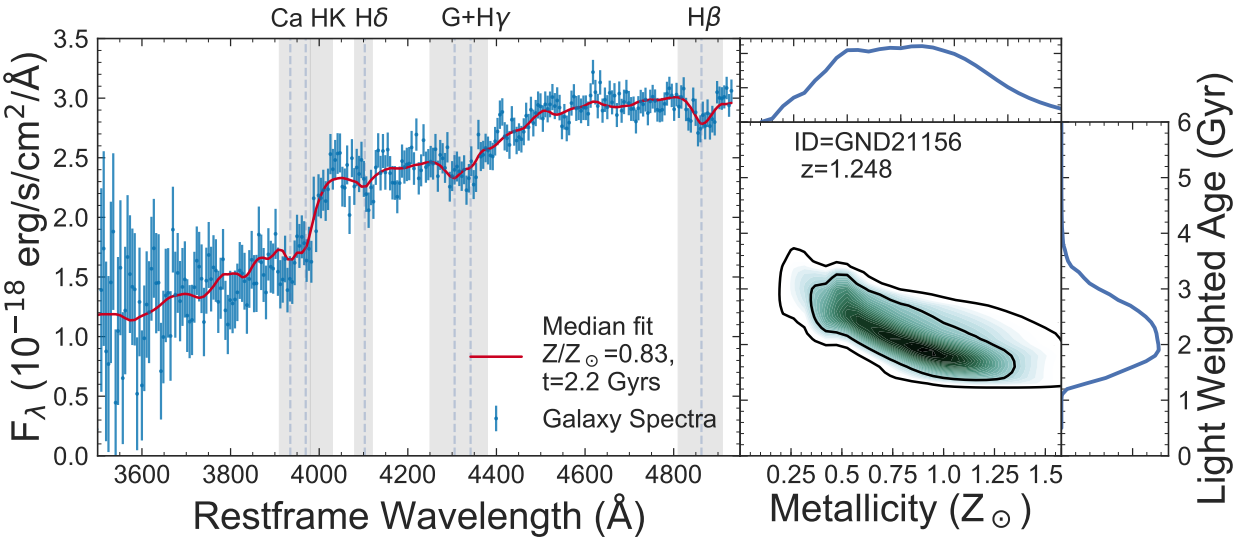

Figure 2.11: **Left**: The 1D G102 grism 12-orbit data for the galaxy GND21156 at $z = 1.251$ as a function of rest-frame wavelength. The shaded regions show the locations of prominent spectral features. The red solid line shows a model with parameters given by the median metallicity (Z) and light-weight age (t) derived from the posteriors derived on each parameter. **Right**:The posteriors on the stellar population parameters of metallicity and light-weighted age for the galaxy in the left panel. The main panel shows the joint likelihood (with the 68% and 95% confidence intervals outlined in black) derived on both parameters jointly using Equation 2.6. The sub-panels to the right and above the main panel show the individual posteriors on light-weighted age and metallicity. From these we derived median and 68%-tile ranges for each parameter for each galaxy in our sample.

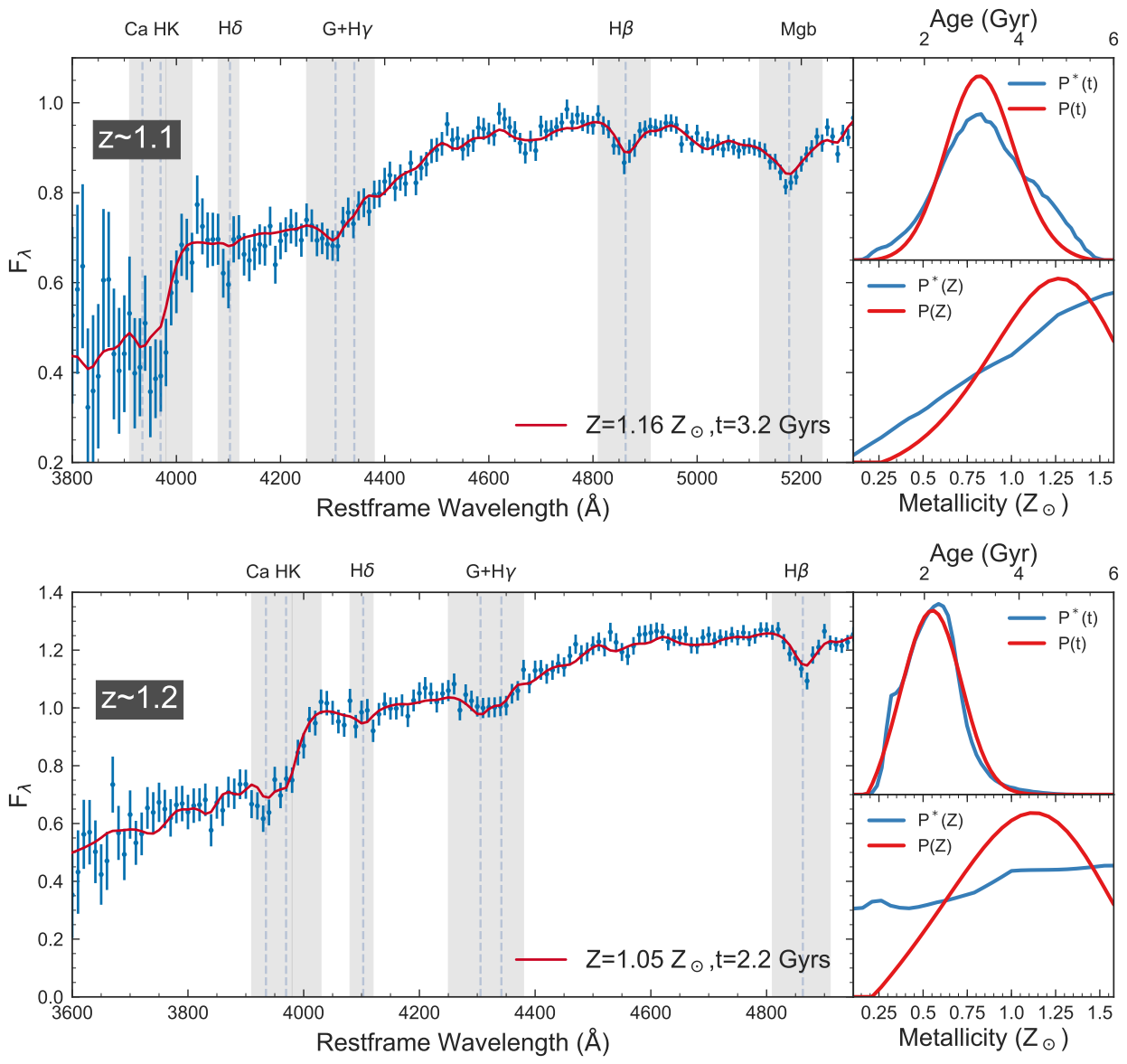

Figure 2.12: Top: Stacked spectra and posteriors for galaxies in the redshift subgroup. The main panel shows the stacked 1D G102 grism data against rest-frame wavelength. The sub-panels on the right show the stacked posteriors (blue:weighted stacking, red:"stack-smooth-iterate" method) on light-weighted age (t) and metallicity (Z) derived using the method described in Section 2.5.2. The red-solid line in the main panel shows a model with the median Z and t taken from these individual-parameter posteriors (i.e., these are *not* best-fit models to the stack). Bottom: Same plots for the redshift subgroup of galaxies.

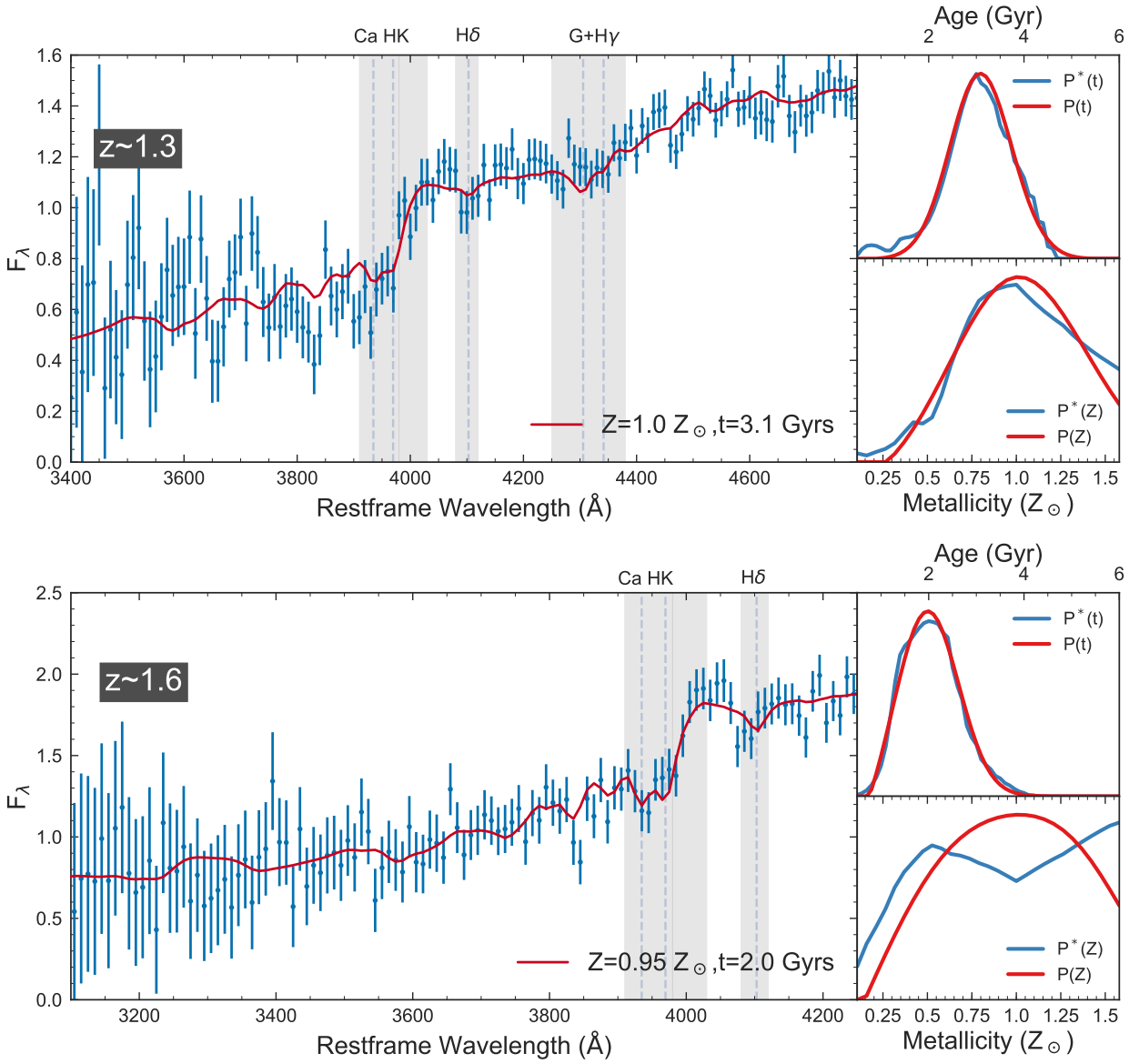

Figure 2.13: Same as Figure 2.12 for galaxies in the (top) and (bottom) galaxy subgroups.

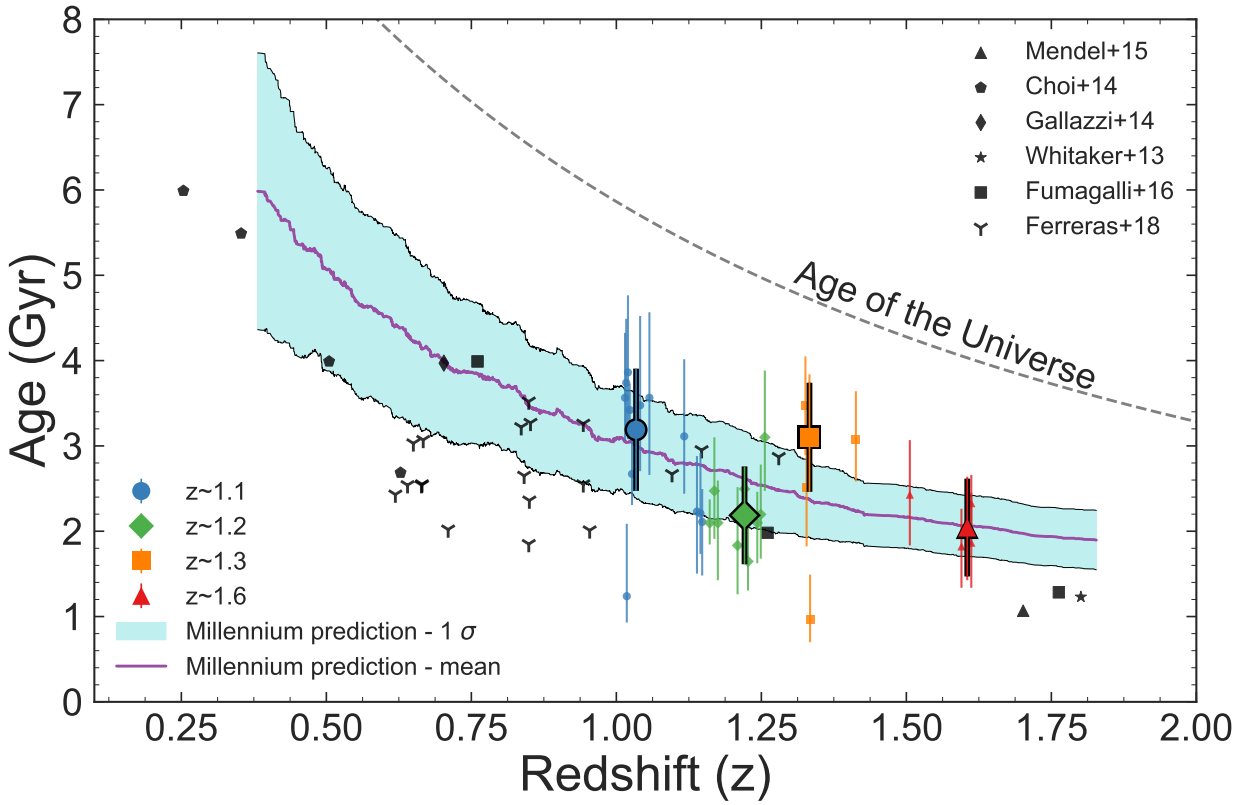

Figure 2.14: The evolution of light-weighted age as a function of redshift. The small, colored data points show results for the individual $1 < z_{grism} < 1.8$ galaxies in our sample. Large colored data points correspond to median values derived from the stacked posteriors for redshift subgroup as labeled. Error bars show 68% confidence intervals. Other small (black) data points correspond to results from (3; 4; 5; 6; 7; 8). Generally, quiescent galaxies have younger stellar populations at higher redshifts, where their light-weighted age has nearly a constant offset from the age of the universe. This agrees with predictions from the Millennium simulation (9), where the shaded band shows the median and 68%-tile scatter in light-weighted ages of quiescent galaxies in their predictions.

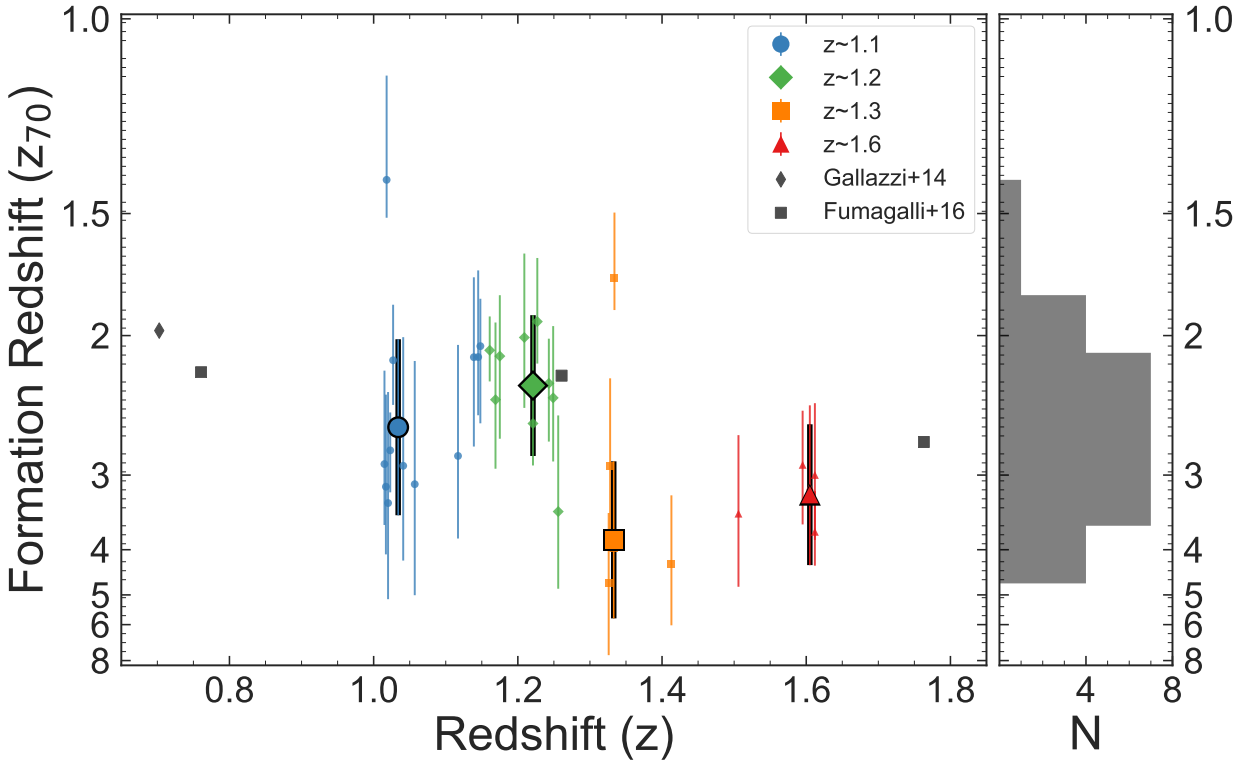

Figure 2.15: Distribution of galaxy formation redshifts. The Left panel shows the derived formation redshifts, z_{70} of quiescent galaxies as a function of observed redshift. The Right panel shows the distribution of median formation redshifts for our samples. The formation redshift, $z_{\rm form}$, corresponds to the redshift where the galaxies had formed more than 68% of their stellar mass (see Section 2.6.2). Here, we only include age measurements (shown in black) from studies which measured light-weighted ages. The quiescent galaxies at $1 < z_{grism} < 1.8$ in our sample have formation redshifts $z_{\rm form} > 2 - 3$ nearly independent of observed galaxy redshift.

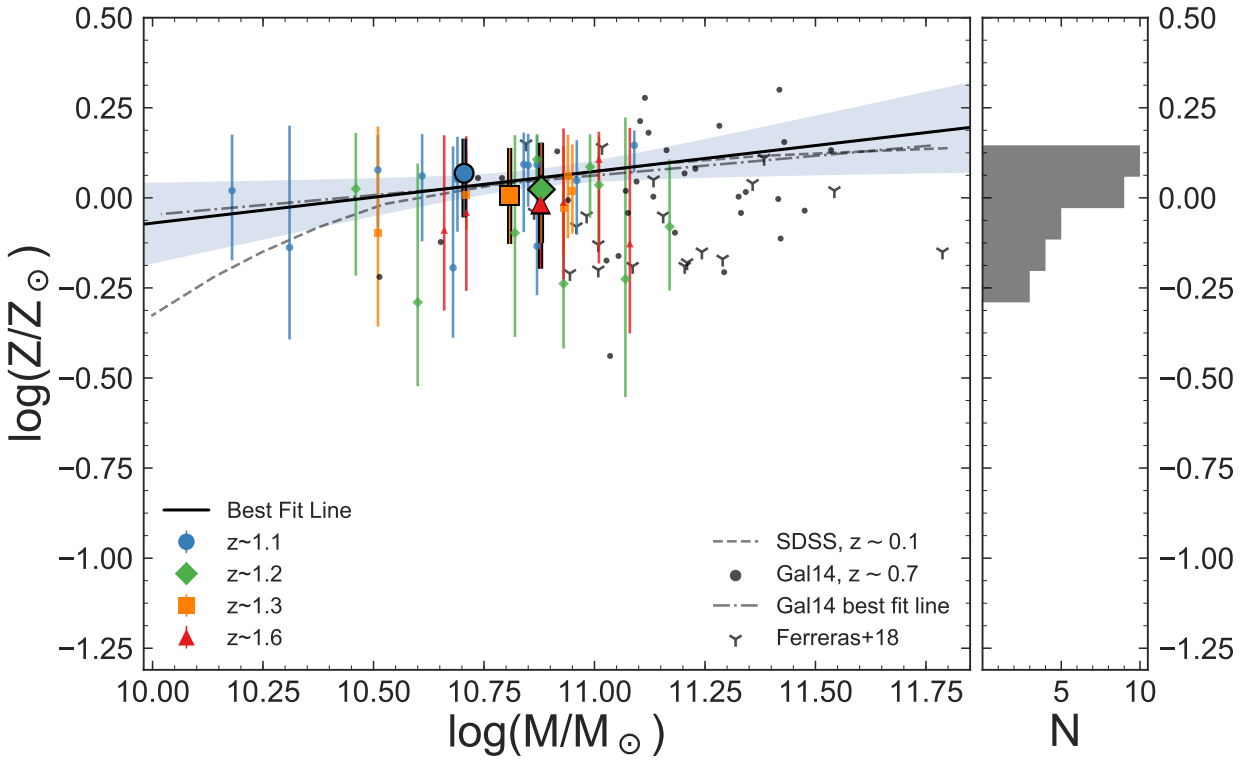

Figure 2.16: Left panel: Mass–metallicity relation for quiescent galaxies at $1.0 < z_{grism} < 1.7$. The small, colored data points and error bars show the median values and 68%-tile range for the individual galaxies in our redshift subgroups, as labeled in the figure legend. The large colored data points show the metallicities from the stacked posteriors for each subgroup. The thick solid line shows a linear fit to the individual galaxies and the shaded region shows the 68%–tile bound. The dashed and dot–dashed lines show the mass-metallicity relation for quiescent galaxies from lower redshift samples (from SDSS at $z < 0.22$, (10); and $z \sim 0.7$ from Gal14). We also include measurements of individual galaxies from Gal14 and (8). Right panel: Histogram of the median metallicities for the galaxies in our $1.0 < z_{grism} < 1.7$ sub-groups. The majority of the probability density lies around $\approx Z_{\odot}$.

3. EVIDENCE FOR EARLY FORMATION OF THE MOST COMPACT QUIESCENT GALAXIES AT HIGH REDSHIFT*

3.1 Introduction

One of the major outstanding questions in galaxy evolution is "how do massive quiescent galaxies form?". These galaxies exhibit many extreme traits: compact morphologies (e.g. 14; 11), indications of rapid formation histories (including [α/Fe] enhancement and high star-formation rates [SFRs] at early times) (e.g., 23; 25; 24; 28), old stellar populations (10; 27; 5; 13), and high overall metallicity ($Z \simeq Z_{\odot}$) (13; 8; 28).

Multiple theories have been proposed to explain the inability of massive galaxies to continue star-formation. A very important difference in these models is the timescale of quenching (e.g., 124). Studies in this area have led to the identification of "fast" and "slow" evolutionary paths, which describe the relative rate of quenching (115; 125; 126).

The slow path applies to galaxies that quench their star-formation by experiencing a gradual slowdown in their gas accretion rates combined with the consumption or heating of their existing gas (as may be the case in the Milky Way, 127).

These galaxies can have compact morphologies if they formed in the early universe (when densities were higher, e.g. 125) or if they undergo (secular) compaction events or dissipative mergers (114; 125; 128).

The fast path normally requires a fast-acting compaction event (i.e., major mergers, extreme disk instabilities). This can drive extreme star-formation and/or supermassive black hole accretion, the feedback from which quenches star-formation. Due to higher gas fractions, the fast quenching path may be more common in the early universe (114; 129).

The key difference in the physical processes of quenching is the speed at which it occurs. This

**Reprinted with permission from "CLEAR II: Evidence for Early Formation of the Most Quiescent Galaxies at High Redshift" by Estrada-Carpenter, Vicente; Papovich, Casey; Momcheva, Ivelina; Brammer, Gabriel; Simons, Raymond; Bridge, Joanna; Cleri, Nikko J.; Ferguson, Henry; Finkelstein, Steven L.; Giavalisco, Mauro; Jung, Intae; Matharu, Jasleen; Trump, Jonathan R.; Weiner, Benjamin 2020. The Astrophysical Journal, Volume 893, id.171, Copyright 2020 by The American Astronomical Society.*

can be studied using constraints on the galaxies' star-formation histories (SFHs). Quenching can be correlated with galaxy morphology if the quenching mechanism involves reorganization of the galaxies' stellar component (such as compaction), or a natural consequence of "inside-out" growth combined with disk fading e.g., (130)). Therefore, deriving the SFHs and comparing them to the morphologies of galaxies has the potential to constrain the quenching mechanisms.

Here, we aim to constrain the SFHs of a large sample of massive quiescent galaxies ($\log M_*/M_\odot > 10.5$) at $z1$ and study these as a function of morphology. Throughout we use a cosmology with $\Omega_{m,0} = 0.3$, $\Omega_{\Lambda,0} = 0.7$, and $H_0 = 70$ km s^{-1} Mpc^{-1}.

3.2 Data

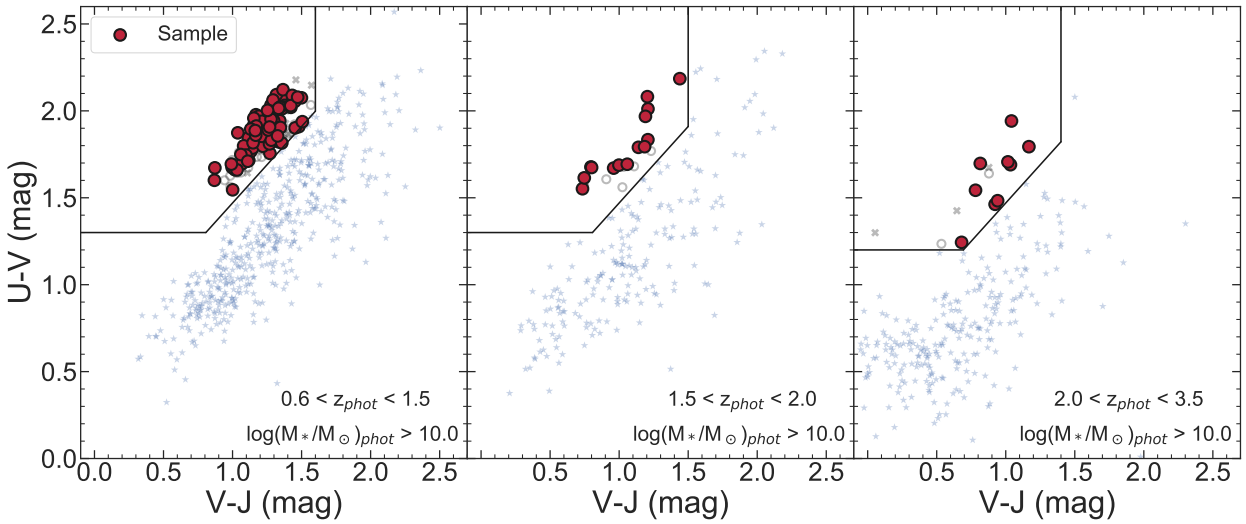

Figure 3.1: $V - J$ versus $U - V$ rest-frame color-color diagram ("UVJ" plot) of all CLEAR galaxies with $0.6 < z_{\rm phot} < 3.5$ and $\log(M_{\rm phot}/M_\odot) > 10.0$. Galaxies which fall into the quiescent wedge (upper left region in each panel) are candidate quiescent galaxies and constitute our parent sample. The red larger points show galaxies that satisfy our final sample selection of $0.7 < z_{\rm grism} < 2.5$ and $\log(M_{\rm grism}/M_\odot) > 10.5$ (and satisfy our X-ray and 24 μm selection, see Section 3.2.1). Blue stars show galaxies that fail the quiescent-galaxy selection (i.e., they are star-forming galaxies). Grey X's mark quiescent galaxies that were rejected (mostly because they have grism-redshits outside our final redshift range). Open grey circles show quiescent galaxies that are rejected for falling under our final stellar-mass limit $\log(M_*/M_\odot) > 10.5$.

We use data from the CLEAR survey (a Cycle 23 *HST* program, PI: Papovich), which consists

of deep (12 orbit) *HST*/WFC3 G102 slitless grism spectroscopy covering $0.8 - 1.2$ within 12 fields split between the CANDELS GOODS-North (GN) and GOODS-South (GS) fields (see, 71; 72; 13). These fields overlap with the 3D-HST GOODS fields (65), which provide shallow (2 orbit depth) slitless G141 grism coverage from $1.1 - 1.65$. The galaxies of interest lie at $0.7 < z_{grism} < 2.5$, where our spectral coverage includes many metallicity and age features. These include the 4000 Å break, Balmer lines (Hδ, Hγ, Hβ, Hα), Ca HK, Mgb, and other absorption features. We also utilize the broadband photometry available (using an updated catalog from (16) that includes photometry in the Y-band from *HST*/WFC3 in F098M or F105W, see (13) and CLEAR collaboration, in prep). The broadband photometric data spans 0.3–8 (rest-frame UV to near-IR) allowing for better SFH constraints. We include all bands available in (16) (now including the WFC3 F098M and F105W data), with the exceptions of the MOIRCS J, and Suprime-cam I, Z-bands in GOODS-N, and with the exceptions of the ISAAC JHK, the ESO/WFI I-band, and the IA768, IA797 filters in GOODS-S. These bands consistently showed large biases in the flux calibration (up to 0.3 mag) compared to residuals between the galaxies' data and our best-fit models. While these flux-calibration offsets were consistent with those reported by (16), we found very larger scatter, which made their flux calibration uncertain. In all cases the excluded bands are significantly shallower than other bands that cover these wavelengths (by up to $1 - 1.5$ mag), and excluding these bands had no impact on our final fits.

Figure 3.2 shows examples of the full data coverage for the broadband photometry and grism spectroscopy. We used the *Grism redshift & line* analysis software Grizli[1] for spectral extractions and grism forward modeling. For our analysis, we include all *HST*/WFC3 grism data available. The primary dataset is from CLEAR, but we include additional WFC3/G102 data from GO 13420 (PI: Barro) and Faint Infrared Grism Survey (FIGS) (131) when these overlap with galaxies in the CLEAR fields, as these additional data help to reduce contamination and increase the overall signal to noise of the grism data. Due to the nature of grism data there are instances when the spectra of our galaxies show residual contamination from the spectra of nearby objects (especially in the case

[1] https://github.com/gbrammer/grizli

that the nearby objects are significantly brighter in flux). For our sample, we visually inspected the individual beams of each object. In cases where we observed any residual contamination, we either removed those beams or masked the residual emission. This affected individual beams in 9% of the objects in our sample. The residuals from contamination subtraction are frequently worse in the G141 spectra. This is primarily due to the fact that these data are taken with only a single *HST* ORIENT. Therefore the contamination (collisions from the spectra of nearby galaxies) is modeled in only a single role angle, where multiple role angles improve the correction by modeling the galaxy spectra at independent locations (see discussion in, e.g., 13). In part, this was one reason that we included in our models additional (nuisance) parameters that allow for a bias or tilt to the grism data (see Section 3.3.1). The residuals from contaminating spectra are less severe in the G102 spectra, which include multiple orbits (at least 3 ORIENTs). As discussed below, we include with this *Paper* an online, interactive appendix that shows the data for each of the galaxies in our sample, see also Appendix B.2.

For our analysis below, we also make use of MIPS 24 data for the GOODS-N and GOODS-S fields from the GOODS Spitzer Legacy program (PI: M. Dickinson, see, 132). We use here an updated catalog derived from photometry derived using prior source positions from *Spitzer*/IRAC (using the same procedures and methods identical to that of (132); [H. Inami and M. Dickinson, private communication]). These catalogs are also discussed in (127).

3.2.1 Sample Selection

Following (13), we select quiescent galaxies using a rest-frame $(U-V)$–$(V-J)$ color-color diagram (UVJ) selection (see 81),

$$\begin{aligned}
(U-V) &\geq 0.88\times(V-J)+0.59,\\
(U-V)\geq 1.3,\ (V-J) &\leq 1.6\ [0.0<z<1.5],\\
(U-V)\geq 1.3,\ (V-J) &\leq 1.5\ [1.5<z<2.0],\\
(U-V)\geq 1.2,\ (V-J) &\leq 1.4\ [2.0<z<3.5]
\end{aligned} \tag{3.1}$$

as seen in Figure 3.1. For our parent sample we select galaxies with $0.6 < z_{\rm phot} < 3.5$ and $\log(M_{\rm phot}/M_{\odot}) > 10.0$ using updated photometric redshifts ($z_{\rm phot}$), stellar masses ($M_{\rm phot}$), and rest-frame colors derived from the broad-band photometry derived from EAZY-py[2]. Our parent sample then consists of 174 candidate quiescent galaxies using these selection criteria. These are shown in Figure 3.1, subdivided by photometric redshift. We use the redshifts from the broad-band data to select the parent sample even when we have redshifts from grism data using the Grizli extractions ($z_{\rm grizli}$). This is because it is possible for Grizli to misidentify emissions lines, which occur either in low signal-to-noise data, or in cases where objects have residual contamination (e.g., emission lines from nearby objects which are removed post extraction as explained in Section 3.2).

We therefore use the EAZY-py fits to the broad-band data to define our initial sample (from $z_{\rm phot}$ and the rest-frame $U-V$ and $V-J$ colors) and then subsequently refine our sample using the fits to the broad-band photometry and both the G102 and G141 grism data from our analysis below ($z_{\rm grism}$, see Section 3.3 below). Here, we provide some comparisons between the different redshifts. Comparing our adopted redshifts ($z_{\rm grism}$) to either those from Grizli ($z_{\rm grizli}$) or to those from the broad-band photometry alone ($z_{\rm phot}$), the difference is small. We find a small scatter for the redshifts derived from the grism data, with $\sigma(z_{\rm grizli} - z_{\rm grism}) \sim 0.008$. Fewer than 8% of the galaxies (13 of 174) show differences in redshift as large as $|z_{\rm grizli} - z_{\rm grism}| > 0.2$, and this appears to be the result of the misidentification of weak emission lines where the grism data is noisy. The difference between our adopted redshifts ($z_{\rm grism}$) and those from the broad-band photometry alone ($z_{\rm phot}$) have larger scatter, $\sigma(z_{\rm phot} - z_{\rm grism}) \sim 0.03$, but this is consistent with the uncertainty of the photometric redshifts derived from broad-band photometry compared to spectroscopy (see, e.g., 133; 16; 134).

We then apply a secondary sample selection using the results from our new stellar population fits to the broad-band data and grism data (see Section 3.3 below). First we remove 12 galaxies that had poor quality grism spectra, either because they had low SNR (< 1 pixel^{-1}), had severe contamination from nearby objects, and/or fell near the edge of the WFC3 grism field (where they

[2]https://github.com/gbrammer/eazy-py

had <30% spectroscopic coverage in the grism data). We then refine the selection to include only galaxies with $0.7 < z_{\rm grism} < 2.5$ and $\log(M_{\rm grism}/M_{\odot}) > 10.5$, where the $\mathtt{grism}$ subscript denotes quantities deriving using our fits to the broad-band photometry and G102+G141 grism data (see Section 3.3). The redshift range is used to ensure that the *HST*/WFC3 G102+G141 data include important rest-optical spectral features that are sensitive to age and metallicity (see below), while the stellar mass limit corresponds to (approximately) a volume limited sample limited in stellar mass $\log(M_{\rm grism}/M_{\odot}) > 10.5$ over this redshift range for our SNR requirement. Furthermore, the bias and scatter between the stellar masses from EAZY-py (used for the parent sample) and the grism-derived method (used for the final sample) are small (0.07 dex and 0.05 dex, respectively) so this does not affect our final sample which uses a higher stellar-mass limit. We then removed X-ray sources by cross-matching our catalog with sources with $r \leq 0.5$ within any source in the the 2 Ms Chandra Deep Field-North Survey (78) and 7 Ms Chandra Deep Field-South Survey catalogs (79). We also incorporate morphological information using results from Sersic-fits, derived using GALFIT (135), from (11). We remove galaxies with a fit quality flag of 3 (or "no fit"). Finally we limit our sample to a stellar mass surface density (Σ_1) of $\log(\Sigma_1) > 9.6$ to remove potential satellites. The final sample passing all our selection criteria includes 98 quiescent galaxies. We show these as large red symbols in Figure 3.1.

Several previous studies (e.g., 6; 136) have shown that the UVJ selection of quiescent galaxies is susceptible to contamination from dust-reddened star-forming galaxies. We tested for this possibility in our own sample by cross-correlating the sources in our catalog against those in the MIPS 24 data for these fields. Of our 98 quiescent galaxies we find matches for 15 of our galaxies within 0.5. Because the MIPS 24 μm point-spread function (FWHM $\simeq$6) is substantially larger than that of *HST*/WFC3 (FWHM $\simeq$ 02) we inspected the sources visually using the *HST*/WFC3 images (F125W, F160W bands), *Spitzer*/IRAC images (3.6, 4.5, 5.8, 8.0 μm bands) and MIPS 24 μm image. From this, we determined that 9/15 of the 24 μm detections are likely a result of flux from nearby sources (as evidenced from the fact that the nearby neighbor is brighter in the IRAC data). We therefore do not remove these galaxies from our sample. In the remaining 6/15 of the 24 μm

sources, only two have SNR(24μm) > 5. For completeness, we keep these galaxies in our sample, however, we find that excluding them has no impact on our conclusions as they span a range of stellar mass surface density and formation redshift see below). In addition, all our galaxies have derived specific SFRs (sSFR; averaged over the last 100 Myr) from the broad-band photometry and grism data of $\log(\mathrm{sSFR}/\mathrm{yr}^{-1}) - 10.2$, consistent with them being quiescent as they all lie at least 1.5 dex below the star-forming main sequence (137). Therefore, even if these objects have obscured star-formation or AGN, it is not a significant contributor to the light dominating the *HST* grism data and photometry, which instead appears to originate from passively evolving stellar populations.

3.3 Methods

3.3.1 Modeling the Stellar Populations and Star-Formation Histories

To constrain the stellar population parameters of our galaxies we build on our forward modeling technique described in (13), previously applied solely to WFC3/G102 grism data.

We use Flexible Stellar Population Synthesis (FSPS) models (e.g., 91), using a combination of MILeS and BaSeL libraries and assuming a Kroupa initial mass function (138), to fit our SEDs.

We have updated our methodology to use the dynamic nested sampling algorithm engine from Dynesty (139). This allows us to model additional parameters, and take advantage of improvements in computational speed and parallelization. Dynesty allows us to include additional (nuisance) parameters to handle possible systematics which arise when fitting the two spectroscopic data sets (deep G102 and shallow G141 grism spectra) and broadband photometry simultaneously. We include a parameter allowing for an additional linear slope applied to the grism data (to account for corrections to the contamination subtraction). We also introduce parameters to account for correlated noise terms in the grism data described in (140). Our methods will be described fully in a future paper (V. Estrada-Carpenter et al. in prep), where we will apply this method to the full CLEAR sample to study the co-evolution of star-forming and quiescent galaxies.

Here we applied this method to all the quiescent galaxies in our parent sample (Section 2.1). We use the WFC3 G102 + G141 data, and broad-band photometry (see Section 2).

In this study we focus on the SFHs of quiescent galaxies at $0.7 < z_{grism} < 2.5$. We adopt a

"non-parameteric" SFH parameterization (141), which include parameters to describe the SFR in 10 time bins and allows for much greater flexibility in the SFHs. The time bins are wider at larger look-back times (further in the past), except for the last (oldest) time bin, which is slightly smaller to allow for more dynamic range in the SFH. We allowed the time spanned by the full SFH to vary (however the fractional amount of time spanned in each time bin is fixed, see discussion in (141)).

Our full stellar population models have 23 fitted parameters: metallicity (Z), age, SFH (10 total parameters), redshift, dust attenuation (assuming a Milky Way model (142)), stellar mass ($\log(M_*/M_\odot)$), and 8 nuisance parameters (1 tilt parameter and 3 correlated noise parameters for each of the two grism spectra). The choice of prior on the SFH is important (as each prior has its own systematics), and should be motivated by properties of the sample. We use the continuity prior for our SFHs, as this has the effect of weighting towards SFHs that evolve more smoothly (see discussion in Section 2.2.3, 141).

We then applied this method to all the quiescent galaxies in our parent sample (defined in Section 2.1) using the WFC3 G102+G141 grism data and the broad-band photometry in these fields (see Section 2). For each galaxy, we derive posteriors on each parameter in the model. To generate constraints on our SFHs, we randomly draw from the posteriors generating 5000 realizations of the SFH, we then derive the median SFH and 68%-tile range. Figure 3.2 shows examples of fits and constraints on the SFHs for three galaxies in our sample. For each galaxy, we show 1000 individual SFH draws, the median SFH, and the 68%-tiles. Each case in this figure illustrates galaxies with qualitatively different SFHs, including one galaxy with evidence of early formation and rapid quenching (GSD 39170), one with evidence for early formation with a slowly declining SFR (GND 21156), one with evidence for a early, nearly constant SFR, followed by slow quenching (GSD 40862), and one with what is possibly a burst of star-formation at a look-back time of ~ 0.5 Gyr (GSD 24569). These are characteristic of the galaxies in our sample. In addition, we provide with this *Paper* an interactive appendix with the fits and constraints on all the galaxies in our sample, see the information and hyperlink in Appendix B.2.

We define the "formation" redshift, z_{50}, of a galaxy by integrating the SFH to the redshift where

the galaxy had formed 50% of its stellar mass.

We define the 68%-tile on z_{50} from the SFH using the highest density region (the smallest region that contains 68% of the probability density, 17). The constraints on z_{50} are illustrated for the three galaxies in Figure 3.2.

To understand to what extent the galaxy photometric or spectroscopic features are driving these differences in formation redshift, we inspected a subsample of galaxies at redshifts $0.9 < z_{grism} < 1.1$. We limit our sample to this redshift interval so that our SFHs will have similar look-back times and the data will have similar features present in the spectra. We then split this sample into "early" forming galaxies ($z_{50} > 2.9$) and "late" forming galaxies ($z_{50} < 2.9$), normalize the data at rest-frame $6000 - 6500$ Å, and stack them (Figure 3.3).

Figure 3.3 shows that the "late" forming galaxies exhibit a flux excess at $\lambda < 5500$ Å, which increases into the rest-UV. The gradient is largest around the 4000 Å-break in the ratio of the grism data (around the G+Hγ feature), implying younger stellar populations exist in the "late-forming" $z_{50} < 2.9$ subsample. This is borne out in an inspection of other features as well. For example, the ratio shows "negative" fluctuations at the locations of all the Balmer lines (Hα, Hβ, Hγ, and (possibly) Hδ). This is consistent with the differences in the subsamples being stellar populations with ages of 1 Gyr, where we expect such absorption to be strongest (i.e., dominated by A-type stars). Furthermore, the stacked SFHs of the subsamples (inset panel in Figure 3.3) show that the "early" forming galaxies have high SFRs at early times, peaking at $z \gg 4$, followed by a relatively steep decline. In comparison the "late" forming galaxies show more extended star formation that peaks at $z \sim 2.5 - 3$ followed by a gradual decline. We conclude the excess flux density in the data at rest-frame UV/blue wavelengths drive the fits to require more recent star formation in the "late" forming galaxies compared to the "early" forming galaxies.

3.3.2 Measuring Compactness

We parameterize galaxy compactness using the stellar mass density within 1 pkpc (proper kpc), Σ_1 (e.g. 143). Σ_1 has advantages for quantifying compactness as it uses information about the total surface-brightness profile and is less sensitive to uncertainties and correlations in quantities such

as Sersic index (n_s) and effective radius, $R_{1/2}$, (144). Furthermore, using Σ_1 is less susceptible to color gradients that can impact quantities such as the half-light radius (e.g., 145; 146).

We define Σ_1 using the measured (total) stellar mass and the measured surface-brightness profile,

$$\Sigma_1 = \frac{\int_0^{1\ \mathrm{kpc}} I_X(r)\ 2\pi r\ dr}{\int_0^{\infty} I_X(r)\ 2\pi r\ dr} \frac{L_{\mathrm{GALFIT}}}{L_{\mathrm{phot}}} \frac{M_*}{\pi(1\ \mathrm{pkpc})^2} \tag{3.2}$$

where $I_X(r)$ is the Sérsic profile measured in bandpass X from (11). The ratio of the integrals measures the fraction of light within 1 pkpc compared to the total light. The ratio $L_{\mathrm{GALFIT}}/L_{\mathrm{phot}}$ corrects for differences in the total magnitude from the GALFIT fits and the measured total photometry. M_* is the total stellar mass from our fits. To account for changes in rest-frame wavelength, we use the surface-brightness profile measured in the WFC3/F125 (J_{125}) bandpass for galaxies at $z_{grism} < 1.5$ and those measured in the WFC3/F160W (H_{160}) bandpass for galaxies at $z_{grism} > 1.5$ (see 11).

Figure 3.4 shows the relation between the effective radii (major axis) and stellar masses for the galaxies in our samples (i.e., the size-mass relation). The size (hue) of the data points are scaled by the Σ_1 (z_{grism}) values. Galaxies with the largest Σ_1 (highest compactness) tend to sit at the high-mass/low-size end of the distribution. This is to be expected as Σ_1 is derived based on both the stellar mass and the surface-brightness profiles (which depends on $R_{1/2}$). Furthermore, we see no significant correlation between Σ_1 and z_{grism} (the redshift measured from our WFC3/G102 + G141 grism data): galaxies with the highest (and lowest) Σ_1 among our sample span a range of observed redshift.

3.4 Results

3.4.1 Compact Galaxy Formation

Figure 3.5a shows the main result of our study: galaxies with compact stellar mass surface brightnesses $\log(\Sigma_1)/(M_\odot\ \mathrm{kpc}^{-2}) > 10.25$ favor almost exclusively earlier z_{50} values ($z_{50} > 3$). Among the subsample of objects that fall in this "ultra-compact" region (defined by $\log(\Sigma_1)/(M_\odot\ \mathrm{kpc}^{-2}) > 10.25$) there are no examples of galaxies with lower formation redshifts. Recall that all the galaxies

in Figure 3.5 are classified as "quiescent" using the same (UVJ) selection criteria, and have no explicit selection by galaxy morphology. Therefore, it is striking that the SFHs of the most compact galaxies, as defined by Σ_1, disfavor low formation redshifts, z_{50}. We find the same conclusion if we define "quiescent" using a selection of sSFR $< 10^{-11}$ yr^{-1}.

Figure 3.5b reinforces the observation that the stellar mass surface density, Σ_1, is related to the formation epoch z_{50}. Here we smooth z_{50} as a function of Σ_1 using locally weighted scatterplot smoothing (LOWESS) and see that the relationship monotonically rises as a function of compactness. Figure 3.5c shows that the standard deviation in z_{50} of the sample changes as a function of compactness (using LOWESS as well), reinforcing that the dynamic range of z_{50} is dependent on Σ_1.

Figure 3.5d shows z_{50} as a function of $\log\left(M_*/M_\odot\right)_{grism}$ using LOWESS. Galaxies with higher stellar masses do tend to have earlier z_{50} than lower mass galaxies, though this relationship seems to plateau for $\log(M_*/M_\odot)_{grism}11$, where z_{50} increases more slowly for increasing stellar mass ($dz/d\log(M) \simeq 1.2$). In contrast, there is a steeper relation between z_{50} and Σ_1: $dz/d\log(\Sigma_1) \simeq 2.7$ for $\log(\Sigma_1)/(M_\odot\ \mathrm{kpc}^{-2}) > 10$. Therefore, while z_{50} is correlated with both stellar mass and stellar-mass surface density, the trend is stronger with the latter.

The preference for early formation of the most compact galaxies does not appear to be due to redshift selection effects. The galaxies in our sample do span a range of *observed* redshift, and if there is a correlation between observed redshift and formation redshift, then this could account for our findings. Figure 3.5e shows this is not the case. The distribution of z_{50} for quiescent galaxies shows that the more compact quiescent galaxies tend towards higher formation redshifts, z_{50}. This separation is most pronounced for redshifts $z1.25$ (Figure 3.5e). At higher redshifts, $z1.25$, there is no difference in the distribution of z_{50} and observed redshift. A larger sample of high redshift galaxies would be necessary to see if the separation observed at $z1.25$ extends to higher redshift.

We also considered (and rejected) the possibility that our Σ_1 values are dependent on color gradients. For the sample with $z_{grism} < 1.5$ we recalculated Σ_1 using the H–band surface-brightess profile fits (from 26). The Σ_1 values change by $<5\%$ implying the stellar surface densities for

$r < 1$ pkpc are robust to color gradients observed to affect the effective radii of galaxies (e.g., 145; 146).

There is also no apparent bias between Σ_1 and SFH. The derivation of SFH constraints and the measurement of Σ_1 are almost entirely independent. The stellar-mass surface density stems from the morphological surface brightness profile. While the morphological profile can affect the spectroscopic resolution of the *HST*/WFC3 grisms (galaxies with more compact morphologies have higher resolution, see 33; 13), this is mild for the galaxies in our sample (the spectroscopic resolution changes by a factor of 2). Moreover, as shown in Figure 3.3 the differences in the spectral energy distributions of "early" and "late" forming galaxies extends through the full broadband photometry. Therefore, our results show that ultra-compact massive quiescent galaxies had at least 50% of their stellar-mass in-place at $z3$.

3.4.2 Quenching Timescales

The main question that arises from our results is what specific properties of galaxies drive the lack of ultracompact quiescent galaxies with $z_{50} < 3$? There are measurable differences in the SFHs of galaxies as a function of $\log(\Sigma_1)$. Figure 3.6a shows the mean SFHs for all galaxies with $z_{50} > 2.9$ as a function of $\log(\Sigma_1)$. In this figure, each curve corresponds to the mean SFH within a 0.2 dex bin of $\log(\Sigma_1)$centered on the value illustrated by the color bar. The peak SFR increases with $\log(\Sigma_1)$, and the shape of the SFH varies with Σ_1. Galaxies with lower Σ_1 have a flatter overall shape to their SFHs with a more gradual decline in SFR.

These differences in the SFH with Σ_1 for the $z_{50} > 2.9$ galaxies are evident in the time evolution of the cumulative fraction of stellar mass, illustrated in Figure 3.6b. Qualitatively, both Figures 3.6a and B show that galaxies with the largest stellar-mass surface densities (Σ_1) formed their stellar mass more rapidly and at earlier times compared to galaxies with lower Σ_1.

We can quantify this point by defining a "quenching timescale", t_Q, as the time (in Gyr) needed for the SFH to form 50% of the mass to 90% of the mass ($t_Q \equiv t_{50} - t_{90}$, illustrated in Figure 3.6b). Figure 3.6c shows the t_Q values as a function of Σ_1 for the galaxies with $z_{50} > 2.9$, with errors derived from bootstrapping. There is an apparent (anti-)correlation between stellar-mass surface

density, Σ_1 and quenching timescale, t_Q. Galaxies at lower Σ_1 ($\log \Sigma_1/(M_\odot \text{ kpc}^{-2}) < 10.0$) have $t_Q 1.4$ Gyr. In contrast, galaxies with the highest stellar mass surface density ($\log \Sigma_1/(M_\odot \text{ kpc}^{-2}) > 10.2$) have shorter quenching times, with $t_Q \simeq 1.2 - 1.4$ Gyr. The faster quenching timescales of the ultra-compact ($\log \Sigma_1/(M_\odot \text{ kpc}^{-2}) > 10.25$) sub-sample indicates that these galaxies have an overall more rapid SFH with faster quenching (shorter t_Q).

3.5 Discussion

The main finding of our study of the broad-band photometry and *HST*/WFC3 grism spectroscopy of quiescent galaxies at $0.7 < z_{grism} < 2.5$ is that they show evidence for a relation between their SFHs (e.g., formation redshifts, z_{50}), and their morphologies parameterized by their stellar-mass surface density within 1 (proper) kpc, Σ_1 (Figure 3.5). Galaxies with high Σ_1, ($\log \Sigma_1/(M_\odot \text{ kpc}^{-2}) > 10$), typically have higher z_{50} values, where ultra-compact galaxies with $\log \Sigma_1/(M_\odot \text{ kpc}^{-2}) > 10.25$ all have $z_{50} > 2.9$. They are "early forming". Less compact galaxies ($\log \Sigma_1/(M_\odot \text{ kpc}^{-2}) < 10$) on the whole have lower average formation redshifts, but they span a wide range, $z_{50} \sim 1 - 8$. Galaxies with higher Σ_1 show SFHs that have higher peak SFRs at earlier times, with more rapid quenching times. Both the shorter quenching times and earlier z_{50} values for ultracompact galaxies suggests that these properties are a symptom of the physics related to galaxy quenching.

3.5.1 Our Results in Context

Our findings reinforce some earlier studies (e.g., 147; 148; 144; 46), which found evidence of older ages in compact galaxies when compared to extended galaxies. Likewise, some studies found that compact galaxies also show evidence of quenching more rapidly (115; 128; 149). In addition, many of our galaxies have relatively high formation redshifts ($z_{50}5$), suggesting they may be the descendants of quenched galaxies recently identified at high redshift ($z3$) (e.g., 37; 38; 150; 39; 40; 151; 152; 153). Indeed, quiescent galaxy candidates at $3 < z < 4$ have very compact sizes (154), consistent with idea that these galaxies have high Σ_1 and could be among the progenitors of the early-forming galaxies in our sample.

Our conclusions depend on the reliability of the SFH constraints. To gauge this, we compared

our results to other studies of massive galaxies at similar redshifts. These broadly show a correlation between stellar mass, and shorter, more intense formation periods at higher redshift (97; 40; 140; 155).

Our results are in line with these studies, where we do see a trend between z_{50} and stellar mass (Figure 3.5d).

3.5.2 Implications for the Evolutionary Paths of Quiescent Galaxies

A key new result is evidence for a trend between (increasing) stellar-mass surface density, Σ_1, and (higher) formation redshift, z_{50}, for galaxies in our sample. The "early-forming" galaxies (z_{50}>2.9) have quenching timescales (t_Q) that decrease with increasing Σ_1 (Figure 3.6).

3.5.2.1 On the Origin of Early-Forming Galaxies with High Σ_1

The origin of galaxies with high stellar mass surface density ($\log \Sigma_1/(M_\odot\ \mathrm{kpc}^{-2}) > 10.25$) at higher z_{50} is expected as a consequence of the gravitational collapse of galaxies at high redshift (to overcome the cosmic background density, e.g., (125; 130)).

(125) show simulations where the earliest forming quiescent galaxies achieve central stellar densities of $\log \rho(< 1\ \mathrm{kpc})/(M_\odot\ \mathrm{kpc}^{-3}) > 10$ by $z > 5$.

Other explanations for high Σ_1 seem less likely. Mergers seem insufficient as major mergers are expected to leave Σ_1 roughly unchanged, while minor mergers can *decrease* Σ_1 (see (156) and below). These galaxies are also unlikely to be the product of the "compaction" (e.g., 114; 115) or from gas-rich mergers (e.g., 125). These processes should be more frequent at later times, where we do not observe any galaxy with $\log \Sigma_1/(M_\odot\ \mathrm{kpc}^2) > 10.25$ and $z_{50} < 2.9$. Compaction events or major gas-rich mergers for these galaxies are either rare or are unable increase the mass surface density to $\log \Sigma_1/(M_\odot\ \mathrm{kpc}^2) > 10.25$.

3.5.2.2 On the Origin of Early-Forming Galaxies with Low Σ_1

There are two possibilities to explain the existence of galaxies with both high formation redshift ($z_{50} > 2.9$) and lower Σ_1 ($\log \Sigma_1/(M_\odot\ \mathrm{kpc}^{-2}) < 10.25$). These galaxies could form with intrinsically lower Σ_1, but this is unexpected given the arguments above. Alternatively, these

galaxies may form the bulk (50%) of their stellar populations at $z > 2.9$ with high Σ_1, but then experience evolution that reduces Σ_1. This could come from the adiabatic expansion through mass losses from late stages of stellar evolution (e.g. 26; 128). However, this becomes more efficient at later times, and there is only $\sim$4 Gyr between $z \sim 2.9$ and $z \sim 1$ for this to manifest. (125) show the central density within 1 kpc of an early-forming compact quiescent galaxy at $z \sim 5$ declines by 0.1 dex by $z \sim 2$. Furthermore, it is unclear why this affects only some of the ultracompact galaxies when stellar evolution should impact all.

One important clue comes from the correlation between (longer) quenching times, t_Q, and (decreasing) Σ_1. The early-forming galaxies (with $z_{50} > 2.9$) and lower Σ_1 ($\log \Sigma_1/(M_\odot \text{ kpc}^2) < 10.25$) have longer quenching times, compared to galaxies with $\log \Sigma_1/(M_\odot \text{ kpc}^2) > 10.25$ (see Figure 3.6c).

An explanation for this correlation is that all early-forming massive galaxies begin with high Σ_1. Galaxies then experience a unique assembly history, where the frequency, orbital configuration, and distribution of mass-ratios of mergers and accretion events dictates the change in Σ_1. (156) show minor mergers (mass ratios 1:10) can decrease Σ_1, while major mergers (mass ratios greater than 1:4) leave Σ_1 mostly unchanged.

Minor mergers involve high-mass and low-mass systems. The latter have more prolonged SFHs (see Section 3.5.1). We tested how this would impact the formation times t_{50} (corresponding to z_{50}) and the quenching time t_Q using a series of simulations. We simulated galaxy SFHs as "delayed-τ" models (e.g., 13) using the correlations between SFH and stellar mass (see above). We then randomly "merged" galaxies of different mass ratios, summing their SFHs to simulate the effects of mergers on the integrated SFH. Figure 3.6d shows the results. Major mergers have little effect on neither t_{50} nor t_Q, which change by $<$0.25 Gyr (recall that $t_Q \equiv t_{90} - t_{50}$). Minor mergers, on the other hand, have little effect on t_{50} (change by 0.2 Gyr) but can extend the SFHs with an increase in t_{90}, making t_Q longer with a scatter of up to $\sim$ 2 Gyr. Therefore, minor mergers provide a mechanism to increase the scatter in t_Q with only a small change in z_{50} (the redshift corresponding to t_{50}), *and* decrease Σ_1 (156), which is consistent with the observations.

3.5.3 On the lack of "Early-Forming" Galaxies at low-redshift

Figure 3.5e shows an absence of quiescent galaxies at lower observed redshifts ($z_{grism} < 0.9$) and early formation times, $z_{50} > 4$. We considered several reasons that could explain this absence, some systematic to the data/analysis and others physical.

One potential systematic reason (which we ultimately reject) could be that galaxies at lower redshifts lack (grism) spectroscopic coverage in the rest-frame UV, and this could limit our ability to constrain the current SFRs in those cases. The WFC3 G102 grism covers >0.8 μm, corresponding to 4000 Å in the rest-frame for $z \sim 1$ galaxies. We therefore tested if this could limit our ability to identify objects with early star-formation at these observed redshifts. We simulated the spectral energy distribution of a quiescent galaxy at $z = 0.8$ with early quenching, with $z_{50} = 8$. We then perturbed the photometry and grism data for this object by the measured uncertainties, and repeated the model fitting using our procedures applied to the real CLEAR galaxies. In this case we reliably recover this z_{50} value, within a 68% confidence interval of $\pm$ 0.15 Gyr. Therefore it appears that if galaxies at $z = 0.8$ with $z_{50} \gg 4$ existed in our dataset we would identify them as such.

One other systematic reason for the lack of objects with $z_{\rm grism} < 0.9$ and $z_{50} \gg 4$ could be that the CLEAR data sample a relatively small volume. For example, the comoving volume probed by our study is ≈8 times larger for $1 < z < 2.5$ than $0.7 < z < 1.0$, and these objects with early formation and lower observed redshift may simply be rarer at these redshifts. Future studies using larger datasets should be able to test this systematic more fully.

Alternatively, the rarity of early-forming quiescent galaxies ($z_{50} \gg 4$) at $z < 0.9$ could be indicative of how these galaxies evolve. Building off the discussion above (Section 3.5.2.2) we expect that quiescent galaxies grow in size through mergers, and this evolution depends on the galaxies' individual assembly histories. Our toy model argues these mergers both lower Σ_1 and *decrease* z_{50} and that the magnitude of both affects should grow with time. We therefore can predict that galaxies with early quenching observed at lower redshift would have lower (measured) z_{50} and lower Σ_1 and this effect should become more pronounced with decreasing redshift.

Interestingly, our results support this interpretation. Figure 3.7 shows the relationship between

formation *age*, t_{50}, and observed redshift z. Here, t_{50} is the lookback time between the observed redshift and the formation redshift z_{50} for each galaxy. In the figure we split our quiescent galaxies into samples of compact and extended based on $\log \Sigma_1/(M_\odot \text{ kpc}^{-2}) > 10$ or < 10, respectively (see Figure 3.5). Both the compact and extended galaxies have similar evolution at $z1.25$: their quenching time, t_{50} is (on average) roughly 1.5 Gyr delayed from the Big Bang (and this is consistent with the currently earliest known galaxies with older stellar populations, 39; 41; 152; 153).

However, the trend between observed redshift and t_{50} for the extended and compact quiescent galaxies diverges at observed redshifts of $z1.25$. Here the extended galaxies show lower t_{50} (at fixed observed redshift) compared to the compact galaxies. This could be a result of the hypothesis that the extended galaxies have experienced more frequent growth due to minor mergers, causing a faster decrease in Σ_1 (making them "extended" as described in Section 3.5.2.2) and in t_{50}. However, the subsample of quiescent galaxies at $z < 0.9$ in our sample remains small, and larger samples will be needed to confirm these trends.

3.6 Conclusions

In this paper we constrain the star-formation histories of quiescent galaxies at $0.7 < z < 2.5$ and correlate these with galaxy masses and morphologies, using "non-parametric" star-formation histories and a nested sampling algorithm. We derived constraints for the formation and quenching timescales for a sample of nearly 100 quiescent galaxies with deep *HST* grism spectroscopy and photometry from the CLEAR (CANDELS Lyman$-\alpha$ Emission at Reionization) survey. In addition to the results presented here, we provide in Appendix B.2 a hyperlink to, and a description of, an online appendix that contains similar fits and information for all the galaxies in our sample. Our conclusions from this study are as follows.

1. The galaxy formation redshifts, z_{50} (defined as the point where they had formed 50% of their stellar mass) range from $z_{50} \sim 2$ (shortly prior to the observed epoch) up to $z_{50} \simeq 5 - 8$. We correlate the formation redshifts with the stellar-mass surface densities, $\log \Sigma_1/(M_\odot \text{ kpc}^{-2})$, where Σ_1 is the stellar mass within a 1 pkpc (proper kpc).

2. Quiescent galaxies with the highest stellar-mass surface density, $\Sigma_1 > 10.25$, show a *minimum* formation redshift: all such objects in our sample have $z_{50} > 2.9$.

3. Quiescent galaxies with lower surface density, $\log \Sigma_1/(M_\odot \, \mathrm{kpc}^{-2}) = 9.6 - 10.25$, show a range of formation epochs ($z_{50} \simeq 1.5 - 8$), implying these galaxies experienced a range of formation and assembly histories.

4. We argue that the surface density threshold $\log \Sigma_1/(M_\odot \, \mathrm{kpc}^{-2}) > 10.25$ uniquely identifies galaxies that formed in the first few Gyr after the Big Bang

We then discuss the implications this has for galaxy formation and quenching. Based on our data, the ultracompact quiescent galaxies ($\log \Sigma_1/(M_\odot \, \mathrm{kpc}^{-2}) > 10.25$) appear to identify galaxies with early formation ($z_{50} > 2.9$) and a lower fraction of mergers (at the time they are observed, see Section 3.5.2.2). If these exist in the present Universe, they could be compact cores of galaxies. It could be instructive to identify objects with high density cores, and study their ages, abundances, and gradients. Additional simulations would be useful both to understand the formation and the evolution of these galaxies, and if later time processes (such as adiabatic expansion or mergers) destroy them. Alternatively, it may be that examples of these objects still exist in the present-day Universe. If so, the most compact passive galaxies today may host the oldest stellar populations and be the remnant of these bygone eras.

We favor the conclusion that stochasticity in the mergers/accretion history of lower-mass early-forming galaxies ($z_{50} > 2.9$) explains the relation between the quenching timescale and stellar mass surface density: the lower Σ_1 ($\log \Sigma_1/(M_\odot \, \mathrm{kpc}^{-2})10.1$) and longer quenching times ($t_Q > 1.4$ Gyr) of these galaxies is a result of their history of (minor) mergers.

The formation redshift, z_{50} (or age, t_{50}) can be reduced through subsequent evolution through minor mergers and this can lead to both galaxies with high z_{50} and lower stellar-mass surface densities as well as account for the lack of observed galaxies at $z0.9$ with early formation times (high t_{50}). The obvious caveat to this interpretation is that we have neglected the contribution of "progenitor bias" (see, e.g., 157) whereby newly quenched galaxies are continuously becoming

"quiescent" at later times. As the more recently-quiescent galaxies will (by definition) have lower t_{50} and likely have lower Σ_1, they can also contribute to the trend seen between observed redshift and quenching time (t_{50}) in Figure 3.7 (though see, e.g., 114; 115; 125). Ultimately, it is likely that both the effects of early formation plus minor mergers and progenitor bias are at work. This makes an interesting prediction that spatially resolved studies should see variations in the SFH (or possibly abundance histories) as a function of galactic radius in these galaxies. This may be testable with data from either the *James Webb Space Telescope* (*JWST*) or 25–30 m-class telescopes.

We thank our colleagues on the CLEAR team for their valuable conversations and contributions. We also thank Kartheik Iyer, Rob Kennicutt, Arjen van der Wel, Sandro Tacchella, and Christina Williams for productive comments, feedback, suggestions, and information. We also thank Mark Dickinson and Hanae Inami for providing and assisting with the 24 μm catalog. We are also grateful to the anonymous referee whose comments and queries improved the quality and clarity of this paper. VEC acknowledges support from the NASA Headquarters under the Future Investigators in NASA Earth and Space Science and Technology (FINESST) award 19-ASTRO19-0122, as well as support from the Hagler Institute for Advanced Study at Texas A&M University. This work is based on data obtained from the Hubble Space Telescope through program number GO-14227. Support for Program number GO-14227 was provided by NASA through a grant from the Space Telescope Science Institute, which is operated by the Association of Universities for Research in Astronomy, Incorporated, under NASA contract NAS5-26555. This work is supported in part by the National Science Foundation through grants AST 1614668. The authors acknowledge the Texas A&M University Brazos HPC cluster and Texas A&M High Performance Research Computing Resources (HPRC, `http://hprc.tamu.edu`) that contributed to the research reported here.

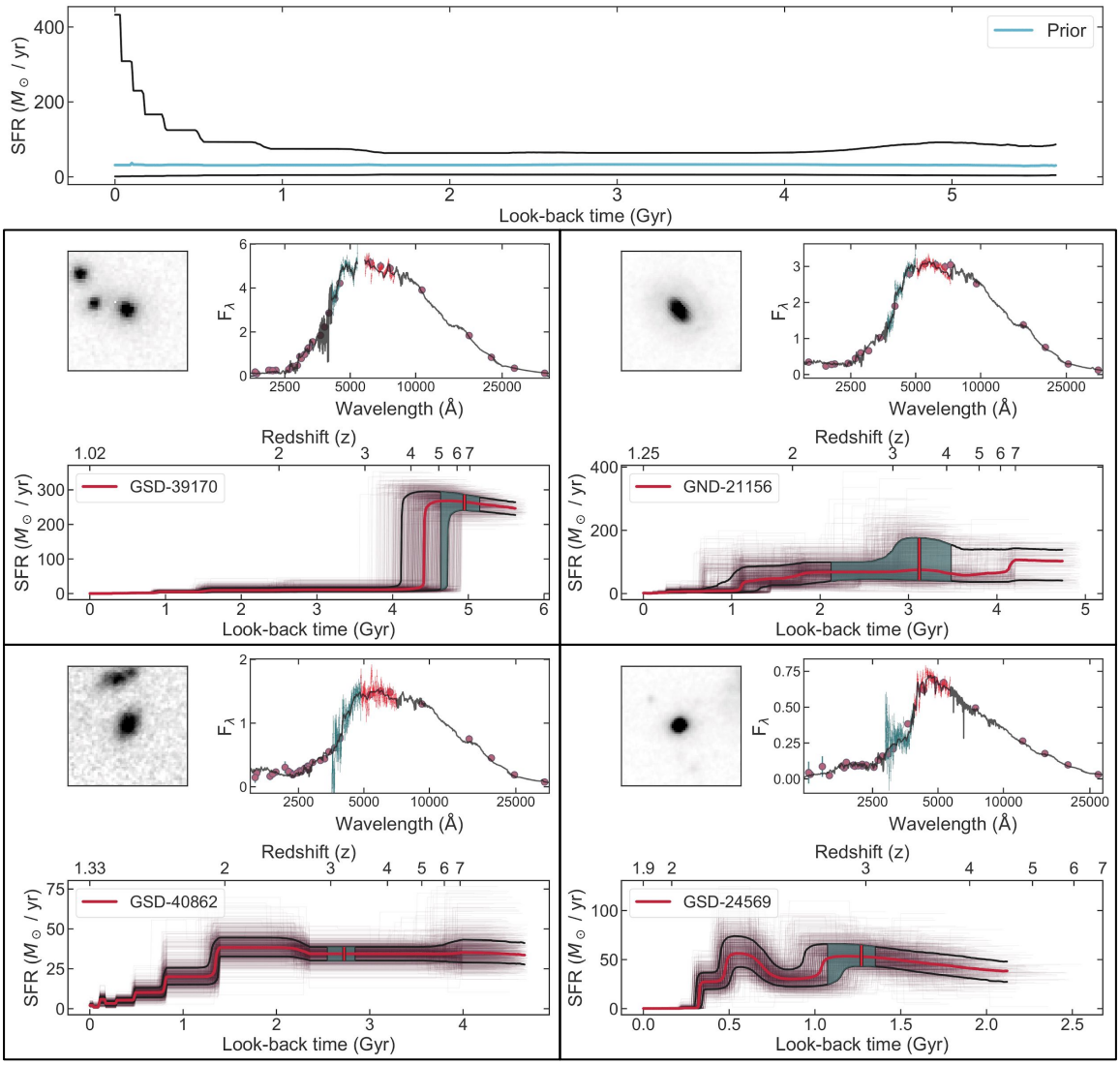

Figure 3.2: Example spectral energy distribution (SED) fits to galaxies from our sample. Each set of bottom four sub-panels shows results for one galaxy (with CLEAR IDs labeled). The top sub-panel shows the shape of the prior used for the SFH (median in blue and the 68% credible region in black). The prior shown is specifically for a galaxy at $z = 1.02$ with stellar mass $\log M/M_\odot = 11.40$ (like GSD-39170), and changes to the redshift and stellar mass affect the span of the star-formation history (set by redshift) and SFR normalization (set by mass); the overall shape of the prior is the same for all galaxies. In each of the following sub-panels, the top-left sub-panels shows a 4" $\times$ 4" F160W image centered on the galaxy. The top right sub-panels show the full SED including the broadband photometry (purple circles) and WFC3 grism spectra (blue line: WFC2/G102; red line: WFC3/G141) along with median FSPS stellar population model from the posterior (black line). The bottom figure in each sub-panel shows the derived star-formation history (SFH). The purple lines show individual draws for the SFH, the thick red line shows the median, and the thick black lines show the 68% credible interval. The vertical red line shows z_{50}, the formation redshift (where 50% of the stellar mass had formed), and the green-shaded region shows the 68% highest density region on z_{50}. In Appendix B.2 we provide a hyperlink to, and a description of, an online appendix that contains similar fits and information for all the galaxies in our sample.

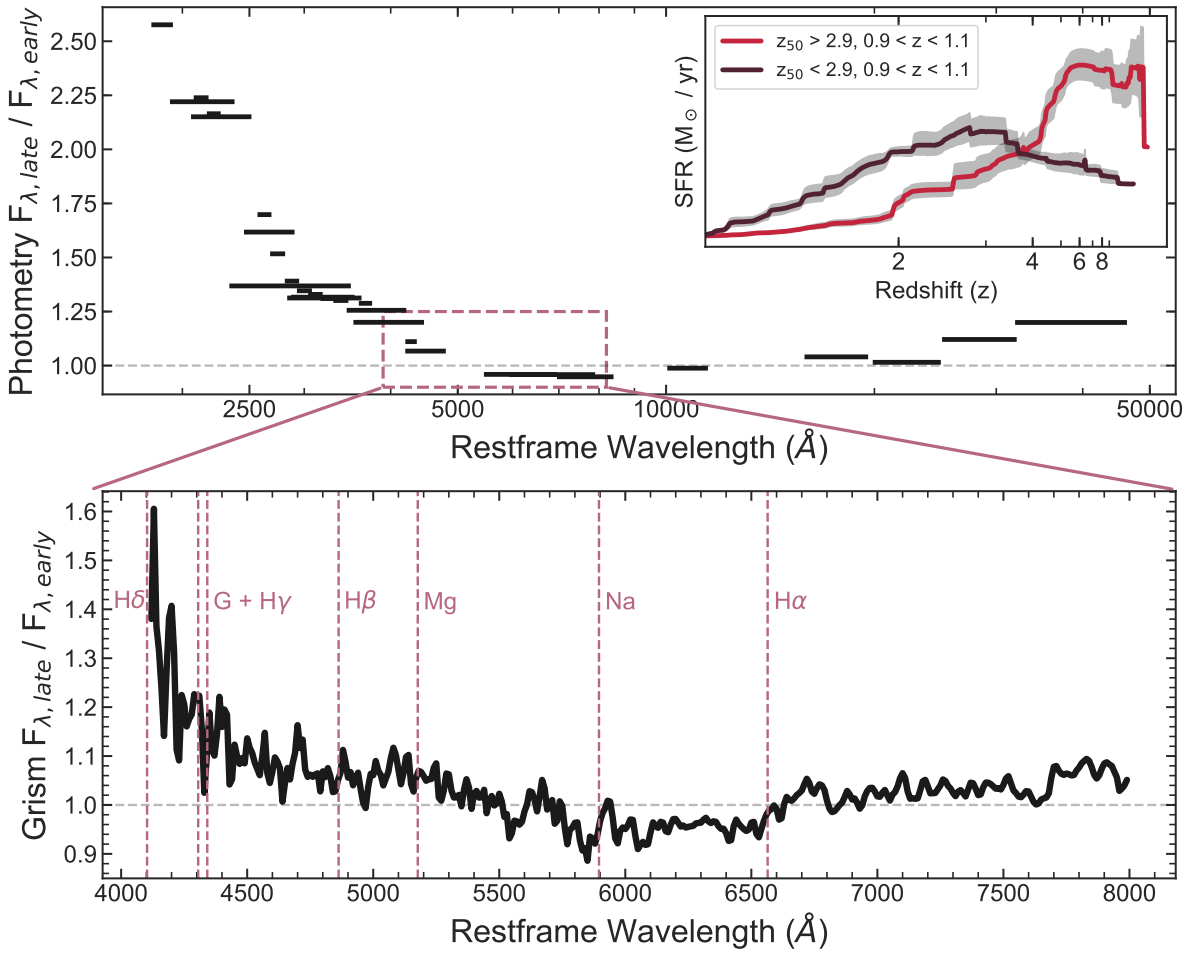

Figure 3.3: Comparison between the photometric and spectroscopic (grism) data for the subset of our quiescent galaxies at $0.9 < z_{grism} < 1.1$, split by their measured formation redshift (z_{50}, where 50% of their stellar mass had formed). The two groups are $z_{50} < 2.9$ ("late" forming galaxies) and $z_{50} > 2.9$ ("early" forming galaxies). The top plot shows the ratio of the median flux densities measured in each broadband photometric band for the "late" forming sample to the "early" forming sample. The biggest difference occurs at rest UV wavelengths, which indicates the "late" forming galaxies show evidence of more recently formed stars (which contributes to the lower z_{50}). The bottom panel shows a ratio of their stacked combined G102 + G141 grism spectra. Dashed vertical lines show wavelengths of common spectral features. For both the top and bottom panels we normalize the stacks/medians at 6000 - 6500 Å in the rest-frame. The inset in the top panel shows a mean stack of the SFHs for the late-forming and early-forming galaxies (as labeled). When comparing the two SFHs we can see that the SFH of the $z_{50} > 2.9$ sub-sample has the majority of mass formed more rapidly with a steeper decline, while the SFH of the $z_{50} < 2.9$ subsample has a more gradual decline in SFR (with more star formation in the recent past).

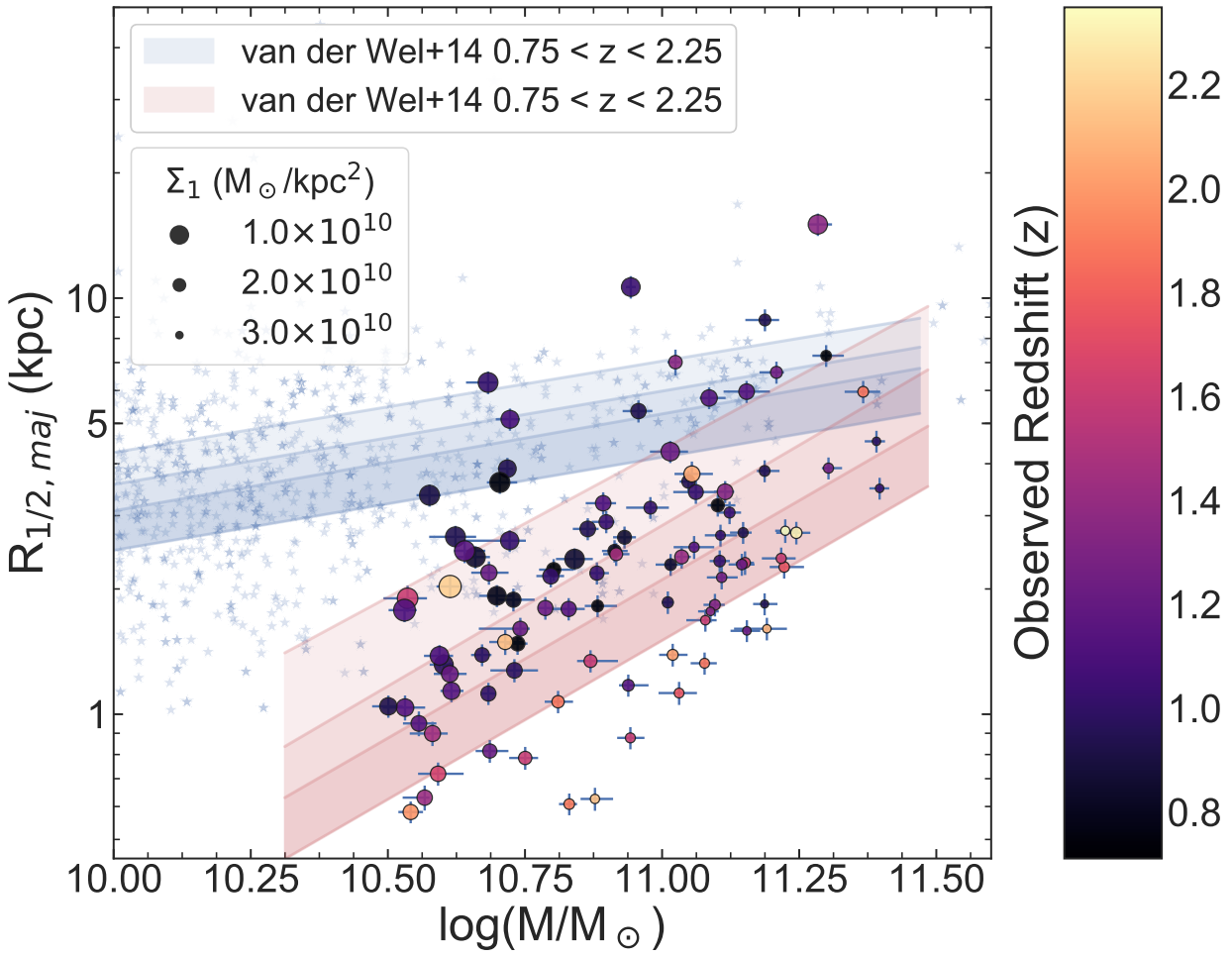

Figure 3.4: Size mass relation for the $0.7 < z_{\rm grism} < 2.5$ sample. The sizes of the points are scaled by their Σ_1 values, and their colors are scaled by their redshift (star-forming galaxies in the CLEAR sample are shown as blue stars with no scaling). Size mass relations for star-forming (blue) and quiescent (red) galaxies from (11) are shown. These span a range from $0.75 < z < 2.25$ where the shading becomes darker with increasing redshift. Following the results of the simulations of (12), we add a 6% systematic error in quadrature to the $R_{1/2}$ values to account for flux-dependent modeling uncertainties.

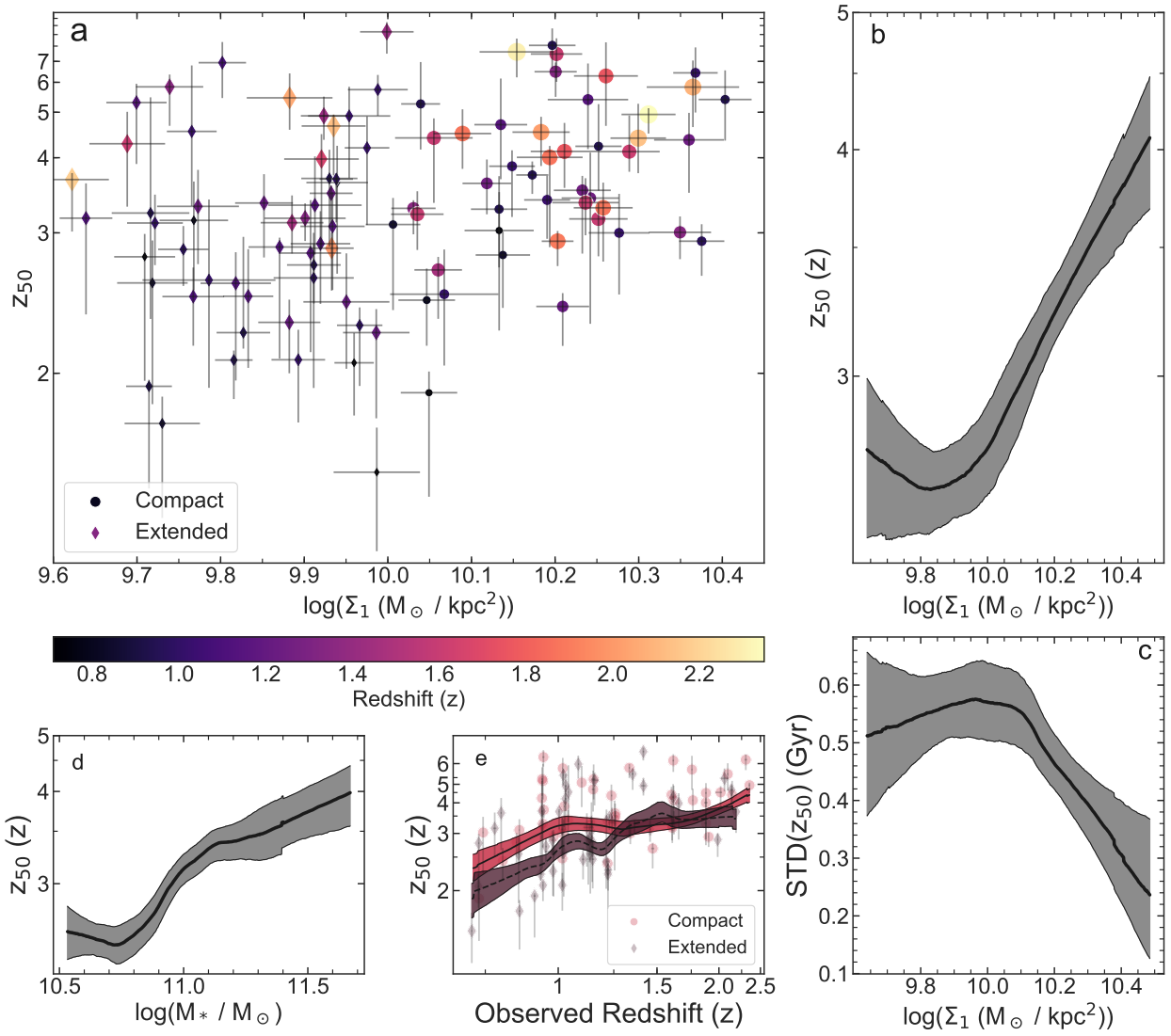

Figure 3.5: Relationship between formation redshift z_{50} (the redshift by when 50% of the stellar mass had formed), the observed redshift z_{grism}, and Σ_1 (the stellar mass surface density within 1 (proper) kpc). (a) shows z_{50} as a function of $\log(\Sigma_1)$ for the quiescent galaxies in our sample. Galaxies with $\log \Sigma_1/(M_\odot \text{ kpc}^{-2})) > 10$ (< 10) are shown as circles (diamonds). The color and size of the all points scales with increasing z_{grism}. Galaxies with $\log \Sigma_1/(M_\odot \text{ kpc}^{-2}) < 10$ span a larger range of z_{50}. Galaxies with $\log \Sigma_1/(M_\odot \text{ kpc}^{-2}) > 10$ favor higher formation redshifts of $z_{50} > 3$. (b) shows the change in z_{50} as a function of $\log(\Sigma_1)$ using a LOWESS algorithm with bootstrapping to estimate the 68% confidence region. (c) shows the scatter in z_{50} as a function of $\log(\Sigma_1)$ (using LOWESS). Galaxies with higher Σ_1 tend towards higher z_{50} with lower scatter. (d) shows the change in z_{50} as function of $\log(M_*/M_\odot)_{grism}$ using LOWESS. Higher mass galaxies tend towards higher z_{50}, though this relation is less steep while there is a continued rise between z_{50} versus the stellar-mass surface density, Σ_1. (e) shows the formation redshift, z_{50}, against the observed redshift. Galaxies with $\log(\Sigma_1)/(M_\odot \text{kpc}^{-2}) > 10$ (< 10) are indicated by red (purple) points, using a LOWESS algorithm to show the trend. We see here that more compact galaxies (i.e., with higher Σ_1) tend to have higher z_{50}, particularly for $z1.25$.

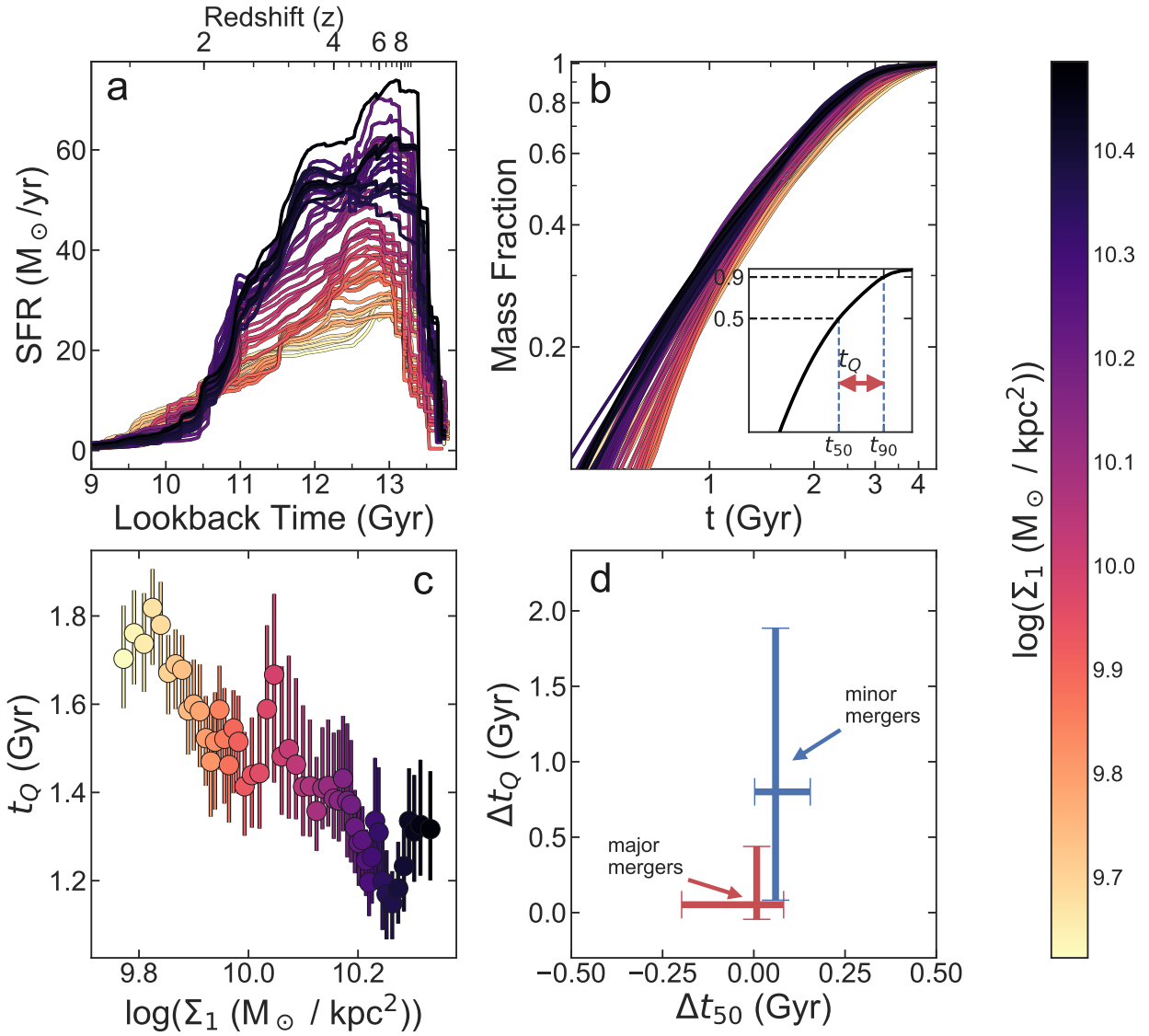

Figure 3.6: The relation between SFHs, quenching times, and stellar mass surface density (Σ_1) for "early-forming" galaxies ($z_{50} > 2.9$). (a) shows a the mean SFH for galaxies stacked as a function of $\log(\Sigma_1)$in bins of 0.2 dex. (b) shows the cumulative fraction of stellar mass formed. Both (a) and (b) show that galaxies with higher $\log(\Sigma_1)$ form more stellar mass earlier with higher peak SFRs, and experience a more rapid decline in their SFR compared to galaxies with lower Σ_1. (c) shows the quenching timescale (t_Q) defined as the time between when the galaxy had formed 50% and 90% of its stellar mass, as a function of Σ_1, with error bars derived from bootstrapping. Galaxies with higher Σ_1 have shorter quenching times. (d) shows the effects of mergers on the SFH timescales. We randomly merged simulated galaxies and measured the change in t_Q and t_{50} from major-mergers (mass ratios >1:4; red) and minor-mergers (mass ratios <1:10; blue). The error bars show the inter-68%-tile scatter (68% of the simulations fall in this range).

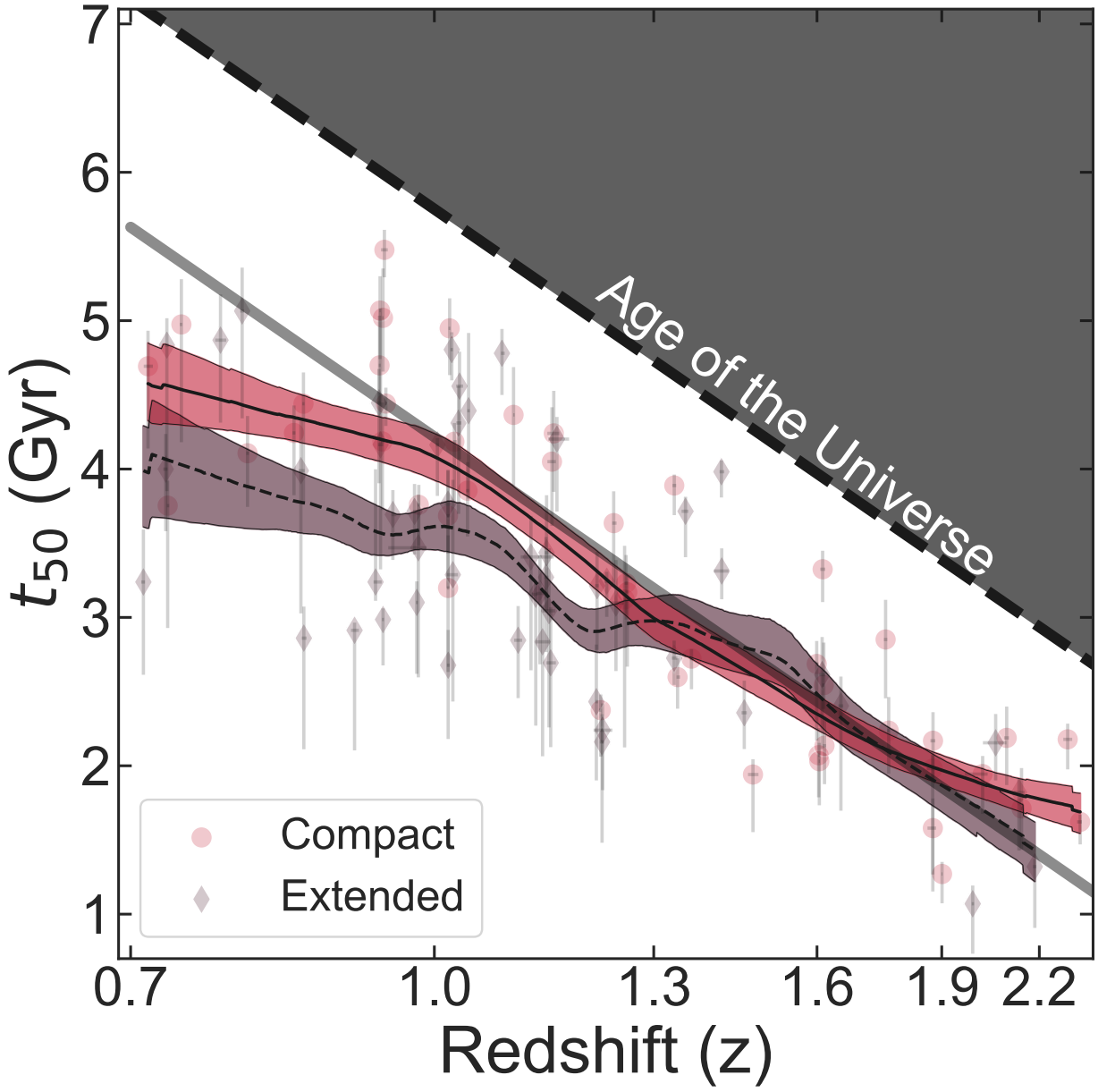

Figure 3.7: The formation age (t_{50}) as a function of observed redshift, $z_{\rm grism}$ for the quiescent galaxy sample. The formation age is the lookback time from the observed redshift for a galaxy to its formation redshift, z_{50}, when it had formed 50% of its stellar mass. The symbols divide the sample into subsamples of compact (red circles, $\log \Sigma_1/(M_\odot\ {\rm kpc}^{-2}) > 10$) and extended sources (purple diamonds, $\log \Sigma_1/(M_\odot\ {\rm kpc}^{-2}) < 10$). The solid swath tracks the trend for each subsample using a LOWESS algorithm with bootstrapping. The dashed diagonal line demarcates the age of the Universe at the observed redshfit, and the solid grey line shows the age of the Universe minus 1.5 Gyr. At high redshift, $z1.25$ the galaxies' formation ages mostly track the age of the Universe offset by $\sim$1.5 Gyr. At lower redshifts the populations skew toward more recent formation, but at different redshifts. The extended sample skews toward lower t_{50} at earlier times ($z1.25$) while the compact galaxies skew toward lower t_{50} at later times ($z_{50}0.9$).

4. CLEAR: STUDYING GALAXIES AS THEY CROSS THE GREEN VALLEY

4.1 Introduction

Current work in the field of galaxy evolution has begun to outline the formation and quenching pathways of high redshift massive quiescent galaxies (e.g., 126; 13; 28; 158; 159; 15). The goals of this area of study are to understand how the star-formation, chemical, morphological, and quenching histories of galaxies evolve with redshift. By studying galaxies at high redshift, which have quenched their star-formation, we can better constrain these formation history properties as the uncertainty on stellar timescales is quasi-logarithmic which translates to logarithmic uncertainties on galaxy ages. Therefore, by studying galaxies closer to their formation epochs (at younger absolute ages) the uncertainties are smaller in an absolute sense. This is an area of study which has benefited much from modern telescopes, instruments, and methods as these galaxies become difficult to study at high redshift due to lower luminosity's due to the domination of older stellar populations, smaller sample sizes as the fraction of quiescent galaxies shrinks at higher redshifts (29; 30; 31), and a high density of telluric emission lines contaminating the rest-frame optical in ground based telescopes (32).

The story of the formation of high redshift massive quiescent galaxies cannot be completely told in by quiescent galaxies alone. There is a gap in our understanding of these galaxies which exist and stems from the gaps between quiescent and star-forming galaxies. These two populations have comparatively bimodal properties such as morphology and age. By studying galaxies that are in transition from star-forming to quiescent we can study what happens when galaxies cross the green valley, what properties change during this journey, and what properties are seemingly set before they transition.

Transitioning galaxies are difficult to identify as their number densities are much smaller than their quiescent and star-forming peers, this is because galaxies cross the green valley fairly quickly (160; 161). In this work we develop a novel approach to identifying transitioning galaxies by

deriving the probability that a galaxy is star-forming, P_{sf} using the shape of the specific star-formation rate (sSFR) distribution with a large sample ($\sim$ 500) massive galaxies ($\log(M/M_{\odot}) >$ 10.2) at 0.7 $<$ z $<$ 1.65. In Section 4.2 we describe our data and sample selection. In Section 4.3 we outline our fitting methodology and development of P_{sf}. In Section 4.4 we discuss our modeling of P_{sf} and how it compares to literature results. In Section 4.5 we describe the implications of the evolutionary properties we see within the transitional galaxies. Finally in Section 4.6 we summarize our results. Throughout this work, we assume a cosmology with $\Omega_{m,0} = 0.3$, $\Omega_{\lambda,0} = 0.7$, and $H_0 = 70$ km s^{-1}.

4.2 Data

For this work, we use data from the CLEAR (CANDELS Lyman$-\alpha$ Emission at Reionization) survey which includes *HST* WFC3/G102 grism spectra, *HST* WFC3/G141 grism spectra, and photometry (see 13; 158) Our parent sample selection consist of massive galaxies ($\log(M/M_{\odot})$ > 9.8), using masses from derived from Eazy-py[1] within a redshift range of $0.6 < z < 2.8$ using z_{grism} measurements from Grizli[2] and z_{phot} from Eazy-py. We use both redshift measurements as the z_{grism} measurements accurately recover redshifts for emission-line galaxies while the z_{phot} measurements would add back quiescent galaxies which were mismeasured by Grizli (see 158). We then exclude any galaxies which do not have *HST*/WFC3 G102 coverage. Finally, we exam the 1D spectra for every exposure by eye to look for any residual contamination, where we either remove it (if possible) or exclude the galaxy if it is too contaminated. We are then left with a sample of 1390 galaxies. These galaxies were all then fit for their stellar populations using the methods described in Section 4.3. We then remove any galaxies from our sample which have X-ray detections likely from AGN ((78; 79), and Simons et al. in prep). Our parent sample selection is shown in Figure 4.1 Panel A, where the CLEAR sample is shown in blue and galaxies which match our parent sample selection criteria with red outlines.

Several cuts are then applied to our parent sample using our stellar population fits. As we are

[1]https://github.com/gbrammer/eazy-py
[2]https://github.com/gbrammer/grizli

interested in the sSFR distribution we are careful to select a sample with a complete representation of high and low sSFRs, therefore we use a volume-limited sample. To do this we found the minimum stellar mass needed for a detection of $Y_{F105W} = 25$ AB mag (magnitude limit used for extraction in the CLEAR dataset) by modeling a single stellar population formed at z = 5. Figure 4.1 Panel B illustrates how we chose our final sample. Here we show galaxies with $\log(sSFR\,(yr^{-1})) < 10.5$ (as these are the galaxies we are likely to miss in our sample) as red points, our measured minimum mass needed for our volume-limited sample is shown as a black line, and our final selection window is shown as the blue shaded region. This region was selected as it maximizes our sample of quiescent galaxies ($\log(sSFR\,(yr^{-1})) < 10.5$) resulting in a selection window of $\log(M/M_{\odot}) > 10.2$ and $0.7 < z_{grism} < 1.65$, with a sample of 454 galaxies.

4.3 Method

Our approach to deriving the stellar populations of our galaxies is to use the forward modeling approached outlined in (13) using flexible SFHs from (141) and the nested sampling algorithm Dynesty (139), as briefly mentioned in (158). Utilizing the full capacity of the CLEAR data set allows us to simultaneously fit *HST* WFC3/G102 grism spectra, *HST* WFC3/G141 grism spectra, a set of photometry that covers rest-frame UV to IR.

As our sample covers quiescent and star-forming galaxies we take slightly different (though consistent) approaches to fitting these disparate galaxies. The reason for the slightly different approach to fitting for quiescent and star-forming galaxies has to do with different approaches to fitting metallicity, dust, redshift, and SFH (which are outlined below). First, we use a UVJ color-color diagram (80; 2; 81) to classify galaxies as star-forming and quiescent using rest-frame colors derived from Eazy-py and the UVJ parameterization from (81). With our galaxies classified we can then move on to our fitting utilizing the Flexible Stellar Population Synthesis (FSPS) models (91), with MILeS and BaSeL libraries and assuming a Kroupa initial mass function (138)

Our approach to fitting spectra and photometry simultaneously is to assume that the flux calibration of the photometry is truth, but allow the grism spectra to be scaled along with the models. This is because different approaches were used in extracting the photometry and grism spectra,

therefore one should assume that there is some flux offset between the two. Additionally, we are not fitting emission lines, so when present we mask them out, this was done for each galaxy individually.

The parameters we fit for are stellar metallicity ($Z_{\odot}$), SFH span (t_{span} - Gyr), stellar mass formed within SFH time bins ($M_{\odot}$), $\log(M/M_{\odot})$, redshift (z), dust (A_v), and a set of nuisance parameters (outlined in (158) and include parameters to account for under/over corrections from contamination subtraction, and correlated noise in the grism data). We fit metallicity differently for quiescent and star-forming galaxies because metallicity values measured from star-forming galaxies are highly uncertain. Therefore we apply a metallicity prior for star-forming galaxies (derived from (5)) which evolves with stellar mass, while we use a Gaussian prior for quiescent galaxies. SFH span is the total span (in Gyrs) of our SFHs with the maximum value set by redshift. For our SFHs we use the flexible SFHs from (141) utilizing the continuity prior. The difference in our approach for quiescent and star-forming galaxies is the amount of time-bins we employ, using 10 time-bins for the quiescent sample and 6 for star-forming galaxies. This is mostly driven by computer run time as our SFHs accounted for the majority of the run time (reducing our run time by 50%). We justify this decision because quiescent galaxies had most of their star-formation at large lookback times and therefore having more time-bins adds more temporal resolution at early times, while star-forming galaxies formed most of their stars more recently and therefore do not need the higher temporal resolution at early times. For redshift, we set the value for star-forming galaxies while we fit for the redshift for the quiescent sample. The reason for this is that we mask the emission lines of our star-forming galaxies, which doing dynamically would have added too much to the run time, additionally the presence of emission lines added more confidence to the Grizli measured redshifts. For dust, we use milky way model (142) for our quiescent galaxies and a Calzetti model (101) for star-forming sample, as these models are more appropriate for their respective samples.

There are several parameters which we derive post fitting, these include light-weighted age (t_{lwa} - Gyr), t_{50} (lookback time to when the galaxy formed 50% of its mass - Gyr), t_{90} (lookback time to when the galaxy formed 90% of its mass - Gyr), t_q (quenching timescale, t_{50} - t_{90} - Gyr), z_{50} (formation redshift - redshift when galaxy formed 50% of its mass), z_{90} (redshift when galaxy

formed 90% of its mass), and $\log(sSFR\,(yr^{-1}))$ (averaged over the last 1X10^8 yr - $\log(yr^{-1})$). We derive light-weighted age using the output from our Dynesty run, recreating each model selected during fitting and measuring its t_{lwa} we then extract P(t_{lwa}) using the same weights used by Dynesty to extract posteriors. t_{50}, t_{90}, t_q, z_{50}, z_{90}, and $\log(sSFR\,(yr^{-1}))$ are measured from our SFHs which are generated by sampling our posteriors for t_{span}, SFH time bins, and $\log(M/M_{\odot})$ 5000 times. From our generated sample we measure our SFH to be the 50th percentile at each lookback time and are also able to measure the inner 68th percentile.

Figure 4.2 show the *HST* WFC3/G102 grism spectra (blue), *HST* WFC3/G141 grism spectra (red), and photometry (green) for four different galaxies with their best fit models (black). Each of the galaxies here represents different types of galaxies (e.g. star-forming, transitioning, quiescent). We can see here that our fitting approach fits the grism spectra + photometry well, and do so for all types of galaxies.

4.3.1 P_{sf}

Most methods to classify galaxy formation activity end up using a bimodal approach, either classifying galaxies as star-forming and quiescent. This approach is fine for the general population of galaxies as most galaxies show traditional traits of either star-forming or quiescent galaxies. Where these approaches fail is in classifying galaxies that have ambiguous traits. For most classification schemes galaxies that are in transition from star-forming to quiescence sit at the separating line, and are often treated as contamination in either sample.

Our approach here is to assign to each galaxy its probability of being star-forming, P_{sf}. Most galaxies fall into traditional quiescent and star-forming roles, these galaxies will therefore lie at the extremes of our probability distribution as there is little ambiguity to their star-formation activity status. Where we will benefit is in identifying galaxies that do not easily fall into traditional quiescent or star-forming roles, galaxies which (depending on the selection criteria) could fall into either classification, therefore this method excels in selecting galaxies that are crossing the green valley.

To estimate P_{sf} we use the shape of the $\log(sSFR\,(yr^{-1}))$ distribution. Figure 4.3 illustrates

how the sSFR distribution evolves with redshift. Here we show the $\log(sSFR\,(yr^{-1}))$ distribution for three redshift bins(A: 0.7 $< z_{grism} <$ 1.0, B: 1.0 $< z_{grism} <$ 1.25, C: 1.25 $< z_{grism} <$ 1.65). In Figure 4.3 we see that the peak of the star-forming region evolves to lower values at lower redshifts, indicating an evolution in the star-forming main sequence. In addition, we see that the quiescent portion of the distributions lessons at higher redshifts. As shown in Figure 4.3 the shape of the measured sSFR distribution is bimodal. The true shape of the sSFR distribution is likely not bimodal and is instead a distribution with a long tail (162), the bimodality of the measured sSFR distribution comes from the inability of SED fitting codes to measure extremely low SFRs. These codes fail to recover SFRs for galaxies with low or no star-formation, and the expectation values will be scattered to higher values of SFR. This upward scatter is code dependent, and in testing our fitting code (by fitting mock spectra with SFRs = 0 $M_{\odot}$/yr) we found that they scattered up to $\log(sSFR\,(yr^{-1}))$ values with a mean of -12 with a variance of $\sim$ 0.6 dex. While this upward scattering is problematic the values of the scattered up points are still squarely in the quiescent region of the sSFR distribution. These upward scattered points create the "bump" seen in the quiescent region of the distribution. In the end these upward scatter points will not be a problem in our modeling as our results are not affected by these points.

4.3.2 Modeling the sSFR Distribution and Measuring P_{sf}

Here we will outline how we model the $\log(sSFR\,(yr^{-1}))$ distribution and how we use this to derive P_{sf}. We provide Figure 4.4 as guidance through the process. Step 1) is to gather galaxies within a certain window of lookback time. Since the $\log(sSFR\,(yr^{-1}))$ distribution evolves with redshift we derive P_{sf} in bins of redshift. Here we chose a lookback time window of 1.5 Gyrs as it provides samples that are just large enough to provide a "smooth" measurement. We then apply a weighted stack (see 13) to the $\log(sSFR\,(yr^{-1}))$ posteriors, generating the $\log(sSFR\,(yr^{-1}))$ distribution for that sample. Step 2) is to then model the star-forming region as a Gaussian function, $D_{sf}(\log(sSFR\,(yr^{-1})))$. This was done by identifying the peak of the star-forming region (this was our μ value), selecting $\log(sSFR\,(yr^{-1})) > \mu$, and measuring the 1 σ value from this region. Step 3) we then subtract the model of the star-forming region from the $\log(sSFR\,(yr^{-1}))$ distribution

leaving behind the quiescent region, $D_q(\log(sSFR\,(yr^{-1})))$. As can be seen in Figure 4.4 Panel D the resulting quiescent region does contain some residual probability at higher values, this is the result in the inexactness of the Gaussian function to model the star-forming region, and as this probability is from the star-forming region we can simply remove it. Panel E shows how well we can recover the $\log(sSFR\,(yr^{-1}))$ distribution with only a slight offset seen in the star-forming region (which ultimately does not affect our measurements). With our two regions, we can now measure $P_{sf}(\log(sSFR\,(yr^{-1})))$ using the following function.

$$x = \log\,(sSFR), \tag{4.1}$$

$$P_{sf}(x) \equiv \frac{\int_{x-\epsilon}^{x+\epsilon} D_{sf}(x')dx'}{\int_{x-\epsilon}^{x+\epsilon} D_{sf}(x')dx' + \int_{x-\epsilon}^{x+\epsilon} D_q(x')dx'} \tag{4.2}$$

The P_{sf} values as a function of $\log(sSFR\,(yr^{-1}))$ are shown if the Panel G of Figure 4.3. As can be seen, here much of the space is dominated by values of 0 or 1 (quiescent or star-forming) with a short transitional period. These results mirror what is seen in most studies, that the transition from star-forming to quiescent is short-lived.

While P_{sf} might seem like a complex idea, at its core P_{sf} is just a remapping of $\log(sSFR\,(yr^{-1}))$ which accounts for the evolution of the star-forming main sequence and focuses on galaxies in transition. As this is an unorthodox approach we wish to outline some of the parameterizations we will be using in this paper. Our goal here is to describe the star-formation activity of galaxies continuously with P_{sf}, though we still see it fit to group galaxies into larger groups. We define quiescent galaxies as galaxies with a low probability of being star-forming ($P_{sf} < 0.1$). Star-forming galaxies will therefore be defined at galaxies with a high probability of being star-forming ($P_{sf} > 0.9$). Galaxies which are crossing the green valley will be defined as galaxies with $0.1 < P_{sf} < 0.9$, we justify our selection of these values in Section 4.4.

4.4 Results

4.4.1 P_{sf} Measurement

Our measurement of P_{sf} is shown in Figure 4.5. Our method (which is outlined in Figure 4.4) is applied running as a function of redshift. In Figure 4.5 we color code our results as indicated, but generally, quiescent galaxies are shown in red, star-forming galaxies are shown in blue, and galaxies in transition are shown in green. We see here (as was also shown in Figure 4.5) that the distribution of $\log(sSFR\,(yr^{-1}))$is dominated by $P_{sf} \approx 0$ or ≈ 1 with only a brief transition period $0 < P_{sf} < 1$. We see in Figure 4.5 that the transitional period evolves with redshift to lower $\log(sSFR\,(yr^{-1}))$ values at lower redshift. This evolution is likely influenced by the evolution of the star-forming main sequence which shows a similar trend.

In Figure 4.6 we compare our transitional region to a result from literature. Here we compare to the parameterization of the green valley from (15) where a star-forming galaxy is defined as a galaxy with sSFR $> (1/3)t_U(Z)$, where $t_U(Z)$ is the age of the universe at a given redshift, and a quiescent galaxy is defined as a galaxy with a sSFR $< (1/20)t_U(Z)$, therefore everything within $(1/20)t_U(Z)$ $<$ sSFR $< (1/3)t_U(Z)$ lies in the green valley. In Figure 4.6 we compare the green valley from (15) to our selection of $0.1 < P_{sf} < 0.9$, we see that the two regions agree nicely and we will therefore use the inner 80 percentile region to signify our green valley. That our parameterization of the green valley follows the analytical form used in (15) nicely is not by design and is rather a point to how well our approach of using P_{sf} does at characterizing galaxies.

4.4.2 Stacked Grism Spectra

Beyond grouping galaxies by their $\log(sSFR\,(yr^{-1}))$ we also wish to see what the spectra of these different groups look like (star-forming - transitional - quiescent), we show this in Figures 4.7 and 4.8. Moving forward in the paper we will break our sample into two mass bins, low-mass galaxies ($10.2 < \log(M/M_\odot) < 10.8$) and high-mass galaxies ($\log(M/M_\odot) > 10.8$) as a way to examine the effect stellar-mass has on galaxies which are crossing the green valley.

Here we stack galaxies using a weighted mean. The weights are derived from two values added

in quadrature. The first values are the measurement errors derived from the Grizli extractions, the second is a weight derived from jackknifing as outlined in (13). This process down weights the effect outlier spectra have on the stack. We normalize the spectra in the rest-frame region of $5400 < \lambda < 5800$ Å using the best fit FSPS models. In both Figures 4.7 and 4.8 the four panels refer to: A star-forming galaxies, B transitional galaxies, C quiescent galaxies, D residual spectra defined as (type stacked spectra) / quiescent galaxies stacked spectra.

Panel A in Figures 4.7 and 4.8 show the star-forming galaxies stacked spectra. We see that both the low-mass and high-mass sample stacks have strong Hα emission as well as OII emission present. The lower mass sample contains OIII and Hβ, though these two lines are not present in the higher mass sample, likely due to older/longer lived stars dominating the stellar populations. Panel B in Figures 4.7 and 4.8 show the transitional galaxies. These galaxies also have strong Hα emission as well as OII emission present, though these galaxies also have several deep Balmer absorption features and the presence of the 4000 Å break. The main difference seen between the higher and lower mass galaxy stacks is that the lower mass galaxies have many more Balmer absorption lines present with Hγ and Hδ visible, also the region blueward of the 4000 Å break is steeper in the higher mass galaxies, again pointing towards an older stellar population. These transitional galaxies share the traits of star-forming and quiescent galaxies. Panel C shows the quiescent galaxies, these spectra are very similar having the traditional markings of quiescent spectra (4000 Å break, Balmer absorption lines, no Hα emission). Again the difference between the stacks seems to stem from the higher mass populations having older stellar populations. Panel D shows the residual spectra for the different galaxy groups. Here the quiescent galaxies stacked spectra are used as the control so we only see it as a flat line. We can see in both Figures 4.7 and 4.8 as galaxies decrease in P_{sf} several changes begin to happen. Hα decreases in strength until it's completely gone at lower P_{sf} values. We also see a decrease in the UV flux again pointing towards the disappearance of the shorter-lived stellar populations.

4.5 Discussion

Using P_{sf} we can track the galaxy populations as they cross the green valley, by doing this we can begin to outline what sorts of quenching tracks are preferred at higher redshifts.

4.5.1 Age

First, we looked at how P_{sf} is related to age. In Figure 4.9 Panels A and D we focus on two types of age parameterizations, light-weighted age (t_{lwa}) and t_{50}. t_{lwa} is a measure of age weighed by the light in a photometric band, here we use the Sloan Digital Sky Survey g-band. This value is derived directly from our stellar population fitting. t_{50} is the lookback time to when the galaxy formed half its mass, measured from our flexible SFHs. t_{50} is related more to the formation redshift of a galaxy while t_{lwa} is related more directly to the spectra, as a result t_{lwa} is much better at separating galaxies by formation activity and is more correlated to sSFR.

Figure 4.9 shows how galaxies evolve with age as they cross the green valley. Panel A (D) shows the relationship between P_{sf} and t_{lwa} (t_{50}) for galaxies at $0.9 < z_{grism} < 1.1$, focusing on a narrow range of redshift so as to remove any evolutionary effects. In both Panels A and D we see a clear track showing the relationship P_{sf} has with age, showing clearly as galaxies age they hit a certain value then begin to transition. We can see by the spread of the transition galaxies that this event is short-lived, We also see that the ages that galaxies cross the green valley are generally uniform. Therefore by tracking this crossover age we can better understand how galaxies are quenching. Here we focus on the two parameterizations of age because of the properties they each have. As t_{lwa} separates each type of galaxy more cleanly we can use it to study the general trends seen in all populations, but since t_{50} as a concept is easier to understand (as it is simply related to the formation redshift) we can use this property to make more definite statements.

Figure 4.9 Panels B and C show the relation between t_{lwa} and redshift. In both panels, we show the entire sample colored by their P_{sf} values (as shown in the color bar, as well as trend lines, for the quiescent (red), transitioning (green), and star-forming (blue) galaxies, derived using a LOWESS algorithm and bootstrapping. In Panels B we show t_{lwa}/tU and see that all three different types

of galaxies have a $\sim$ flat relationship with redshift. This means that the transitioning population exists for some fraction age of the universe, and therefore quiescent galaxies (with a low probability of star-formation) are typically 45$\%$ the age of the universe, transitioning galaxies are $\sim$ 30$\%$ the age of the universe, and star-forming galaxies are at around 15$\%$ the age of the universe. While this trend seems consistent with redshift (at least over our redshift range) the implication from B is the age properties of what defines what a galaxy is changing with redshift which is seen in Panel C. We see that all groups are younger at lower redshift, while this is expected this implies that the transition from star-forming to quiescent happens at younger ages at higher redshifts, this is likely an indication of evolution in the formation rates of galaxies, meaning that at higher redshifts galaxies are forming faster.

In Figure 4.9 Panels E and F we see how the transition age (here t_{50}) evolves with redshift for our low-mass (purple stars) and high-mass (cyan diamonds) samples. We find that the low-mass samples transition at higher redshift with younger ages. To illustrate this we a LOWESS algorithm with bootstrapping to estimate the trend with a 68$\%$ confidence interval as outlined in (158). We see that the trend monotonically falls at higher redshifts. We see that the high-mass sample follows along with the low-mass sample until a redshift of $z_{grism} > 1.2$ where it flattens. This suggests that high-mass galaxies at higher redshifts may prefer a more rapid formation pathway. This is backed up by Panel E where we see the formation redshifts. Again we see that the two mass samples follow closely at lower redshifts but the higher redshifts $z_{grism} > 1.2$ high-mass galaxies have higher formation redshifts. Taking the full Figure 4.9 into consideration, what we can gather from these results is that all massive galaxies ($\log(M/M_{\odot}) > 10.2$) have formation timescales that evolve with redshift such that higher redshift galaxies form their mass at a more rapid pace. This pace slows down as a function of redshift and allows for star-forming galaxies at low redshift to have similar ages (t_{lwa}) to high redshift quiescent galaxies. We also see that there is a mass dependency on this relationship such that higher mass galaxies prefer faster formation routes as well at least (in our sample) til a $z_{grism} < 1.2$ where they evolve similarly. There may be several reasons for the trends we see. One reason could be that rejuvenation (when a quiescent galaxy resumes forming

stars) may be more common in high-mass / high-redshift galaxies. This would result in a galaxy with an already old population (i.e. high t_{50}) leaving the quiescent regime, though (as discussed in (158)) this frosting of star-formation would not be enough to impact t_{50}. Another possibility would be galaxies that have an initial burst of formation but never quite quench. These galaxies would have high t_{50} values, but as they never fully quench would still be forming stars at high enough of a rate to place them in the transitional region. Future work could be to compare our results with simulations to see if these populations exist, and what formation histories they possess.

4.5.2 Morphologies

One big area of discussion is the evolution of the physical properties of galaxies as they evolve and quench. Several studies have shown (115; 163) an apparent change in morphology as a function SFR. What is shown in these works is that as galaxies quench their morphologies become more compact. This can be shown by comparing the Σ_1, stellar mass surface density - as defined in Chapter 3, values of star-forming and quiescent galaxies. In general star-forming galaxies are more extended, and therefore have lower Σ_1 values. We illustrate this in Figure 4.10 which shows $\log(\Sigma_1)$ versus$\log(sSFR\,(yr^{-1}))$ showing that quiescent galaxies have compact morphologies, while star-forming galaxies have a much greater range and have much more extended profiles. The main question we can address with our novel approach is when does this apparent change in morphology happen. Is it while the galaxy is star-forming or does this occur while the galaxy is quenching and therefore in the transitional phase.

Figure 4.10 is a cartoon that shows the relationship between $\log(\Sigma_1)$ and $\log(sSFR\,(yr^{-1}))$, and tracks which outline how galaxies travel through this space. In purple, we outline how galaxies would evolve if they become more compact as they quench. We can see in Figure 4.10 that most galaxies seem to take this track. In orange, we show the track galaxies would take if they had become compact before quenching. These galaxies would likely experience some violent event that would cause the formation of a compact star-forming galaxy. We see in Figure 4.10 that this is a track less taken as compact star-forming galaxies are rare.

If a galaxy's morphology is set before the galaxy transitions then we should expect that the

galaxies crossing the green should do so with a flat trend with $\log(\Sigma_1)$, but if the change occurs during the transition then we should see a slope in the relationship between $\log(\Sigma_1)$ and P_{sf}. What we find is a mixture of both. We see in Figure 4.11 Panel A that the lower-mass sample becomes more compact as it crosses green valley ($\delta\log(\Sigma_1) = 0.4$) while the higher-mass sample has a flatter relationship ($\delta\log(\Sigma_1) = 0.2$) using a linear fit to illustrate this point. This outcome suggests that both pathways of morphological evolution are valid, but the pathway which changes the morphology before transitioning may be more common in high-mass galaxies.

One complicating factor is that $\log(\Sigma_1)$ is highly correlated with stellar mass. Therefore this trend may be driven more by a change in stellar mass than morphology. We therefore look at the relationship between $\log(M/M_\odot)$ and P_{sf} in Figure 4.11 Panel C. What we find here is that both the lower-mass and higher-mass samples increase in stellar mass as they cross the green valley. This suggests that the trend seen with $\log(\Sigma_1)$ is not driven by stellar mass. This is further backed up with Figure 4.11 Panel D which shows $\log(M/M_\odot)$ versus$\log(sSFR\,(yr^{-1}))$ where we see that there is no relationship between the two values.

We also look at the mass-independent compactness of a galaxy using the core-to-total mass ratio (C_1) in Figure 4.11 Panel E, where C_1 is defined as

$$C_1 \equiv \frac{\Sigma_1 * \pi}{M/M_\odot} \tag{4.3}$$

C_1 is a ratio of the core mass (defined as the mass within 1 kpc and derived from Σ_1) to the total stellar mass. What we find here is that as the lower-mass galaxies cross the green valley their C_1 value increases, while the C_1 values of higher mass galaxies stay the same. This means that the relationship in Figure 4.11 Panel A likely stems from a change in morphology. A key question, therefore, is what is causing lower-mass galaxies to become more compact as they cross the green valley. The clue for this may be in simulations but is beyond the scope of this work.

4.6 Conclusion

In this work, we use a novel approach to identify galaxies that are transitioning from star-forming to quiescent for a sample of massive galaxies ($\log(M/M_{\odot}) > 10.2$) at $0.7 < z_{grism} < 1.65$ from the CLEAR survey using stellar population fits utilizing a forward modeling approach. Our approach to finding these transitioning galaxies uses the shape of the $\log(sSFR\,(yr^{-1}))$ distribution to generate a probability of whether a galaxy is star-forming, P_{sf}. We apply this method running as a function of redshift to account for the evolution of the $\log(sSFR\,(yr^{-1}))$ distribution.

We find that the transitional phase for galaxies goes to higher $\log(sSFR\,(yr^{-1}))$ values at higher redshifts. This evolution is likely linked to the evolution of the star-forming main sequence (14).

We also compare our estimation of the transitional phase with estimates from the literature and find that our values agree with green valley estimates from the analytical approach used in (15). The agreement seen here displays how well our approach works as our results are derived using the $\log(sSFR\,(yr^{-1}))$ distribution while the analytical approach from (15) is derived from color-color relationships. This comparison guided our classification of quiescent - transitional - star-forming galaxies.

Studying the stacked grism spectra we find that transitioning galaxies show spectral features of both typical star-forming and quiescent galaxies. Using P_{sf} we see how spectral features evolve as galaxies cross the green valley.

We also find that the crossover age shifts to younger ages at higher redshifts, suggesting that higher redshift galaxies follow more rapid formation channels. This is also evidence that there is an evolution in which quenching mechanisms dominate as a function of redshift. We also see evidence that rejuvenation may be more common in high-mass at high redshift.

Finally, we study the evolution of morphology as a function of P_{sf}. The goal here is to understand when galaxies form the compact morphologies seen in quiescent galaxies. We find that most galaxies compact while they cross the green valley, but high-mass galaxies show evidence that they may have higher occurrences of compact morphology formation before quenching. We will

expand on this work by studying the evolution of morphologies in simulations.

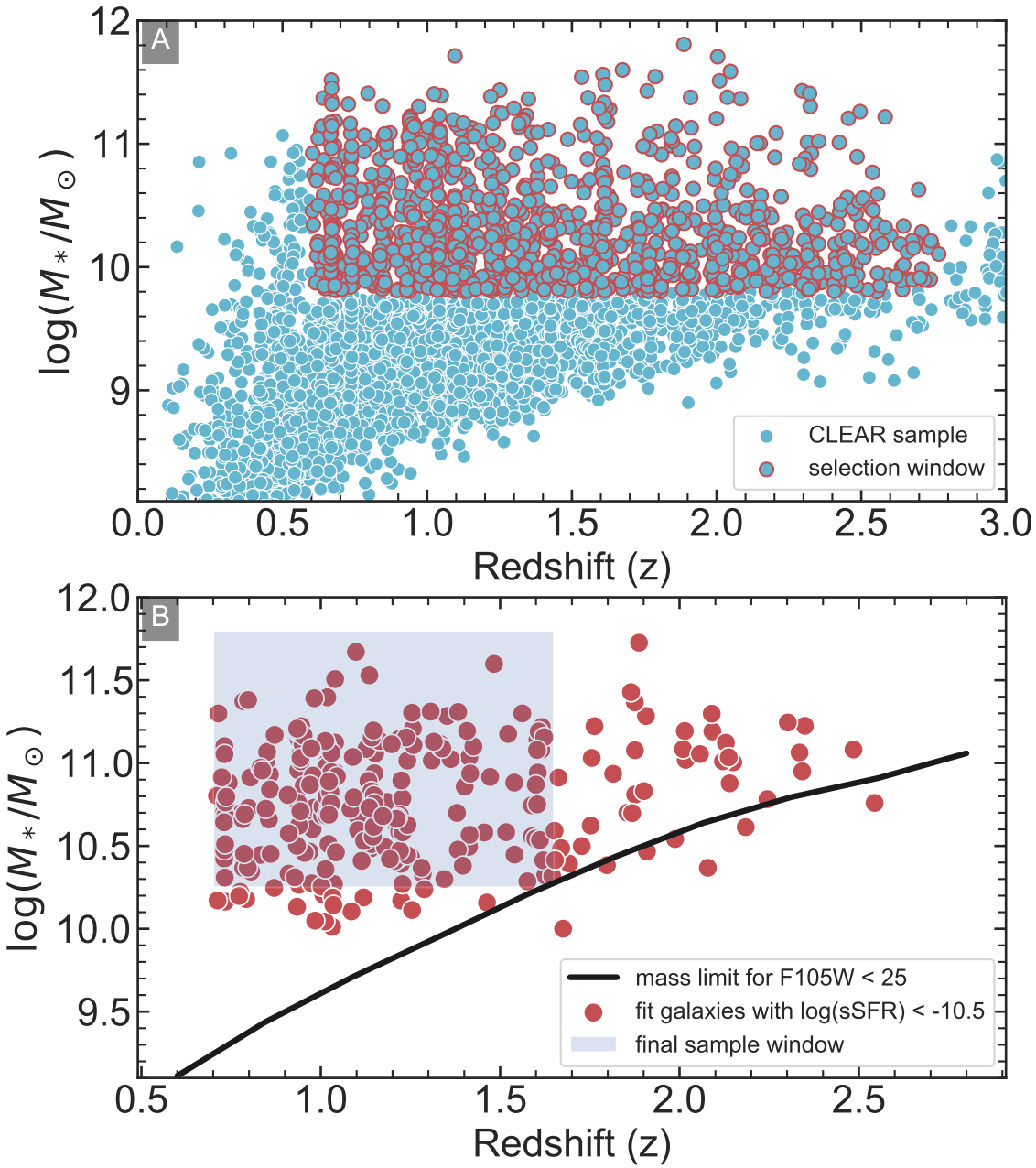

Figure 4.1: Sample selection of the parent and study sample. Panel A shows the CLEAR sample (blue) with stellar masses from Eazy-py and redshifts measured by Grizli and Eazy-py. We select galaxies to fit with $\log(M/M_{\odot}) > 9.8$ and $0.6 < z < 2.8$ (points outlined in red). For this study, we apply a mass limit corresponding to an AB magnitude of F105W < 25 mag, shown as a black line in Panel B. This limit was derived by generating a model single stellar populations formed at z = 5 and measured what minimum mass was necessary for detection. Panel B shows galaxies that were fit for their stellar populations with log(sSFR) < -10.5 (red points), roughly corresponding to a quiescent sample, along with the sample mass/magnitude limit. The blue region was the sample selection for this study ($\log(M/M_{\odot}) >$ 10.2 and 0.7 $< z_{grism} <$ 1.65) chosen to maximize the amount of low $\log(sSFR\,(yr^{-1}))$ (< -10.5) galaxies. For our sample selection, we chose to go with a volume-limited sample (defined by this blue-shaded region in Panel B) to make sure quiescent galaxies were properly represented at each redshift.

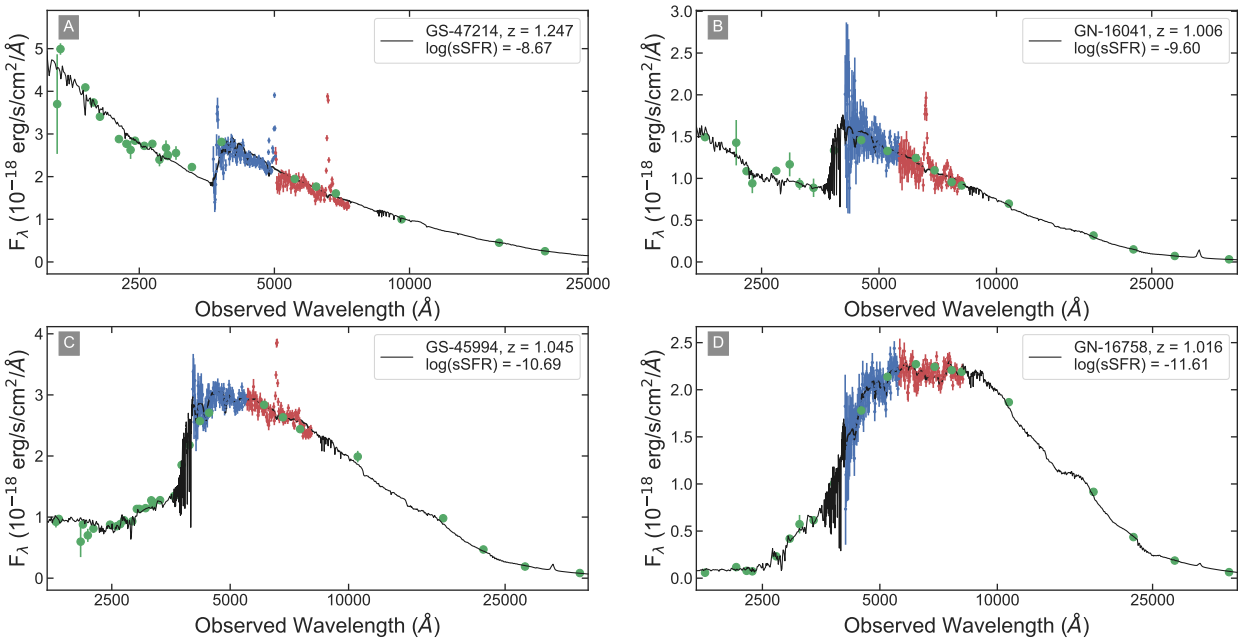

Figure 4.2: Example spectra and best-fit models (black) from our stellar population fits with *HST* WFC3/G102 spectrum in blue, *HST* WFC3/G141 spectrum in red, and photometry in green. As the panels progress from A to D we are stepping to lower $\log(sSFR\,(yr^{-1}))$ values, as we do this the features of the spectra resemble a more mature stellar population.

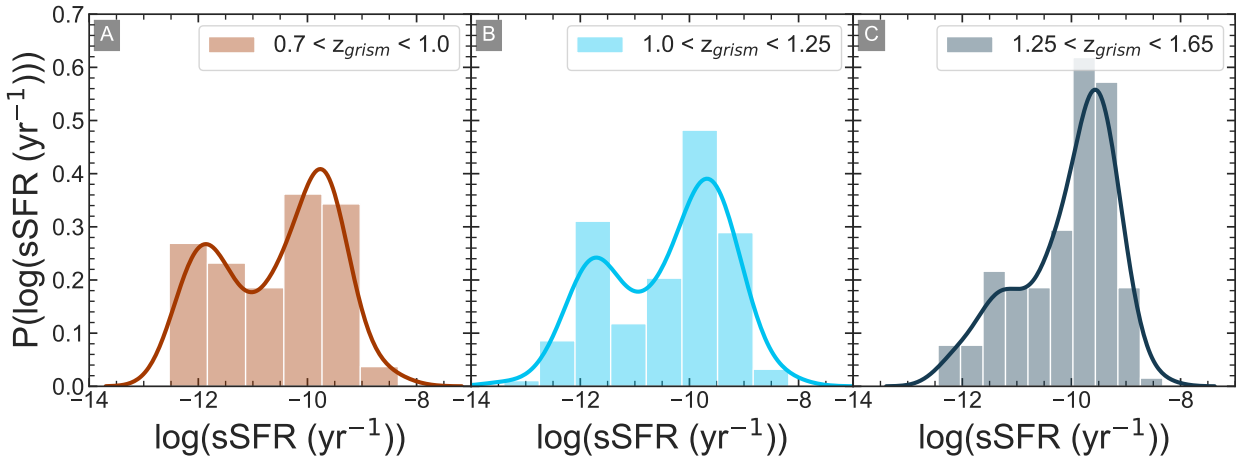

Figure 4.3: The $\log(sSFR\,(yr^{-1}))$ distribution at different redshifts. We can see several evolutionary changes in the samples. First, we can see that the measured $\log(sSFR\,(yr^{-1}))$ distribution is bimodal. Second, we can see that the shape of the star-forming region is roughly Gaussian in shape. We also see that the contribution of the quiescent region is lessened at higher redshifts and that the peak of the star-forming region shifts to lower $\log(sSFR\,(yr^{-1}))$ values at lower redshifts. We can use several of these properties to derive P_{sf} and identify the galaxies which are in transition.

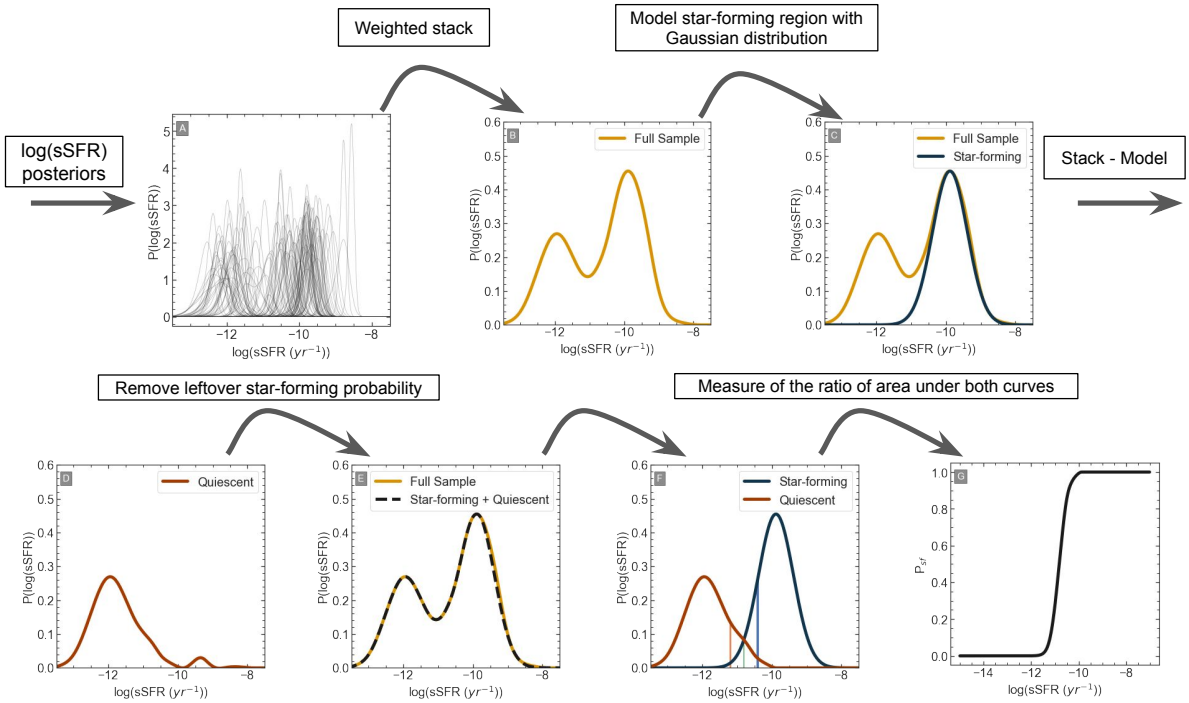

Figure 4.4: An outline of how P_{sf} is derived. Note that we apply this running as a function of redshift so this will only be applied to a portion of the sample as a time. First, we gather the $\log(sSFR\,(yr^{-1}))$ posteriors for galaxies in our redshift group, then we stack using the weighted stacking method outlined in (13). we then fit a Gaussian distribution to the star-forming region by identifying the higher $\log(sSFR\,(yr^{-1}))$ peak (this will be our μ), we then isolate the region $\log(sSFR\,(yr^{-1})) > \mu$ and from this portion we measure the 1 σ value. Panel C shows the resulting fit. We then subtract our model star-forming region from the stacked distribution to obtain the quiescent region. The resulting quiescent region will likely contain a residual portion of the star-forming region stemming from the inexactness of the Gaussian fit, we remove this portion of the distribution as it is not part of the quiescent region. Panel E shows the stacked $\log(sSFR\,(yr^{-1}))$ distribution and the summation of our star-forming and quiescent region. We can see that it is an excellent match, with a very slight difference seen in the star-forming region (the quiescent region is exact by design). P_{sf} is then derived by measuring the area under the star-forming distribution and comparing that to the stacked distribution to derive its contribution. Panel F shows the 10%, 50%, and 90% P_{sf} regions. The resulting measurement of P_{sf} versus$\log(sSFR\,(yr^{-1}))$ is shown in G. We can see that it is dominated by high and low probability values with a short transitional period.

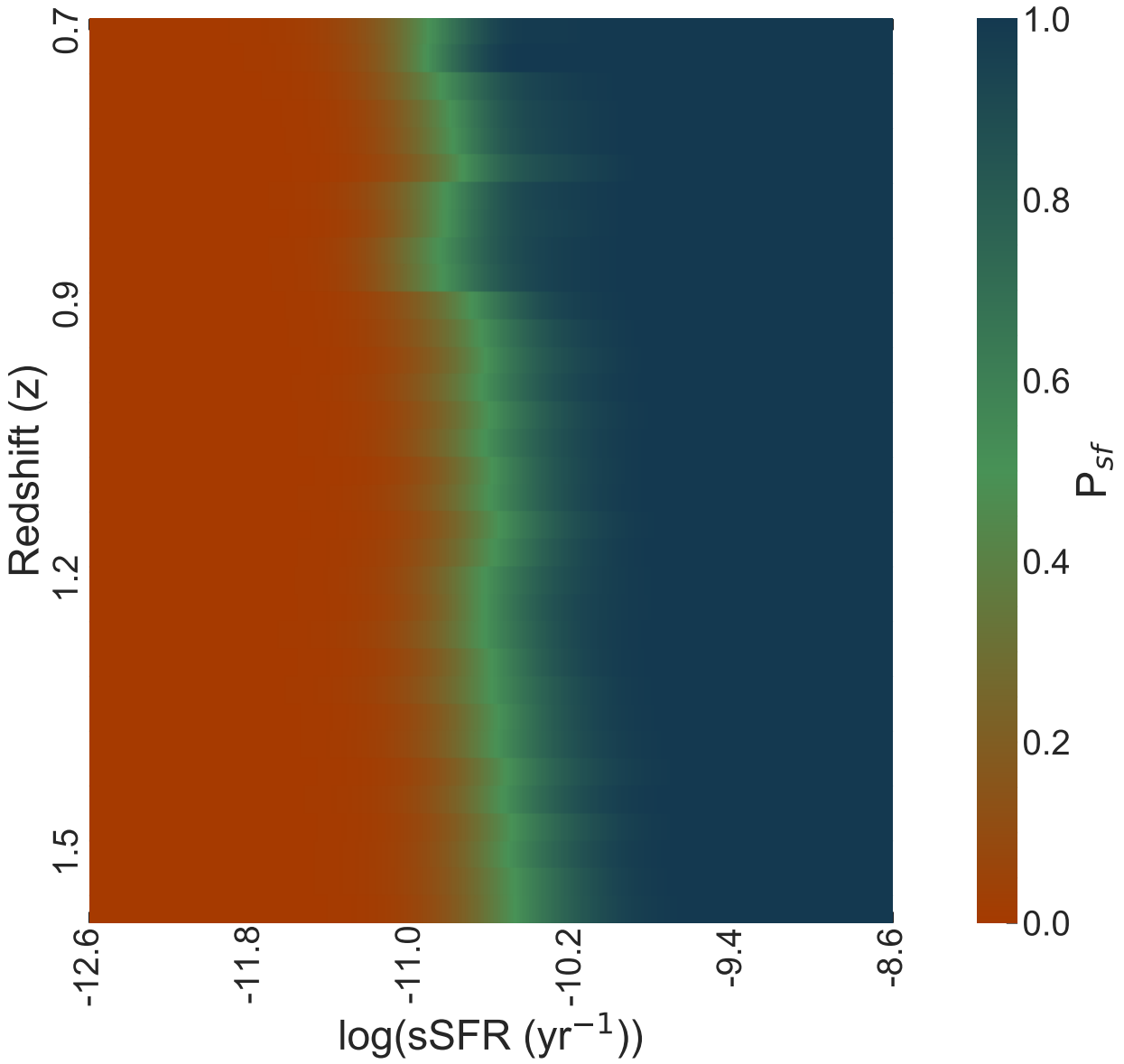

Figure 4.5: Evolution of P_{sf} as a function of redshift. Here we see that the majority of the sample is dominated by star-forming and quiescent galaxies with the transitional region occupying a smaller space. We also see that the transitional region evolves to lower $\log(sSFR\ (yr^{-1}))$ at lower redshifts, a similar behavior to what is seen in the evolution of the star-forming main sequence (14).

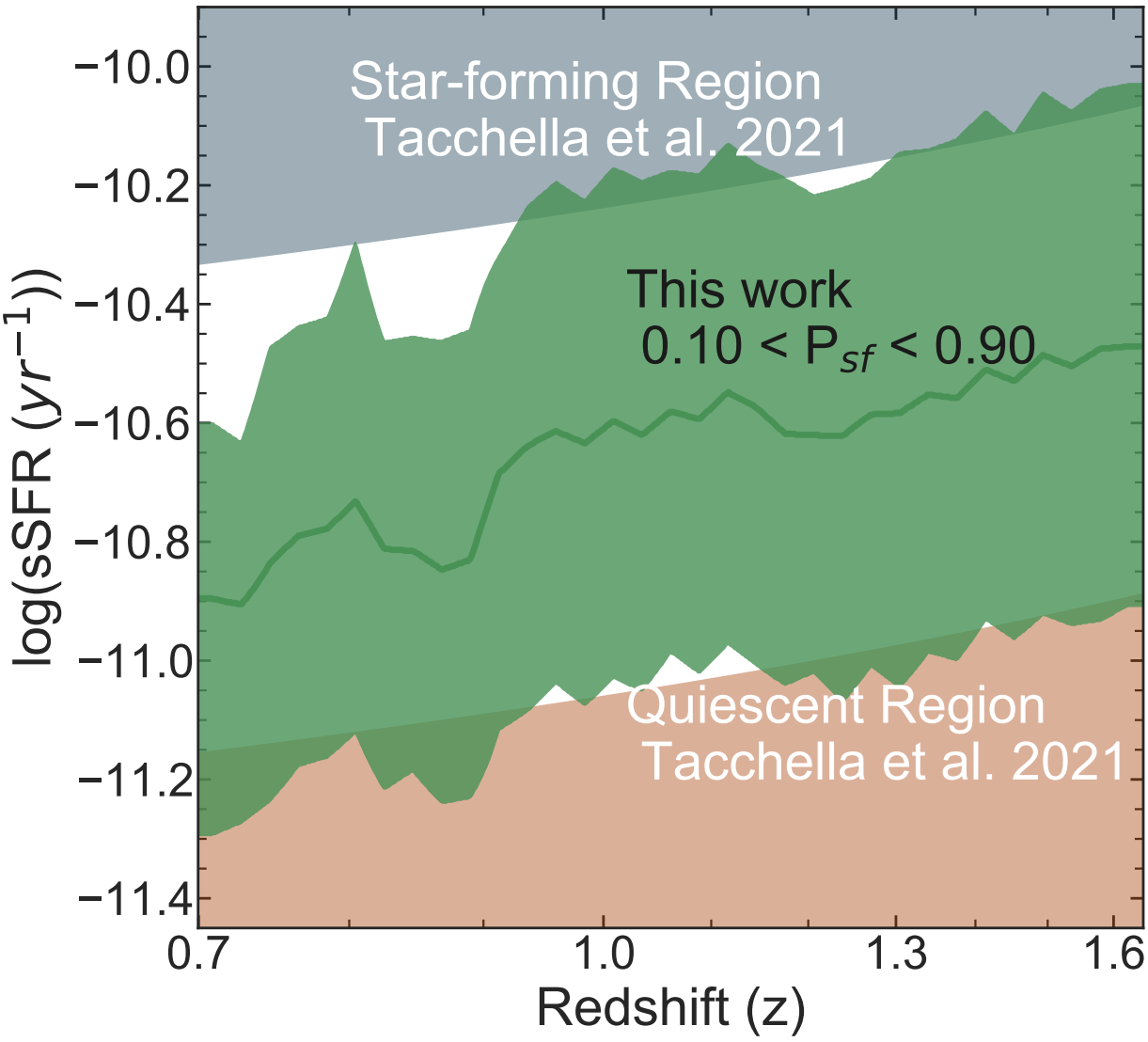

Figure 4.6: A comparison of our transitional galaxies to limits used in (15). By the parameterization outlined in (15), Star-forming galaxies lie in the blue region (and above) while quiescent galaxies would lie in the red region (and below), therefore leaving green valley galaxies in the white region where we have included our transitional galaxies. Here we see agreement with the literature results.

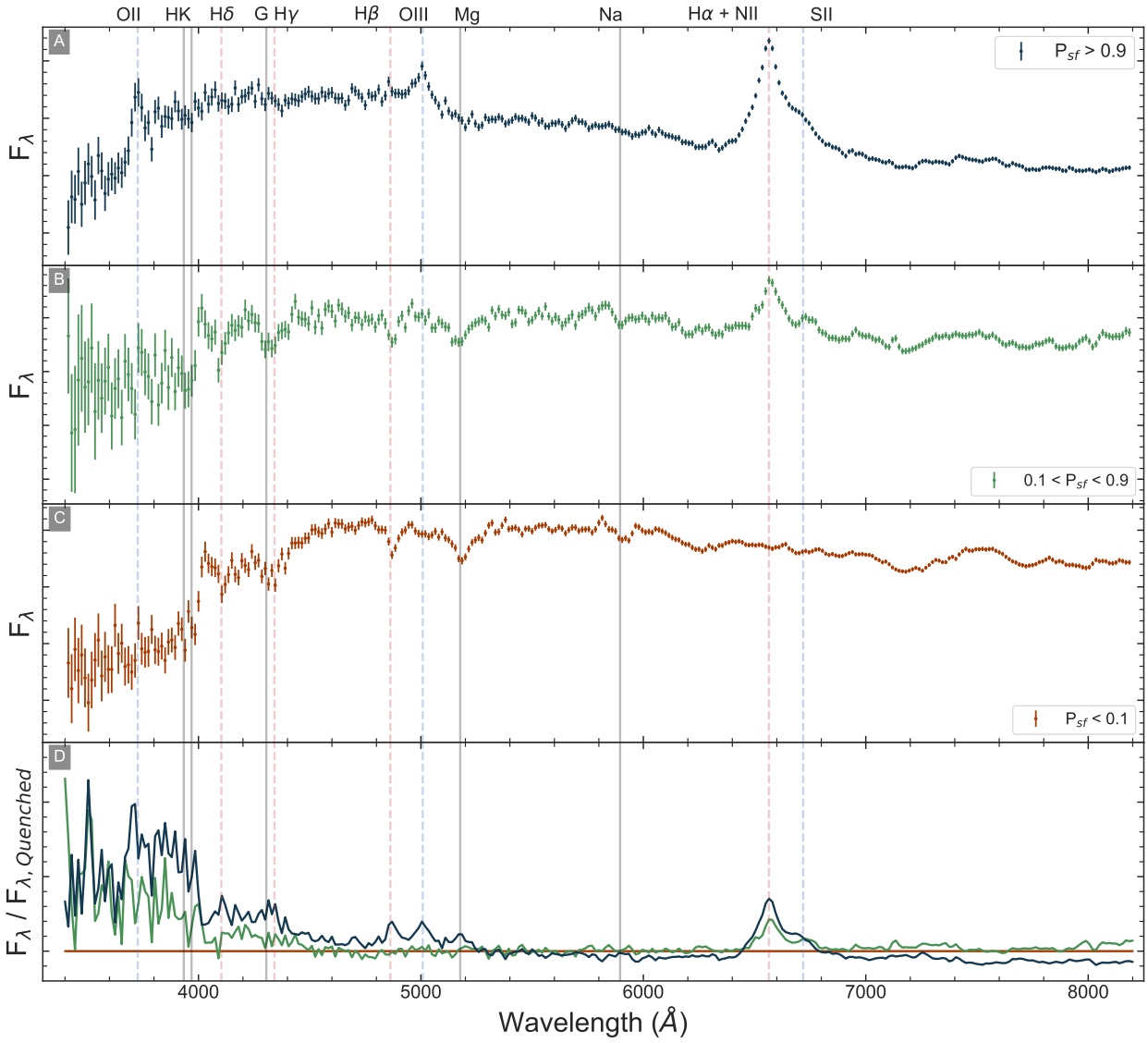

Figure 4.7: Stacked spectra of the three different P_{sf} regions for our low mass sample ($10.2 < \log(M/M_{\odot}) < 10.8$). Panel A shows the star-forming galaxies ($P_{sf} > 0.9$) which have clear Hα, OIII, Hβ, and OII emission. In Panel B we show the transitional galaxies ($0.1 < P_{sf} < 0.9$) with Hα, possible OII, and several absorption features. Panel C shows the quiescent galaxies ($P_{sf} > 0.1$), this spectra has all the expected features of a quiescent galaxy, 4000 Å break, Balmer absorption lines, several other metallicity absorption features (Ca HK, G, Mgb, Na). In Panel D we show a comparison of the stacked spectra to the quiescent stacked spectra. We can see that the star-forming and transitional samples have more UV flux and Hα emission. We also see that other than the previously mentioned features, that the transitional galaxy stacked spectra matches that of the quiescent galaxies, showing that these galaxies have spectra that have features of both star-forming and quiescent galaxies.

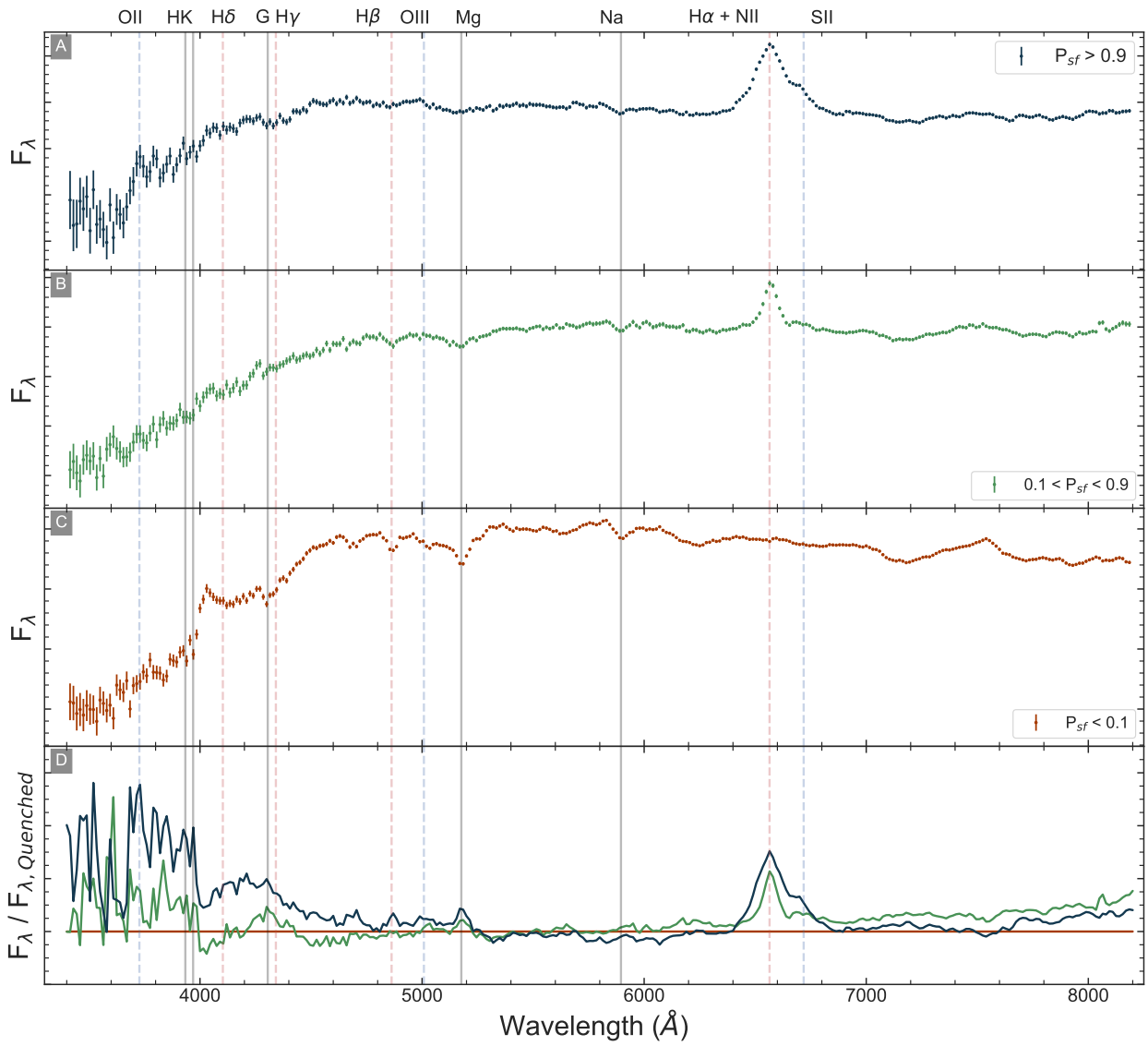

Figure 4.8: Stacked spectra similar to what is seen in Figure 4.7, but for our high mass sample ($\log(M/M_{\odot}) < 10.8$). Panel A shows the star-forming galaxies ($P_{sf} > 0.9$) which have clear Hα, OII emission, differentiating if from the low mass sample in its lack of Hβ emission and OIII. These differences are likely due to higher mass galaxies have more evolved (older) stellar populations. In Panel B we show the transitional galaxies ($0.1 < P_{sf} < 0.9$) with Hα and several absorption features. Panel C shows the quiescent galaxies ($P_{sf} > 0.1$), this spectrum has all the expected features of a quiescent galaxy, 4000 Å break, Balmer absorption lines, several other metallicity absorption features (Ca HK, G, Mgb, Na). In Panel D we show a comparison of the stacked spectra to the quiescent stacked spectra. We can see that the star-forming and transitional samples have more UV flux, Hα emission. Like in Figure 4.7 we see that that the transitional galaxies stacked spectra is a mixture of star-forming and quiescent galaxy spectra features. The differences in the continuum between all samples are less than the low mass sample (likely due to the domination of older stellar populations), we can still see that the star-forming and quiescent samples disagree at the marked features.

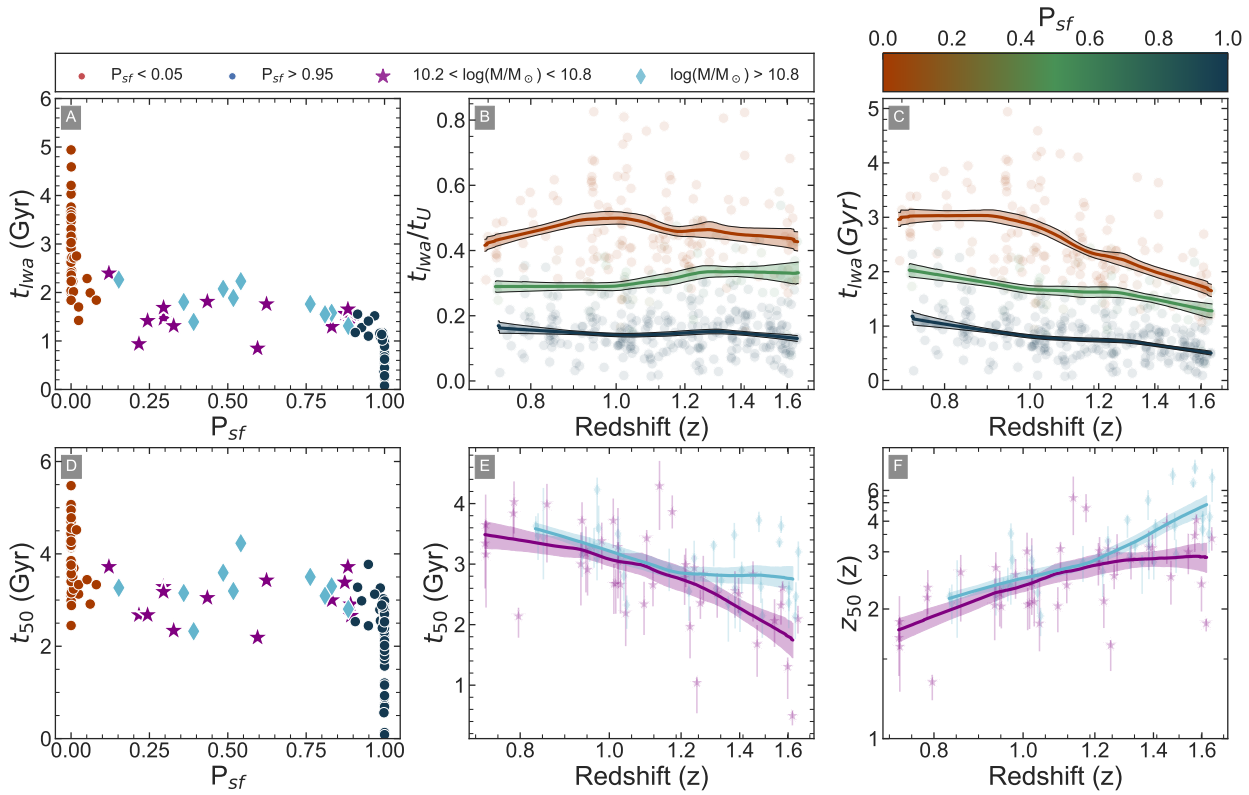

Figure 4.9: Here we show the relationship between age and P_{sf} highlighting two different parameterizations of age t_{lwa} and t_{50}. Panels A and D show the crossing ages of each parameterization with star-forming galaxies shown in blue and quiescent galaxies shown in red. Our transitioning galaxies are split in to high and low mass samples (cyan diamonds and purple stars respectively). Panels B and C show the evolution of t_{lwa} with redshift. Here we see that each of the galaxy classifications stays at a steady percentage age of the universe while their actual ages decrease at higher redshift. This means that galaxies transition at younger ages at higher redshifts. Panel E shows the evolution of the crossing age (t_{50}) of high and low mass quiescent galaxies. The populations have similar trends until $z_{grism} > 1.2$. Panel F shows the formation redshift as a function of redshift for the high and low mass transitioning galaxies and implies that the high-mass high redshift sample formed early.

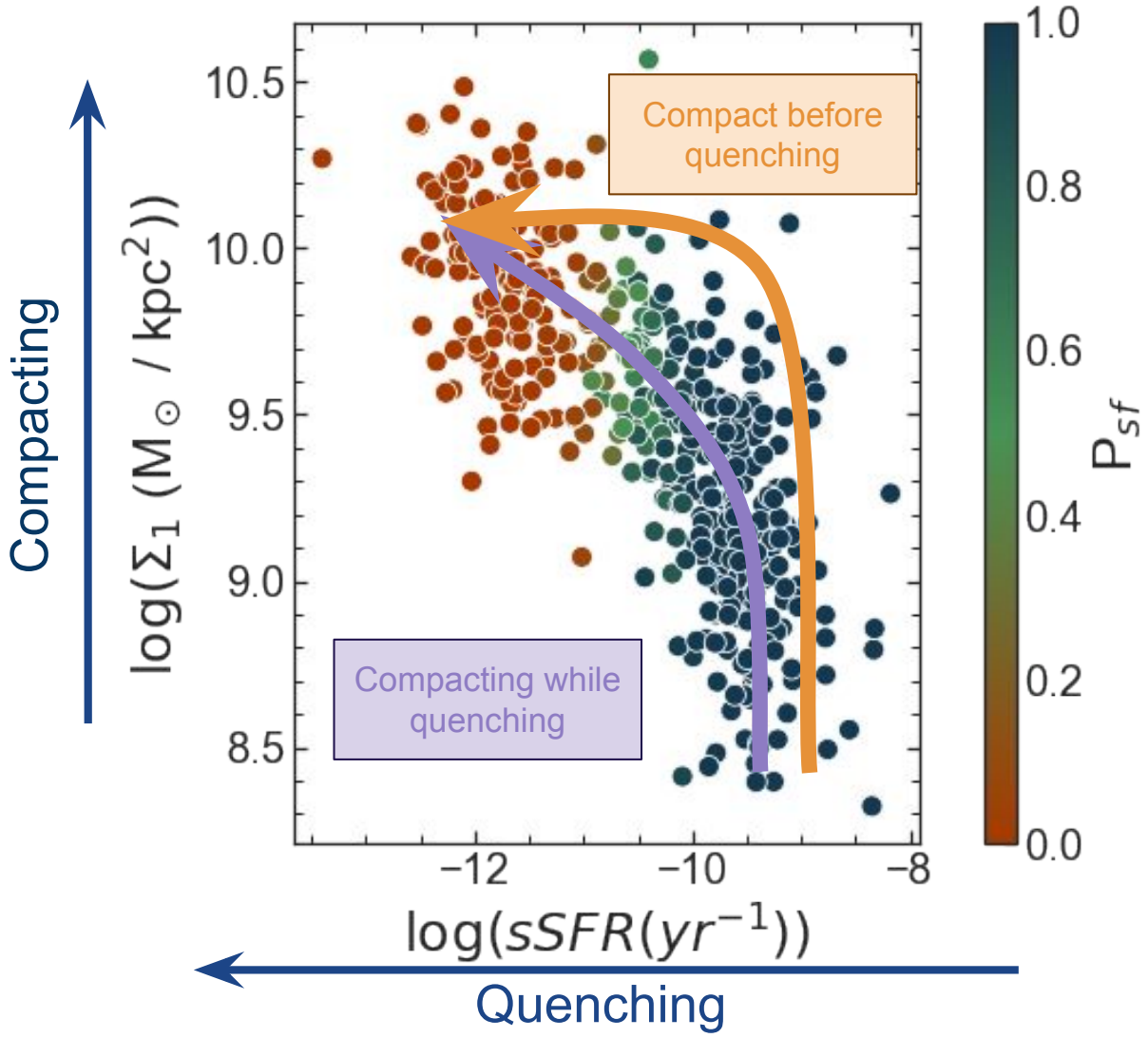

Figure 4.10: A cartoon explaining the two tracks galaxies may take to forming their quenched morphologies. Here we show the relationship between $\log(\Sigma_1)$ and $\log(sSFR\,(yr^{-1}))$. We see a clear trend in the evolution of morphology as it relates to quenching. The purple track outlines galaxies that become more compact as they quench. We see that this is likely the track taken by most galaxies. In orange, we show the track galaxies which become compact before quenching take. These galaxies will likely experience some violent event that causes the formation of a compact star-forming galaxy. We see that this is a less taken track.

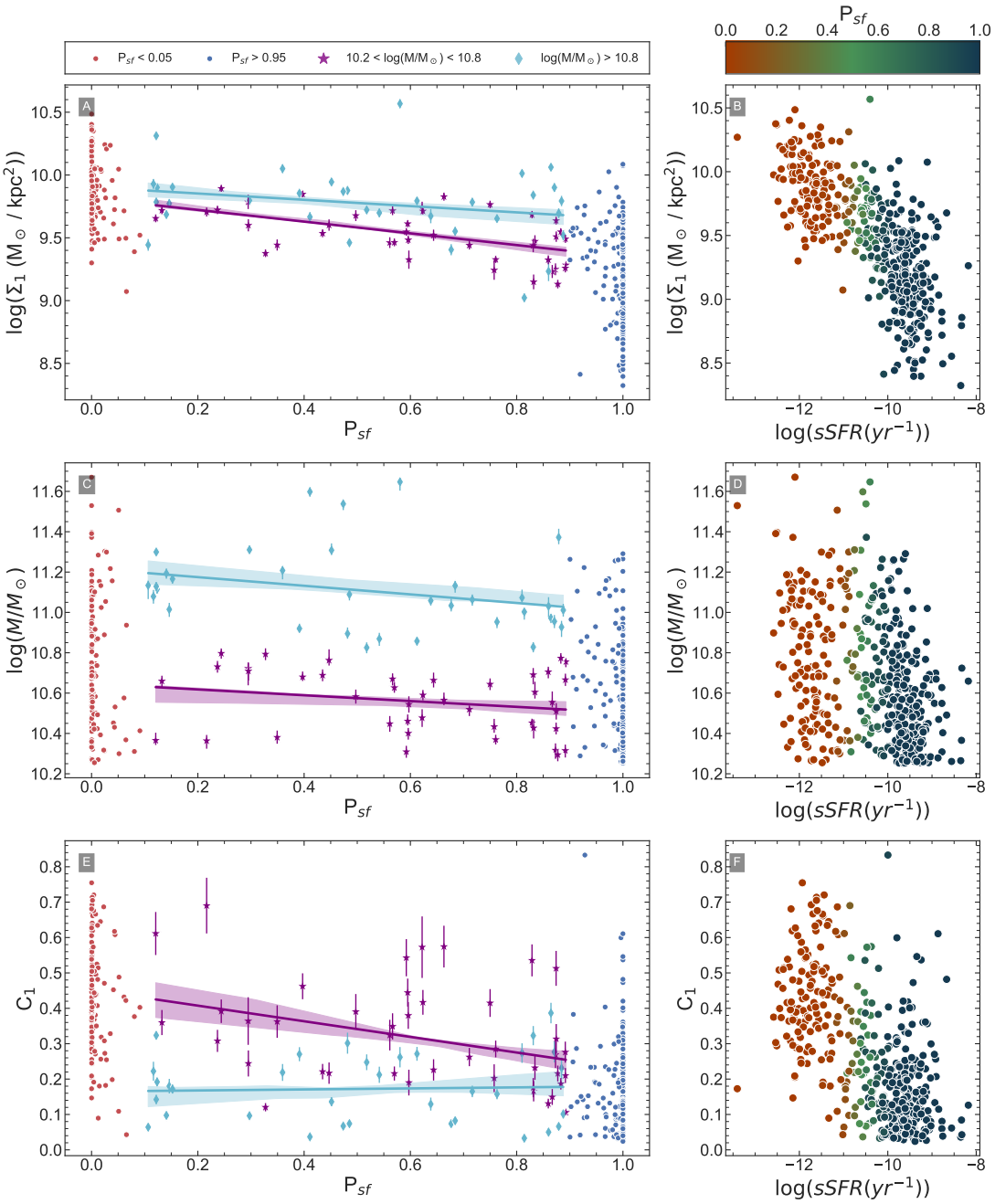

Figure 4.11: Here we show how several physical properties evolve as a function of P_{sf}. In Panels A, C, and E quiescent galaxies are shown in red, star-forming galaxies are shown in blue, and the transitional galaxies are separated in to high and low mass samples (shown as cyan diamonds and purple stars respectively). In Panels B, D, and F points are colored by their P_{sf} value, shown in the color bar. Panels A and B focus on $\log(\Sigma_1)$, Panels C and D focus on $\log(M/M_\odot)$, Panels E and F focus on the core to total mass (C_1). A suggests that low-mass galaxies become more compact as they cross the green valley, while high-mass galaxies form their compact morphologies before quenching more often. We also see no difference in how these galaxies evolve with stellar mass but show a significant difference in the evolution of C_1.

5. SUMMARY AND FUTURE DIRECTIONS

Here we have used a forward modeling process to fit the stellar populations of massive galaxies from the CANDELS Lyman-α Emission at Reionization (CLEAR) survey. The work here has allowed us to study several relationships at their highest redshifts yet.

Using *HST* WFC3 G102 grism spectra from the CLEAR survey we tested the ability of this data type to be used to study the stellar populations of massive quiescent galaxies. Our results show that grism data does have the capability to recover stellar population properties, showing that these data will be important for future space-based missions like the James Webb Space Telescope and the Roman Space Telescope. In addition, we studied the mass-stellar metallicity relationship to the highest redshift yet. We found that the relationship does not evolve as a function of redshift (up to z $= 1.7$).

In our second paper, we expanded our dataset to include *HST* WFC3 G102 grism spectra, *HST* WFC3 G141 grism spectra, and photometry. This expansion allowed us to increase our redshift range. In this work, we studied the relationship between a galaxy's morphology and its formation redshift. We found that the most compact galaxies all formed at high formation redshifts, such that none of the most compact galaxies in our sample had z_{50} values below $z_{50} < 2.9$. We also showed that galaxies with more extended morphological profiles had extended star-formation histories.

In our last paper, we focused on a sample of transitional galaxies by developing a novel approach to categorizing a galaxy by formation activity by deriving its probability of being star-forming. We found that our method matched well with the literature results and that our parameterization of the green valley evolved with redshift such that at higher redshifts the green valley had higher $\log(sSFR\,(yr^{-1}))$. We found that galaxies at higher redshift have more rapid formation, and favored faster quenching mechanisms. In addition, we found that most galaxies change their apparent morphologies as they cross the green valley, but higher-mass galaxies form their morphologies before quenching more often than lower-mass galaxies.

REFERENCES

[1] V. A. Epanechnikov, "Non-Parametric Estimation of a Multivariate Probability Density," *Theory of Probability and its Applications*, vol. 14, p. 153, 1969.

[2] R. J. Williams, R. F. Quadri, M. Franx, P. van Dokkum, and I. Labbé, "Detection of Quiescent Galaxies in a Bicolor Sequence from Z = 0-2," , vol. 691, pp. 1879–1895, Feb. 2009.

[3] J. T. Mendel, R. P. Saglia, R. Bender, A. Beifiori, J. Chan, M. Fossati, D. J. Wilman, K. Bandara, G. B. Brammer, N. M. Förster Schreiber, A. Galametz, S. Kulkarni, I. G. Momcheva, E. J. Nelson, P. G. van Dokkum, K. E. Whitaker, and S. Wuyts, "First Results from the VIRIAL Survey: The Stellar Content of UVJ-selected Quiescent Galaxies at 1.5 z 2 from KMOS," , vol. 804, p. L4, May 2015.

[4] J. Choi, C. Conroy, J. Moustakas, G. J. Graves, B. P. Holden, M. Brodwin, M. J. I. Brown, and P. G. van Dokkum, "The Assembly Histories of Quiescent Galaxies since z = 0.7 from Absorption Line Spectroscopy," , vol. 792, p. 95, Sept. 2014.

[5] A. Gallazzi, E. F. Bell, S. Zibetti, J. Brinchmann, and D. D. Kelson, "Charting the Evolution of the Ages and Metallicities of Massive Galaxies since z = 0.7," , vol. 788, p. 72, June 2014.

[6] K. E. Whitaker, P. G. van Dokkum, G. Brammer, I. G. Momcheva, R. Skelton, M. Franx, M. Kriek, I. Labbé, M. Fumagalli, B. F. Lundgren, E. J. Nelson, S. G. Patel, and H.-W. Rix, "Quiescent Galaxies in the 3D-HST Survey: Spectroscopic Confirmation of a Large Number of Galaxies with Relatively Old Stellar Populations at z ˜ 2," , vol. 770, p. L39, June 2013.

[7] M. Fumagalli, M. Franx, P. van Dokkum, K. E. Whitaker, R. E. Skelton, G. Brammer, E. Nelson, M. Maseda, I. Momcheva, M. Kriek, I. Labbé, B. Lundgren, and H.-W. Rix, "Ages of Massive Galaxies at 0.5 z 2.0 from 3D-HST Rest-frame Optical Spectroscopy," , vol. 822, p. 1, May 2016.

[8] I. Ferreras, A. Pasquali, N. Pirzkal, J. Pharo, S. Malhotra, J. Rhoads, N. Hathi, R. Windhorst, A. Cimatti, L. Christensen, S. L. Finkelstein, N. Grogin, B. Joshi, K. Kim, A. Koekemoer, R. O'Connell, G. Östlin, B. Rothberg, and R. Ryan, "FIGS: spectral fitting constraints on the

star formation history of massive galaxies since the cosmic noon," , vol. 486, pp. 1358–1376, Jun 2019.

[9] B. M. B. Henriques, S. D. M. White, P. A. Thomas, R. Angulo, Q. Guo, G. Lemson, V. Springel, and R. Overzier, "Galaxy formation in the Planck cosmology - I. Matching the observed evolution of star formation rates, colours and stellar masses," , vol. 451, pp. 2663–2680, Aug. 2015.

[10] A. Gallazzi, S. Charlot, J. Brinchmann, S. D. M. White, and C. A. Tremonti, "The ages and metallicities of galaxies in the local universe," , vol. 362, pp. 41–58, Sept. 2005.

[11] A. van der Wel, M. Franx, P. G. van Dokkum, R. E. Skelton, I. G. Momcheva, K. E. Whitaker, G. B. Brammer, E. F. Bell, H.-W. Rix, S. Wuyts, H. C. Ferguson, B. P. Holden, G. Barro, A. M. Koekemoer, Y.-Y. Chang, E. J. McGrath, B. Häussler, A. Dekel, P. Behroozi, M. Fumagalli, J. Leja, B. F. Lundgren, M. V. Maseda, E. J. Nelson, D. A. Wake, S. G. Patel, I. Labbé, S. M. Faber, N. A. Grogin, and D. D. Kocevski, "3D-HST+CANDELS: The Evolution of the Galaxy Size-Mass Distribution since z = 3," , vol. 788, p. 28, June 2014.

[12] B. Häussler, D. H. McIntosh, M. Barden, E. F. Bell, H.-W. Rix, A. Borch, S. V. W. Beckwith, J. A. R. Caldwell, C. Heymans, K. Jahnke, S. Jogee, S. E. Koposov, K. Meisenheimer, S. F. Sánchez, R. S. Somerville, L. Wisotzki, and C. Wolf, "GEMS: Galaxy Fitting Catalogs and Testing Parametric Galaxy Fitting Codes: GALFIT and GIM2D," , vol. 172, pp. 615–633, Oct. 2007.

[13] V. Estrada-Carpenter, C. Papovich, I. Momcheva, G. Brammer, J. Long, R. F. Quadri, J. Bridge, M. Dickinson, H. Ferguson, and S. Finkelstein, "CLEAR. I. Ages and Metallicities of Quiescent Galaxies at 1.0 < z < 1.8 Derived from Deep Hubble Space Telescope Grism Data," , vol. 870, p. 133, Jan 2019.

[14] K. E. Whitaker, M. Kriek, P. G. van Dokkum, R. Bezanson, G. Brammer, M. Franx, and I. Labbé, "A Large Population of Massive Compact Post-starburst Galaxies at z > 1: Implications for the Size Evolution and Quenching Mechanism of Quiescent Galaxies," , vol. 745, p. 179, Feb 2012.

[15] S. Tacchella, C. Conroy, S. Faber, L. Hernquist, D. Eisenstein, B. Johnson, and J. Leja, "Fast, Slow, Early, Late: Quenching Massive Galaxies at z $\sim$ 0.8," in *Extragalactic Spectroscopic Surveys: Past*, p. 59, Apr. 2021.

[16] R. E. Skelton, K. E. Whitaker, I. G. Momcheva, G. B. Brammer, P. G. van Dokkum, I. Labbé, M. Franx, A. van der Wel, R. Bezanson, E. Da Cunha, M. Fumagalli, N. Förster Schreiber, M. Kriek, J. Leja, B. F. Lundgren, D. Magee, D. Marchesini, M. V. Maseda, E. J. Nelson, P. Oesch, C. Pacifici, S. G. Patel, S. Price, H.-W. Rix, T. Tal, D. A. Wake, and S. Wuyts, "3D-HST WFC3-selected Photometric Catalogs in the Five CANDELS/3D-HST Fields: Photometry, Photometric Redshifts, and Stellar Masses," , vol. 214, p. 24, Oct. 2014.

[17] C. A. L. Bailer-Jones, J. Rybizki, M. Fouesneau, G. Mantelet, and R. Andrae, "Estimating Distance from Parallaxes. IV. Distances to 1.33 Billion Stars in Gaia Data Release 2," , vol. 156, p. 58, Aug 2018.

[18] B. Alcalde Pampliega, P. G. Pérez-González, G. Barro, H. Domínguez Sánchez, M. C. Eliche-Moral, N. Cardiel, A. Hernán-Caballero, L. Rodriguez-Muñoz, P. Sánchez Blázquez, and P. Esquej, "Optically Faint Massive Balmer Break Galaxies at z > 3 in the CANDELS/GOODS Fields," , vol. 876, p. 135, May 2019.

[19] P. Guarnieri, C. Maraston, D. Thomas, J. Pforr, V. Gonzalez-Perez, J. Etherington, J. Carlsen, X. Morice-Atkinson, C. J. Conselice, J. Gschwend, M. Carrasco Kind, T. Abbott, S. Allam, D. Brooks, D. Burke, A. Carnero Rosell, J. Carretero, C. Cunha, C. D'Andrea, L. da Costa, J. De Vincente, D. DePoy, H. Thomas Diehl, P. Doel, J. Frieman, J. Garcia-Bellido, D. Gruen, G. Gutierrez, D. Hanley, D. Hollowood, K. Honscheid, D. James, T. Jeltema, K. Kuehn, M. Lima, M. A. G. Maia, J. Marshall, P. Martini, P. Melchior, F. Menanteau, R. Miquel, A. Plazas Malagon, S. Richardson, K. Romer, E. Sanchez, V. Scarpine, R. Schindler, I. Sevilla, M. Smith, M. Soares-Santos, F. Sobreira, E. Suchyta, G. Tarle, A. Walker, and W. Wester, "Candidate massive galaxies at z ~ 4 in the Dark Energy Survey," , vol. 483, pp. 3060–3081, Mar. 2019.

[20] B. D. Oppenheimer, R. Davé, N. Katz, J. A. Kollmeier, and D. H. Weinberg, "The intergalactic

medium over the last 10 billion years - II. Metal-line absorption and physical conditions," , vol. 420, pp. 829–859, Feb. 2012.

[21] R. S. Somerville and R. Davé, "Physical Models of Galaxy Formation in a Cosmological Framework," , vol. 53, pp. 51–113, Aug. 2015.

[22] P. Torrey, M. Vogelsberger, L. Hernquist, R. McKinnon, F. Marinacci, R. A. Simcoe, V. Springel, A. Pillepich, J. Naiman, R. Pakmor, R. Weinberger, D. Nelson, and S. Genel, "Similar star formation rate and metallicity variability time-scales drive the fundamental metallicity relation," , vol. 477, pp. L16–L20, June 2018.

[23] C. Papovich, L. A. Moustakas, M. Dickinson, E. Le Floc'h, G. H. Rieke, E. Daddi, D. M. Alexander, F. Bauer, W. N. Brandt, T. Dahlen, E. Egami, P. Eisenhardt, D. Elbaz, H. C. Ferguson, M. Giavalisco, R. A. Lucas, B. Mobasher, P. G. Pérez-González, A. Stutz, M. J. Rieke, and H. Yan, "Spitzer Observations of Massive, Red Galaxies at High Redshift," , vol. 640, pp. 92–113, Mar. 2006.

[24] M. Kriek, A. E. Shapley, N. A. Reddy, B. Siana, A. L. Coil, B. Mobasher, W. R. Freeman, L. de Groot, S. H. Price, R. Sanders, I. Shivaei, G. B. Brammer, I. G. Momcheva, R. E. Skelton, P. G. van Dokkum, K. E. Whitaker, J. Aird, M. Azadi, M. Kassis, J. S. Bullock, C. Conroy, R. Davé, D. Kereš, and M. Krumholz, "The MOSFIRE Deep Evolution Field (MOSDEF) Survey: Rest-frame Optical Spectroscopy for 1500 H-selected Galaxies at 1.37 < z < 3.8," *The Astrophysical Journal Supplement Series*, vol. 218, p. 15, June 2015.

[25] I. Lonoce, M. Longhetti, C. Maraston, D. Thomas, C. Mancini, A. Cimatti, F. Ciocca, A. Citro, E. Daddi, S. di Serego Alighieri, A. Gargiulo, R. Maiolino, F. Mannucci, M. Moresco, L. Pozzetti, S. Quai, and P. Saracco, "Old age and supersolar metallicity in a massive z 1.4 early-type galaxy from VLT/X-Shooter spectroscopy," , vol. 454, pp. 3912–3919, Dec 2015.

[26] P. G. van Dokkum, R. Bezanson, A. van der Wel, E. J. Nelson, I. Momcheva, R. E. Skelton, K. E. Whitaker, G. Brammer, C. Conroy, N. M. Förster Schreiber, M. Fumagalli, M. Kriek, I. Labbé, J. Leja, D. Marchesini, A. Muzzin, P. Oesch, and S. Wuyts, "Dense Cores in Galaxies Out to z = 2.5 in SDSS, UltraVISTA, and the Five 3D-HST/CANDELS Fields," ,

vol. 791, p. 45, Aug. 2014.

[27] D. Thomas, C. Maraston, R. Bender, and C. Mendes de Oliveira, "The Epochs of Early-Type Galaxy Formation as a Function of Environment," , vol. 621, pp. 673–694, Mar. 2005.

[28] M. Kriek, S. H. Price, C. Conroy, K. A. Suess, L. Mowla, I. Pasha, R. Bezanson, P. van Dokkum, and G. Barro, "Stellar Metallicities and Elemental Abundance Ratios of z 1.4 Massive Quiescent Galaxies," , vol. 880, p. L31, Aug 2019.

[29] A. Muzzin, D. Marchesini, M. Stefanon, M. Franx, H. J. McCracken, B. Milvang-Jensen, J. S. Dunlop, J. P. U. Fynbo, G. Brammer, I. Labbé, and P. G. van Dokkum, "The Evolution of the Stellar Mass Functions of Star-forming and Quiescent Galaxies to z = 4 from the COSMOS/UltraVISTA Survey," , vol. 777, p. 18, Nov. 2013.

[30] A. R. Tomczak, R. F. Quadri, K.-V. H. Tran, I. Labbé, C. M. S. Straatman, C. Papovich, K. Glazebrook, R. Allen, G. B. Brammer, G. G. Kacprzak, L. Kawinwanichakij, D. D. Kelson, P. J. McCarthy, N. Mehrtens, A. J. Monson, S. E. Persson, L. R. Spitler, V. Tilvi, and P. van Dokkum, "Galaxy Stellar Mass Functions from ZFOURGE/CANDELS: An Excess of Low-mass Galaxies since z = 2 and the Rapid Buildup of Quiescent Galaxies," , vol. 783, p. 85, Mar. 2014.

[31] L. Kawinwanichakij, C. Papovich, R. F. Quadri, K. Glazebrook, G. G. Kacprzak, R. J. Allen, E. F. Bell, D. J. Croton, A. Dekel, H. C. Ferguson, B. Forrest, N. A. Grogin, Y. Guo, D. D. Kocevski, A. M. Koekemoer, I. Labbé, R. A. Lucas, T. Nanayakkara, L. R. Spitler, C. M. S. Straatman, K.-V. H. Tran, A. Tomczak, and P. van Dokkum, "Effect of Local Environment and Stellar Mass on Galaxy Quenching and Morphology at 0.5 z 2.0," , vol. 847, p. 134, Oct. 2017.

[32] P. W. Sullivan and R. A. Simcoe, "A Calibrated Measurement of the Near-IR Continuum Sky Brightness Using Magellan/FIRE," , vol. 124, p. 1336, Dec. 2012.

[33] P. G. van Dokkum, G. Brammer, M. Fumagalli, E. Nelson, M. Franx, H.-W. Rix, M. Kriek, R. E. Skelton, S. Patel, K. B. Schmidt, R. Bezanson, F. Bian, E. da Cunha, D. K. Erb, X. Fan, N. Förster Schreiber, G. D. Illingworth, I. Labbé, B. Lundgren, D. Magee, D. Marchesini,

P. McCarthy, A. Muzzin, R. Quadri, C. C. Steidel, T. Tal, D. Wake, K. E. Whitaker, and A. Williams, "First Results from the 3D-HST Survey: The Striking Diversity of Massive Galaxies at z 1," , vol. 743, p. L15, Dec. 2011.

[34] I. Labbé, J. Huang, M. Franx, G. Rudnick, P. Barmby, E. Daddi, P. G. van Dokkum, G. G. Fazio, N. M. F. Schreiber, A. F. M. Moorwood, H.-W. Rix, H. Röttgering, I. Trujillo, and P. van der Werf, "IRAC Mid-Infrared Imaging of the Hubble Deep Field-South: Star Formation Histories and Stellar Masses of Red Galaxies at z2," , vol. 624, pp. L81–L84, May 2005.

[35] P. Madau and M. Dickinson, "Cosmic Star-Formation History," , vol. 52, pp. 415–486, Aug. 2014.

[36] C. Schreiber, D. Elbaz, M. Pannella, L. Ciesla, T. Wang, A. Koekemoer, M. Rafelski, and E. Daddi, "Observational evidence of a slow downfall of star formation efficiency in massive galaxies during the past 10 Gyr," , vol. 589, p. A35, May 2016.

[37] L. R. Spitler, C. M. S. Straatman, I. Labbé, K. Glazebrook, K.-V. H. Tran, G. G. Kacprzak, R. F. Quadri, C. Papovich, S. E. Persson, P. van Dokkum, R. Allen, L. Kawinwanichakij, D. D. Kelson, P. J. McCarthy, N. Mehrtens, A. J. Monson, T. Nanayakkara, G. Rees, V. Tilvi, and A. R. Tomczak, "Exploring the z = 3-4 Massive Galaxy Population with ZFOURGE: The Prevalence of Dusty and Quiescent Galaxies," , vol. 787, p. L36, June 2014.

[38] C. M. S. Straatman, I. Labbé, L. R. Spitler, R. Allen, B. Altieri, G. B. Brammer, M. Dickinson, P. van Dokkum, H. Inami, K. Glazebrook, G. G. Kacprzak, L. Kawinwanichakij, D. D. Kelson, P. J. McCarthy, N. Mehrtens, A. Monson, D. Murphy, C. Papovich, S. E. Persson, R. Quadri, G. Rees, A. Tomczak, K.-V. H. Tran, and V. Tilvi, "A Substantial Population of Massive Quiescent Galaxies at z ˜ 4 from ZFOURGE," , vol. 783, p. L14, Mar. 2014.

[39] K. Glazebrook, C. Schreiber, I. Labbé, T. Nanayakkara, G. G. Kacprzak, P. A. Oesch, C. Papovich, L. R. Spitler, C. M. S. Straatman, K.-V. H. Tran, and T. Yuan, "A massive, quiescent galaxy at a redshift of 3.717," , vol. 544, pp. 71–74, Apr. 2017.

[40] C. Schreiber, K. Glazebrook, T. Nanayakkara, G. G. Kacprzak, I. Labbé, P. Oesch, T. Yuan,

K. V. Tran, C. Papovich, L. Spitler, and C. Straatman, "Near infrared spectroscopy and star-formation histories of $3 \leq z \leq 4$ quiescent galaxies," , vol. 618, p. A85, Oct. 2018.

[41] C. Schreiber, I. Labbé, K. Glazebrook, G. Bekiaris, C. Papovich, T. Costa, D. Elbaz, G. G. Kacprzak, T. Nanayakkara, P. Oesch, M. Pannella, L. Spitler, C. Straatman, K. V. Tran, and T. Wang, "Jekyll & Hyde: quiescence and extreme obscuration in a pair of massive galaxies 1.5 Gyr after the Big Bang," , vol. 611, p. A22, Mar. 2018.

[42] P. Torrey, M. Vogelsberger, F. Marinacci, R. Pakmor, V. Springel, D. Nelson, J. Naiman, A. Pillepich, S. Genel, R. Weinberger, and L. Hernquist, "The evolution of the mass-metallicity relation in IllustrisTNG," *ArXiv e-prints*, Nov. 2017.

[43] F. Matteucci, "Abundance ratios in ellipticals and galaxy formation.," , vol. 288, pp. 57–64, Aug. 1994.

[44] S. C. Trager, S. M. Faber, G. Worthey, and J. J. González, "The Stellar Population Histories of Early-Type Galaxies. II. Controlling Parameters of the Stellar Populations," , vol. 120, pp. 165–188, July 2000.

[45] A. Renzini, "Stellar Population Diagnostics of Elliptical Galaxy Formation," *Annual Review of Astronomy and Astrophysics*, vol. 44, pp. 141–192, Sept. 2006.

[46] P.-F. Wu, A. van der Wel, A. Gallazzi, R. Bezanson, C. Pacifici, C. Straatman, M. Franx, I. Barišić, E. F. Bell, G. B. Brammer, J. Calhau, P. Chauke, J. van Houdt, M. V. Maseda, A. Muzzin, H.-W. Rix, D. Sobral, J. Spilker, J. van de Sande, P. van Dokkum, and V. Wild, "Stellar Populations of over 1000 $z \sim 0.8$ Galaxies from LEGA-C: Ages and Star Formation Histories from D_n4000 and Hδ," , vol. 855, Mar. 2018.

[47] C. A. Tremonti, T. M. Heckman, G. Kauffmann, J. Brinchmann, S. Charlot, S. D. M. White, M. Seibert, E. W. Peng, D. J. Schlegel, A. Uomoto, M. Fukugita, and J. Brinkmann, "The Origin of the Mass-Metallicity Relation: Insights from 53,000 Star- forming Galaxies in the Sloan Digital Sky Survey," , vol. 613, pp. 898–913, Oct. 2004.

[48] D. K. Erb, A. E. Shapley, M. Pettini, C. C. Steidel, N. A. Reddy, and K. L. Adelberger, "The Mass-Metallicity Relation at z> 2," , vol. 644, pp. 813–828, June 2006.

[49] H. J. Zahid, G. I. Dima, R.-P. Kudritzki, L. J. Kewley, M. J. Geller, H. S. Hwang, J. D. Silverman, and D. Kashino, "The Universal Relation of Galactic Chemical Evolution: The Origin of the Mass-Metallicity Relation," , vol. 791, Aug. 2014.

[50] M. Onodera, C. M. Carollo, S. Lilly, A. Renzini, N. Arimoto, P. Capak, E. Daddi, N. Scoville, S. Tacchella, S. Tatehora, and G. Zamorani, "ISM Excitation and Metallicity of Star-forming Galaxies at z 3.3 from Near-IR Spectroscopy," , vol. 822, p. 42, May 2016.

[51] R. L. Sanders, A. E. Shapley, M. Kriek, W. R. Freeman, N. A. Reddy, B. Siana, A. L. Coil, B. Mobasher, R. Davé, I. Shivaei, M. Azadi, S. H. Price, G. Leung, T. Fetherholf, L. de Groot, T. Zick, F. M. Fornasini, and G. Barro, "The MOSDEF survey: a stellar mass-SFR-metallicity relation exists at $z\sim 2.3$," $ArXive - prints, p. arXiv : 1711.00224, Nov.2017.$

[52] D. Thomas, C. Maraston, K. Schawinski, M. Sarzi, and J. Silk, "Environment and self-regulation in galaxy formation," , vol. 404, pp. 1775–1789, June 2010.

[53] C. Conroy, G. J. Graves, and P. G. van Dokkum, "Early-type Galaxy Archeology: Ages, Abundance Ratios, and Effective Temperatures from Full-spectrum Fitting," , vol. 780, Jan. 2014.

[54] D. R. Weisz, A. E. Dolphin, E. D. Skillman, J. Holtzman, K. M. Gilbert, J. J. Dalcanton, and B. F. Williams, "The Star Formation Histories of Local Group Dwarf Galaxies. I. Hubble Space Telescope/Wide Field Planetary Camera 2 Observations," , vol. 789, p. 147, July 2014.

[55] K.-V. H. Tran, M. Franx, G. D. Illingworth, P. van Dokkum, D. D. Kelson, J. P. Blakeslee, and M. Postman, "A Keck Spectroscopic Survey of MS 1054-03 (z = 0.83): Forming the Red Sequence," , vol. 661, pp. 750–767, June 2007.

[56] P. R. M. Eisenhardt, M. Brodwin, A. H. Gonzalez, S. A. Stanford, D. Stern, P. Barmby, M. J. I. Brown, K. Dawson, A. Dey, M. Doi, A. Galametz, B. T. Jannuzi, C. S. Kochanek, J. Meyers, T. Morokuma, and L. A. Moustakas, "Clusters of Galaxies in the First Half of the Universe from the IRAC Shallow Survey," , vol. 684, Sept. 2008.

[57] J. P. Blakeslee, A. Jordán, S. Mei, P. Côté, L. Ferrarese, L. Infante, E. W. Peng, J. L. Tonry, and M. J. West, "The ACS Fornax Cluster Survey. V. Measurement and Recalibration of

Surface Brightness Fluctuations and a Precise Value of the Fornax-Virgo Relative Distance," , vol. 694, pp. 556–572, Mar. 2009.

[58] C. Papovich, I. Momcheva, C. N. A. Willmer, K. D. Finkelstein, S. L. Finkelstein, K.-V. Tran, M. Brodwin, J. S. Dunlop, D. Farrah, S. A. Khan, J. Lotz, P. McCarthy, R. J. McLure, M. Rieke, G. Rudnick, S. Sivanandam, F. Pacaud, and M. Pierre, "A Spitzer-selected Galaxy Cluster at z = 1.62," , vol. 716, pp. 1503–1513, June 2010.

[59] M. Onodera, C. M. Carollo, A. Renzini, M. Cappellari, C. Mancini, N. Arimoto, E. Daddi, R. Gobat, V. Strazzullo, S. Tacchella, and Y. Yamada, "The Ages, Metallicities, and Element Abundance Ratios of Massive Quenched Galaxies at z 1.6," , vol. 808, p. 161, Aug. 2015.

[60] M. Kriek, C. Conroy, P. G. van Dokkum, A. E. Shapley, J. Choi, N. A. Reddy, B. Siana, F. van de Voort, A. L. Coil, and B. Mobasher, "A massive, quiescent, population II galaxy at a redshift of 2.1," , vol. 540, pp. 248–251, Dec 2016.

[61] S. Toft, J. Zabl, J. Richard, A. Gallazzi, S. Zibetti, M. Prescott, C. Grillo, A. W. S. Man, N. Y. Lee, C. Gómez-Guijarro, M. Stockmann, G. Magdis, and C. L. Steinhardt, "A massive, dead disk galaxy in the early Universe," , vol. 546, pp. 510–513, June 2017.

[62] E. Daddi, A. Renzini, N. Pirzkal, A. Cimatti, S. Malhotra, M. Stiavelli, C. Xu, A. Pasquali, J. E. Rhoads, M. Brusa, S. di Serego Alighieri, H. C. Ferguson, A. M. Koekemoer, L. A. Moustakas, N. Panagia, and R. A. Windhorst, "Passively Evolving Early-Type Galaxies at 1.4 < z < 2.5 in the Hubble Ultra Deep Field," , vol. 626, pp. 680–697, June 2005.

[63] P. G. van Dokkum and G. Brammer, "Hubble Space Telescope WFC3 Grism Spectroscopy and Imaging of a Growing Compact Galaxy at z = 1.9," , vol. 718, pp. L73–L77, Aug. 2010.

[64] K. E. Whitaker, M. Franx, J. Leja, P. G. van Dokkum, A. Henry, R. E. Skelton, M. Fumagalli, I. G. Momcheva, G. B. Brammer, I. Labbé, E. J. Nelson, and J. R. Rigby, "Constraining the Low-mass Slope of the Star Formation Sequence at 0.5 < z < 2.5," , vol. 795, p. 104, Nov. 2014.

[65] I. G. Momcheva, G. B. Brammer, P. G. van Dokkum, R. E. Skelton, K. E. Whitaker, E. J. Nelson, M. Fumagalli, M. V. Maseda, J. Leja, M. Franx, H.-W. Rix, R. Bezanson, E. Da

Cunha, C. Dickey, N. M. Förster Schreiber, G. Illingworth, M. Kriek, I. Labbé, J. Ulf Lange, B. F. Lundgren, D. Magee, D. Marchesini, P. Oesch, C. Pacifici, S. G. Patel, S. Price, T. Tal, D. A. Wake, A. van der Wel, and S. Wuyts, "The 3D-HST Survey: Hubble Space Telescope WFC3/G141 Grism Spectra, Redshifts, and Emission Line Measurements for ˜ 100,000 Galaxies," , vol. 225, p. 27, Aug. 2016.

[66] D. B. Lee-Brown, G. H. Rudnick, I. G. Momcheva, C. Papovich, J. M. Lotz, K.-V. H. Tran, B. Henke, C. N. A. Willmer, G. B. Brammer, M. Brodwin, J. Dunlop, and D. Farrah, "The Ages of Passive Galaxies in a z = 1.62 Protocluster," , vol. 844, July 2017.

[67] T. Morishita, L. E. Abramson, T. Treu, X. Wang, G. B. Brammer, P. Kelly, M. Stiavelli, T. Jones, K. B. Schmidt, M. Trenti, and B. Vulcani, "Metal Deficiency in Two Massive Dead Galaxies at z $\sim$ 2," , vol. 856, p. L4, Mar. 2018.

[68] Planck Collaboration, P. A. R. Ade, N. Aghanim, M. Arnaud, M. Ashdown, J. Aumont, C. Baccigalupi, A. J. Banday, R. B. Barreiro, J. G. Bartlett, and et al., "Planck 2015 results. XIII. Cosmological parameters," , vol. 594, p. A13, Sept. 2016.

[69] A. G. Riess, L. M. Macri, S. L. Hoffmann, D. Scolnic, S. Casertano, A. V. Filippenko, B. E. Tucker, M. J. Reid, D. O. Jones, J. M. Silverman, R. Chornock, P. Challis, W. Yuan, P. J. Brown, and R. J. Foley, "A 2.4% Determination of the Local Value of the Hubble Constant," , vol. 826, p. 56, July 2016.

[70] J. B. Oke and J. E. Gunn, "Secondary standard stars for absolute spectrophotometry," , vol. 266, pp. 713–717, Mar. 1983.

[71] N. A. Grogin, D. D. Kocevski, S. M. Faber, H. C. Ferguson, A. M. Koekemoer, A. G. Riess, V. Acquaviva, D. M. Alexander, O. Almaini, M. L. N. Ashby, M. Barden, E. F. Bell, F. Bournaud, T. M. Brown, K. I. Caputi, S. Casertano, P. Cassata, M. Castellano, P. Challis, R.-R. Chary, E. Cheung, M. Cirasuolo, C. J. Conselice, A. Roshan Cooray, D. J. Croton, E. Daddi, T. Dahlen, R. Davé, D. F. de Mello, A. Dekel, M. Dickinson, T. Dolch, J. L. Donley, J. S. Dunlop, A. A. Dutton, D. Elbaz, G. G. Fazio, A. V. Filippenko, S. L. Finkelstein, A. Fontana, J. P. Gardner, P. M. Garnavich, E. Gawiser, M. Giavalisco,

A. Grazian, Y. Guo, N. P. Hathi, B. Häussler, P. F. Hopkins, J.-S. Huang, K.-H. Huang, S. W. Jha, J. S. Kartaltepe, R. P. Kirshner, D. C. Koo, K. Lai, K.-S. Lee, W. Li, J. M. Lotz, R. A. Lucas, P. Madau, P. J. McCarthy, E. J. McGrath, D. H. McIntosh, R. J. McLure, B. Mobasher, L. A. Moustakas, M. Mozena, K. Nandra, J. A. Newman, S.-M. Niemi, K. G. Noeske, C. J. Papovich, L. Pentericci, A. Pope, J. R. Primack, A. Rajan, S. Ravindranath, N. A. Reddy, A. Renzini, H.-W. Rix, A. R. Robaina, S. A. Rodney, D. J. Rosario, P. Rosati, S. Salimbeni, C. Scarlata, B. Siana, L. Simard, J. Smidt, R. S. Somerville, H. Spinrad, A. N. Straughn, L.-G. Strolger, O. Telford, H. I. Teplitz, J. R. Trump, A. van der Wel, C. Villforth, R. H. Wechsler, B. J. Weiner, T. Wiklind, V. Wild, G. Wilson, S. Wuyts, H.-J. Yan, and M. S. Yun, "CANDELS: The Cosmic Assembly Near-infrared Deep Extragalactic Legacy Survey," , vol. 197, p. 35, Dec. 2011.

[72] A. M. Koekemoer, S. M. Faber, H. C. Ferguson, N. A. Grogin, D. D. Kocevski, D. C. Koo, K. Lai, J. M. Lotz, R. A. Lucas, E. J. McGrath, S. Ogaz, A. Rajan, A. G. Riess, S. A. Rodney, L. Strolger, S. Casertano, M. Castellano, T. Dahlen, M. Dickinson, T. Dolch, A. Fontana, M. Giavalisco, A. Grazian, Y. Guo, N. P. Hathi, K.-H. Huang, A. van der Wel, H.-J. Yan, V. Acquaviva, D. M. Alexander, O. Almaini, M. L. N. Ashby, M. Barden, E. F. Bell, F. Bournaud, T. M. Brown, K. I. Caputi, P. Cassata, P. J. Challis, R.-R. Chary, E. Cheung, M. Cirasuolo, C. J. Conselice, A. Roshan Cooray, D. J. Croton, E. Daddi, R. Davé, D. F. de Mello, L. de Ravel, A. Dekel, J. L. Donley, J. S. Dunlop, A. A. Dutton, D. Elbaz, G. G. Fazio, A. V. Filippenko, S. L. Finkelstein, C. Frazer, J. P. Gardner, P. M. Garnavich, E. Gawiser, R. Gruetzbauch, W. G. Hartley, B. Häussler, J. Herrington, P. F. Hopkins, J.-S. Huang, S. W. Jha, A. Johnson, J. S. Kartaltepe, A. A. Khostovan, R. P. Kirshner, C. Lani, K.-S. Lee, W. Li, P. Madau, P. J. McCarthy, D. H. McIntosh, R. J. McLure, C. McPartland, B. Mobasher, H. Moreira, A. Mortlock, L. A. Moustakas, M. Mozena, K. Nandra, J. A. Newman, J. L. Nielsen, S. Niemi, K. G. Noeske, C. J. Papovich, L. Pentericci, A. Pope, J. R. Primack, S. Ravindranath, N. A. Reddy, A. Renzini, H.-W. Rix, A. R. Robaina, D. J. Rosario, P. Rosati, S. Salimbeni, C. Scarlata, B. Siana, L. Simard, J. Smidt, D. Snyder, R. S.

Somerville, H. Spinrad, A. N. Straughn, O. Telford, H. I. Teplitz, J. R. Trump, C. Vargas, C. Villforth, C. R. Wagner, P. Wandro, R. H. Wechsler, B. J. Weiner, T. Wiklind, V. Wild, G. Wilson, S. Wuyts, and M. S. Yun, "CANDELS: The Cosmic Assembly Near-infrared Deep Extragalactic Legacy SurveyThe Hubble Space Telescope Observations, Imaging Data Products, and Mosaics," , vol. 197, p. 36, Dec. 2011.

[73] R. A. Windhorst, S. H. Cohen, N. P. Hathi, P. J. McCarthy, R. E. Ryan, Jr., H. Yan, I. K. Baldry, S. P. Driver, J. A. Frogel, D. T. Hill, L. S. Kelvin, A. M. Koekemoer, M. Mechtley, R. W. O'Connell, A. S. G. Robotham, M. J. Rutkowski, M. Seibert, A. N. Straughn, R. J. Tuffs, B. Balick, H. E. Bond, H. Bushouse, D. Calzetti, M. Crockett, M. J. Disney, M. A. Dopita, D. N. B. Hall, J. A. Holtzman, S. Kaviraj, R. A. Kimble, J. W. MacKenty, M. Mutchler, F. Paresce, A. Saha, J. I. Silk, J. T. Trauger, A. R. Walker, B. C. Whitmore, and E. T. Young, "The Hubble Space Telescope Wide Field Camera 3 Early Release Science Data: Panchromatic Faint Object Counts for 0.2-2 μm Wavelength," , vol. 193, p. 27, Apr. 2011.

[74] E. Bertin and S. Arnouts, "SExtractor: Software for source extraction.," , vol. 117, pp. 393–404, June 1996.

[75] G. B. Brammer, P. G. van Dokkum, and P. Coppi, "EAZY: A Fast, Public Photometric Redshift Code," , vol. 686, pp. 1503–1513, Oct. 2008.

[76] M. Kriek, P. G. van Dokkum, I. Labbé, M. Franx, G. D. Illingworth, D. Marchesini, and R. F. Quadri, "An Ultra-Deep Near-Infrared Spectrum of a Compact Quiescent Galaxy at z = 2.2," , vol. 700, pp. 221–231, July 2009.

[77] G. Chabrier, "Galactic Stellar and Substellar Initial Mass Function," *Publications of the Astronomical Society of the Pacific*, vol. 115, pp. 763–795, July 2003.

[78] Y. Q. Xue, B. Luo, W. N. Brandt, D. M. Alexander, F. E. Bauer, B. D. Lehmer, and G. Yang, "The 2 Ms Chandra Deep Field-North Survey and the 250 ks Extended Chandra Deep Field-South Survey: Improved Point-source Catalogs," , vol. 224, p. 15, June 2016.

[79] B. Luo, W. N. Brandt, Y. Q. Xue, B. Lehmer, D. M. Alexander, F. E. Bauer, F. Vito, G. Yang, A. R. Basu-Zych, A. Comastri, R. Gilli, Q. S. Gu, A. E. Hornschemeier, A. Koekemoer,

T. Liu, V. Mainieri, M. Paolillo, P. Ranalli, P. Rosati, D. P. Schneider, O. Shemmer, I. Smail, M. Sun, P. Tozzi, C. Vignali, and J. X. Wang, "The Chandra Deep Field-South Survey: 7 Ms Source Catalogs," *The Astrophysical Journal Supplement Series*, vol. 228, p. 2, Jan. 2017.

[80] S. Wuyts, I. Labbé, M. Franx, G. Rudnick, P. G. van Dokkum, G. G. Fazio, N. M. Förster Schreiber, J. Huang, A. F. M. Moorwood, H.-W. Rix, H. Röttgering, and P. van der Werf, "What Do We Learn from IRAC Observations of Galaxies at 2 < z < 3.5?," , vol. 655, pp. 51–65, Jan 2007.

[81] K. E. Whitaker, I. Labbé, P. G. van Dokkum, G. Brammer, M. Kriek, D. Marchesini, R. F. Quadri, M. Franx, A. Muzzin, R. J. Williams, R. Bezanson, G. D. Illingworth, K.-S. Lee, B. Lundgren, E. J. Nelson, G. Rudnick, T. Tal, and D. A. Wake, "The NEWFIRM Medium-band Survey: Photometric Catalogs, Redshifts, and the Bimodal Color Distribution of Galaxies out to z ˜ 3," , vol. 735, p. 86, July 2011.

[82] C. Papovich, R. Bassett, J. M. Lotz, A. van der Wel, K.-V. Tran, S. L. Finkelstein, E. F. Bell, C. J. Conselice, A. Dekel, J. S. Dunlop, Y. Guo, S. M. Faber, D. Farrah, H. C. Ferguson, K. D. Finkelstein, B. Häussler, D. D. Kocevski, A. M. Koekemoer, D. C. Koo, E. J. McGrath, R. J. McLure, D. H. McIntosh, I. Momcheva, J. A. Newman, G. Rudnick, B. Weiner, C. N. A. Willmer, and S. Wuyts, "CANDELS Observations of the Structural Properties of Cluster Galaxies at z = 1.62," , vol. 750, p. 93, May 2012.

[83] M. Kriek, P. G. van Dokkum, M. Franx, R. Quadri, E. Gawiser, D. Herrera, G. D. Illingworth, I. Labbé, P. Lira, D. Marchesini, H.-W. Rix, G. Rudnick, E. N. Taylor, S. Toft, C. M. Urry, and S. Wuyts, "Spectroscopic Identification of Massive Galaxies at z ˜ 2.3 with Strongly Suppressed Star Formation," , vol. 649, pp. L71–L74, Oct. 2006.

[84] G. B. Brammer, P. G. van Dokkum, M. Franx, M. Fumagalli, S. Patel, H.-W. Rix, R. E. Skelton, M. Kriek, E. Nelson, K. B. Schmidt, R. Bezanson, E. da Cunha, D. K. Erb, X. Fan, N. Förster Schreiber, G. D. Illingworth, I. Labbé, J. Leja, B. Lundgren, D. Magee, D. Marchesini, P. McCarthy, I. Momcheva, A. Muzzin, R. Quadri, C. C. Steidel, T. Tal, D. Wake, K. E. Whitaker, and A. Williams, "3D-HST: A Wide-field Grism Spectroscopic Survey with the

Hubble Space Telescope," , vol. 200, p. 13, June 2012.

[85] A. N. Straughn, H. Kuntschner, M. Kümmel, J. R. Walsh, S. H. Cohen, J. P. Gardner, R. A. Windhorst, R. W. O'Connell, N. Pirzkal, G. Meurer, P. J. McCarthy, N. P. Hathi, S. Malhotra, J. Rhoads, B. Balick, H. E. Bond, D. Calzetti, M. J. Disney, M. A. Dopita, J. A. Frogel, D. N. B. Hall, J. A. Holtzman, R. A. Kimble, M. Mutchler, F. Paresce, A. Saha, J. I. Silk, J. T. Trauger, A. R. Walker, B. C. Whitmore, E. T. Young, and C. Xu, "Hubble Space Telescope WFC3 Early Release Science: Emission-line Galaxies from Infrared Grism Observations," , vol. 141, p. 14, Jan. 2011.

[86] G. Brammer, N. Pirzkal, P. McCullough, and J. MacKenty, "Time-varying Excess Earth-glow Backgrounds in the WFC3/IR Channel," tech. rep., Apr. 2014.

[87] V. Tilvi, N. Pirzkal, S. Malhotra, S. L. Finkelstein, J. E. Rhoads, R. Windhorst, N. A. Grogin, A. Koekemoer, N. L. Zakamska, R. Ryan, L. Christensen, N. Hathi, J. Pharo, B. Joshi, H. Yang, C. Gronwall, A. Cimatti, J. Walsh, R. O'Connell, A. Straughn, G. Ostlin, B. Rothberg, R. C. Livermore, P. Hibon, and J. P. Gardner, "First Results from the Faint Infrared Grism Survey (FIGS): First Simultaneous Detection of Lyα Emission and Lyman Break from a Galaxy at z = 7.51," , vol. 827, p. L14, Aug. 2016.

[88] J. M. Lotz, A. Koekemoer, D. Coe, N. Grogin, P. Capak, J. Mack, J. Anderson, R. Avila, E. A. Barker, D. Borncamp, G. Brammer, M. Durbin, H. Gunning, B. Hilbert, H. Jenkner, H. Khandrika, Z. Levay, R. A. Lucas, J. MacKenty, S. Ogaz, B. Porterfield, N. Reid, M. Robberto, P. Royle, L. J. Smith, L. J. Storrie-Lombardi, B. Sunnquist, J. Surace, D. C. Taylor, R. Williams, J. Bullock, M. Dickinson, S. Finkelstein, P. Natarajan, J. Richard, B. Robertson, J. Tumlinson, A. Zitrin, K. Flanagan, K. Sembach, B. T. Soifer, and M. Mountain, "The Frontier Fields: Survey Design and Initial Results," , vol. 837, p. 97, Mar. 2017.

[89] J. C. Lee, N. Pirzkal, and B. Hilbert, "Flux Calibration Monitoring: WFC3/IR G102 and G141 Grisms," tech. rep., Jan. 2014.

[90] C. Conroy, J. E. Gunn, and M. White, "The Propagation of Uncertainties in Stellar Population Synthesis Modeling. I. The Relevance of Uncertain Aspects of Stellar Evolution and the

Initial Mass Function to the Derived Physical Properties of Galaxies," , vol. 699, pp. 486–506, July 2009.

[91] C. Conroy and J. E. Gunn, "The Propagation of Uncertainties in Stellar Population Synthesis Modeling. III. Model Calibration, Comparison, and Evaluation," , vol. 712, pp. 833–857, Apr. 2010.

[92] G. Bruzual and S. Charlot, "Stellar population synthesis at the resolution of 2003," , vol. 344, pp. 1000–1028, Oct. 2003.

[93] E. E. Salpeter, "The Luminosity Function and Stellar Evolution.," , vol. 121, p. 161, Jan. 1955.

[94] C. C. Steidel, A. L. Strom, M. Pettini, G. C. Rudie, N. A. Reddy, and R. F. Trainor, "Reconciling the Stellar and Nebular Spectra of High-redshift Galaxies," , vol. 826, p. 159, Aug. 2016.

[95] C. Papovich, S. L. Finkelstein, H. C. Ferguson, J. M. Lotz, and M. Giavalisco, "The rising star formation histories of distant galaxies and implications for gas accretion with time," , vol. 412, pp. 1123–1136, Apr. 2011.

[96] V. Simha, D. H. Weinberg, C. Conroy, R. Dave, M. Fardal, N. Katz, and B. D. Oppenheimer, "Parametrising Star Formation Histories," *ArXiv e-prints*, p. arXiv:1404.0402, Apr. 2014.

[97] C. Pacifici, S. A. Kassin, B. J. Weiner, B. Holden, J. P. Gardner, S. M. Faber, H. C. Ferguson, D. C. Koo, J. R. Primack, E. F. Bell, A. Dekel, E. Gawiser, M. Giavalisco, M. Rafelski, R. C. Simons, G. Barro, D. J. Croton, R. Davé, A. Fontana, N. A. Grogin, A. M. Koekemoer, S.-K. Lee, B. Salmon, R. Somerville, and P. Behroozi, "The Evolution of Star Formation Histories of Quiescent Galaxies," , vol. 832, p. 79, Nov. 2016.

[98] K. Iyer and E. Gawiser, "Reconstruction of Galaxy Star Formation Histories through SED Fitting:The Dense Basis Approach," , vol. 838, p. 127, Apr. 2017.

[99] C. Papovich, M. Dickinson, and H. C. Ferguson, "The Stellar Populations and Evolution of Lyman Break Galaxies," , vol. 559, pp. 620–653, Oct. 2001.

[100] B. Salmon, C. Papovich, S. L. Finkelstein, V. Tilvi, K. Finlator, P. Behroozi, T. Dahlen,

R. Davé, A. Dekel, M. Dickinson, H. C. Ferguson, M. Giavalisco, J. Long, Y. Lu, B. Mobasher, N. Reddy, R. S. Somerville, and R. H. Wechsler, "The Relation between Star Formation Rate and Stellar Mass for Galaxies at 3.5 = z = 6.5 in CANDELS," , vol. 799, p. 183, Feb. 2015.

[101] D. Calzetti, L. Armus, R. C. Bohlin, A. L. Kinney, J. Koornneef, and T. Storchi-Bergmann, "The Dust Content and Opacity of Actively Star-forming Galaxies," , vol. 533, pp. 682–695, Apr. 2000.

[102] A. C. Carnall, R. J. McLure, J. S. Dunlop, and R. Davé, "Inferring the star-formation histories of massive quiescent galaxies with BAGPIPES: Evidence for multiple quenching mechanisms," *ArXiv e-prints*, p. arXiv:1712.04452, Dec. 2017.

[103] J. Bak and T. S. Statler, "The Intrinsic Shape Distribution of a Sample of Elliptical Galaxies," , vol. 120, pp. 110–122, July 2000.

[104] W. S. Cleveland, "Robust locally weighted regression and smoothing scatterplots," *Journal of the American Statistical Association*, vol. 74, no. 368, pp. 829–836, 1979.

[105] Y. Guo, M. Giavalisco, P. Cassata, H. C. Ferguson, C. C. Williams, M. Dickinson, A. Koekemoer, N. A. Grogin, R.-R. Chary, H. Messias, E. Tundo, L. Lin, S.-K. Lee, S. Salimbeni, A. Fontana, A. Grazian, D. Kocevski, K.-S. Lee, E. Villanueva, and A. van der Wel, "Rest-frame UV-Optically Selected Galaxies at 2.3 < z < 3.5: Searching for Dusty Star-forming and Passively Evolving Galaxies," , vol. 749, p. 149, Apr. 2012.

[106] E. Merlin, A. Fontana, M. Castellano, P. Santini, M. Torelli, K. Boutsia, T. Wang, A. Grazian, L. Pentericci, C. Schreiber, L. Ciesla, R. McLure, S. Derriere, J. S. Dunlop, and D. Elbaz, "Chasing passive galaxies in the early Universe: a critical analysis in CANDELS GOODS-South," , vol. 473, pp. 2098–2123, Jan. 2018.

[107] T. Dahlen, L.-G. Strolger, A. G. Riess, S. Mattila, E. Kankare, and B. Mobasher, "The Extended Hubble Space Telescope Supernova Survey: The Rate of Core Collapse Supernovae to z 1," , vol. 757, p. 70, Sept. 2012.

[108] M. Friedmann and D. Maoz, "The rate of Type-Ia supernovae in galaxy clusters and the

delay-time distribution out to redshift 1.75," *ArXiv e-prints*, p. arXiv:1803.04421, Mar. 2018.

[109] B. H. Andrews and P. Martini, "The Mass-Metallicity Relation with the Direct Method on Stacked Spectra of SDSS Galaxies," , vol. 765, p. 140, Mar. 2013.

[110] K.-i. Tadaki, T. Kodama, I. Tanaka, M. Hayashi, Y. Koyama, and R. Shimakawa, "Nature of Hα Selected Galaxies at z > 2. I. Main- sequence and Dusty Star-forming Galaxies," , vol. 778, p. 114, Dec. 2013.

[111] A. L. Muratov, D. Kereš, C.-A. Faucher- Giguère, P. F. Hopkins, E. Quataert, and N. Murray, "Gusty, gaseous flows of FIRE: galactic winds in cosmological simulations with explicit stellar feedback," , vol. 454, pp. 2691–2713, Dec. 2015.

[112] C. R. Christensen, R. Davé, F. Governato, A. Pontzen, A. Brooks, F. Munshi, T. Quinn, and J. Wadsley, "In-N-Out: The Gas Cycle from Dwarfs to Spiral Galaxies," , vol. 824, p. 57, June 2016.

[113] A. van der Wel, H.-W. Rix, S. Wuyts, E. J. McGrath, A. M. Koekemoer, E. F. Bell, B. P. Holden, A. R. Robaina, and D. H. McIntosh, "The Majority of Compact Massive Galaxies at z 2 are Disk Dominated," , vol. 730, p. 38, Mar. 2011.

[114] A. Dekel, R. Sari, and D. Ceverino, "Formation of Massive Galaxies at High Redshift: Cold Streams, Clumpy Disks, and Compact Spheroids," , vol. 703, pp. 785–801, Sept. 2009.

[115] G. Barro, S. M. Faber, P. G. Pérez-González, D. C. Koo, C. C. Williams, D. D. Kocevski, J. R. Trump, M. Mozena, E. McGrath, A. van der Wel, S. Wuyts, E. F. Bell, D. J. Croton, D. Ceverino, A. Dekel, M. L. N. Ashby, E. Cheung, H. C. Ferguson, A. Fontana, J. Fang, M. Giavalisco, N. A. Grogin, Y. Guo, N. P. Hathi, P. F. Hopkins, K.-H. Huang, A. M. Koekemoer, J. S. Kartaltepe, K.-S. Lee, J. A. Newman, L. A. Porter, J. R. Primack, R. E. Ryan, D. Rosario, R. S. Somerville, M. Salvato, and L.-T. Hsu, "CANDELS: The Progenitors of Compact Quiescent Galaxies at z 2," , vol. 765, p. 104, Mar. 2013.

[116] T. A. Thompson, E. Quataert, and N. Murray, "Radiation Pressure-supported Starburst Disks and Active Galactic Nucleus Fueling," , vol. 630, pp. 167–185, Sept. 2005.

[117] S. L. Ellison, D. R. Patton, L. Simard, and A. W. McConnachie, "Clues to the Origin of the

Mass-Metallicity Relation: Dependence on Star Formation Rate and Galaxy Size," , vol. 672, p. L107, Jan. 2008.

[118] A. Zolotov, A. Dekel, N. Mandelker, D. Tweed, S. Inoue, C. DeGraf, D. Ceverino, J. R. Primack, G. Barro, and S. M. Faber, "Compaction and quenching of high-z galaxies in cosmological simulations: blue and red nuggets," , vol. 450, pp. 2327–2353, July 2015.

[119] C. M. Casey, C.-C. Chen, L. L. Cowie, A. J. Barger, P. Capak, O. Ilbert, M. Koss, N. Lee, E. Le Floc'h, D. B. Sanders, and J. P. Williams, "Characterization of SCUBA-2 450 μm and 850 μm selected galaxies in the COSMOS field," , vol. 436, pp. 1919–1954, Dec. 2013.

[120] J. S. Spilker, D. P. Marrone, J. E. Aguirre, M. Aravena, M. L. N. Ashby, M. Béthermin, C. M. Bradford, M. S. Bothwell, M. Brodwin, J. E. Carlstrom, S. C. Chapman, T. M. Crawford, C. de Breuck, C. D. Fassnacht, A. H. Gonzalez, T. R. Greve, B. Gullberg, Y. Hezaveh, W. L. Holzapfel, K. Husband, J. Ma, M. Malkan, E. J. Murphy, C. L. Reichardt, K. M. Rotermund, B. Stalder, A. A. Stark, M. Strandet, J. D. Vieira, A. Weiß, and N. Welikala, "The Rest-frame Submillimeter Spectrum of High-redshift, Dusty, Star- forming Galaxies," , vol. 785, p. 149, Apr. 2014.

[121] S. Toft, V. Smolčić, B. Magnelli, A. Karim, A. Zirm, M. Michalowski, P. Capak, K. Sheth, K. Schawinski, J. K. Krogager, S. Wuyts, D. Sanders, A. W. S. Man, D. Lutz, J. Staguhn, S. Berta, H. Mccracken, J. Krpan, and D. Riechers, "Submillimeter Galaxies as Progenitors of Compact Quiescent Galaxies," , vol. 782, p. 68, Feb. 2014.

[122] J. M. Simpson, I. Smail, A. M. Swinbank, O. Almaini, A. W. Blain, M. N. Bremer, S. C. Chapman, C.-C. Chen, C. Conselice, K. E. K. Coppin, A. L. R. Danielson, J. S. Dunlop, A. C. Edge, D. Farrah, J. E. Geach, W. G. Hartley, R. J. Ivison, A. Karim, C. Lani, C. J. Ma, R. Meijerink, M. J. Michałowski, A. Mortlock, D. Scott, C. J. Simpson, M. Spaans, A. P. Thomson, E. van Kampen, and P. P. van der Werf, "The SCUBA-2 Cosmology Legacy Survey: ALMA Resolves the Rest-frame Far- infrared Emission of Sub-millimeter Galaxies," , vol. 799, p. 81, Jan. 2015.

[123] K.-i. Tadaki, K. Kohno, T. Kodama, S. Ikarashi, I. Aretxaga, S. Berta, K. I. Caputi, J. S.

Dunlop, B. Hatsukade, M. Hayashi, D. H. Hughes, R. Ivison, T. Izumi, Y. Koyama, D. Lutz, R. Makiya, Y. Matsuda, K. Nakanishi, W. Rujopakarn, Y. Tamura, H. Umehata, W.-H. Wang, G. W. Wilson, S. Wuyts, Y. Yamaguchi, and M. S. Yun, "SXDF-ALMA 1.5 arcmin² Deep Survey: A Compact Dusty Star- forming Galaxy at z = 2.5," , vol. 811, p. L3, Sept. 2015.

[124] A. Man and S. Belli, "Star formation quenching in massive galaxies," *Nature Astronomy*, vol. 2, pp. 695–697, Sep 2018.

[125] S. Wellons, P. Torrey, C.-P. Ma, V. Rodriguez-Gomez, M. Vogelsberger, M. Kriek, P. van Dokkum, E. Nelson, S. Genel, A. Pillepich, V. Springel, D. Sijacki, G. Snyder, D. Nelson, L. Sales, and L. Hernquist, "The formation of massive, compact galaxies at z = 2 in the Illustris simulation," , vol. 449, pp. 361–372, May 2015.

[126] S. Belli, A. B. Newman, and R. S. Ellis, "MOSFIRE Spectroscopy of Quiescent Galaxies at 1.5 < z < 2.5. II. Star Formation Histories and Galaxy Quenching," , vol. 874, p. 17, Mar 2019.

[127] C. Papovich, I. Labbé, R. Quadri, V. Tilvi, P. Behroozi, E. F. Bell, K. Glazebrook, L. Spitler, C. M. S. Straatman, K.-V. Tran, M. Cowley, R. Davé, A. Dekel, M. Dickinson, H. C. Ferguson, S. L. Finkelstein, E. Gawiser, H. Inami, S. M. Faber, G. G. Kacprzak, L. Kawinwanichakij, D. Kocevski, A. Koekemoer, D. C. Koo, P. Kurczynski, J. M. Lotz, Y. Lu, R. A. Lucas, D. McIntosh, N. Mehrtens, B. Mobasher, A. Monson, G. Morrison, T. Nanayakkara, S. E. Persson, B. Salmon, R. Simons, A. Tomczak, P. van Dokkum, B. Weiner, and S. P. Willner, "ZFOURGE/CANDELS: On the Evolution of M* Galaxy Progenitors from z = 3 to 0.5," , vol. 803, p. 26, Apr. 2015.

[128] G. Barro, S. M. Faber, D. C. Koo, A. Dekel, J. J. Fang, J. R. Trump, P. G. Pérez-González, C. Pacifici, J. R. Primack, R. S. Somerville, H. Yan, Y. Guo, F. Liu, D. Ceverino, D. D. Kocevski, and E. McGrath, "Structural and Star-forming Relations since z 3: Connecting Compact Star-forming and Quiescent Galaxies," , vol. 840, p. 47, May 2017.

[129] E. Daddi, D. Elbaz, F. Walter, F. Bournaud, F. Salmi, C. Carilli, H. Dannerbauer, M. Dickin-

son, P. Monaco, and D. Riechers, "Different Star Formation Laws for Disks Versus Starbursts at Low and High Redshifts," , vol. 714, pp. L118–L122, May 2010.

[130] S. J. Lilly and C. M. Carollo, "Surface Density Effects in Quenching: Cause or Effect?," , vol. 833, p. 1, Dec 2016.

[131] N. Pirzkal, S. Malhotra, R. E. Ryan, B. Rothberg, N. Grogin, S. L. Finkelstein, A. M. Koekemoer, J. Rhoads, R. L. Larson, L. Christensen, A. Cimatti, I. Ferreras, J. P. Gardner, C. Gronwall, N. P. Hathi, P. Hibon, B. Joshi, H. Kuntschner, G. R. Meurer, R. W. O'Connell, G. Oestlin, A. Pasquali, J. Pharo, A. N. Straughn, J. R. Walsh, D. Watson, R. A. Windhorst, N. L. Zakamska, and A. Zirm, "FIGS—Faint Infrared Grism Survey: Description and Data Reduction," , vol. 846, p. 84, Sep 2017.

[132] B. Magnelli, D. Elbaz, R. R. Chary, M. Dickinson, D. Le Borgne, D. T. Frayer, and C. N. A. Willmer, "Evolution of the dusty infrared luminosity function from z = 0 to z = 2.3 using observations from Spitzer," , vol. 528, Apr. 2011.

[133] T. Dahlen, B. Mobasher, S. M. Faber, H. C. Ferguson, G. Barro, S. L. Finkelstein, K. Finlator, A. Fontana, R. Gruetzbauch, S. Johnson, J. Pforr, M. Salvato, T. Wiklind, S. Wuyts, V. Acquaviva, M. E. Dickinson, Y. Guo, J. Huang, K.-H. Huang, J. A. Newman, E. F. Bell, C. J. Conselice, A. Galametz, E. Gawiser, M. Giavalisco, N. A. Grogin, N. Hathi, D. Kocevski, A. M. Koekemoer, D. C. Koo, K.-S. Lee, E. J. McGrath, C. Papovich, M. Peth, R. Ryan, R. Somerville, B. Weiner, and G. Wilson, "A Critical Assessment of Photometric Redshift Methods: A CANDELS Investigation," , vol. 775, p. 93, Oct. 2013.

[134] C. M. S. Straatman, L. R. Spitler, R. F. Quadri, I. Labbé, K. Glazebrook, S. E. Persson, C. Papovich, K.-V. H. Tran, G. B. Brammer, M. Cowley, A. Tomczak, T. Nanayakkara, L. Alcorn, R. Allen, A. Broussard, P. van Dokkum, B. Forrest, J. van Houdt, G. G. Kacprzak, L. Kawinwanichakij, D. D. Kelson, J. Lee, P. J. McCarthy, N. Mehrtens, A. Monson, D. Murphy, G. Rees, V. Tilvi, and K. E. Whitaker, "The FourStar Galaxy Evolution Survey (ZFOURGE): Ultraviolet to Far-infrared Catalogs, Medium-bandwidth Photometric Redshifts with Improved Accuracy, Stellar Masses, and Confirmation of Quiescent Galaxies to z 3.5," ,

vol. 830, p. 51, Oct. 2016.

[135] C. Y. Peng, L. C. Ho, C. D. Impey, and H.-W. Rix, "Detailed Structural Decomposition of Galaxy Images," , vol. 124, pp. 266–293, Jul 2002.

[136] M. Fumagalli, I. Labbé, S. G. Patel, M. Franx, P. van Dokkum, G. Brammer, E. da Cunha, N. M. Förster Schreiber, M. Kriek, R. Quadri, H.-W. Rix, D. Wake, K. E. Whitaker, B. Lundgren, D. Marchesini, M. Maseda, I. Momcheva, E. Nelson, C. Pacifici, and R. E. Skelton, "How Dead are Dead Galaxies? Mid-infrared Fluxes of Quiescent Galaxies at Redshift 0.3 < z < 2.5: Implications for Star Formation Rates and Dust Heating," , vol. 796, p. 35, Nov. 2014.

[137] P. Santini, A. Fontana, M. Castellano, M. Di Criscienzo, E. Merlin, R. Amorin, F. Cullen, E. Daddi, M. Dickinson, J. S. Dunlop, A. Grazian, A. Lamastra, R. J. McLure, M. J. Michałowski, L. Pentericci, and X. Shu, "The Star Formation Main Sequence in the Hubble Space Telescope Frontier Fields," , vol. 847, p. 76, Sept. 2017.

[138] P. Kroupa, "On the variation of the initial mass function," , vol. 322, pp. 231–246, Apr. 2001.

[139] J. S. Speagle, "dynesty: A Dynamic Nested Sampling Package for Estimating Bayesian Posteriors and Evidences," *arXiv e-prints*, p. arXiv:1904.02180, Apr 2019.

[140] A. C. Carnall, R. J. McLure, J. S. Dunlop, F. Cullen, D. J. McLeod, V. Wild, B. D. Johnson, S. Appleby, R. Davé, R. Amorin, M. Bolzonella, M. Castellano, A. Cimatti, O. Cucciati, A. Gargiulo, B. Garilli, F. Marchi, L. Pentericci, L. Pozzetti, C. Schreiber, M. Talia, and G. Zamorani, "The VANDELS survey: the star-formation histories of massive quiescent galaxies at 1.0 < z < 1.3," , vol. 490, pp. 417–439, Nov 2019.

[141] J. Leja, A. C. Carnall, B. D. Johnson, C. Conroy, and J. S. Speagle, "How to Measure Galaxy Star Formation Histories. II. Nonparametric Models," , vol. 876, p. 3, May 2019.

[142] J. A. Cardelli, G. C. Clayton, and J. S. Mathis, "The Relationship between Infrared, Optical, and Ultraviolet Extinction," , vol. 345, p. 245, Oct 1989.

[143] J. J. Fang, S. M. Faber, D. C. Koo, and A. Dekel, "A Link between Star Formation Quenching and Inner Stellar Mass Density in Sloan Digital Sky Survey Central Galaxies," , vol. 776,

p. 63, Oct 2013.

[144] B. Lee, M. Giavalisco, K. Whitaker, C. C. Williams, H. C. Ferguson, V. Acquaviva, A. M. Koekemoer, A. N. Straughn, Y. Guo, J. S. Kartaltepe, J. Lotz, C. Pacifici, D. J. Croton, R. S. Somerville, and Y. Lu, "The Intrinsic Characteristics of Galaxies on the SFR-M $_*$ Plane at 1.2 < z < 4: I. The Correlation between Stellar Age, Central Density, and Position Relative to the Main Sequence," , vol. 853, p. 131, Feb 2018.

[145] D. Szomoru, M. Franx, P. G. van Dokkum, M. Trenti, G. D. Illingworth, I. Labbé, and P. Oesch, "The Stellar Mass Structure of Massive Galaxies from z = 0 to z = 2.5: Surface Density Profiles and Half-mass Radii," , vol. 763, p. 73, Feb 2013.

[146] K. A. Suess, M. Kriek, S. H. Price, and G. Barro, "Half-mass Radii of Quiescent and Star-forming Galaxies Evolve Slowly from 0 $z \leq 2.5$: Implications for Galaxy Assembly Histories," , vol. 885, p. L22, Nov 2019.

[147] S. Tacchella, C. M. Carollo, S. M. Faber, A. Cibinel, A. Dekel, D. C. Koo, A. Renzini, and J. Woo, "On the Evolution of the Central Density of Quiescent Galaxies," , vol. 844, p. L1, July 2017.

[148] C. C. Williams, M. Giavalisco, R. Bezanson, N. Cappelluti, P. Cassata, T. Liu, B. Lee, E. Tundo, and E. Vanzella, "Morphology Dependence of Stellar Age in Quenched Galaxies at Redshift

1.2: Massive Compact Galaxies Are Older than More Extended Ones," , vol. 838, p. 94, Apr. 2017.

[149] J. P. Nogueira-Cavalcante, T. S. Gonçalves, K. Menéndez-Delmestre, I. G. de la Rosa, and A. Charbonnier, "Compact Galaxies at intermediate redshifts quench faster than normal-sized Galaxies," , vol. 484, pp. 3022–3035, Apr 2019.

[150] Z. C. Marsan, D. Marchesini, G. B. Brammer, M. Stefanon, A. Muzzin, A. Fernández-Soto, S. Geier, K. N. Hainline, H. Intema, A. Karim, I. Labbé, S. Toft, and P. G. van Dokkum, "Spectroscopic Confirmation of an Ultra Massive and Compact Galaxy at z = 3.35: a Detailed Look at an Early Progenitor of Local Giant Ellipticals," , vol. 801, p. 133, Mar. 2015.

[151] M. Tanaka, F. Valentino, S. Toft, M. Onodera, R. Shimakawa, D. Ceverino, A. L. Faisst, A. Gallazzi, C. Gómez-Guijarro, M. Kubo, G. E. Magdis, C. L. Steinhardt, M. Stockmann, K. Yabe, and J. Zabl, "Stellar Velocity Dispersion of a Massive Quenching Galaxy at z = 4.01," , vol. 885, p. L34, Nov. 2019.

[152] B. Forrest, M. Annunziatella, G. Wilson, D. Marchesini, A. Muzzin, M. C. Cooper, Z. C. Marsan, I. McConachie, J. C. C. Chan, P. Gomez, E. Kado-Fong, F. La Barbera, I. Labbé, D. Lange-Vagle, J. Nantais, M. Nonino, T. Peña, P. Saracco, M. Stefanon, and R. F. J. van der Burg, "An Extremely Massive Quiescent Galaxy at $z = 3.493$: Evidence of Insufficiently Rapid Quenching Mechanisms in Theoretical Models," *arXiv e-prints*, p. arXiv:1910.10158, Oct 2019.

[153] F. Valentino, M. Tanaka, I. Davidzon, S. Toft, C. Gómez-Guijarro, M. Stockmann, M. Onodera, G. Brammer, D. Ceverino, A. L. Faisst, A. Gallazzi, C. C. Hayward, O. Ilbert, M. Kubo, G. E. Magdis, J. Selsing, R. Shimakawa, M. Sparre, C. Steinhardt, K. Yabe, and J. Zabl, "Quiescent Galaxies 1.5 Billion Years after the Big Bang and Their Progenitors," , vol. 889, p. 93, Feb. 2020.

[154] C. M. S. Straatman, I. Labbé, L. R. Spitler, K. Glazebrook, A. Tomczak, R. Allen, G. B. Brammer, M. Cowley, P. van Dokkum, G. G. Kacprzak, L. Kawinwanichakij, N. Mehrtens, T. Nanayakkara, C. Papovich, S. E. Persson, R. F. Quadri, G. Rees, V. Tilvi, K.-V. H. Tran, and K. E. Whitaker, "The Sizes of Massive Quiescent and Star-forming Galaxies at z 4 with ZFOURGE and CANDELS," , vol. 808, p. L29, Jul 2015.

[155] T. Morishita, L. E. Abramson, T. Treu, G. B. Brammer, T. Jones, P. Kelly, M. Stiavelli, M. Trenti, B. Vulcani, and X. Wang, "Massive Dead Galaxies at z 2 with HST Grism Spectroscopy. I. Star Formation Histories and Metallicity Enrichment," , vol. 877, p. 141, Jun 2019.

[156] R. Bezanson, P. G. van Dokkum, T. Tal, D. Marchesini, M. Kriek, M. Franx, and P. Coppi, "The Relation Between Compact, Quiescent High-redshift Galaxies and Massive Nearby Elliptical Galaxies: Evidence for Hierarchical, Inside-Out Growth," , vol. 697, pp. 1290–1298,

Jun 2009.

[157] P. G. van Dokkum, M. Franx, D. Fabricant, D. D. Kelson, and G. D. Illingworth, "A High Merger Fraction in the Rich Cluster MS 1054-03 at Z = 0.83: Direct Evidence for Hierarchical Formation of Massive Galaxies," , vol. 520, pp. L95–L98, Aug. 1999.

[158] V. Estrada-Carpenter, C. Papovich, I. Momcheva, G. Brammer, R. Simons, J. Bridge, N. J. Cleri, H. Ferguson, S. L. Finkelstein, M. Giavalisco, I. Jung, J. Matharu, J. R. Trump, and B. Weiner, "CLEAR. II. Evidence for Early Formation of the Most Compact Quiescent Galaxies at High Redshift," , vol. 898, p. 171, Aug. 2020.

[159] K. A. Suess, M. Kriek, S. H. Price, and G. Barro, "Color Gradients along the Quiescent Galaxy Sequence: Clues to Quenching and Structural Growth," , vol. 899, p. L26, Aug. 2020.

[160] O. I. Wong, K. Schawinski, S. Kaviraj, K. L. Masters, R. C. Nichol, C. Lintott, W. C. Keel, D. Darg, S. P. Bamford, D. Andreescu, P. Murray, M. J. Raddick, A. Szalay, D. Thomas, and J. Vandenberg, "Galaxy Zoo: building the low-mass end of the red sequence with local post-starburst galaxies," , vol. 420, pp. 1684–1692, Feb. 2012.

[161] H.-Y. Jian, L. Lin, Y. Koyama, I. Tanaka, K. Umetsu, B.-C. Hsieh, Y. Higuchi, M. Oguri, S. More, Y. Komiyama, T. Kodama, A. J. Nishizawa, and Y.-Y. Chang, "Redshift Evolution of Green Valley Galaxies in Different Environments from the Hyper Suprime-Cam Survey," , vol. 894, p. 125, May 2020.

[162] R. Feldmann, "Are star formation rates of galaxies bimodal?," , vol. 470, pp. L59–L63, Sept. 2017.

[163] K. A. Suess, M. Kriek, S. H. Price, and G. Barro, "Dissecting the size-mass and Σ_1-mass relations at $1.0 < z < 2.5$: galaxy mass profiles and color gradients as a function of spectral shape," *arXiv e-prints*, p. arXiv:2101.05820, Jan. 2021.

[164] B. Salmon, C. Papovich, J. Long, S. P. Willner, S. L. Finkelstein, H. C. Ferguson, M. Dickinson, K. Duncan, S. M. Faber, N. Hathi, A. Koekemoer, P. Kurczynski, J. Newman, C. Pacifici, P. G. Pérez-González, and J. Pforr, "Breaking the Curve with CANDELS: A Bayesian Approach to Reveal the Non-Universality of the Dust-Attenuation Law at High Redshift," ,

vol. 827, p. 20, Aug. 2016.

[165] H. Jeffreys *Journal of the Royal Statistical Society*, vol. 98, no. 39, p. 39, 1935.

[166] R. E. Kass and A. E. Raftery, "Bayes factors," *Journal of the American Statistical Association*, vol. 90, no. 430, pp. 773–795, 1995.

APPENDIX A

A.1 Bayesian Evidence Between the Stellar Population Models

A.2 Results of fitting stellar population models to all sample galaxies

In this appendix we show the spectra for each galaxy along with the model fit from our analysis. In Figure A.1 and A.2 we show the 1D G102 grism data for all the galaxies in our sample. The red line in each figure shows the “median" model fit, the stellar population model with parameter values equal to the median values in Table 2.3. For each galaxy, the figures also show the joint posterior on the (light-weighted) age and metallicity from the stellar population model fitting.

A.3 Template Error Function

To calculate our template error function we first find the best-fit model to the data for each galaxy (see Section 2.4.2). We then calculate a likelihood, $\mathcal{L}$, of the form

$$\mathcal{L} \propto \frac{1}{\sqrt{2\pi}s} \exp\left(-x^2/(2s^2)\right) \tag{A.1}$$

where $x = F_\lambda - M$ the difference between the data and model, and $s = \sqrt{\sigma_{F_\lambda}^2 + (E(\lambda)F_\lambda)^2}$ is the sum (in quadrature) of the errors on the data (σ_{F_λ}) and the “template error function”, $E(\lambda)$. We then take $d\mathcal{L}/dE(\lambda) = 0$, and solve to find

$$E(\lambda) = \sqrt{\left(\frac{F_\lambda - M}{F_\lambda}\right)^2 - \left(\frac{\sigma_{F_\lambda}}{F_\lambda}\right)^2} \tag{A.2}$$

where the first term is the normalized residuals and the second term is the normalized error. We then follow the steps outlined in (75) to derive $E(\lambda)$.

The top panel in Figure A.3 shows the distribution of $(F_\lambda - M)$ / F_λ for all of our spectra. The bottom panel shows absolute median of this distribution as a function of wavelength, and shows

the contributions from photometric uncertainties, and the error function, $E(\lambda)$. For wavelengths longward of 3500 Å, there is only a small template error function ($\approx$5%). At shorter wavelengths, below $\sim$3500 Å, the template error function increases to as high as 30%, and may result of model uncertainties in the rest-frame UV. We include this error function in our fits, but in practice this has little effect on our results (as the data for rest-frame 3500 Å typically have lower S/N, so contribute little to the probably density).

A.4 Bayesian Evidence Between the Stellar Population Models

In this study we performed model fits using two sets of composite stellar population synthesis models, those from FSPS and BC03 (see Section 2.4.1). In our analysis we favored results from FSPS, for the reason that it better fits the rest-frame wavelength region probed by the G102 data for our sample, approximately, $3000 < \lambda_{\rm rest}/\text{Å} < 5800$. Similar results are found by Fum16 for quiescent galaxies at different redshifts with similar rest-frame wavelength coverage. Here, we use Bayesian evidence to support our use of the FSPS models in our conclusions.

We followed the description of the model selection process describe in (164, see also Kass & Raftery 1995). We used the results from the fit of each set of models (BC03 and FSPS) to each galaxy in our sample using the same range of age and SFH parameters. For FSPS we use the same metallicity griding we use in our fitting, while for BC03 we use several of the metallicities made available (Z =[0.02, 0.2, 0.4, 1.0, 2.5] $Z_{\odot}$) . To compare the models, we consider all parameters, Θ, as nuisance parameters. Marginalizing over the full parameter space includes probability contributions from all possible combinations of parameters for a given model, and the ratio of these then contains information about the relative probability for one model compared to the other. We may use this to derive the "odds" that favor one model over the other using the ratio of the model posteriors:

$$\frac{P(m_1|D)}{P(m_2|D)} = \frac{P(D|m_1)}{P(D|m_2)} \times \frac{P(m_1)}{P(m_2)} \tag{A.3}$$

for the different stellar population models, m_1 and m_2, where m_i is the i-th model (e.g., 1=FSPS, 2=BC03). In Equation A.3, the term on the left-hand side is the ratio of posteriors ("Posterior

Odds"). On the right-hand side, the last term is the ratio of priors ("Prior Odds"), and the first term is the so-called "Bayes Factor" (e.g., 165; 166), defined as

$$\text{Bayes Factor} \equiv B_{12} = \frac{P(D|m_1)}{P(D|m_2)}, \tag{A.4}$$

where the values $P(D|m_{1,2})$ are the normalizations of the posteriors for each model, derived by marginalizing the posteriors over the full set of parameters,

$$P(D|m_{1,2}) = \int_{\Theta} P(D|\Theta, m_{1,2})\ P(\Theta|m_{1,2})\ d\Theta. \tag{A.5}$$

Conceptually, the Bayes factor is the ratio of the normalizations of the posteriors. A model that produces an overall better fit (over the full range of parameters, Θ) will yield a higher normalization, and the ratio of these normalizations then indicates whether one model generally fits the data better, and is thus favored.

We quantified this using the definition of the Bayes-factor evidence (ζ) (166), which is related to the Bayes factor by, $\zeta_j = 2 \ln B_{12,j}$. Here the subscript j corresponds to each galaxy in our sample. We then sum over all ζ_j to measure the significance of the Bayes factor evidence. If both models ($m_{1,2}$) fit the data equally well then $\Sigma\zeta_j = 0$. A positive sum of the Bayes factor evidence ($\Sigma\zeta > 0$) shows evidence in favor of model 1 (m_1), while a negative sum of the Bayes factor evidence ($\Sigma\zeta < 0$) shows evidence towards model 2 (m_2). (166) provide significance statements based on value of the Bayes factor evidence, which we adopt here.

We computed the Bayes factor for the FSPS and BC03 models for each galaxy in our sample, and then derived the overall Bayes factor evidence (the distribution of values are shown in Figure A.4). Summing over ζ_j for all j galaxies, we derived $\Sigma\ \zeta = 164$. This corresponds to "very strong" evidence (defined as $\Sigma\ \zeta > 10$) against BC03 in favor of FSPS for the galaxies in our sample. We note that the grid of FSPS models is much finer in metallicity than BC03, and this could be a driving factor. We therefore recomputed the Bayes factor evidence using a set of FSPS models with the same metallicity griding as for BC03. In this case we derive $\zeta = 96$, which is still "very

strong" evidence for FSPS compared to BC03, and argues that for the galaxies in our sample the FSPS models provide a better overall fit to the data. For these reasons we adopt the FSPS for the conclusions in this study.

A.5 Testing the "Stack–Smooth–Iterate" Method to Combine Parameter Likelihoods

Here we test the stacking method described in Section 2.5.2 to see how well it reproduces a known true parent distribution. This process is illustrated in Figure A.5. The test is done as follows: (1) We take a parent (Gaussian) distribution (shown in the first panel of Figure A.5). (2) We randomly draw from it several data points (here we use 12 samplings to approximate a sample size similar to what we have in our redshift subgroup) with random errors (this is similar to a situation where some galaxies constrain their parameters better than others): this is illustrated in the middle panel of Figure A.5. (3) Then we iteratively stack our sample posteriors to recover an approximation of the parent distribution following the method of Section 2.5.2. This is illustrated in the right panel of Figure A.5. In that panel, the blue curve shows the recovered distribution after performing the weighted summation (the first step in the stacking process, which is identical to a weighted stack of the likelihoods). After the first step, the weighted distribution contains sharp peaks from objects with highly constrained likelihood functions. If these sharp peaks are not removed the iteration process will tend to follow the peaks, and the final product will be highly skewed. The red curve shown in panel 3 is the final product of the iterative stacking process. This included 20 iterations, although even a few iterations ($\sim$5) produce a good approximation of the correct distribution (and subsequent iterations approach an estimation of the truth distribution asymptotically). With a fixed sample size, n=12 in this case, the algorithm may converge to some estimate, but this will not be the true distribution. Convergence to the true distribution is only expected as the sample size gets larger.

One of the limitations of the stacking process described above is that it can fail in cases where the parameter space does not fully encompass the parent distribution (90% of the probability). When this occurs much of the probability mass will lie at the edge of the parameter space, and when the iterative stacking is applied the resulting distribution is driven to the edge (as seen in panel 3 of Figure A.6). In order to resolve this we extend the parameter space artificially during the

stacking process. This allows the distribution to fold over during the stacking process, preventing the distribution from sticking to the edge. This extended-iterative stack better reproduces the median value (though it often underestimates the confidence intervals).

Figure A.7 shows the outcome of this "stack-smooth-iterate" process applied to our data for the galaxies in our sample. Here we see the differences between the weighted sum and iterated stack. There is a very slight shift in the median, $\sim 5\%$ for metallicity and $\sim 1\%$ for light-weighted age. The 68% confidence ranges are slightly tighter by $\sim 40\%$ for metallicity and $\sim 10\%$ for light-weighted age. The reason that the iterated distribution is "tighter" is that the presence of sharply peaked likelihoods from individual galaxies are smoothed in successive iterations as the method converges. We apply this method to all the galaxies in each of our redshift groups (, , ,) to derive probability density functions parameters for each population.

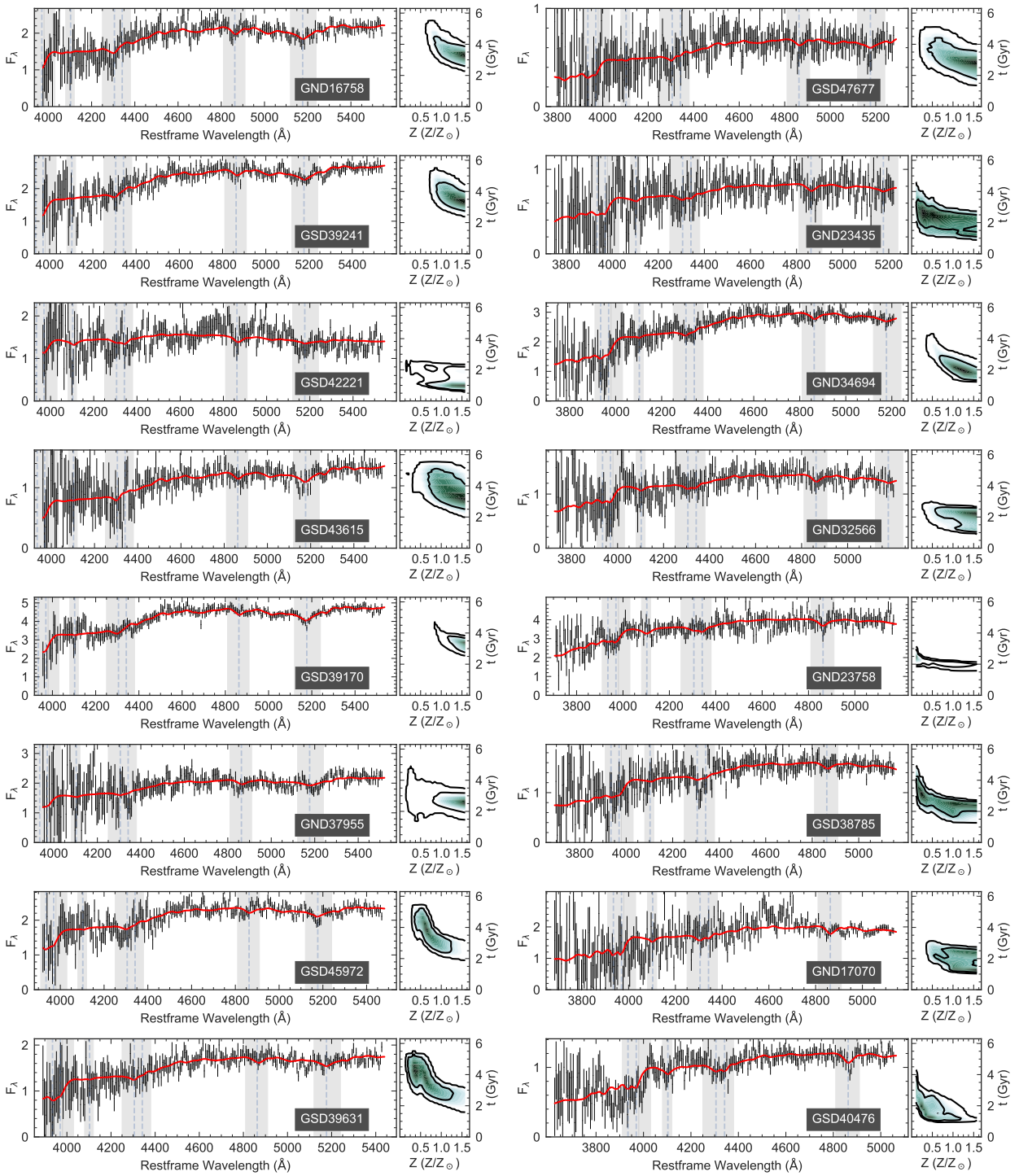

Figure A.1: The data and model fits for the first 16 of the 31 galaxies in our sample. In the left hand panel of each subplot, the gray data points show the measured spectra (and uncertainties). The red lines show the model fits using median values for the parameters. The shaded regions correspond to the metallicity–age spectral features. The right hand panel of each subplot shows the metallicity and (light-weighted) age joint likelihoods. The legend shows the galaxy ID, and Table 2.3 gives the derived values for each model parameter for each galaxy.

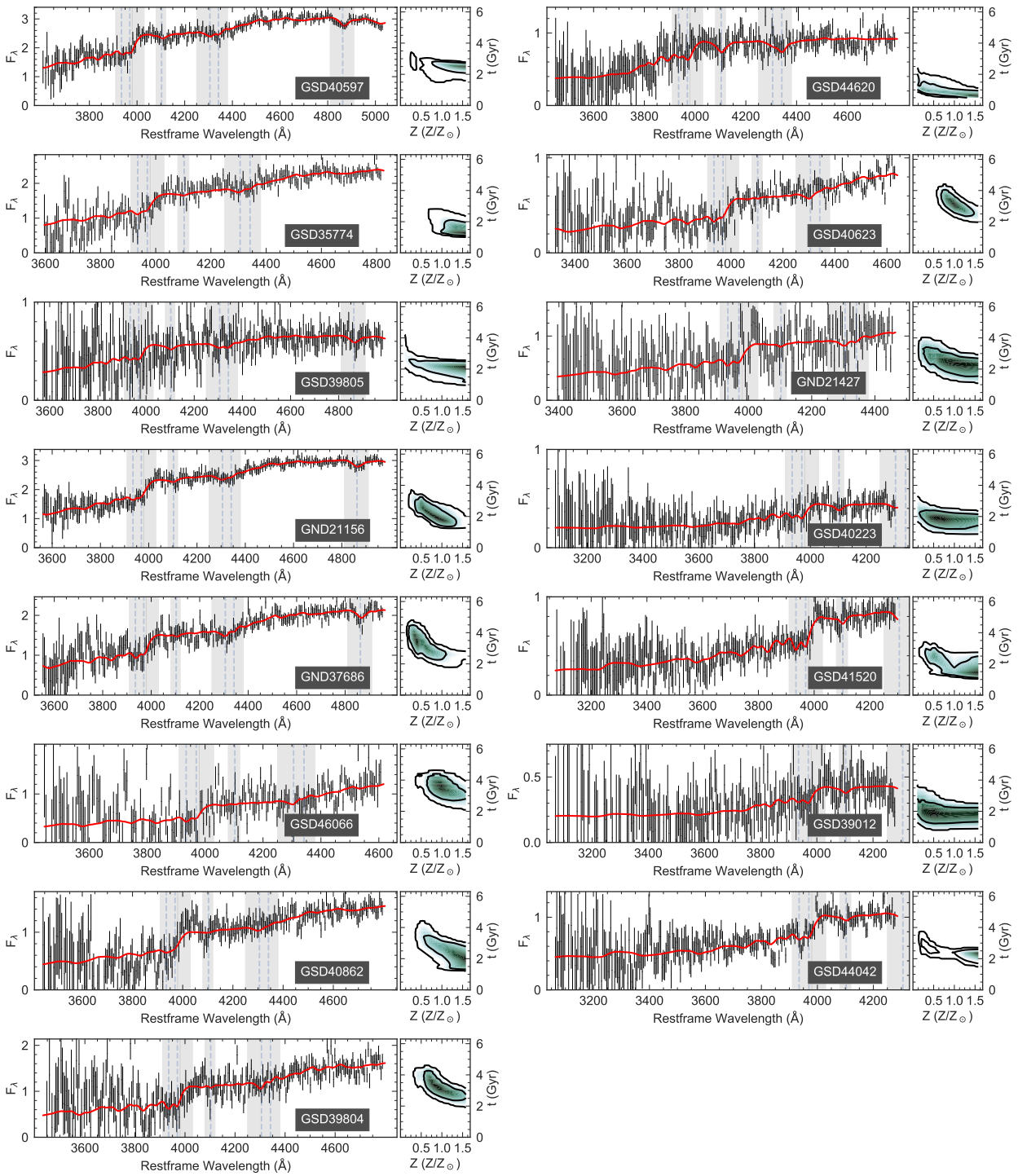

Figure A.2: Same as Figure A.1 showing the remaining 15 of 31 galaxies in our dataset.

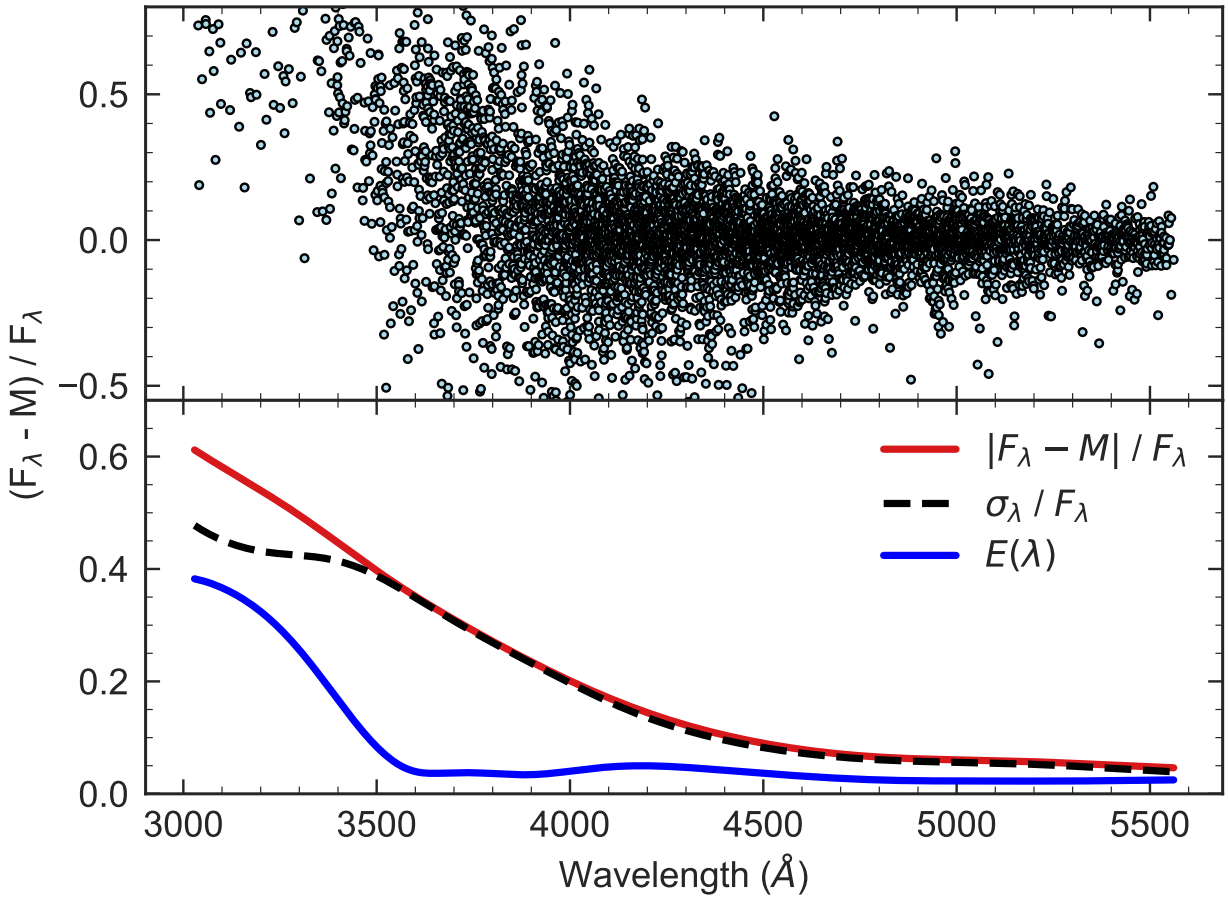

Figure A.3: Distribution of the normalized residuals and the template error function. The top panel shows $((F_\lambda - M) \,/\, F_\lambda)$ as a function of wavelength for all galaxies in the rest-frame, where F_λ are the observed data (e.g., the G102 spectra) for each galaxy, M is the best-fit model for each galaxy. The bottom panel shows the smoothed absolute normalized residuals (red, solid line; derived from the data in the top plot) along with the smoothed relative error ($(\sigma_\lambda \,/\, F_\lambda)$, black dashed line, where σ_λ are the measured uncertainties on the data) and the derived template error function ($E(\lambda)$, blue solid line) as described in the text.

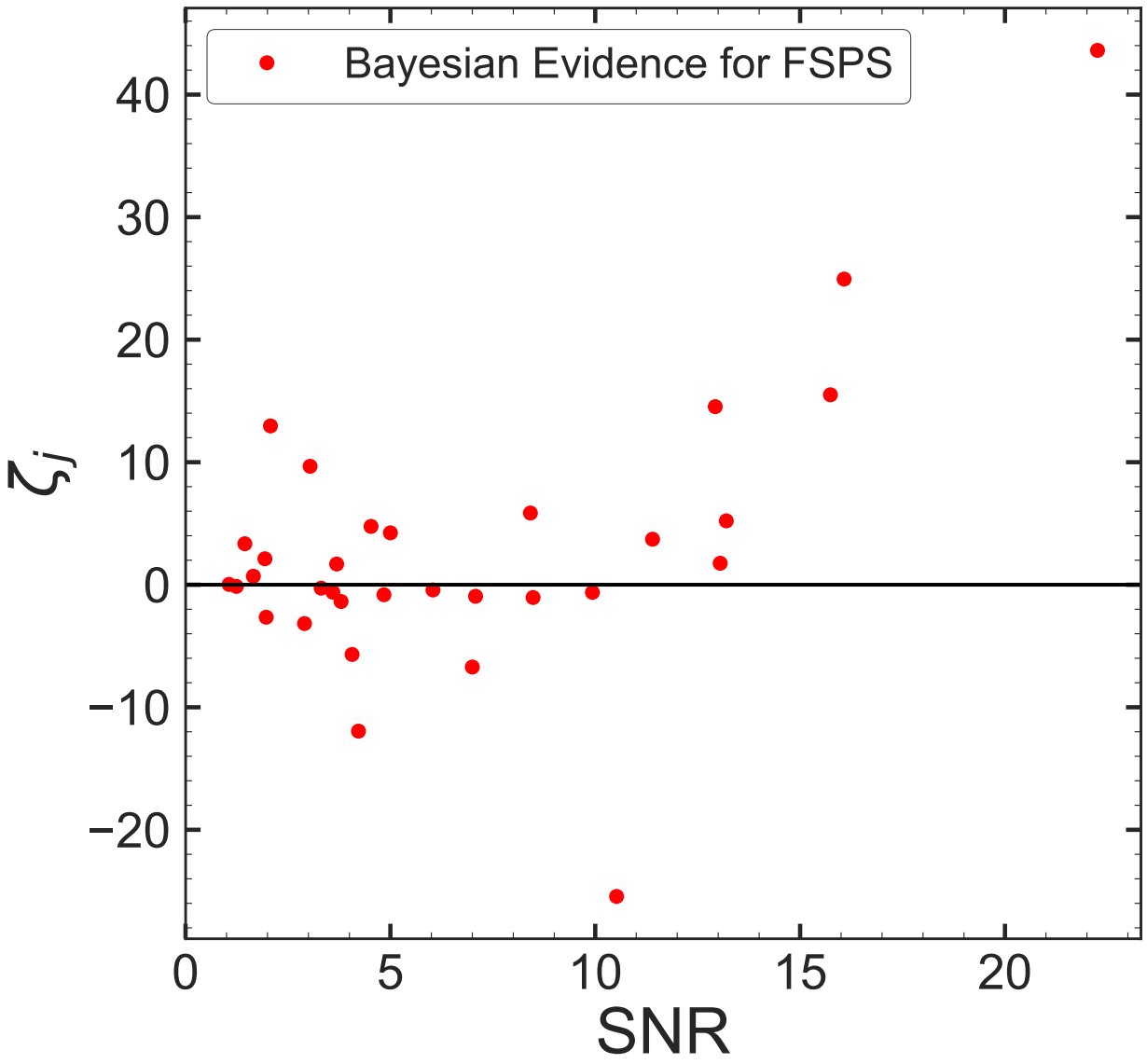

Figure A.4: Distribution of Bayes-factor evidence (ζ_j), for each galaxy j in our sample, as a function of SNR. Positive (negative) values of $zeta_j$ denote galaxies with evidence against (in favor of) the BC03 models compared to the FSPS models.

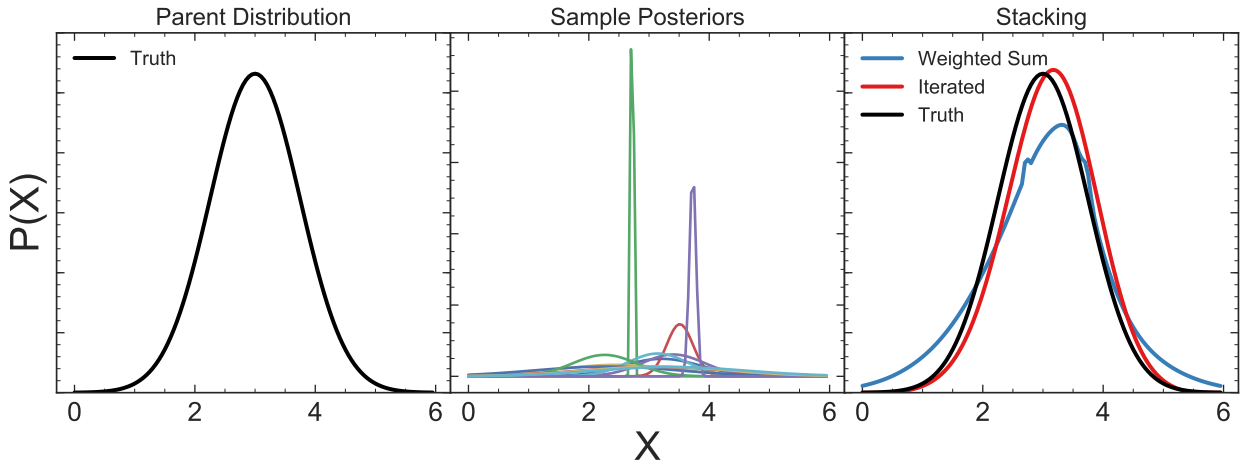

Figure A.5: Test of our stacking method to recover a parent distribution. Panel 1 shows the true distribution, panel 2 show the randomly selected sample from distribution, and panel 3 displays a weighted sum of the sample posteriors along with the fully processed stacked posterior.

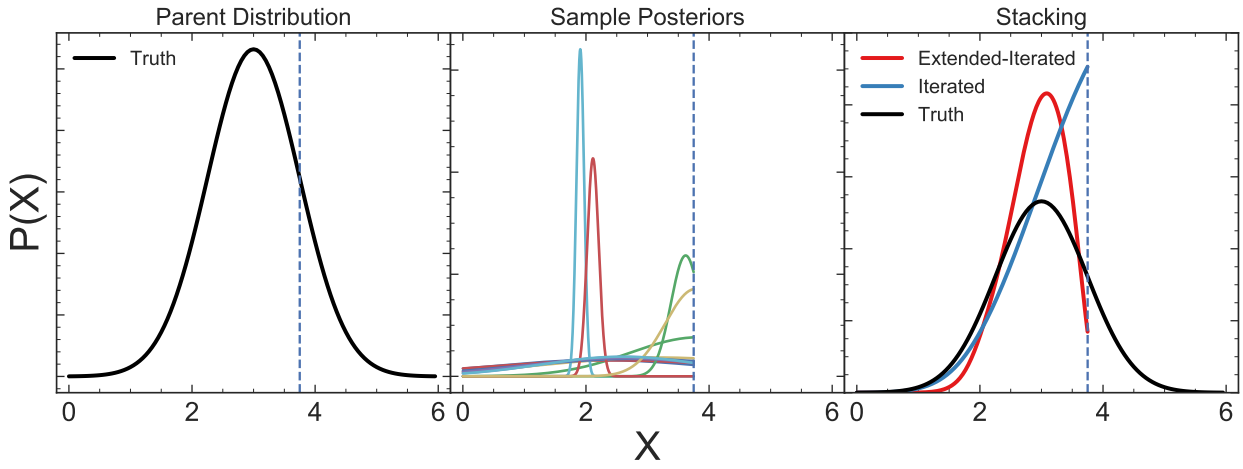

Figure A.6: Test of our stacking method to recover a parent distribution when our parameter space does not cover the entirety of the parent distribution. Panel 1 shows the true distribution, panel 2 show the randomly selected sample from distribution, and panel 3 displays the fully processed stacked posterior with and without extending the parameter space.

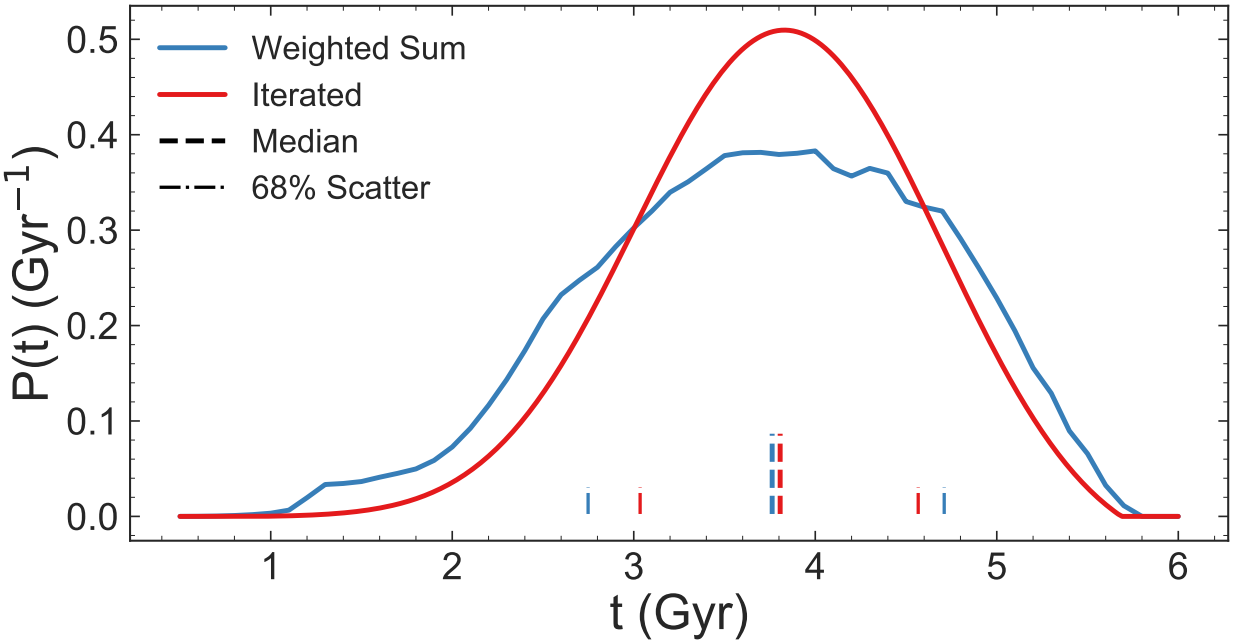

Figure A.7: An example of the stacking method applied to the light-weighted age posteriors of our redshift group. The solid blue line shows the direct weighted sum (the result of direct stacking in the first step of the interaction using Equation 2.11). This yields the median and 68% confidence range illustrated by the blue dashed and dot-dashed lines. The solid red line shows the results after iterating. Because the iterations smooth over objects with sharply peaked likelihoods it yields a slightly tighter (and smoother) final likelihood. The red dashed and dot-dashed lines show the change in the median and 68% confidence range, respectively. We use the "stack-smooth-iterate" method to derive likelihoods from the galaxies in each of our redshift subgroups.

APPENDIX B

B.1 Data Tables

We report here the catalog for the galaxies in the sample used here. These include two tables. Table B.1 reports values for each galaxy derived without the analysis of the grism data (including galaxy ID numbers, coordinates, photometric redshift, photometric masses, and circularized radii). Table B.2 reports values derived from our fits to the photometry and grism data here (including redshifts, masses, specific star-formation rates, dust attenuations, stellar-mass surface densities, quenching timescales, and formation redshifts).

B.2 Interactive Online Model Fits for the Galaxy Sample

We include with this paper an interactive appendix, which shows the properties and model fits for all the galaxies in our sample. The appendix is available here: interactive online appendix[1]. At this link the reader can see galaxy properties on multiple plots simultaneously (Figure B.1), and also access individual galaxy morphology, photometric and spectroscopic data and model fits (Figure B.2). The user can interact with the star-formation history, and spectral energy distribution. The online material also includes a hyperlink to show all galaxy SFHs and morphologies ordered by z_{50}[2] on a single figure (Figure B.3).

Table B.1: Catalog Properties of Quiescent Galaxy Sample

ID	RA (deg, J2000)	DEC (deg, J2000)	$z_{\rm phot}$	$\log(M_{\rm phot})$ ($\log M_\odot$)	$R_{\rm eff}$ (kpc)
(1)	(2)	(3)	(4)	(5)	(6)
GND-29879	189.254227	62.291579	$0.69^{0.01}_{0.01}$	10.9	$1.12^{0.13}_{0.01}$
GSD-41147	53.081634	-27.717718	$0.70^{0.01}_{0.01}$	10.8	$1.46^{0.09}_{0.01}$

[1]Also available at https://vince-ec.github.io/appendix/appendix
[2]Also available at https://vince-ec.github.io/appendix/fullfig

GSD-47140	53.131853	-27.687304	$0.73^{0.01}_{0.01}$	10.8	$2.91^{0.22}_{0.04}$
GSD-46001	53.120312	-27.691486	$0.72^{0.01}_{0.01}$	11.2	$3.00^{0.19}_{0.02}$
GND-27006	189.263714	62.275807	$0.71^{0.02}_{0.02}$	10.8	$1.11^{0.11}_{0.01}$
GND-22358	189.081040	62.251545	$0.82^{0.02}_{0.02}$	10.7	$1.66^{0.12}_{0.02}$
GND-36838	189.251622	62.344526	$0.80^{0.01}_{0.02}$	10.8	$1.46^{0.12}_{0.03}$
GND-37186	189.243199	62.349892	$0.80^{0.02}_{0.01}$	11.0	$1.68^{0.15}_{0.03}$
GND-13774	189.179829	62.211733	$0.83^{0.01}_{0.01}$	11.1	$1.78^{0.14}_{0.01}$
GND-32108	189.277164	62.305097	$0.82^{0.01}_{0.01}$	10.7	$1.77^{0.15}_{0.03}$
GND-23459	189.310355	62.258286	$0.86^{0.01}_{0.01}$	11.0	$1.99^{0.16}_{0.02}$
GND-24795	189.202555	62.264622	$0.85^{0.01}_{0.01}$	10.9	$2.31^{0.14}_{0.01}$
GND-14158	189.192218	62.212927	$0.87^{0.01}_{0.01}$	10.6	$2.91^{0.21}_{0.04}$
GND-29183	189.245464	62.287267	$0.94^{0.02}_{0.03}$	10.6	$0.74^{0.06}_{0.01}$
GND-24177	189.343191	62.262053	$0.91^{0.01}_{0.02}$	11.0	$4.70^{0.33}_{0.06}$
GND-23081	189.334875	62.255800	$0.90^{0.02}_{0.02}$	11.2	$2.23^{0.17}_{0.02}$
GND-22213	189.201365	62.252076	$0.88^{0.01}_{0.01}$	11.2	$1.10^{0.11}_{0.01}$
GND-33453	189.264307	62.314325	$0.88^{0.03}_{0.02}$	10.7	$2.45^{0.17}_{0.05}$
GND-23758	189.217983	62.260352	$0.89^{0.02}_{0.02}$	11.2	$7.96^{0.54}_{0.07}$
GND-22246	189.220896	62.252424	$0.87^{0.01}_{0.01}$	11.1	$3.58^{0.22}_{0.03}$
GND-26673	189.279210	62.274483	$0.92^{0.02}_{0.02}$	10.8	$3.22^{0.24}_{0.05}$
GND-27951	189.226202	62.281984	$0.94^{0.02}_{0.01}$	11.1	$3.54^{0.23}_{0.03}$
GND-37340	189.289100	62.352859	$0.88^{0.01}_{0.01}$	11.0	$1.75^{0.12}_{0.03}$
GND-12793	189.236022	62.205604	$0.96^{0.01}_{0.02}$	10.9	$2.56^{0.17}_{0.03}$
GSD-38191	53.141108	-27.732652	$0.97^{0.01}_{0.01}$	10.7	$1.27^{0.08}_{0.02}$
GSD-39850	53.173100	-27.724355	$0.96^{0.01}_{0.01}$	10.7	$0.91^{0.08}_{0.01}$
GND-36161	189.201410	62.336077	$0.92^{0.02}_{0.02}$	10.7	$1.20^{0.08}_{0.03}$
GSD-19148	53.164983	-27.819326	$0.97^{0.01}_{0.01}$	11.5	$3.90^{0.27}_{0.02}$
GND-22363	189.169647	62.251296	$0.99^{0.01}_{0.02}$	10.7	$1.00^{0.07}_{0.01}$

GND-27185	189.242059	62.277510	$1.04^{0.02}_{0.01}$	11.2	$1.72^{0.16}_{0.02}$
GSD-42221	53.079234	-27.711869	$1.03^{0.02}_{0.02}$	10.8	$5.14^{0.39}_{0.10}$
GND-16758	189.162357	62.224840	$0.98^{0.01}_{0.01}$	11.1	$1.45^{0.19}_{0.01}$
GND-12078	189.166744	62.202054	$0.99^{0.01}_{0.01}$	10.7	$1.99^{0.13}_{0.02}$
GSD-39170	53.041826	-27.725868	$1.03^{0.01}_{0.01}$	11.4	$3.20^{0.21}_{0.02}$
GSD-43615	53.093057	-27.707368	$1.03^{0.01}_{0.01}$	10.9	$1.50^{0.13}_{0.02}$
GND-22633	189.161700	62.252923	$1.00^{0.03}_{0.02}$	10.7	$1.40^{0.16}_{0.02}$
GSD-39241	53.042327	-27.726209	$1.03^{0.01}_{0.01}$	11.1	$2.23^{0.14}_{0.02}$
GSD-39631	53.042169	-27.725928	$0.99^{0.02}_{0.01}$	11.0	$2.24^{0.18}_{0.03}$
GND-37955	189.337824	62.371137	$0.98^{0.04}_{0.01}$	11.0	$3.17^{0.22}_{0.07}$
GND-37210	189.252761	62.350806	$1.04^{0.02}_{0.01}$	11.2	$2.67^{0.19}_{0.04}$
GSD-45972	53.115984	-27.693568	$1.03^{0.01}_{0.01}$	11.1	$8.36^{0.65}_{0.13}$
GSD-44620	53.249645	-27.702048	$1.09^{0.01}_{0.02}$	10.7	$4.11^{0.31}_{0.05}$
GSD-29928	53.154965	-27.768904	$1.09^{0.01}_{0.01}$	11.7	$6.50^{0.47}_{0.01}$
GND-30358	189.299204	62.293310	$0.94^{0.02}_{0.03}$	10.6	$1.17^{0.08}_{0.02}$
GND-23857	189.070894	62.259299	$1.15^{0.04}_{0.04}$	10.6	$1.62^{0.11}_{0.04}$
GSD-47691	53.273156	-27.681599	$1.12^{0.01}_{0.01}$	11.2	$5.23^{0.35}_{0.02}$
GND-21724	189.063257	62.248675	$1.10^{0.02}_{0.02}$	11.0	$2.69^{0.20}_{0.05}$
GND-37325	189.251371	62.351582	$1.19^{0.03}_{0.04}$	10.6	$0.81^{0.07}_{0.03}$
GND-22027	189.065790	62.249816	$1.14^{0.02}_{0.03}$	10.9	$1.68^{0.11}_{0.03}$
GND-34694	189.147840	62.323647	$1.07^{0.02}_{0.02}$	11.1	$4.62^{0.36}_{0.05}$
GND-38102	189.339219	62.375874	$1.24^{0.01}_{0.02}$	10.7	$0.58^{0.06}_{0.03}$
GND-28451	189.247715	62.282931	$1.14^{0.02}_{0.01}$	10.7	$1.01^{0.07}_{0.01}$
GND-20432	189.362767	62.242309	$1.14^{0.02}_{0.02}$	11.1	$1.15^{0.07}_{0.01}$
GND-17746	189.049436	62.228979	$1.16^{0.02}_{0.01}$	11.1	$1.32^{0.16}_{0.04}$
GSD-39805	53.163237	-27.724724	$1.15^{0.02}_{0.01}$	10.8	$2.33^{0.16}_{0.06}$
GSD-40476	53.108262	-27.721924	$1.18^{0.02}_{0.01}$	10.9	$1.13^{0.10}_{0.02}$

GSD-37828	53.158121	-27.734502	$1.20^{0.02}_{0.02}$	10.7	$1.09^{0.08}_{0.03}$
GSD-40597	53.148451	-27.719472	$1.23^{0.01}_{0.01}$	11.4	$1.79^{0.14}_{0.02}$
GND-34419	189.311828	62.320264	$1.20^{0.01}_{0.01}$	10.8	$0.71^{0.05}_{0.02}$
GND-13191	189.217041	62.207326	$1.28^{0.02}_{0.02}$	10.8	$1.77^{0.14}_{0.04}$
GND-14713	189.236333	62.214608	$1.23^{0.03}_{0.02}$	10.8	$1.51^{0.11}_{0.03}$
GND-17070	189.268086	62.226445	$1.24^{0.01}_{0.02}$	11.3	$0.83^{0.10}_{0.01}$
GSD-38785	53.168249	-27.727300	$1.14^{0.04}_{0.04}$	11.1	$3.43^{0.26}_{0.04}$
GND-21156	189.239409	62.247548	$1.21^{0.02}_{0.02}$	11.4	$2.88^{0.24}_{0.03}$
GSD-35774	53.158775	-27.742385	$1.23^{0.01}_{0.01}$	11.3	$6.35^{0.40}_{0.07}$
GND-37686	189.274474	62.360820	$1.28^{0.02}_{0.02}$	11.2	$1.84^{0.14}_{0.05}$
GSD-40862	53.048020	-27.719743	$1.34^{0.02}_{0.01}$	11.2	$2.71^{0.21}_{0.03}$
GSD-46066	53.061039	-27.693501	$1.32^{0.02}_{0.01}$	11.2	$1.74^{0.11}_{0.03}$
GSD-39804	53.178423	-27.724640	$1.36^{0.01}_{0.01}$	11.2	$0.84^{0.11}_{0.01}$
GSD-45775	53.158558	-27.694968	$1.37^{0.02}_{0.01}$	11.4	$13.68^{0.93}_{0.21}$
GND-36530	189.275620	62.340723	$1.39^{0.03}_{0.02}$	11.1	$6.06^{0.49}_{0.24}$
GSD-40623	53.130480	-27.721152	$1.43^{0.02}_{0.02}$	11.1	$2.21^{0.15}_{0.04}$
GND-24345	189.244758	62.261225	$1.35^{0.03}_{0.03}$	10.6	$0.49^{0.04}_{0.02}$
GND-16574	189.233886	62.223678	$1.50^{0.03}_{0.03}$	10.7	$0.77^{0.06}_{0.03}$
GND-21427	189.368121	62.247344	$1.50^{0.02}_{0.02}$	11.0	$2.34^{0.15}_{0.05}$
GSD-40223	53.124956	-27.722957	$1.66^{0.02}_{0.03}$	11.0	$1.06^{0.08}_{0.02}$
GSD-39649	53.059630	-27.725792	$1.66^{0.01}_{0.02}$	10.9	$0.74^{0.05}_{0.02}$
GSD-42487	53.116396	-27.712701	$1.69^{0.02}_{0.03}$	11.0	$0.65^{0.05}_{0.01}$
GSD-38843	53.107039	-27.729749	$1.61^{0.04}_{0.03}$	10.6	$1.31^{0.13}_{0.06}$
GSD-39012	53.064240	-27.727621	$1.62^{0.04}_{0.04}$	11.3	$1.62^{0.15}_{0.05}$
GSD-41520	53.152726	-27.716251	$1.64^{0.02}_{0.02}$	11.2	$1.20^{0.10}_{0.02}$
GSD-44042	53.104570	-27.705421	$1.81^{0.02}_{0.02}$	11.4	$2.19^{0.15}_{0.03}$
GND-33775	189.188648	62.315319	$1.65^{0.06}_{0.08}$	10.7	$0.60^{0.05}_{0.02}$

GSD-42615	53.127414	-27.712062	$1.67^{0.03}_{0.03}$	11.2	$1.03^{0.07}_{0.02}$
GSD-41148	53.127925	-27.718885	$1.79^{0.02}_{0.02}$	11.4	$2.19^{0.14}_{0.03}$
GND-33780	189.202025	62.317153	$1.92^{0.06}_{0.05}$	11.6	$5.79^{0.37}_{0.09}$
GND-17735	189.060905	62.228977	$1.90^{0.02}_{0.03}$	11.1	$1.09^{0.08}_{0.01}$
GND-19850	189.090085	62.239244	$1.85^{0.02}_{0.02}$	10.9	$0.80^{0.07}_{0.01}$
GSD-24569	53.158798	-27.797153	$1.90^{0.02}_{0.02}$	11.0	$0.52^{0.04}_{0.01}$
GSD-24315	53.162991	-27.797654	$2.01^{0.02}_{0.02}$	10.7	$0.42^{0.04}_{0.01}$
GND-14132	189.190249	62.211662	$2.01^{0.03}_{0.03}$	11.1	$1.11^{0.09}_{0.02}$
GSD-43572	53.142153	-27.707427	$2.05^{0.03}_{0.04}$	11.2	$3.14^{0.26}_{0.12}$
GND-21738	189.210937	62.248818	$2.11^{0.03}_{0.02}$	11.4	$1.19^{0.10}_{0.02}$
GND-32933	189.156358	62.309106	$2.13^{0.04}_{0.04}$	10.7	$1.06^{0.10}_{0.04}$
GND-17599	189.121464	62.228903	$2.12^{0.01}_{0.02}$	11.0	$0.36^{0.04}_{0.01}$
GSD-44133	53.110407	-27.703706	$2.09^{0.02}_{0.01}$	10.4	$1.59^{0.13}_{0.03}$
GND-23018	189.277544	62.254617	$2.25^{0.03}_{0.03}$	11.3	$2.39^{0.17}_{0.04}$
GSD-48464	53.144819	-27.682470	$2.34^{0.03}_{0.03}$	11.4	$2.08^{0.18}_{0.06}$

Table B.1: (1) catalog ID number (matching those in (16)); (2) right ascension; (3) declination; (4) photometric redshift; (5) stellar mass from Eazy-py; (6) *circularized* effective radius (derived from (11) and defined as r$\sqrt{b/a}$, where r is the radius of the semi-major axis in kpc, b/a is the axis ratio)

Table B.2: Derived Properties of Quiescent Galaxy Sample

ID	$z_{\rm grism}$	$\log(M_{\rm grism})$	log sSFR	A_V	$\log(\Sigma_1)$	t_Q	z_{50}
		$(\log M_\odot)$	$(\log {\rm yr}^{-1})$	(mag)	$(\log M_\odot\ {\rm kpc}^{-2})$	(Gyr)	
(1)	(2)	(3)	(4)	(5)	(6)	(7)	(8)
GND-29879	$0.711^{0.001}_{0.002}$	$10.80^{0.04}_{0.03}$	$-12.2^{0.4}_{0.5}$	$0.22^{0.30}_{0.14}$	$9.99^{0.05}_{0.05}$	$1.3^{0.4}_{0.8}$	$1.6^{0.2}_{0.2}$
GSD-41147	$0.730^{0.002}_{0.002}$	$10.74^{0.02}_{0.02}$	$-11.6^{0.4}_{0.1}$	$0.20^{0.24}_{0.15}$	$9.96^{0.02}_{0.02}$	$2.5^{0.3}_{0.5}$	$2.1^{0.2}_{0.3}$
GSD-47140	$0.731^{0.002}_{0.002}$	$10.70^{0.03}_{0.02}$	$-12.0^{0.2}_{0.1}$	$0.00^{0.02}_{0.00}$	$9.71^{0.04}_{0.04}$	$1.9^{0.4}_{1.1}$	$2.8^{0.2}_{0.8}$
GSD-46001	$0.732^{0.001}_{0.001}$	$11.10^{0.03}_{0.02}$	$-11.7^{0.5}_{0.1}$	$0.43^{0.47}_{0.35}$	$10.05^{0.03}_{0.03}$	$1.8^{0.3}_{0.8}$	$1.9^{0.1}_{0.4}$

GND-27006	$0.743^{0.001}_{0.001}$	$10.88^{0.04}_{0.02}$	$-12.0^{0.6}_{0.2}$	$0.26^{0.34}_{0.20}$	$10.13^{0.04}_{0.04}$	$2.3^{0.5}_{1.0}$	$3.0^{0.5}_{0.8}$
GND-22358	$0.779^{0.005}_{0.005}$	$10.70^{0.03}_{0.03}$	$-11.6^{0.1}_{0.2}$	$0.18^{0.26}_{0.13}$	$9.77^{0.04}_{0.04}$	$1.9^{0.5}_{0.6}$	$3.1^{0.5}_{0.6}$
GND-36838	$0.799^{0.002}_{0.002}$	$10.73^{0.04}_{0.03}$	$-12.4^{0.6}_{0.3}$	$0.03^{0.10}_{0.01}$	$9.94^{0.04}_{0.04}$	$1.9^{0.5}_{0.8}$	$3.6^{0.6}_{1.0}$
GND-37186	$0.804^{0.001}_{0.001}$	$10.91^{0.02}_{0.02}$	$-11.9^{0.6}_{0.1}$	$0.01^{0.06}_{0.01}$	$10.05^{0.03}_{0.03}$	$1.4^{0.4}_{0.5}$	$2.4^{0.2}_{0.3}$
GND-13774	$0.849^{0.001}_{0.001}$	$11.02^{0.02}_{0.03}$	$-12.4^{1.1}_{0.1}$	$0.01^{0.01}_{0.01}$	$10.14^{0.03}_{0.03}$	$0.5^{0.4}_{0.6}$	$2.8^{0.2}_{0.4}$
GND-32108	$0.855^{0.004}_{0.002}$	$10.66^{0.03}_{0.03}$	$-11.2^{0.1}_{0.2}$	$0.33^{0.51}_{0.26}$	$9.72^{0.04}_{0.04}$	$2.1^{0.4}_{1.1}$	$2.6^{0.4}_{0.7}$
GND-23459	$0.858^{0.001}_{0.001}$	$10.93^{0.02}_{0.02}$	$-12.2^{0.5}_{0.4}$	$0.41^{0.48}_{0.31}$	$10.01^{0.03}_{0.03}$	$1.6^{0.4}_{0.8}$	$3.1^{0.3}_{0.7}$
GND-24795	$0.858^{0.003}_{0.002}$	$10.84^{0.03}_{0.03}$	$-11.9^{0.5}_{0.3}$	$0.00^{0.07}_{0.00}$	$9.73^{0.05}_{0.05}$	$1.3^{0.3}_{0.8}$	$1.8^{0.1}_{0.3}$
GND-14158	$0.911^{0.005}_{0.004}$	$10.58^{0.02}_{0.02}$	$-11.3^{0.3}_{0.1}$	$0.00^{0.02}_{0.00}$	$9.71^{0.03}_{0.03}$	$1.1^{0.2}_{1.0}$	$1.9^{0.1}_{0.4}$
GND-29183	$0.933^{0.007}_{0.002}$	$10.50^{0.03}_{0.03}$	$-11.5^{0.3}_{0.6}$	$0.45^{0.58}_{0.34}$	$9.83^{0.03}_{0.03}$	$1.6^{0.8}_{0.9}$	$2.2^{0.7}_{0.1}$
GND-24177	$0.937^{0.002}_{0.002}$	$10.96^{0.03}_{0.03}$	$-12.2^{0.5}_{0.2}$	$0.00^{0.04}_{0.00}$	$9.93^{0.03}_{0.03}$	$1.7^{0.4}_{0.7}$	$3.7^{0.5}_{0.8}$
GND-23081	$0.938^{0.001}_{0.001}$	$11.15^{0.02}_{0.02}$	$-12.2^{0.2}_{0.2}$	$0.17^{0.22}_{0.14}$	$10.25^{0.03}_{0.03}$	$1.3^{0.5}_{1.8}$	$4.2^{1.0}_{0.7}$
GND-22213	$0.938^{0.001}_{0.001}$	$11.19^{0.02}_{0.02}$	$-12.2^{0.5}_{0.1}$	$0.01^{0.09}_{0.01}$	$10.40^{0.03}_{0.03}$	$2.1^{0.4}_{0.5}$	$5.4^{1.2}_{1.1}$
GND-33453	$0.939^{0.003}_{0.003}$	$10.62^{0.04}_{0.05}$	$-12.2^{0.3}_{0.6}$	$0.18^{0.26}_{0.12}$	$9.72^{0.05}_{0.05}$	$2.1^{1.0}_{1.2}$	$3.2^{2.2}_{0.9}$
GND-23758	$0.941^{0.002}_{0.002}$	$11.19^{0.03}_{0.04}$	$-11.9^{0.4}_{0.2}$	$0.49^{0.55}_{0.35}$	$10.13^{0.03}_{0.03}$	$1.5^{0.3}_{0.6}$	$3.3^{0.4}_{0.6}$
GND-22246	$0.942^{0.001}_{0.001}$	$11.05^{0.01}_{0.02}$	$-12.2^{0.2}_{0.3}$	$0.00^{0.02}_{0.00}$	$10.04^{0.02}_{0.02}$	$2.2^{0.6}_{0.9}$	$5.2^{1.7}_{1.1}$
GND-26673	$0.942^{0.001}_{0.001}$	$10.72^{0.01}_{0.02}$	$-11.9^{0.1}_{0.5}$	$0.07^{0.10}_{0.04}$	$9.82^{0.02}_{0.02}$	$1.1^{0.2}_{0.4}$	$2.1^{0.1}_{0.2}$
GND-27951	$0.943^{0.004}_{0.004}$	$11.19^{0.03}_{0.01}$	$-12.3^{0.1}_{0.5}$	$0.09^{0.13}_{0.06}$	$10.20^{0.03}_{0.03}$	$0.4^{0.2}_{0.4}$	$8.1^{1.6}_{1.4}$
GND-37340	$0.945^{0.001}_{0.001}$	$11.01^{0.01}_{0.01}$	$-12.4^{0.1}_{0.3}$	$0.02^{0.02}_{0.01}$	$10.17^{0.02}_{0.02}$	$1.3^{0.2}_{0.2}$	$3.7^{0.2}_{0.3}$
GND-12793	$0.953^{0.004}_{0.002}$	$10.86^{0.02}_{0.03}$	$-11.4^{0.2}_{0.2}$	$0.14^{0.23}_{0.08}$	$9.91^{0.03}_{0.03}$	$1.9^{0.2}_{0.4}$	$2.7^{0.2}_{0.3}$
GSD-38191	$0.977^{0.003}_{0.002}$	$10.60^{0.02}_{0.03}$	$-11.6^{0.7}_{0.1}$	$0.21^{0.24}_{0.14}$	$9.76^{0.03}_{0.03}$	$1.4^{0.2}_{0.6}$	$2.8^{0.2}_{0.3}$
GSD-39850	$0.980^{0.001}_{0.001}$	$10.67^{0.02}_{0.02}$	$-12.3^{0.4}_{0.4}$	$0.04^{0.08}_{0.02}$	$9.97^{0.03}_{0.03}$	$1.8^{0.2}_{0.6}$	$2.3^{0.1}_{0.3}$
GND-36161	$0.981^{0.010}_{0.034}$	$10.73^{0.04}_{0.04}$	$-11.7^{0.5}_{0.3}$	$0.00^{0.04}_{0.00}$	$9.91^{0.05}_{0.05}$	$1.3^{0.5}_{1.1}$	$2.6^{0.4}_{0.7}$
GSD-19148	$0.982^{0.001}_{0.001}$	$11.39^{0.02}_{0.02}$	$-12.6^{0.2}_{0.4}$	$0.18^{0.24}_{0.11}$	$10.38^{0.03}_{0.03}$	$0.9^{0.5}_{1.2}$	$2.9^{0.2}_{0.3}$
GND-22363	$1.004^{0.002}_{0.002}$	$10.68^{0.01}_{0.01}$	$-11.9^{0.2}_{0.1}$	$0.01^{0.02}_{0.01}$	$9.94^{0.02}_{0.02}$	$1.4^{0.2}_{0.4}$	$3.7^{0.1}_{0.5}$
GND-27185	$1.016^{0.003}_{0.002}$	$11.11^{0.03}_{0.03}$	$-11.8^{0.5}_{0.2}$	$0.35^{0.43}_{0.26}$	$10.28^{0.04}_{0.04}$	$2.0^{0.4}_{0.5}$	$3.0^{0.5}_{0.5}$
GSD-42221	$1.016^{0.003}_{0.004}$	$10.68^{0.02}_{0.04}$	$-11.6^{0.1}_{0.2}$	$0.02^{0.09}_{0.01}$	$9.72^{0.03}_{0.03}$	$1.2^{0.4}_{0.4}$	$3.1^{0.3}_{0.4}$

GND-16758	$1.016^{0.001}_{0.001}$	$10.98^{0.03}_{0.04}$	$-11.7^{0.2}_{0.4}$	$0.56^{0.62}_{0.51}$	$10.07^{0.06}_{0.06}$	$1.2^{0.5}_{0.6}$	$2.5^{0.4}_{0.4}$
GND-12078	$1.016^{0.002}_{0.001}$	$10.80^{0.02}_{0.03}$	$-10.9^{0.9}_{0.1}$	$0.27^{0.36}_{0.17}$	$9.89^{0.03}_{0.03}$	$1.8^{0.2}_{0.5}$	$2.1^{0.2}_{0.3}$
GSD-39170	$1.018^{0.001}_{0.001}$	$11.40^{0.02}_{0.02}$	$-12.5^{0.6}_{0.1}$	$0.02^{0.05}_{0.01}$	$10.37^{0.03}_{0.03}$	$0.5^{0.2}_{1.6}$	$6.4^{1.5}_{1.4}$
GSD-43615	$1.021^{0.001}_{0.002}$	$10.88^{0.02}_{0.01}$	$-11.8^{0.1}_{0.4}$	$0.39^{0.42}_{0.34}$	$9.99^{0.04}_{0.04}$	$0.4^{0.3}_{0.3}$	$5.7^{0.6}_{0.8}$
GND-22633	$1.022^{0.006}_{0.007}$	$10.72^{0.03}_{0.08}$	$-10.8^{0.4}_{0.3}$	$0.87^{0.93}_{0.73}$	$9.79^{0.08}_{0.08}$	$2.1^{0.8}_{0.9}$	$2.6^{0.8}_{0.7}$
GSD-39241	$1.024^{0.003}_{0.001}$	$11.11^{0.02}_{0.02}$	$-11.9^{0.3}_{0.1}$	$0.26^{0.30}_{0.22}$	$10.15^{0.03}_{0.03}$	$1.4^{0.2}_{0.4}$	$3.9^{0.3}_{0.7}$
GSD-39631	$1.029^{0.003}_{0.003}$	$10.90^{0.02}_{0.03}$	$-12.9^{0.7}_{0.6}$	$0.25^{0.36}_{0.22}$	$9.98^{0.03}_{0.03}$	$0.9^{0.4}_{1.8}$	$4.2^{0.7}_{1.1}$
GND-37955	$1.030^{0.004}_{0.004}$	$11.06^{0.04}_{0.04}$	$-12.0^{0.2}_{0.5}$	$0.23^{0.39}_{0.17}$	$9.95^{0.05}_{0.05}$	$1.1^{0.3}_{1.6}$	$4.9^{0.9}_{1.2}$
GND-37210	$1.040^{0.002}_{0.002}$	$11.12^{0.02}_{0.02}$	$-12.2^{0.3}_{0.2}$	$0.00^{0.02}_{0.00}$	$10.19^{0.03}_{0.03}$	$1.2^{0.4}_{0.4}$	$3.4^{0.3}_{0.4}$
GSD-45972	$1.041^{0.001}_{0.002}$	$10.94^{0.01}_{0.01}$	$-11.9^{0.3}_{0.4}$	$0.00^{0.02}_{0.00}$	$9.77^{0.03}_{0.03}$	$2.3^{0.8}_{0.7}$	$4.5^{2.3}_{1.2}$
GSD-44620	$1.083^{0.004}_{0.001}$	$10.72^{0.02}_{0.03}$	$-11.8^{0.1}_{0.3}$	$0.05^{0.09}_{0.01}$	$9.80^{0.03}_{0.03}$	$0.5^{0.5}_{0.4}$	$6.9^{1.4}_{1.5}$
GSD-29928	$1.098^{0.001}_{0.001}$	$11.67^{0.01}_{0.01}$	$-12.1^{0.3}_{0.4}$	$0.35^{0.36}_{0.31}$	$10.49^{0.03}_{0.03}$	$1.5^{0.5}_{0.6}$	$5.1^{1.6}_{1.3}$
GND-30358	$1.104^{0.005}_{0.005}$	$10.59^{0.02}_{0.03}$	$-12.6^{0.4}_{0.7}$	$0.03^{0.09}_{0.01}$	$9.77^{0.04}_{0.04}$	$1.4^{0.3}_{0.5}$	$2.5^{0.2}_{0.3}$
GND-23857	$1.121^{0.031}_{0.014}$	$10.53^{0.02}_{0.03}$	$-11.6^{0.1}_{0.5}$	$0.00^{0.03}_{0.00}$	$9.64^{0.03}_{0.03}$	$1.7^{0.4}_{0.9}$	$3.2^{0.4}_{0.8}$
GSD-47691	$1.127^{0.002}_{0.005}$	$11.09^{0.03}_{0.02}$	$-11.5^{0.3}_{0.4}$	$0.36^{0.49}_{0.30}$	$9.87^{0.04}_{0.04}$	$1.7^{0.2}_{0.9}$	$2.9^{0.1}_{0.8}$
GND-21724	$1.133^{0.007}_{0.005}$	$10.89^{0.02}_{0.03}$	$-11.8^{0.4}_{0.3}$	$0.25^{0.44}_{0.18}$	$9.92^{0.04}_{0.04}$	$1.2^{0.4}_{0.6}$	$2.9^{0.3}_{0.5}$
GND-37325	$1.136^{0.009}_{0.009}$	$10.53^{0.04}_{0.04}$	$-11.2^{0.3}_{0.5}$	$0.63^{0.74}_{0.40}$	$9.82^{0.04}_{0.04}$	$1.8^{0.3}_{0.8}$	$2.6^{0.3}_{0.6}$
GND-22027	$1.141^{0.004}_{0.002}$	$10.83^{0.03}_{0.03}$	$-12.0^{0.5}_{0.2}$	$0.00^{0.17}_{0.00}$	$9.93^{0.04}_{0.04}$	$1.1^{0.5}_{0.6}$	$3.1^{0.4}_{0.6}$
GND-34694	$1.142^{0.003}_{0.002}$	$11.15^{0.04}_{0.04}$	$-11.4^{0.3}_{0.3}$	$0.32^{0.38}_{0.22}$	$9.91^{0.06}_{0.06}$	$1.9^{0.5}_{0.5}$	$3.3^{0.7}_{0.5}$
GND-38102	$1.145^{0.008}_{0.009}$	$10.56^{0.03}_{0.03}$	$-11.7^{0.4}_{0.4}$	$0.00^{0.15}_{0.00}$	$9.91^{0.04}_{0.04}$	$1.8^{0.5}_{0.9}$	$2.8^{0.6}_{0.7}$
GND-28451	$1.148^{0.007}_{0.006}$	$10.62^{0.02}_{0.02}$	$-11.7^{0.4}_{0.2}$	$0.02^{0.04}_{0.01}$	$9.83^{0.03}_{0.03}$	$1.5^{0.4}_{0.7}$	$2.5^{0.4}_{0.4}$
GND-20432	$1.149^{0.005}_{0.006}$	$10.94^{0.04}_{0.02}$	$-11.8^{0.4}_{0.2}$	$0.19^{0.32}_{0.14}$	$10.14^{0.03}_{0.03}$	$1.5^{0.5}_{0.5}$	$4.7^{1.5}_{1.0}$
GND-17746	$1.152^{0.008}_{0.009}$	$11.06^{0.04}_{0.04}$	$-12.1^{0.5}_{0.3}$	$0.35^{0.45}_{0.26}$	$10.24^{0.05}_{0.05}$	$1.5^{0.4}_{0.6}$	$5.4^{1.5}_{1.2}$
GSD-39805	$1.156^{0.017}_{0.012}$	$10.64^{0.04}_{0.02}$	$-12.0^{0.4}_{0.3}$	$0.08^{0.18}_{0.03}$	$9.70^{0.04}_{0.04}$	$1.7^{0.3}_{0.5}$	$5.3^{0.7}_{1.4}$
GSD-40476	$1.212^{0.003}_{0.001}$	$10.74^{0.02}_{0.08}$	$-12.8^{0.6}_{0.7}$	$0.25^{0.32}_{0.20}$	$9.95^{0.05}_{0.05}$	$0.9^{0.5}_{0.7}$	$2.4^{0.4}_{0.4}$
GSD-37828	$1.213^{0.002}_{0.003}$	$10.61^{0.03}_{0.03}$	$-11.9^{0.3}_{0.4}$	$0.23^{0.30}_{0.12}$	$9.85^{0.03}_{0.03}$	$1.7^{0.3}_{0.6}$	$3.3^{0.4}_{0.6}$
GSD-40597	$1.219^{0.001}_{0.003}$	$11.15^{0.02}_{0.02}$	$-12.4^{0.4}_{0.7}$	$0.52^{0.57}_{0.47}$	$10.21^{0.03}_{0.03}$	$1.0^{0.1}_{0.3}$	$2.4^{0.1}_{0.2}$

GND-34419	$1.221^{0.003}_{0.003}$	$10.69^{0.03}_{0.03}$	$-12.2^{0.5}_{0.5}$	$0.01^{0.04}_{0.01}$	$9.99^{0.04}_{0.04}$	$1.1^{0.2}_{0.7}$	$2.2^{0.1}_{0.4}$
GND-13191	$1.221^{0.015}_{0.013}$	$10.68^{0.04}_{0.03}$	$-11.5^{0.6}_{0.3}$	$0.57^{0.73}_{0.43}$	$9.88^{0.04}_{0.04}$	$1.0^{0.2}_{0.4}$	$2.3^{0.2}_{0.3}$
GND-14713	$1.228^{0.004}_{0.003}$	$10.79^{0.01}_{0.01}$	$-11.5^{0.1}_{0.3}$	$0.00^{0.02}_{0.00}$	$9.93^{0.03}_{0.03}$	$0.3^{0.2}_{0.3}$	$3.5^{0.1}_{0.4}$
GND-17070	$1.238^{0.004}_{0.002}$	$11.15^{0.02}_{0.03}$	$-12.0^{0.4}_{0.2}$	$0.00^{0.02}_{0.00}$	$10.36^{0.04}_{0.04}$	$1.5^{0.5}_{0.6}$	$4.3^{0.6}_{0.9}$
GSD-38785	$1.241^{0.011}_{0.010}$	$11.01^{0.03}_{0.04}$	$-11.0^{0.4}_{0.2}$	$0.21^{0.30}_{0.16}$	$9.77^{0.05}_{0.05}$	$1.6^{0.3}_{0.6}$	$3.3^{0.5}_{0.6}$
GND-21156	$1.254^{0.002}_{0.002}$	$11.30^{0.02}_{0.01}$	$-11.3^{0.1}_{0.3}$	$0.33^{0.38}_{0.28}$	$10.24^{0.03}_{0.03}$	$1.6^{0.5}_{1.1}$	$3.4^{0.7}_{1.1}$
GSD-35774	$1.257^{0.003}_{0.002}$	$11.21^{0.01}_{0.03}$	$-12.0^{0.4}_{0.3}$	$0.02^{0.03}_{0.01}$	$10.12^{0.03}_{0.03}$	$1.4^{0.3}_{0.4}$	$3.6^{0.4}_{0.4}$
GND-37686	$1.259^{0.001}_{0.003}$	$11.11^{0.03}_{0.03}$	$-12.2^{0.7}_{0.2}$	$0.03^{0.09}_{0.01}$	$10.23^{0.03}_{0.03}$	$0.5^{0.3}_{1.0}$	$3.5^{0.2}_{0.7}$
GSD-40862	$1.333^{0.005}_{0.004}$	$11.11^{0.02}_{0.02}$	$-10.9^{0.1}_{0.3}$	$0.45^{0.50}_{0.41}$	$9.90^{0.05}_{0.05}$	$1.5^{0.1}_{0.2}$	$3.2^{0.2}_{0.2}$
GSD-46066	$1.333^{0.003}_{0.003}$	$11.10^{0.02}_{0.02}$	$-12.5^{0.1}_{0.3}$	$0.00^{0.01}_{0.00}$	$10.20^{0.03}_{0.03}$	$0.3^{0.2}_{0.2}$	$6.5^{0.5}_{1.0}$
GSD-39804	$1.339^{0.004}_{0.002}$	$11.09^{0.02}_{0.02}$	$-11.5^{0.3}_{0.1}$	$0.34^{0.37}_{0.23}$	$10.35^{0.04}_{0.04}$	$1.0^{0.2}_{0.4}$	$3.0^{0.2}_{0.3}$
GSD-45775	$1.352^{0.005}_{0.007}$	$11.28^{0.03}_{0.02}$	$-11.3^{0.1}_{0.1}$	$0.08^{0.13}_{0.05}$	$9.74^{0.04}_{0.04}$	$1.4^{0.2}_{0.4}$	$5.8^{0.5}_{1.2}$
GND-36530	$1.362^{0.003}_{0.002}$	$11.02^{0.01}_{0.01}$	$-11.3^{0.5}_{0.1}$	$0.00^{0.01}_{0.00}$	$10.03^{0.03}_{0.03}$	$0.7^{0.1}_{0.2}$	$3.3^{0.1}_{0.3}$
GSD-40623	$1.414^{0.005}_{0.003}$	$11.04^{0.02}_{0.01}$	$-12.1^{0.1}_{0.4}$	$0.05^{0.08}_{0.01}$	$10.00^{0.03}_{0.03}$	$0.3^{0.3}_{0.4}$	$9.3^{1.2}_{1.8}$
GND-24345	$1.415^{0.012}_{0.014}$	$10.57^{0.01}_{0.04}$	$-11.6^{0.5}_{0.2}$	$0.00^{0.04}_{0.00}$	$9.92^{0.03}_{0.03}$	$0.9^{0.2}_{0.2}$	$4.9^{0.6}_{0.6}$
GND-16574	$1.456^{0.005}_{0.005}$	$10.58^{0.03}_{0.04}$	$-11.7^{0.2}_{0.5}$	$0.18^{0.34}_{0.05}$	$9.89^{0.04}_{0.04}$	$1.0^{0.3}_{0.3}$	$3.1^{0.3}_{0.3}$
GND-21427	$1.472^{0.010}_{0.009}$	$10.92^{0.02}_{0.02}$	$-11.4^{0.4}_{0.3}$	$0.31^{0.42}_{0.24}$	$10.06^{0.03}_{0.03}$	$1.1^{0.1}_{0.4}$	$2.7^{0.1}_{0.4}$
GSD-40223	$1.599^{0.004}_{0.002}$	$10.87^{0.05}_{0.02}$	$-11.3^{0.3}_{0.3}$	$0.41^{0.46}_{0.32}$	$10.06^{0.05}_{0.05}$	$1.2^{0.2}_{0.6}$	$4.4^{0.5}_{1.0}$
GSD-39649	$1.603^{0.002}_{0.001}$	$10.75^{0.02}_{0.03}$	$-12.1^{0.5}_{0.5}$	$0.29^{0.39}_{0.21}$	$10.04^{0.03}_{0.03}$	$1.3^{0.2}_{0.4}$	$3.2^{0.3}_{0.4}$
GSD-42487	$1.605^{0.001}_{0.001}$	$10.94^{0.03}_{0.02}$	$-11.6^{0.4}_{0.2}$	$0.42^{0.49}_{0.31}$	$10.25^{0.03}_{0.03}$	$1.1^{0.2}_{0.3}$	$3.1^{0.2}_{0.4}$
GSD-38843	$1.611^{0.006}_{0.006}$	$10.54^{0.04}_{0.04}$	$-12.1^{0.5}_{0.5}$	$0.31^{0.40}_{0.19}$	$9.69^{0.05}_{0.05}$	$1.4^{0.3}_{0.5}$	$4.3^{0.8}_{1.0}$
GSD-39012	$1.612^{0.006}_{0.005}$	$11.15^{0.02}_{0.02}$	$-11.7^{0.4}_{0.1}$	$0.49^{0.56}_{0.44}$	$10.20^{0.03}_{0.03}$	$0.3^{0.3}_{0.8}$	$7.4^{1.2}_{1.4}$
GSD-41520	$1.614^{0.001}_{0.004}$	$11.08^{0.02}_{0.03}$	$-11.6^{0.4}_{0.2}$	$0.24^{0.30}_{0.17}$	$10.29^{0.04}_{0.04}$	$1.1^{0.4}_{0.3}$	$4.1^{0.8}_{0.3}$
GSD-44042	$1.616^{0.003}_{0.003}$	$11.22^{0.03}_{0.04}$	$-11.1^{0.2}_{0.1}$	$0.63^{0.70}_{0.57}$	$10.24^{0.04}_{0.04}$	$0.8^{0.2}_{0.3}$	$3.3^{0.3}_{0.4}$
GND-33775	$1.652^{0.005}_{0.006}$	$10.59^{0.05}_{0.04}$	$-11.3^{0.6}_{0.4}$	$0.25^{0.32}_{0.19}$	$9.92^{0.04}_{0.04}$	$1.0^{0.2}_{1.0}$	$4.0^{0.5}_{1.1}$
GSD-42615	$1.755^{0.004}_{0.004}$	$11.03^{0.03}_{0.04}$	$-12.3^{0.4}_{0.5}$	$0.00^{0.31}_{0.00}$	$10.26^{0.04}_{0.04}$	$1.0^{0.4}_{0.4}$	$6.3^{2.0}_{1.6}$
GSD-41148	$1.763^{0.002}_{0.003}$	$11.22^{0.04}_{0.03}$	$-11.8^{0.3}_{0.4}$	$0.33^{0.41}_{0.26}$	$10.21^{0.04}_{0.04}$	$0.9^{0.3}_{0.4}$	$4.1^{0.6}_{0.6}$

GND-33780	$1.876^{0.016}_{0.016}$	$11.37^{0.03}_{0.03}$	$-11.6^{0.6}_{0.6}$	$0.00^{0.05}_{0.00}$	$10.19^{0.04}_{0.04}$	$0.7^{0.2}_{0.8}$	$4.0^{0.2}_{1.1}$
GND-17735	$1.876^{0.009}_{0.014}$	$11.08^{0.02}_{0.03}$	$-11.3^{0.4}_{0.5}$	$0.17^{0.26}_{0.11}$	$10.26^{0.04}_{0.04}$	$0.9^{0.2}_{0.4}$	$3.3^{0.3}_{0.5}$
GND-19850	$1.876^{0.006}_{0.007}$	$10.81^{0.03}_{0.02}$	$-12.1^{0.4}_{0.4}$	$0.00^{0.02}_{0.00}$	$10.09^{0.03}_{0.03}$	$1.2^{0.2}_{0.3}$	$4.5^{0.6}_{0.7}$
GSD-24569	$1.901^{0.001}_{0.002}$	$10.83^{0.01}_{0.02}$	$-11.6^{0.3}_{0.3}$	$0.24^{0.31}_{0.17}$	$10.20^{0.02}_{0.02}$	$0.7^{0.1}_{0.2}$	$2.9^{0.1}_{0.2}$
GSD-24315	$1.988^{0.004}_{0.003}$	$10.54^{0.02}_{0.02}$	$-11.5^{0.5}_{0.7}$	$0.41^{0.52}_{0.25}$	$9.93^{0.03}_{0.03}$	$0.6^{0.1}_{0.3}$	$2.9^{0.2}_{0.3}$
GND-14132	$2.017^{0.015}_{0.052}$	$11.02^{0.03}_{0.02}$	$-11.3^{0.3}_{0.3}$	$0.00^{0.03}_{0.00}$	$10.18^{0.03}_{0.03}$	$1.0^{0.2}_{0.3}$	$4.5^{0.4}_{0.6}$
GSD-43572	$2.057^{0.034}_{0.039}$	$11.05^{0.04}_{0.03}$	$-11.0^{0.5}_{0.2}$	$0.31^{0.43}_{0.20}$	$9.88^{0.05}_{0.05}$	$1.0^{0.2}_{0.3}$	$5.4^{1.0}_{0.9}$
GND-21738	$2.092^{0.007}_{0.008}$	$11.19^{0.04}_{0.06}$	$-11.9^{0.7}_{0.4}$	$0.07^{0.15}_{0.04}$	$10.36^{0.06}_{0.06}$	$1.0^{0.3}_{0.4}$	$5.8^{1.2}_{1.2}$
GND-32933	$2.131^{0.019}_{0.017}$	$10.71^{0.03}_{0.03}$	$-10.3^{0.2}_{0.3}$	$0.36^{0.47}_{0.26}$	$9.94^{0.04}_{0.04}$	$1.1^{0.1}_{0.4}$	$4.6^{0.3}_{0.9}$
GND-17599	$2.140^{0.002}_{0.002}$	$10.88^{0.03}_{0.03}$	$-12.0^{0.7}_{0.4}$	$0.16^{0.27}_{0.09}$	$10.30^{0.03}_{0.03}$	$0.8^{0.3}_{0.3}$	$4.4^{0.9}_{0.6}$
GSD-44133	$2.184^{0.005}_{0.006}$	$10.61^{0.02}_{0.02}$	$-10.7^{0.5}_{0.3}$	$0.33^{0.38}_{0.22}$	$9.62^{0.04}_{0.04}$	$0.9^{0.1}_{0.4}$	$3.6^{0.1}_{0.6}$
GND-23018	$2.302^{0.017}_{0.016}$	$11.24^{0.03}_{0.04}$	$-10.8^{0.1}_{0.1}$	$0.07^{0.09}_{0.05}$	$10.15^{0.04}_{0.04}$	$0.7^{0.1}_{0.2}$	$7.6^{1.0}_{1.4}$
GSD-48464	$2.349^{0.007}_{0.012}$	$11.22^{0.02}_{0.02}$	$-10.7^{0.1}_{0.2}$	$0.34^{0.40}_{0.30}$	$10.31^{0.03}_{0.03}$	$0.8^{0.1}_{0.2}$	$4.9^{0.2}_{0.5}$

Table B.2: (1) catalog ID number (matching those in (16)) and line-matched to those in Table B.1; All other quantities are derived from the model fits to the full grism and photometric dataset. (2) redshift; (3) stellar mass; (4) specific star-formation rate (where the SFR is the time averaged over the previous 100 Myr of the SFH); (5) dust attenuation A_V value for a Milky Way dust law; (6) stellar mass surface density within 1 kpc, $\log(\Sigma_1)$; (7) quenching timescale defined as t_{50} - t_{90}, the difference between the time when the galaxy had formed 50% (t_{50}) and 90% (t_{90}) of its stellar mass; (8) formation redshift (where the galaxy had formed 50% of its stellar mass); Note that we are using a highest density region to estimate our parameter fits, this reports the mode and smallest region containing 68% of the probability (17). Therefore if the mode of the probability distribution function is peaked at the bounds on the parameter, then the uncertainty will also be zero beyond that bound. This is the case for some values of A_V, for example, where the mode of the distribution function is A_V=0.0 mag (and the lower 68%-tile uncertainty is likewise 0.0 mag).

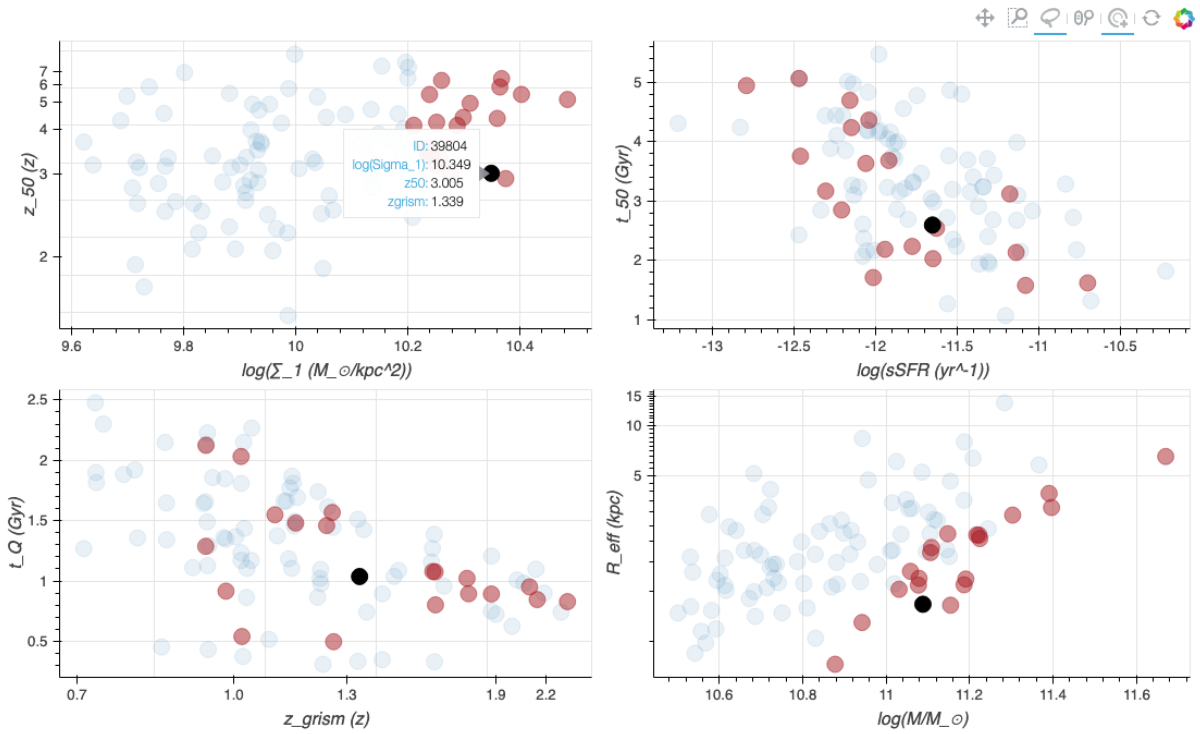

Figure B.1: Here we show an example of the usage of our interactive appendix (all data shown here were discussed in the text). Using the lasso tool we select all galaxies with $\log(\Sigma_1) > 10.2$, this population is highlighted in all plots. Additionally, by hovering over a galaxy, we get more information about it.

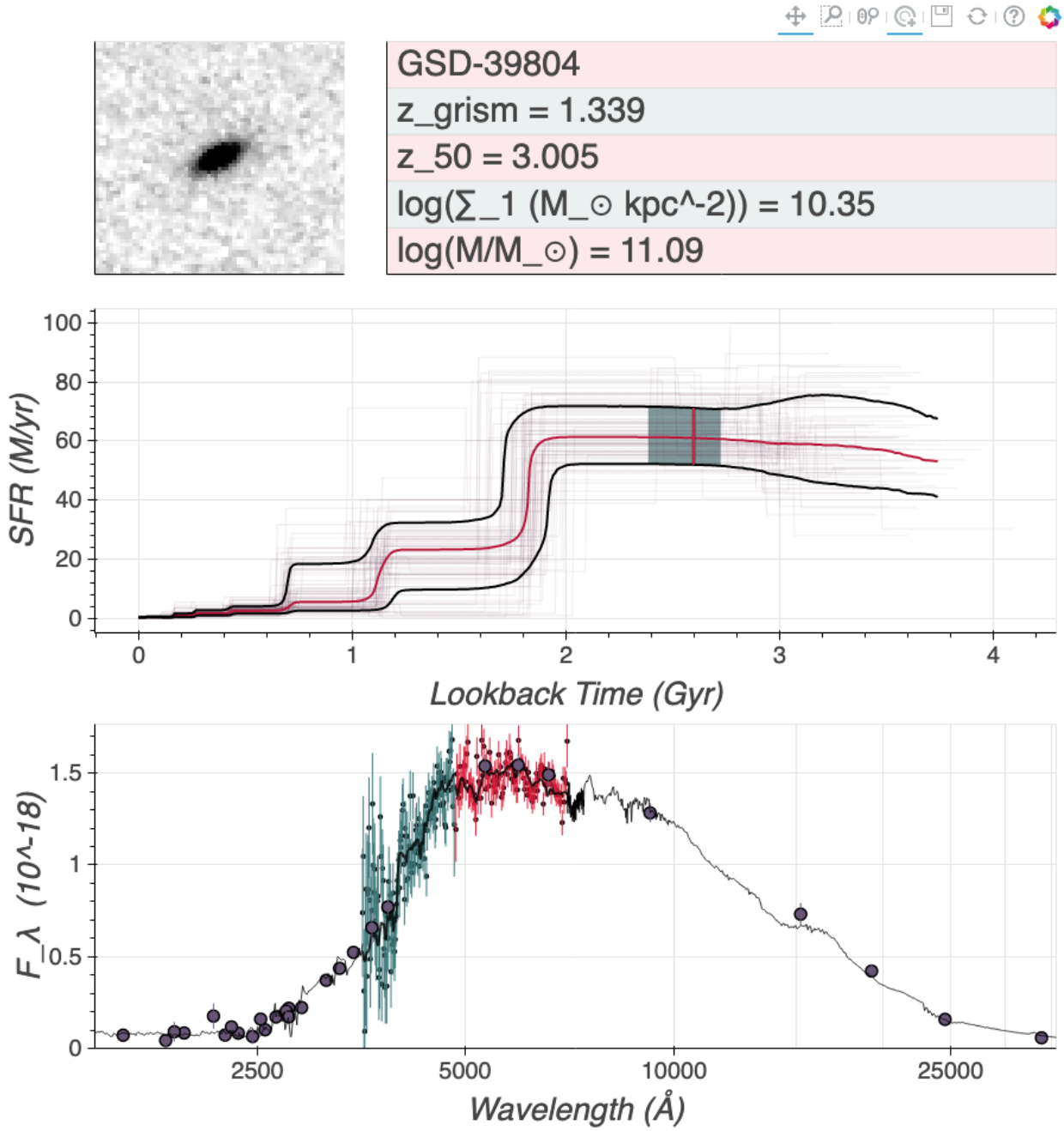

Figure B.2: Example bio page for galaxy GSD-39804. When a point in Figure B.1 is clicked it will bring up the galaxies bio page. These bio pages includes the galaxy's morphology, a data table, interactive SFH, and interactive spectra with best fit model.

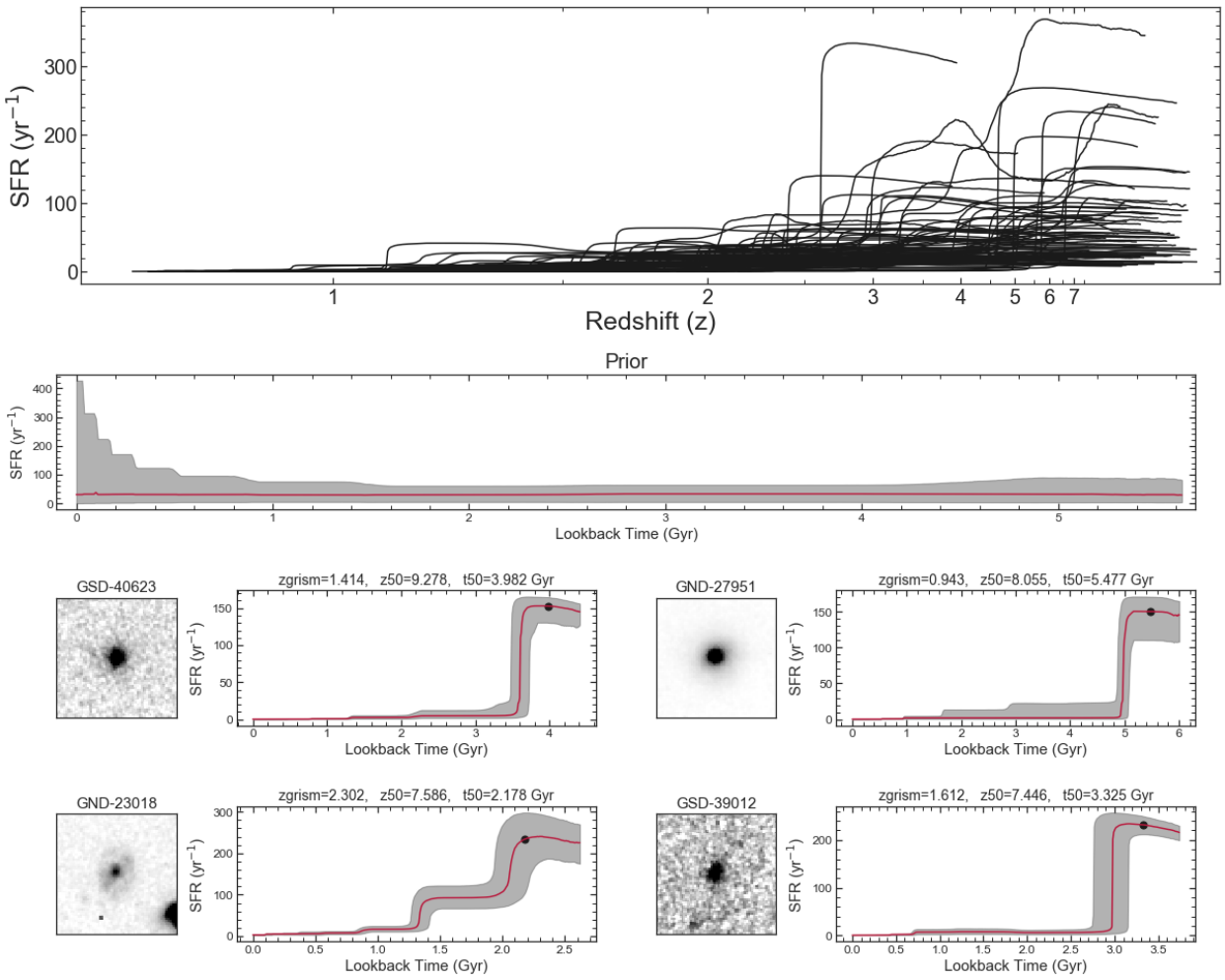

Figure B.3: A representative plot for a figure included in our appendix. The top plot shows all star-formation histories, plotted at their appropriate redshifts. The next plot down shows the prior we used to fit our "non-parametric" star-formation histories. The following plots are then the galaxy cutouts and star-formation histories for each galaxy, with their formation redshift marked with a point, and relevant information shown at the top of the figure (ordered by z_{50}).